Curso 2006/07
CIENCIAS Y TECNOLOGÍAS/20
I.S.B.N.: 978-84-7756-767-7

JUAN PEÑA MARTÍNEZ

Síntesis y caracterización de materiales con estructura tipo perovskita para pilas de combustible de óxido sólido de temperatura intermedia

Directores
PEDRO NÚÑEZ COELLO
JUAN CARLOS RUIZ MORALES

SERVICIO DE PUBLICACIONES
UNIVERSIDAD DE LA LAGUNA

SOPORTES AUDIOVISUALES E INFORMÁTICOS
Serie Tesis Doctorales

This thesis is dedicated to my family

"I believe that water will one day employed as fuel, that hydrogen and oxygen which constitute it, used singly or together, will furnish an inexhaustible source of heat and light".

The Mysterious Island
Jules Verne (1874)

Agradecimientos

Quiero expresar mi agradecimiento a los Doctores D. Pedro Núñez Coello y D. Juan Carlos Ruiz Morales por su acertada dirección, su ayuda en la realización de la presente tesis, sus innumerables comentarios y discusiones, y por haberme dado la gran oportunidad de trabajar con un magnífico grupo de investigación.

Mi agradecimiento más sincero al Dr. D. David Marrero López por sus consejos, su amistad, su compañerismo y su samaritana ayuda. No podría expresar en tan pocas líneas todo lo que realmente ha supuesto su apoyo en este trabajo. Su increíble capacidad de trabajo y bagaje científico ha sido un verdadero ejemplo a seguir. Le deseo todo lo mejor, se lo merece.

Agradezco sinceramente a los profesores Dr. D. John T.S. Irvine y Dr. D. Ludwig J. Gauckler su hospitalidad y ayuda prestada en sus respectivos grupos de investigación en mis estancias en la Universidad de St. Andrews e Instituto Tecnológico de Zürich. Sus discusiones e ideas han ayudado a mejorar notablemente este trabajo.

Agradezco de una manera muy especial a los doctores D. Jesús Canales Vázquez, D. Cristian Savaniu, D. Brandon E. Büergler y Dña. Anna Infortuna, que además de ofrecerme su valiosísima ayuda con diversas técnicas de caracterización y preparativa, hicieron muy amena y fácil mis estancias en St. Andrews y en Zürich. Es más, estoy en deuda con los Doctores J. Canales Vázquez y B.E. Büergler, por sus correcciones, ayuda y análisis de mi trabajo.

Quiero mostrar también mi agradecimiento al resto de los compañeros y amigos del grupo de investigación, Domingo, Diego, Abdel, Agustín, etc., y del Departamento de Química Inorgánica; muy especialmente a D. Luis Hernández González, que siempre y de buen humor ha resuelto innumerables problemas con los equipos y hornos, y a Dña. Asunción Herrera Bello por la ayuda administrativa.

No quisiera olvidarme del Dr. D. José Macías Hernández y de la Dra. Dña. Andrea Brito Alayón, ambos profesores del Departamento de Ingeniería Química, porque con ellos inicie mi tortuosa tesis. Por problemas financieros no pudimos seguir, y tuve que cambiar de grupo de investigación dos veces. En cualquier caso, agradezco sus enseñanzas y la confianza que pusieron en mí.

Por último, mi mayor agradecimiento es para mi familia, sobre todo para mi mujer, Margarita. Ella ha tenido que soportar estoicamente mi "*sin vivir*" y además facilitándome siempre su cariño y apoyo. No quisiera finalizar sin acordarme de mis hijos, Carlos y María, verdaderos expertos en mantenerme en vigilia muchas noches.

Acknowledgements

I want to thanks Dr. Pedro Núñez Coello and Dr. Juan Carlos Ruiz Morales for their guidance and help in the present thesis. We had many hours of interesting and challenging discussions that helped to improve my thesis. I am grateful to them for giving me the opportunity to work in a great research group.

I am deep in debt to Dr. David Marrero López for his advices, suggestions, friendship, and samaritan help. I am not able to express in a few lines how much represents his support on this thesis. His incredible capacity of work and scientific knowledge has been always an example to follow. I wish him all the best.

I would like to express my deep gratitude to Professors Dr. J.T.S. Irvine and Dr. L.J. Gauckler for their hospitality and important help in their research groups in the University of St. Andrews and Swiss Institute of Technology of Zurich. Their ideas and wise discussions have notably improved this work.

My sincerest thanks to Dr. Jesús Canales Vázquez, Dr. Cristian Savaniu, Dr. Brandon E. Büergler and Dr. Anna Infortuna who they help me applying several techniques of characterisation and material preparation. They facilitated me so much my work in St. Andrews and Zürich. Furthermore, Dr. J. Canales Vázquez and B.E. Büergler have been working so hard analysing and correcting my ideas, experimental work, and moreover my "*Spanglish*".

I would also like to thank to my colleagues and friends of the research group and the Inorganic Chemistry Department: Domingo, Diego, Abdel, Agustín, etc. Special thanks to Mr. Luis Hernández González, who has kindly fixed me a lot of problems with the equipments and furnaces, and Ms. Asunción Herrera Bello for her help in the administrative work.

I would like to thanks to Dr. José Macías Hernández and Dr. Andrea Brito Alayón, both professors of the Chemical Engineering Department because they were my first supervisors in my tortuous research work. I started with them however due to financial support problems the research group had to be changed twice. Nevertheless, I am grateful for their help in my initial research works.

Finally, my highest appreciation is addressed to my family, in special to my wife, Margarita, who has constantly supported me. I wouldn't like to finish without remembering my son and daughter, Carlos and María, who have been real experts to keep me awake many nights.

Resumen

El objetivo del presente trabajo ha sido el desarrollo de un pila de combustible de óxidos sólidos (SOFC) para aplicaciones de temperatura intermedia (873-1073 K) basada en materiales con estructura tipo de perovskita. Como materiales cerámicos de electrolito, se han estudiado materiales basados en el galato de lantano, $LaGaO_3$, concretamente $La_{0,9}Sr_{0,1}Ga_{0,8}Mg_{0,2}O_{3-\delta}$ (LSGM) y $La_{0,9}Sr_{0,1}Ga_{0,8}Mg_{0,115}Co_{0,085}O_{3-\delta}$ (LSGMC), debido a su alta conductividad iónica y estabilidad frente a un rango elevado de presiones parciales de oxígeno.

En cuanto a materiales de electrodo, se han investigado diferentes conductores mixtos (iónicos-electrónicos) basados en las manganitas, cobaltitas y cromitas de lantano. Para su síntesis, se han utilizado métodos de precursores como sol-gel y liofilización, además de la clásica reacción en estado sólido, al objeto de reducir el tamaño de grano de los materiales policristalinos, y por lo tanto mejorar la microestructura de dichos materiales. Estos materiales han sido estructural y eléctricamente caracterizados por diversas técnicas, como XRD, SEM, TG/DTA, TMA, DSC, adsorción de N_2, picnometría, espectroscopía de impedancia compleja, métodos de Van der Pauw y Gorelov y tests electroquímicos, mediante ciclo-voltametría, de los distintos materiales ensamblados en pilas monocelda, siguiendo un diseño típico de electrolito soportado, y usando $5\%H_2/Ar$ e H_2 puro humidificados como combustibles, y oxígeno y aire como gases oxidantes.

Empleando LSGM como electrolito, en capa fina preparado por *tape casting* y con un espesor de 120 µm, y como cátodo y ánodo, $La_{0,8}Sr_{0,2}MnO_{3-\delta}$ (LSM) y $La_{0,75}Sr_{0,25}Cr_{0,5}Mn_{0,5}O_{3-\delta}$ (LSCM) respectivamente, se obtuvo una densidad de potencia de 570 $mWcm^{-2}$ a 1073 K. Aun así, se investigaron otros materiales de cara a reducir los sobrepotenciales de electrodo. En este sentido, el sobrepotencial catódico del material $Ba_{0,5}Sr_{0,5}Co_{0,8}Fe_{0,2}O_{3-\delta}$ (BSCF) fue considerablemente inferior al sobrepotencial del material LSM.

Además, se estudió la resistencia de polarización de dichos materiales fijados a LSGM como electrolito, y BSCF fue el material con la menor resistencia de polarización en aire, menos de 0,1 Ωcm^2 a temperaturas superiores a 1025 K, mientras que la resistencia de polarización del material LSCM era la inferior en condiciones reductoras, 0,3 Ωcm^2 a 1073 K. Extrapolando los datos de las curvas corriente-voltaje de la pila BSCF/LSGM/LSCM, se ha estimado una posible densidad de potencia de 1,6 Wcm^{-2} a 3,6 Acm^{-2} usando LSGM en capa fina (120 µm de espesor) y $5\%H_2/Ar$ humidificado como combustible y aire como gas oxidante.

Se ha investigado también un nuevo diseño de pilas SOFC, donde se utiliza el mismo material para cátodo y ánodo (pilas simétricas). Las cromitas de lantano dopadas, al ser estables en ambiente oxidante y reductor cumplen con los requisitos necesarios para funcionar como material de electrodo en este tipo de pilas. Los ensayos realizados indican una posible densidad de potencia de 0,7 Wcm^{-2} a 1073 K con la pila LSCM/LSGM/LSCM, usando 5%H_2/Ar humidificado como combustible y aire como gas oxidante.

Summary

The aim of the present work has been to develop an efficient solid oxide fuel cell (SOFC) for intermediate temperature applications (873-1073 K) based upon perovskite-type structure materials. This study has been focused on the electrochemical performance of doped lanthanum gallate materials i.e $La_{0.9}Sr_{0.1}Ga_{0.8}Mg_{0.2}O_{3-\delta}$ (LSGM) and $La_{0.9}Sr_{0.1}Ga_{0.8}Mg_{0.115}Co_{0.085}O_{3-\delta}$ (LSGMC) used as electrolyte materials due to their high ionic conductivity and chemical stability under a widely range of oxygen partial pressures. Different perovskyte-type structure and mixed ionic electronic conductors i.e. doped lanthanum manganites, cobaltites and chromites have been investigated for electrode materials. It was used alternative synthesis methods e.g. modified sol-gel route and freeze-drying method to the conventional solid-state reaction in order to reduce the grain size of the polycrystalline materials, hence to improve their microstructure. These materials have been structural and electrically characterised by several techniques as XRD, SEM, TG/DTA, TMA, DSC, N_2 adsortion, pycnometry, impedance spectroscopy, Van der Pauw y Gorelov methods and fuel cell tests in double chamber configuration and conventional electrolyte-supported cell design, using wet 5% H_2/Ar and pure hydrogen as fuel and pure O_2 as oxidant.

The best power output, 570 mWcm^{-2} at 1073 K, was achieved using wet H_2 and O_2 with a LSGM electrolyte, prepared by tape casting with a thickness of about 120 μm, and $La_{0.8}Sr_{0.2}MnO_{3-\delta}$ (LSM) and $La_{0.75}Sr_{0.25}Cr_{0.5}Mn_{0.5}O_{3-\delta}$ (LSCM) as cathode and anode materials, respectively. However, further investigations using other perovskite-type materials indicated that the cathodic overpotential of $Ba_{0.5}Sr_{0.5}Co_{0.8}Fe_{0.2}O_{3-\delta}$ (BSCF) material on LSGM electrolyte based cells was considerably lower than the LSM one. An area-specific-resistance (ASR), namely polarisation resistance, study confirmed the low polarisation resistance in air of BSCF on LSGM electrolyte, 0.1 Ωcm^2 at temperatures above 1025 K, whereas the lower polarisation resistance in reducing conditions corresponds to LSCM material, 0.3 Ωcm^2 at 1073 K. A theoretical extrapolation of the current-voltage characteristics of the BSCF/LSGM/LSCM cells showed a possible maximum power density of 1.6 Wcm^{-2} using a 120 μm thick LSGM electrolyte at 3.6 Acm^{-2} and using wet 5%H_2/Ar as fuel and air as oxidant.

A new design of LSGM based SOFCs, where the cathode and the anode are constituted by the same material, therefore with a symmetric configuration, has been also investigated, attending to the structural and chemical stability of doped lanthanum chromites in oxidant and reducing conditions. A theoretical extrapolation of the symmetric LSCM/LSGM/LSCM cell indicated a maximum power density of 0.7 Wcm^{-2} at 1073 K using wet 5%H_2/Ar as fuel and air as oxidant.

Table of contents

Chapter 1. Introduction...23

1.1 Energy and environmental considerations......................................23

1.2. Fuel cells 24
1.2.1. Principle of fuel cells 24
1.2.2. Types of fuel cells. 24

1.3. Solid oxide fuel cell (SOFC) 26
1.3.1. Principle of SOFC...26
1.3.2. Cell components...29
1.3.3. Historical background and the state-of-the-art of SOFCs.............30
1.3.4. Design of SOFCs 32

1.4. Solid oxide ion conductors 33
1.4.1. Defect chemistry in solid oxides..34
1.4.2. Mechanisms of ionic conductivity 36
1.4.3. Electronic and ionic conductivity dependence of Po_2..................37
1.4.4. Typical solid ion conductors...39
1.4.4.1. Fluorite-type structure oxides 39
1.4.4.2. Perovskite and perovskite-related structure oxides................40
1.4.4.3. LAMOX 44
1.4.4.4. Apatites 46
1.4.4.5. Bi_2O_3 and BIVEMOX 46
1.4.4.6. Brownmillerites...46

1.5. Aim of this study 47
1.5.1. Structure of this thesis...49

1.6. References..50

Chapter 2. Experimental 53

2.1. Introduction 53

2.2 Preparative Methods 54
2.2.1 Ceramic method 54
2.2.1.1 Powder preparation 54
2.2.2 Precursor synthesis routes..55
2.2.2.1 The sol-gel method...55
2.2.2.2 Freeze-drying method 56
2.2.3. Thin film electrolyte preparation by tape casting 58

2.3 Structural characterisation...60

2.3.1 X-ray diffraction (XRD) 60
2.3.2. Scanning electron microscopy (SEM) 61

2.4. Thermal analysis 62
2.4.1. Thermogravimetric/Differential Thermal Analysis (TG/DTA) 62
2.4.2. Thermomechanical analysis (TMA) 63
2.4.3. Differential scanning calorimetry (DSC) 63

2.5. Surface area determination by gas adsorption 64

2.6. Density determination by pycnometry 64

2.7. Electrical characterisation 65
2.7.1. Electrochemical impedance spectroscopy (EIS) 65
  2.7.1.1. Impedance spectra 67
  2.7.1.2. Equivalent circuit modelling 68
  2.7.1.3. Calculation of electrical conductivities 71
  2.7.1.4. Experimental set-ups for electrical characterisation 72
    2.7.1.4.1. Total conductivity 72
    2.7.1.4.2. Area specific resistance (ASR) 73
    2.7.1.4.3. Conductivity versus oxygen partial pressure 74
2.7.2. Van der Pauw method 76
2.7.3. Modified *emf* method of Gorelov 76
2.7.5. Fuel cell tests 80
  2.7.5.1. Basic aspects 80
  2.7.5.2. Set-ups for fuel cell tests 83

2.8. References 86

Chapter 3. Anodic Performance and ITSOFC Testing of LSCM 87

3.1. Introduction 87

3.2. Experimental procedures 89
3.2.1. Electrolyte and electrode preparation 89
3.2.2. Tape casting preparation 89
3.2.3. Material characterisation 89
3.2.4. Electrochemistry measurements 90

3.3. Results and discussions 91
3.3.1. Chemical compatibility 91
3.3.2. Fuel Cell Tests 94
  3.3.2.1. Series and polarisation resistances 94
  3.3.2.2. Anodic overpotential 95
  3.3.2.3. Power density 96

3.4. Conclusions......98

3.5. Acknowledgements......98

3.6. References......99

Chapter 4. ITSOFC Testing of BSCF......101

4.1. Introduction......101

4.2. Experimental......102
4.2.1. Preparation and characterisation of the materials......102
4.2.2. Fuel cell tests......103

4.3. Results and Discussion......104
4.3.1. Characterisation and compatibility of the materials......104
4.3.2. Electrolyte and electrode resistances......105
4.3.3. Power density......105
4.3.4. Electrode overpotentials......105
4.3.5. Electrode interfaces......106

4.4. Conclusions......108

4.5. Acknowledgements......108

4.6. References......108

Chapter 5. Fuel Cell Studies of Perovskite-Type Materials......109

5.1. Introduction......109

5.2. Experimental......110
5.2.1. Electrodes and electrolyte preparation......110
5.2.2. Material characterisation......111
5.2.3. Fuel cell tests......111

5.3 Results and Discussion......112
5.3.1. BSCF and SDC characterisation......112
5.3.2. Chemical compatibility......113
5.3.3. Electrochemical characterisation......116
5.3.3.1. Electrolyte and electrode resistances......116
5.3.3.2. Power density......118
5.3.3.3. Electrode overpotentials......120

5.4. Conclusions......121

5.5 Acknowledgements......121

5.6. References...122

Chapter 6. Performance of XSCoF and LSCrX' 123

6.1. Introduction 123

6.2. Experimental...125
6.2.1. Synthesis of electrodes and electrolytes 125
6.2.2. Materials characterisation..126
6.2.3. Electrochemical characterisation 127
6.2.3.1. Area-specific resistance (ASR) measurements 127
6.2.3.2. Fuel cell tests...128

6.3. Results and Discussion 128
6.3.1. Structural characterisation 128
6.3.2. Chemical compatibility study 128
6.3.3. Electrochemical characterisation 131
6.3.3.1 Area-specific resistance (ASR) 131
6.3.3.1.1 ASR of XSCoF (X=Ba, La and Sm) and SSCo.............131
6.3.3.1.2. ASR of LSCrX' (X'=Mn, Fe and Al)............................133
6.3.3.1.3. ASR of SDC composites 133
6.3.3.2. Fuel cell tests...133
6.3.3.2.1. Power density 133
6.3.3.2.2. Series and polarisation resistance.................................134
6.3.3.2.3. Electrode overpotential..136

6.4. Conclusions..140

6.5. Acknowledgements 140

6.6 References..141

Chapter 7. Outlook 143

7.1. Perovskite-type structure materials..143
7.1.1. Doped $LaGaO_3$ compounds as electrolyte materials 143
7.1.2. MIECs as cathode and anode materials 144
7.1.2.1 $La_{0.75}Sr_{0.25}Cr_{0.5}Mn_{0.5}O_{3-\delta}$ as anode 145
7.1.2.2 $Ba_{0.5}Sr_{0.5}Co_{0.8}Fe_{0.2}O_{3-\delta}$ as cathode 145
7.1.2.3.Fuel cell studies of perovskite-type materials....................146
7.1.2.4 XSCoF (X=Ba, La, Sm) and LSCrX' (X'=Mn, Fe, Al) 147

7.2. Preparative methods...148

7.3. Future works...148

7.4 References...150

Conclusions **151**

Conclusiones **153**

Appendix I. Structural studies by X-ray diffraction **157**

Appendix II. BET surface area **161**

Appendix III. Density by helium pycnometry **165**

Appendix IV. Ionic transport numbers **167**

Abbreviations **169**

Symbols **170**

List of publications **171**

Chapter 1

Introduction

Abstract

This chapter provides a general introduction to fuel cells and specifically to solid oxide fuel cells (SOFC) which are the subject of the present work. The state-of-the-art of this technology is reviewed as well as the theoretical background of solid state ionic conduction. Finally, the aim of the thesis is indicated.

1.1 Energy and environmental considerations

It is well established that global warming is due to effluent gas emission, mainly CO_2. During the last century, global surface temperature has increased at a rate of nearly 0.6ºC/century [1]. This trend has dramatically increased during the past 25 years, around 2ºC [2]. Global temperatures in 2001 were 0.52ºC higher than the long-term 1880-2000 average. World emissions of carbon dioxide are expected to increase in a 54% above 1990 levels by 2015, making the earth likely to warm 1.7-4.9ºC over the period 1990-2100 [2].

Indeed, world population is expected to grow at 1.2-2% per year to reach 8,900 million in 2050 [3]. Global demand for energy is expected to increase 3.2% per year over the period 2002-2030 [3]. As worldwide oil supplies decreases, the development of new highly efficiently power generation technologies will become increasingly important.

Energy is one of the main factors that must be considered in discussions of sustainable development. In response to the critical need for a cleaner energy technology, some potential solutions have been involved, including energy conservation through improved energy efficiency, reduction in the consumption of fossil fuels, and an increase in the supply of environmental-friendly energy, such as renewable sources and fuel cells [4]. One kind of these fuel cells are the solid oxide fuel cell (SOFC) which is an efficient and environmental-friendly technology available for generating power from hydrogen, natural gas, and other renewable fuels.

Large-scale, SOFC power generation systems have reached pilot-scale demonstration stages in the US, Europe and Japan. Small-scale SOFC systems are being developed for military, residential, industrial, and transport applications [2,5-7].

1.2. Fuel cells

1.2.1. Principle of fuel cells

Fuel cells are a different way of making electrical power from a variety of fuels. A fuel cell is an energy conversion device that produces electricity (and heat) directly by the electrochemical combination of a fuel and an oxidant without the need of direct combustion as an intermediate step, giving much higher conversion efficiencies than conventional thermal and mechanical energy conversion. In addition to the high conversion efficiency, fuel cells have the following characteristics:

- Environmental compatibility: Fuel cells are capable of using practical fuels as an energy source with insignificant environmental impact. Emissions of key pollutants from fuel cells are several orders of magnitude lower than those produced by conventional power generators. Production of undesirable materials such as NO_x, SO_x, and particles is either negligible or undetectable from fuel cell systems.

- Modularity and flexibility: Fuel cell size can be easily increased or decreased, due to their modular feature. In addition, Fuel cell operation is quiet because a fuel cell has no moving parts; the only source of noises is coming from auxiliary equipment.

- Multifuel capability: Certain types of fuel cells have multifuel capability. Because of their high operation temperature (~1273 K), natural gas fuel can be reformed inside the cell stack eliminating an expensive external reformer system.

The operating principles of fuel cells are similar to those of batteries, i.e., electrochemical combination of reactants to generate electricity. However, unlike a battery, a fuel cell does not run down or require recharging as long as both fuel and oxidant are supplied to the electrodes.

1.2.2. Types of fuel cells.

Fuel cells are generally classified by the chemical characteristics of the electrolyte used as ionic conductor in the cell. Their main characteristics are summarised in Table 1.1. The first three types, proton-exchange membrane (PEMFC), phosphoric acid (PAFC), and alkaline (AFC) are characterised by their low temperature of operation (323-483 K), with electrical generation efficiencies reaching 50%. The latter two types, molten carbonate (MCFC), and solid oxide (SOFC) are characterised by their high temperature of operation (873-1273 K), their ability to use methane directly in the fuel cell and their higher generation efficiency which could be increased with cogeneration or in a bottoming cycle for electric power generation [2,7].

Table 1.1.
Typical characteristics of different fuel cells.

	PEMFC	PAFC	AFC	MCFC	SOFC
Electrolyte	Nafion	H_3PO_4	KOH solution	Li_2CO_3-K_2CO_3	Ceramic
Cathode	PTFE/Pt/C	PTFE/Pt/C	Pt-Au	Li-doped NiO	La(Sr)MnO_3
Anode	PTFE/Pt/C	PTFE/Pt/C	Pt-Pd	Ni	Cermet-Ni
Interconnector	Graphite	Glassy carbon	Ni	SS with Ni	Doped $LaCrO_3$
Operating T (K)	323-353	433-473	323-483	903-923	1073-1273
Fuel	H_2	H_2	H_2	H_2, CO, CH_4	H_2, CO, CH_4
Oxidant	Air, O_2	Air, O_2	Air, O_2	Air, CO_2,O_2	Air, O_2
Efficiency (%)	40-50	40-50	50-55	50-60*	45-60*

PTFE: polytetrafluoroethylene.
Nafion: Perfluorosulfonic acid membrane
SS: Stainless steel clad
*Integrated with combustion turbine power systems: 70-80%

Regarding the characteristics of the electrode materials, the porous electrodes used in low-temperature fuel cells consist of a composite structure that contains platinum (Pt) as electrocatalyst on a high surface area carbon black and a PTFE (polytetrafluoroethylene) as binder. In these porous electrodes, PTFE is hydrophobic (acts as a wet proofing agent) and serves as the gas permeable phase, and carbon black is an electron conductor that provides a high surface area to support the electrocatalyst. Platinum serves as the electrocatalyst, which promotes the rate of electrochemical reactions (oxidation/reduction) for a given surface area. The carbon black is also somewhat hydrophobic, depending on the surface properties of the material. The composite structure of PTFE and carbon establishes an extensive three-phase interface in the porous electrode. The technology used to obtain a stable three-phase interface in MCFC porous electrodes is different from that used in PAFCs. For MCFCs, the stable interface is achieved in the electrodes by carefully tailoring the porous structure of the electrodes and the electrolyte matrix so that the capillary forces establish a dynamic equilibrium in the different porous structures. In a SOFC, there is no liquid electrolyte susceptible of movement in the porous electrode structure, and thus electrode flooding is not a problem. Consequently, the three-phase interface necessary for efficient electrochemical reaction involves two solid phases (solid electrolyte and electrode) and a gas phase. A critical requirement of porous electrodes for SOFC is that they have to be sufficiently thin and porous to provide an extensive electrode/electrolyte interfacial region for electrochemical reaction. However, SOFC is an interesting option for clean and efficient electric power generation from a variety of fuels. In addition, the use of a solid electrolyte avoids material corrosion and electrolyte management problems (liquid electrolytes, for example, could be corrosive and difficult to handle) and it allows unique cell designs with performance improvements.

Besides SOFC, MCFC is another candidate for commercialisation, whereas PEMFC is being developed mainly for space and transportation applications, and the alkaline fuel cell is an important power source for space flights.

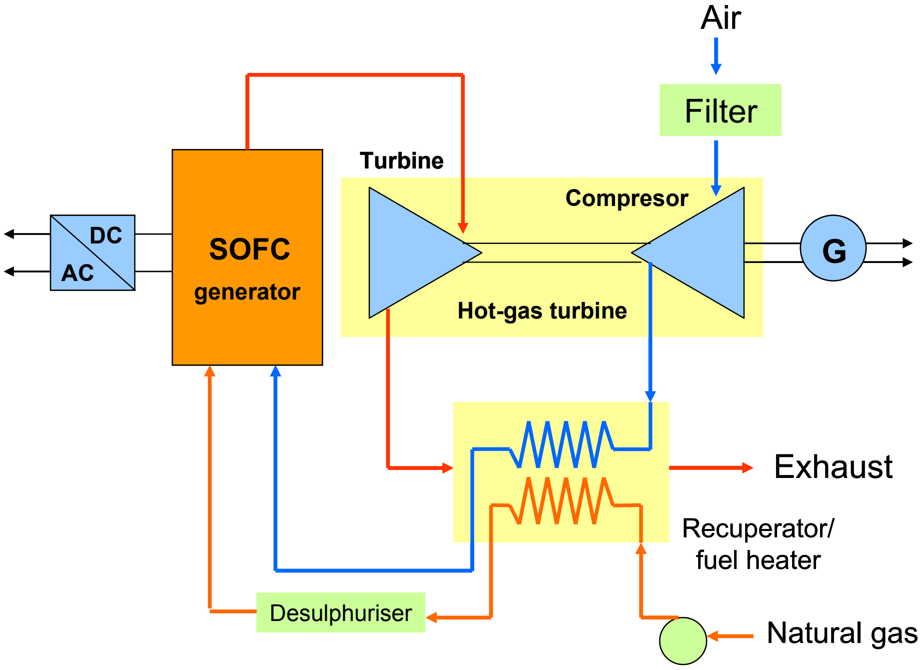

Figure 1.1. SOFC and gas turbine engine combination to improve the efficiency.

Taking into account SOFC operation conditions, the conductivity requirement for the ceramic electrolyte demands high operating temperatures (873 to 1273 K). High operating temperatures promote fast reaction kinetics and allow reforming of hydrocarbon fuels within the fuel cell (internal reforming). Furthermore, they produce high quality byproduct heat for cogeneration or bottoming cycles. Several electrical power companies [7] are working in hybrid fuel cell/gas turbine systems where the combustion chamber of the gas turbine engine is being replaced by the fuel cell module. A flow diagram for a natural gas fueled SOFC/gas turbine hybrid power cycle is presented in Figure 1.1. On the other hand, high operating temperatures restrict the number of available materials to be used as components. Thus the main issue in SOFC technology are the development of suitable materials and fabrication processes to incorporate these materials into the required structures.

1.3. Solid oxide fuel cell (SOFC)

1.3.1. Principle of SOFC

A solid oxide fuel cell (SOFC) is an all-solid-state energy conversion device that produces electricity by the electrochemical combination of gaseous fuel and oxidant through an ionic conducting ceramic. The operating principle of a SOFC is schematically shown in Figure 1.2. A SOFC consists of two electrodes (anode and cathode) separated by a solid electrolyte. Fuel is fed to the anode, undergoes an oxidation reaction, and releases electrons to the external circuit.

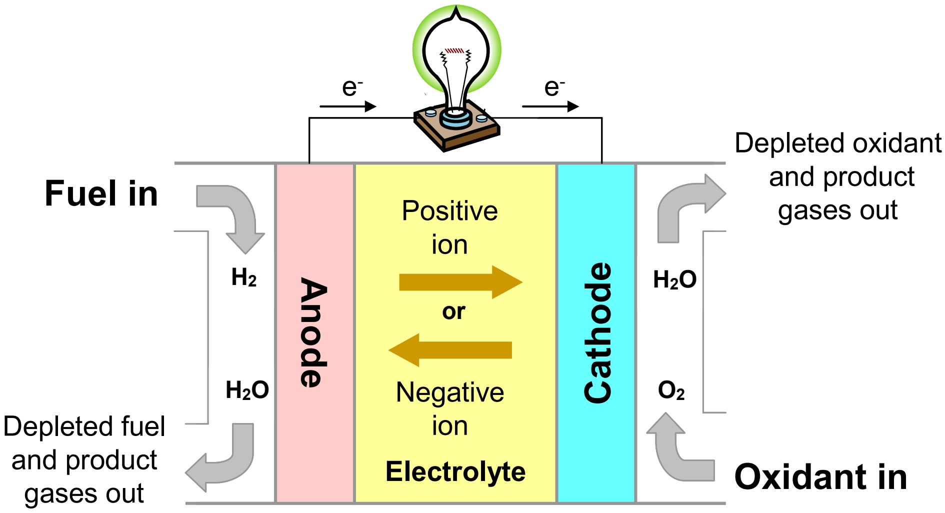

Figure 1.2. Principle of operation of SOFC.

Oxidant is fed to the cathode, accepts electrons from the external circuit, and undergoes a reduction reaction. The electron flow (from the anode to the cathode) produces direct-current electricity. The solid electrolyte conducts ions between the two electrodes. In theory, any gas able of being electrochemically oxidised and reduced can be used as fuel and oxidant, respectively, in a fuel cell. However, hydrogen is currently the most common fuel, since it has high electrochemical reactivity and can be obtained from common fuels such as hydrocarbons, alcohols, or coal. Reforming natural gas or other hydrocarbon fuels to extract the necessary hydrogen can be accomplished within the fuel cell, eliminating the need for an external reformer as it is the case for the other types of fuel cells. On the oxidant, oxygen is the most common since it is readily and economically available from air.

Due to the conductivity requirement for the oxide electrolyte, typical SOFCs operate in the temperature range of 873 K to 1273 K. A fuel cell electrolyte must ionically conduct one of the elements present in the fuel or oxidant. Thus, a solid electrolyte for SOFCs based on the electrochemical reactions of hydrogen and oxygen must conduct either oxide ions or hydrogen ions (protons). Although hydroxide-ion conduction is also possible, it has been shown to be a proton conduction with oxygen-ion carrier species. An oxygen-ion-conductor SOFC can be considered as an oxygen concentration cell, and a proton-conductor SOFC as a hydrogen concentration cell. The main difference between oxide ion- or proton-based SOFCs is the fuel cell side in which water is produced. This will be the fuel side in oxide-ion conductor cells and the oxidant side in proton-conductor cells. To date, almost all of the development work has focused on SOFCs with oxide-ion-conducting electrolytes. The operating principle of a SOFC with an oxide ion conductor is schematically shown in Figure 1.3.

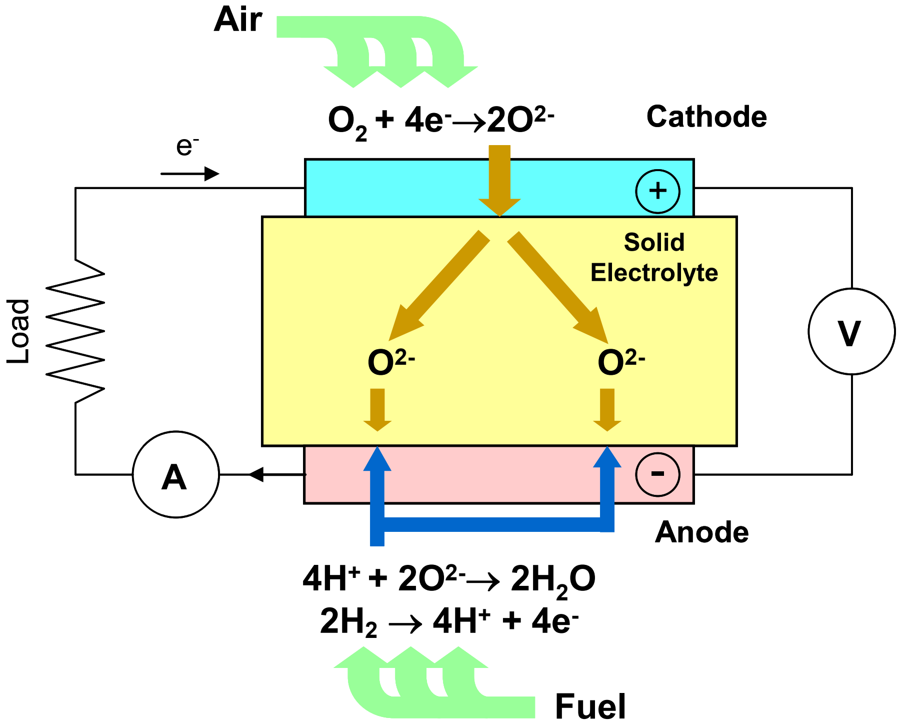

Figure 1.3. Principle of operation of a SOFC with an oxide ion conductor based electrolyte.

When an external load is applied to the cell, oxygen is reduced at the porous air electrode (cathode) to produce oxide ions. These ions migrate through the solid electrolyte to the fuel electrode (anode), and they react with the protons produced by the oxidation of the fuel, H_2, giving rise to H_2O. In the case of use CH_4, it can be oxidised directly on the anode to form CO_2 and H_2O (total oxidation), although other species can be produced such as CO and carbon.

The open-circuit voltage (OCV) of the cell can be calculated from the partial pressure of the oxygen at the cathode, $Po_2(c)$, and the anode, $Po_2(a)$:

$$OCV = \frac{RT}{nF} \ln \frac{Po_2(c)}{Po_2(a)} \tag{1.1}$$

In this equation, R is the gas constant, T the absolute temperature, F the Faraday constant, and n the electron equivalent of oxygen (n=4). The cell voltage at 1273 K is about 1 V for a SOFC working with pure hydrogen and air.

The cell voltage drops as current is drained due to polarisations. The total polarisation of a cell, η, depends on the electrode materials, the electrolyte, the cell design, and the operating temperature.

1.3.2. Cell components

As previously mentioned a SOFC single cell consists of a solid electrolyte between an anode and a cathode. Under typical operating conditions (with hydrogen fuel and oxygen oxidant), a single cell produces less than 1 V. Thus, practical SOFCs are not operated as single units. They are connected in electrical series to produce higher voltages and hence higher performances. Several cells connected in series are referred to as a stack. An extra component is necessary in this configuration to connect the anode of one cell with the cathode of the next one. This element is called interconnector or bipolar plate. SOFC stacks can be configured in series, parallel, both series and parallel, or as single units, depending on the particular application. Thereby, the principal components of a SOFC stack are the electrolyte, the anode, the cathode and the interconnector. The materials for each cell component have to be selected based on the following criteria:

- Proper stability (chemical, phase, morphological, and dimensional) in oxidising and/or reducing conditions.
- Chemical compatibility with other components in order to minimise reactivity and interdiffusion among them.
- Adecuate conductivity to perform their intended cell functions.
- Similar thermal expansion coefficients to avoid delamination or cracking during fabrication and operation.
- The electrolyte and interconnector must be dense to prevent gas mixing, while the anode and cathode must be porous to allow gas transport to the reaction sites.
- High catalytic activity for the reduction of the oxidant (cathode) or for the oxidation of the fuel (anode).

The requirements for the cell components are summarised in Table 1.2.

Table 1.2.
Requirements for SOFC components

Component	Conductivity		Stability	Porosity
	Ionic	Electronic		
Electrolyte	High	Negligible	In fuel and oxidant environments	Fully dense
Cathode	Desirable	High	In oxidant environments	Porous
Anode	Desirable	High	In fuel environments	Porous
Interconnector	Negligible	High	In fuel and oxidant environments	Fully dense

More information of materials, design requirements and fabrication processes for the different fuel cell components can be found elsewhere [8].

1.3.3. Historical background and the state-of-the-art of SOFCs

The principles of fuel cell operation were first reported by Sir William Grove in 1839 [9]. Nerst discovered solid oxygen-ion conductors (ZrO_2 with 15% wt. Y_2O_3) in 1899 [10] and the operation of the first ceramic fuel cell at 1273 K was demonstrated by Baur and Preis in 1937 [11] using mainly ZrO_2-based ionic conductors as the electrolyte, with iron or carbon as the anode and Fe_2O_3 as the cathode. Although SOFC operation was demonstrated, the current outputs were too low to be practical. It has to be noticed that yttria stabilised zirconia with 8-10 mol% Y_2O_3 (YSZ) is still used as the electrolyte in the most advanced SOFCs. Research into solid oxide technology began to accelerate in early 1960s. Weissbart and Ruka [12] of Westinghouse Electric studied the use of platinum as electrode material in 1962 and Tedmon *et al.* [13] of General Electric reported on the cathode performance of perovskite $PrCoO_3$ in 1969, showing a stable power density of 0.3 Wcm^{-2} over 6 months at 1273 K. However, it was found disadvantages such as the thermal expansion mismatch and incompatibility with the electrolyte. Other phases were investigated as electrode materials and doped lanthanum manganites and doped lanthanum chromites have been commonly used as cathode and interconnector materials respectively since 1970s [14]. In fact, the perovskite $LaMnO_3$ doped at the lanthanum site with calcium (at 10-30 mol%) or strontium (at 10-20 mol%) is the most popular cathode material for high temperature SOFCs because of its stability with zirconia electrolytes [8].

The first SOFC module was demonstrated by Brown Boveri in 1975 [15]. The module with 120 series-connected cells produces a total voltage of 110-120 V and a maximum power output of 115 W corresponding to 0.22 Wcm^{-2} operating at 1273 K with H_2/air. Nevertheless its manufacturing process was expensive. A further simplification and a reduction of cell manufacturing cost were possible by using thin-film techniques such as chemical vapour deposition or plasma spraying [8]. Up to the present, large scale SOFC units have been still operated at around 1273 K because no acceptable materials for low temperature SOFCs were available. A lower operating temperature in the range 773-1073 K would have many advantages. Costly lanthanum chromite interconnectors could be replaced by a conventional metallic interconnect (i.e. stainless steel) and the selection of gas-sealing material would be easier. A lower temperature will also ensure a reduction in the thermal stresses in the active ceramic structures, leading to a longer expected lifetime of the system. In addition, a combination of fuel processing with a SOFC has great potential for high energy densities and it is a feasible alternative for portable power supply to batteries [16]. It has been studied the viability of high-energy-density hydrocarbon fuels for portable power applications using the catalytic oxidation reactions for supplying sufficient thermal energy to maintain the SOFC at 773-873 K [17]. Hence, new anode materials are under investigation.

At present nickel is the most common anode because of its high catalytic activity and low cost. Generally, a Ni-YSZ cermet[1] is used as the anode. State-of-the-art Ni-YSZ anodes used in an electrolyte supported SOFC design are typically 100 µm thick [18,19]. The anode must consist of at least 30 vol% of Ni in the reduced state in order to guarantee a sufficient electronic conductivity under SOFC operation [20]. For a sufficient gas supply, the porosity should be adjusted between 30%-50% [20,21]. The high ionic conductivity of the YSZ particles (at high temperature), dispersed in the current collecting Ni matrix, extends the reaction zone away from the named *triple phase boundary*[2], see Figure 1.4, increasing the power density of the cell [22]. Unfortunately, nickel anodes suffer several problems such as incompatibility with some electrolytes [4], carbon deposition [23,24] due to the high catalytic activity of Ni towards the cracking of hidrocarbon fuels, requiring high steam ratios to avoid the process. Furthermore, Ni metal oxidises rapidly at operating temperature, breaking down the Ni matrix upon cycling between oxidising and reducing conditions. The Ni must therefore be maintained in a reducing atmosphere upon heating and cooling and also in the event of an interruption to the fuel supply at the operating temperature. This requires the cell to be fitted with a safety gas procedure to protect the anode. The Ni matrix itself needs to be stable for long operating times. Sintering or agglomeration of the particles over long operating times will lead to a loss in performance of the fuel cell as the surface area of the anode and connectivity to the embedded YSZ particles is reduced. Alternative fuel electrodes are $La_{1-x}Sr_xCr_{1-y}M_yO_{3-\delta}$ (M=Mn, Fe, Co, Ni) [25-27] and $La_2Sr_4Ti_{6-x}M_xO_{19-\delta}$ (M=Ga, Mn, Sc) [28-30] which have demonstrated better resistance to hydrocarbon fuels. More information can be found elsewhere [8,24,31].

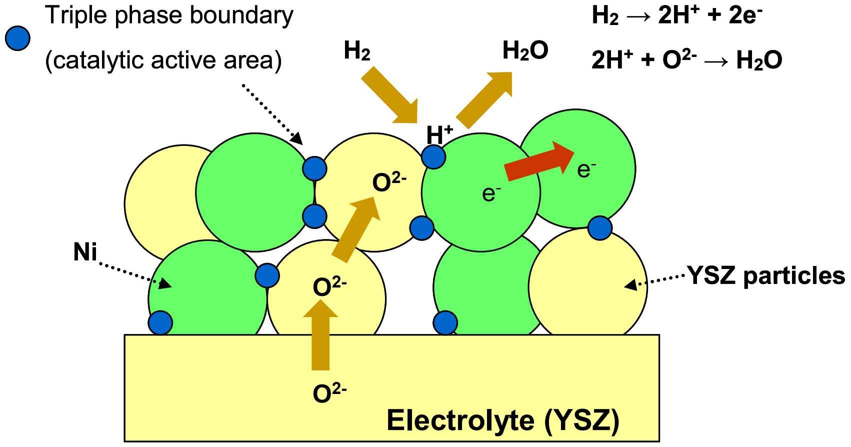

Figure 1.4. Illustration of the triple phase boundary (TPB).

---

[1] Cermet is a mixture of ceramic and metal

[2] The state-of-the-art Ni-YSZ cermet anode consists of three interpenetrating networks of Ni, YSZ, and pores. It is expected that the electrochemically active area is restricted to the zone where the three phases meet each other. This zone is called the triple phase boundary (TPB).

1.3.4. Design of SOFCs

Previous to 1970s, the cell configuration was either a flat-plate design using the electrolyte in the form of a disk, or a segmented-cell-in series design using short tubular segments of the electrolyte joined together with conducting seals. This led to the development of the thin-wall concept to improve cell performance. In 1970s the banded configuration was proposed, which made use of the thin-wall concept in which a number of thin-film cells were deposited on a porous support. In 1980 the sealless tubular design was proposed, with several advantages over the segmented-cell-in-series design. The key features of the sealless tubular design, Figure 1.5a, include individual thin cells formed on a tubular support and electrically connected into a bundle in a fuel-reducing atmosphere. In 1982 the monolithic design was advanced, in which cells are configured in a honeycomb structure resulting in extraordinarily high power density due to the small cell size and large active area, however it has not been enough developed because of the difficulty of suitable materials and fabrication process [14]. At the same time, interest in the flat-plate design has been renewed due to many advances in processing technologies, in Figure 1.5b. a planar-design SOFC is represented. Works summarising planar and tubular SOFC design alternatives can be found in several textbooks and research works [18, 20]. Their discussions on SOFC design include descriptions of typical materials uses and configurations, the advantages and disadvantages of each design, stack performance relationships, and potential application issues. Briefly, Table 1.3 compares the key characteristics of the four common SOFC stack configurations proposed up to the present.

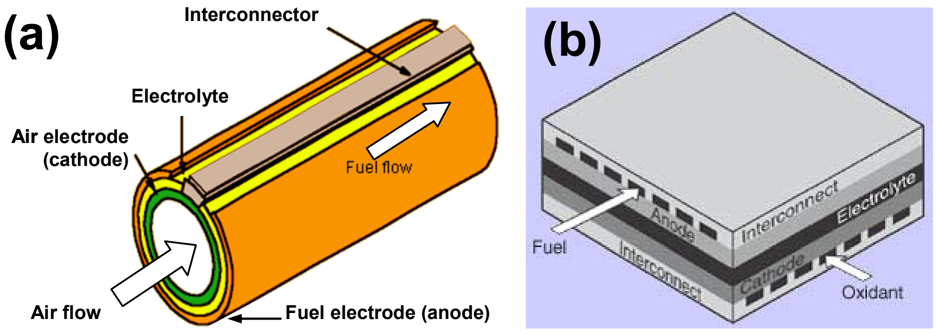

Figure. 1.5.Schematic view of tubular (a) and planar (b) SOFC.

Table 1.3.
Characteristics of SOFC stack designs

	Design			
Feature	Sealless tubular	Segmented-cell-in-series	Monolithic	Flat-plate
Structural support	Yes	Yes[a]	No	No
Internal electrical resistance	High	High	Low	Medium
Gas sealing	No	Yes	No	Yes
Power density	Low	Low	High[b]	Medium

[a] Banded configuration,[b] Coflow configurattion

1.4. Solid oxide ion conductors

Oxide ionic conductors have been studied since their discovery by Nernst in 1899 [10], and the research has been increased due to the requirements in the past decade for new clean energy sources, sensors, and high energy density batteries [4]. Nowadays, these oxides are shown a great interest due to their possibly application in technological devices such as SOFC, oxygen separation membranes, and membranes for the conversion of methane to syngas [32].

In oxygen ion conductors, current flow occurs by the movement of oxide ions through the crystal lattice. This movement is a result of thermally-activated hopping of the oxygen ions, moving from crystal lattice site to crystal lattice site, with a superimposed drift in the direction of the electric field. The ionic conductivity is consequently strongly temperature dependent, although at high temperatures it can approach around 0.1 Scm^{-1} (Figure 1.6a), comparable to the levels of ionic conductivity found in liquid electrolytes. It has to be considered that the crystal must contain unoccupied sites equivalent to those occupied by the lattice oxygen ions, and the energy involved in the process of migration from one site to the unoccupied equivalent site must be small, less than ~ 1 eV. Actually, the materials displaying oxygen ion conductivity must have unusual crystal structures with partially-occupied oxygen sites and, thereby, the number of this kind of oxides is relatively small. In order to obtain a ‘pure’ oxygen ion conductor, the level of the electronic contribution to the total electrical conductivity must be negligible, and it is not easy to achieve. Even very low concentrations of electronic carriers will give rise to a significant electronic component because of the very high mobility of electrons and holes in comparison with the ionic mobilities.

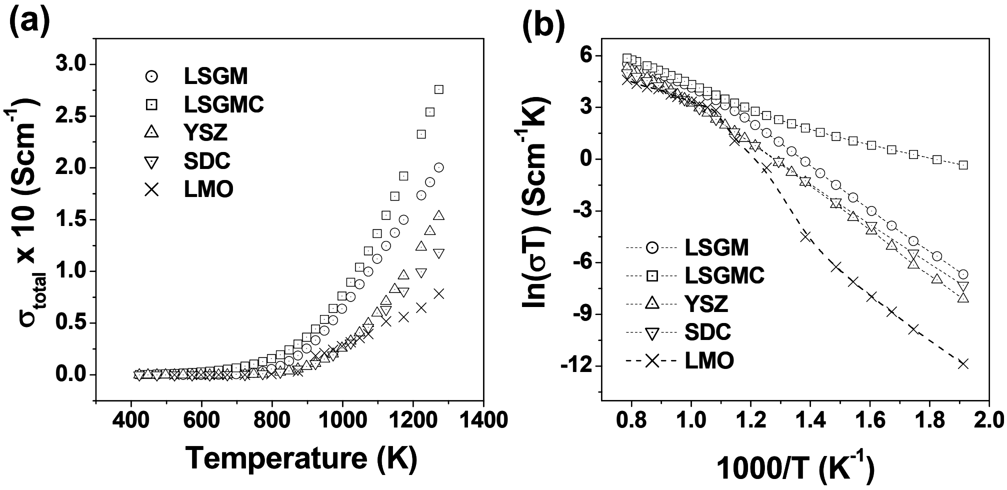

Figure 1.6. (a) Temperature dependence for the overall conductivity of several oxide ion conductors i.e. $La_{0.9}Sr_{0.1}Ga_{0.8}Mg_{0.2}O_{2.85}$ (LSGM), $La_{0.9}Sr_{0.1}Ga_{0.8}Mg_{0.115}Co_{0.085}O_{3-\delta}$ (LSGMC), $Zr_{0.92}Y_{0.08}O_{1.96}$ (YSZ), $Sm_{0.15}Ce_{0.85}O_{2-\delta}$ (SDC), and $La_2Mo_2O_9$ (LMO) and (b) typical Arrhenius plot of these oxide ion conductors.

Most oxygen ion conductors are, therefore, mixed conductors and only very few are capable of being classified as pure ionic conductors. Otherwise, in most technological applications these materials are used under extreme conditions, where an oxygen partial pressure gradient is either applied or generated across a dense membrane of the material. For example, a fuel cell electrolyte will have to remain stable with air applied at the cathode and hydrogen at the anode at a temperature of 1073 K or above. Under such extreme conditions, many oxides will be reduced and the reduction process will create electrons, increasing the electronic contribution.

Very few materials meet the stringent requirements needed to function satisfactorily as an electrolyte in SOFC, thus the need to search for alternative materials. Nevertheless both ionic and mixed conductors have their applications. Ionic conductors can be used as electrolyte in devices such as SOFC and electrolytic oxygen separators, whereas mixed conductors are useful as electrodes for both devices and can be also used as dense selective oxygen separation membranes [33-35].

1.4.1. Defect chemistry in solid oxides

In general, electrical conduction in crystalline solids depends on the material lattice defects [20]. In a perfect crystal all atoms would be on their correct lattice positions in the structure. This situation can only exist at 0 K. Above 0 K defects occur in the structure. These defects may be extended defects such as dislocations. The strength of a material depends very much on the presence (or absence) of extended defects such as dislocations and grain boundaries. Defects can also occur at isolated atomic positions, named as point defects, and can be due to the presence of a foreign atom at a particular site or to a vacancy where normally one would expect an atom.

Energy is required to form a defect and this means that the formation of defects is always an endothermic process. The formation of defects produces a gain in entropy. The change in entropy will be due to the vibration of atoms around the defects and also to the arrangement of the defects [36].

There are two main categories or defects, intrinsic which do not change the overall composition and because of this are also known as stoichiometric defects, and extrinsic or non-stoichiometric defects which are formed as a consequence of a change in the crystal composition e.g. when a foreign atom is inserted into the lattice of the crystal. In addition, intrinsic defects can be classified also in two categories: Schottky defects, which consist of vacancies in the lattice and Frenkel defects where a vacancy is created by an atom or ion moving into an interstitial position [20,36].

Regarding electron defects [32], they may arise either from aliovalent ions with charge different to the normal lattice ions, or as a consequence of the electron jumping from normally filled energy levels, usually the valence band, to normally empty levels, the conduction band. In those cases where an electron is missing, i.e. when there is an electron deficiency, this is usually called an electron hole (often abbreviated to hole). It is also convenient to consider point defects, such as vacancies or electron holes, to be the moving entities in a lattice even though the ions or electrons are actually moving through the lattice in the opposite direction. In the absence of a macroscopic electric field ionic lattices must be electrically neutral. This requires that charged defects must be compensated by the presence of other defects, together having a charge of opposite sign. This is called the electroneutrality condition. This means that these charged defects are always present as a combination of two (or more) types of defects. The charges of defects of the regular lattice particles are defined with respect to the neutral, unperturbed (ideal) lattice and are called effective charges.

The notation used for point defects is from Kröger and Vink [37] and are shown for a number of examples in Table 1.4, where divalent ions are chosen as example with MX as a compound formula with M^{2+}, X^{2-} as cation and anion, respectively. Only fully ionised defects are indicated in this table, and only the effective charges on defects are described by Kröger-Vink notation. These effective charges are indicated by a dot ($^{\bullet}$) for a positive excess charge, by a prime (') for a negative excess charge and by an x (^{x}) for effectively neutral defects i.e. ions having their normal charges corresponding with the stoichiometry of the compound.

Table 1.4.
Kröger–Vink notation for point defects in crystals.

Symbol	Type of defect
V_M''	Metal ion vacancy: vacant metal site with effective charge −2
$V_x^{\bullet\bullet}$	X ion vacancy: vacant X site with effective charge +2
M_M^x , X_x^x	Metal, respectively, X ion on their normal lattice position (neutral)
L_M'	L^+ dopant ion on metal site with effective charge −1
$N_M^{\bullet}$	N^{3+} dopant ion on metal site with effective charge +1
e'	Free electron in conduction band
$h^{\bullet}$	Free electron hole in valence band
$M_i^{\bullet\bullet}$	Interstitial metal ion with effective charge +2
X_i''	Interstitial X ion with effective charge −2
M_M'	Monovalent metal ion on M^{2+} position
$M_M^{\bullet}$	Trivalent metal ion on M^{2+} position

1.4.2. Mechanisms of ionic conductivity

There are two basic mechanisms related to the movement of the oxygen vacancies in an oxygen lattice of solid oxide, illustrated in Figure 1.7. When an ion jumps from its normal position on the lattice to a neighbouring equivalent but vacant site is called vacancy mechanism (Figure 1.7a). Notice that it can be equally be described as the movement of a vacancy rather than the movement of the ion. Interstitial mechanism is where an interstitial ion jumps of hops to an adjacent equivalent site (Figure 1.7b). These kinds of movement are known as the hopping model. In addition, a combination of vacant and interstitial mechanisms is also possible (Figure 1.7c).

Ionic conductivity, σ, is defined in the same way as electronic conductivity:

$$\sigma = nZ\mu \qquad (1.2)$$

where n is the number of charge carriers per unit volume, Z is their charge , and μ is their mobility. Ionic crystals are poor conductors compared with metals due to the difficulty for the movement of the charge-carrier (in this case an ion, although sometimes an electron) through the crystal lattice.

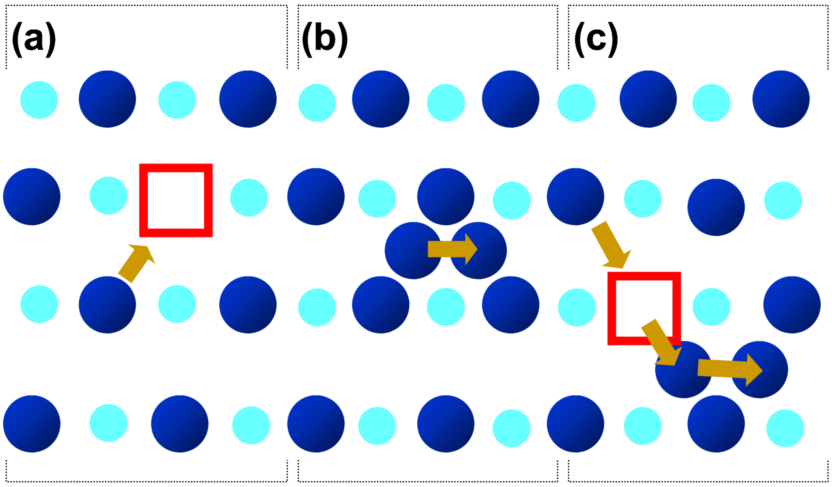

Figure 1.7. Schematic representation of ionic motion by vacancy (a) and interstitial (b) mechanisms, and a mixture of them (c).

Equation 1.2 is a general equation defining conductivity in all conducting materials. However, there are another expression i.e. Arrhenius equation that gives the temperature dependence of the ions mobility, taking into account the energy required to make the jump, E_a, know as the activation energy.

$$\mu = \mu_0 \exp(-E_a / kT) \qquad (1.3)$$

where k is the Boltzmann constant (1.380622×10^{-23} JK^{-1}), μ_0 is a constant known as a pre-exponential factor. This factor depends on the number of times per second that the ion attempt the move, v, called the attempt frequency (this is a frequency of vibration of the lattice), the distance moved by the ion; and the size of the external field. If the external field is small (up to about 300 Vcm^{-1}) temperature dependence of $1/T$ is introduced into the pre-exponential factor, and a new expression for the variation of ionic conductivity with temperature is given by

$$\sigma = \left(\sigma_0 / T\right) \exp(-E_a / kT) \tag{1.4}$$

The term σ_0 contains n and $Z_,$ as well as the information on attempt frequency and jump distance. Taking natural logs of Equation 1.4 as,

$$\ln \sigma T = \ln \sigma_0 - E_a / kT \tag{1.5}$$

and plotting $\ln(\sigma T)$ against 1/T, a straight line with a slope $-E_a/k$ should be produced. One example of the overall conductivity *vs*. temperature of different electrolyte materials is represented in Figure 1.6b.

1.4.3. Electronic and ionic conductivity dependence of Po_2

The electrical conductivity in an oxygen-ion conductor can appear via oxygen-ion vacancies and mobile electronic charge carriers, i.e. both types of conduction (ionic and electronic) can occur simultaneously. The ratio of the ionic conductivity to the total conductivity (the ionic transference number of an oxygen-ion conductor) can vary depending on the oxygen partial pressure (Po_2). Thus, it is possible to modify the defect structure, namely the conductivity, of an oxygen-ion conductor by changing the oxygen partial pressure.

A scan of a wide range of Po_2 should elucidate the electronic and ionic conductivity regimes of the solid oxide, distinguishing p-type from n-type electronic conductivity, and the vacancy concentration dependencies for the respective conduction processes as one can see in Figure 1.8.

Although the oxygen vacancies can be neutral, singly or doubly charged with respect to the normal oxygen lattice site the doubly charged species predominate at high temperature [38].

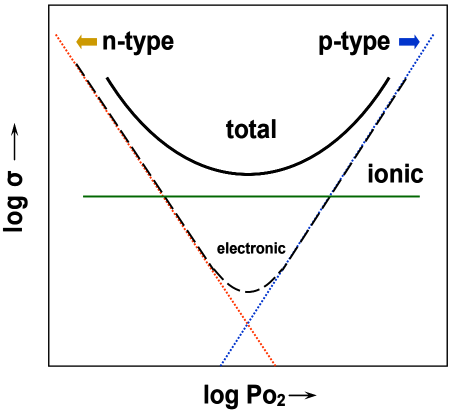

Figure 1.8. Po_2 dependence for overall conductivity and different contributions in a mixed ionic-electronic conductor.

For the case of O^{2-} ionic conduction, the oxygen vacancies are considered to be the mobile species, and are assumed to be in excess compared to those created or destroyed by the change in Po_2 [39]. The mobilities of the electrons, holes and oxygen vacancies are taken to be constant at constant temperature [40], independent of carrier concentration, with the result that the partial conductivities of the mobile species are proportional to their concentrations. Therefore the partial conductivity of oxide ions, due to the oxygen vacancies, is constant over the Po_2 range studied. Where the ionic conduction dominates over the electronic contributions the total observed conductivity would then be independent of Po_2, giving rise to a plateau in the log σ *vs*. Po_2 plot, see Figure 1.8. For n-type electronic conductivity the creation of an oxygen vacancy by a reduction in the Po_2 is associated with the creation of conduction electrons described by the following defect equation

$$O_o^x \rightleftarrows \frac{1}{2}O_2(g) + 2e' + V_o^{\bullet\bullet} \tag{1.6}$$

For p-type conductivity the defect equation for oxygen incorporation into the lattice is

$$\frac{1}{2}O_2(g) + V_o^{\bullet\bullet} \rightleftarrows O_o^x + 2h^{\bullet} \tag{1.11}$$

High Po_2 value means oxygen can be incorporated within the lattice and occupied the oxygen vacancies with creation of charge carriers. Thereby, holes are produced following the reaction 1.11. The expected conductivity for an mixed ionic-electronic oxide is related to $(Po_2)^{\pm 1/n}$ (n=4, 6) [41].

Taking into account n-type (σ_n) and p-type (σ_p) electronic conductivity, the electronic conductivity can be expressed as

$$\sigma_e = \sigma_p + \sigma_n = \sigma_P^o \left(P_{O_2}\right)^{1/n} + \sigma_n^o \left(P_{O_2}\right)^{-1/n} \tag{1.12}$$

where σ^o_p and σ^o_n are the p-type and n-type conductivity at 1 atm. Assuming ionic conductivity (σ_o) remains constant in the Po_2 range, the overall conductivity can be written as

$$\sigma_t = \sigma_o + \sigma_e = \sigma_o + \sigma_P^o \left(P_{O_2}\right)^{1/n} + \sigma_n^o \left(P_{O_2}\right)^{-1/n} \tag{1.13}$$

In short, n-type and p-type electronic conductivity are predominant at low Po_2, and at high Po_2, respectively, whereas ionic conductivity is predominant at intermediate Po_2 values, as one can see in Figure 1.8.

1.4.4. Typical solid ion conductors

1.4.4.1. Fluorite-type structure oxides

The fluorite oxides are the classical oxygen ion conducting oxide materials; The crystal structure consists of a simple cubic oxygen lattice with alternate cubic holes occupied by eight coordinated cations and is shown in Figure 1.9a. The general formula of a fluorite oxide is AO_2, where A is a large tetravalent cation. Typical materials with fluorite crystal structure are uranium dioxide (UO_2), thorium dioxide (ThO_2), and ceria (CeO_2).

Regarding zirconia oxides, the Zr^{4+} cation is too small to sustain the fluorite structure and only forms either at high temperatures or when the zirconium ion is partially substituted with another (usually larger) cation. This substitution is known as doping. Doping is usually performed by substituting with a lower valence cations into the lattice, with the added effect of introducing oxygen vacancies to maintain overall charge neutrality. These oxygen vacancies supply the equivalent sites allowing the oxygen ions to migrate, as mentioned above, and are the prerequisite for high ionic conductivity. A further peculiar feature of the fluorite structure is that it is able to sustain a high degree of substitution and consequent non-stoichiometry, making these very highly disordered materials. Doping of the fluorite oxides is usually achieved by substitution of the host cation with either a rare-earth or an alkaline-earth. Examples of such materials are doped zirconias such as yttria-stabilized zirconia (YSZ) with the general formula $Zr_{1-x}Y_xO_{2-x/2}$.

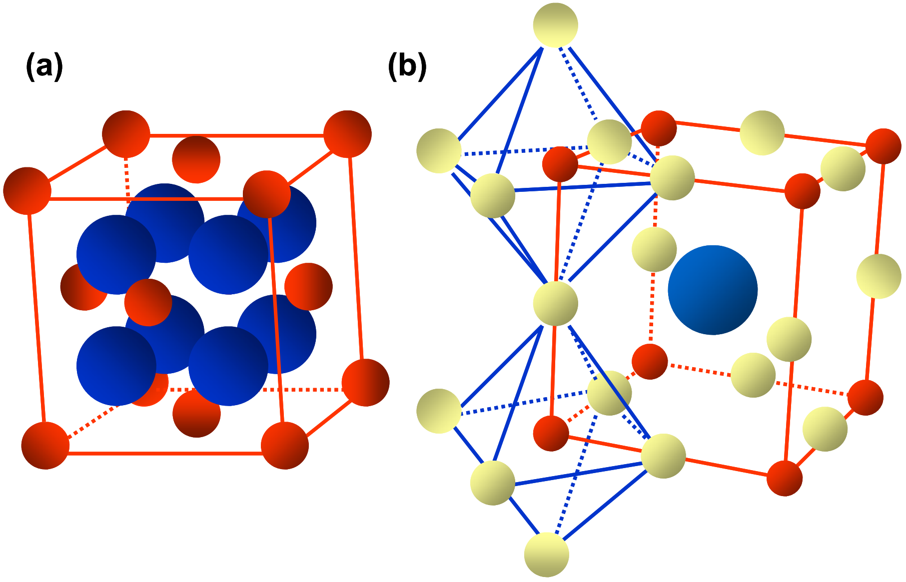

Fig. 1.9. (a) The fluorite (AO_2) oxide structure of thorium oxide. Blue spheres represent the oxygen sites and red spheres the A cation sites. (b) Perovskite ideal structure (ABO_3). The blue sphere represents the A-cation, the red spheres represent the B-cations, and the yellow spheres are oxygen ions

Compositions with Y substitutions close to 10 mol% show very high conductivities at temperatures of 1073 K and above and they are the main choice as electrolyte for applications in the region above this temperature. Increasing the dopant concentration will lead to the introduction of more vacancies into the lattice and should result in higher conductivity. Unfortunately, this correlation only applies at low concentrations of dopant and it is found that at higher concentrations the ionic conductivity is limited. It is clear that the conductivity drops with relatively small additions of the rare-earth ion, when the vacancy concentration is only a few percent. This maximum conductivity is common to all the classical ionic conductors studied and it is caused by the interaction of the substitutional rare-earth ion and the oxygen vacancy [33]. In order to produce good oxide ion conductors it appears that as well as introducing vacancies, leaving the crystal lattice as undisturbed as possible is highly desirable. This explains why some of the best oxide ion conductors are materials such as zirconia-scandia, $Zr_{1-x}Sc_xO_{2-\delta}$, and ceria-gadolinia, $Ce_{1-x}Gd_xO_{2-\delta}$ (CGO) [42,43], where the host and dopant ion are very similar in size.

YSZ, is the standard material for use in high temperature SOFCs, and ceria electrolytes doped with gadolinia (CGO), samarium (SDC), yttria (YDC) and calcium (CDC) are strong candidates for use in cells operating at temperatures as low as 823 K. Otherwise, doped cerias become unstable at low Po_2 as well as above 973 K due to increasing electrical conductivity causing short circuit in the cells because of the reduction of Ce^{4+} to Ce^{3+} [8]. Zirconia-scandia is often not considered based on cost grounds.

1.4.4.2. Perovskite and perovskite-related structure oxides

The perovskite structure, Figure 1.9b, is a relatively simple crystal structure that has the ABO_3 stoichiometry. Typically, the A-site cation is large, such as a rare earth, and will be 12-coordinated by the anions in the lattice. The B-site cation is typically smaller and frequently a transition metal. It will be six-coordinate, forming BO_6 octahedra, as illustrated in Figure 1.9b. It is usually by octahedral distortions that deviations from perfect cubic symmetry occur. The perovskite oxides are very interesting because there are two cation sites upon which to substitute with lower valence cations, leading to a much wider range of possible oxygen ion conducting materials. Furthermore, the total charges on A and B (+6) can be achieved by the combinations of 1+5, 2+4, and 3+3, and also in more complex ways as in $Pb(B'_{1/2}B''_{1/2})O_3$, where B'=Sc or Fe and B''=Nd or Ta, $A'_{1/2}A''_{1/2}TiO_3$ where A'=Li, Na and A''=La, Pr, etc. Hence, perovskite-compounds have been used in SOFC, ferroelectrics, superconducting materials and oxidation catalysts applications [18]. Many of them display both ionic and electronic conductivity. Nevertheless, only few perovskites are purely oxide ion conductors i.e. $LaAlO_3$, $LaGaO_3$, $LaScO_3$ and $CaTiO_3$ based materials.

For example, $CaTi_{0.95}Mg_{0.05}O_3$ exhibits high ionic conductivity at intermediate temperature (923-1073 K), and Ca-doped $LaAlO_3$ e.g. $La_{0.7}Ca_{0.3}AlO_3$ shows a high ionic transport number, always higher than 0.9, and do not have any electronic contribution in reducing atmospheres [18]. On the other hand, the lanthanum gallate ($LaGaO_3$) based compounds are the most promising materials for ionic applications. Electrical conductivity is almost independent of the Po_2, indicating that oxide ion conduction is dominant in these materials. In addition, doping with lower valence cations generally causes oxygen vacancies in order to maintain electrical neutrality. Thus, oxide ion conductivity increases. Electrical conductivity depends strongly on the particular alkaline-earth cation doped onto the La site and e.g. increases in the order Sr > Ba > Ca [44]. Therefore, strontium appears to be the most suitable dopant for $LaGaO_3$. Theoretically, increasing the amount of Sr increases the number of oxygen vacancies and oxide conductivity should increase. However, the solid solubility of Sr on the La site of $LaGaO_3$ is low and secondary phases as $LaSrGaO_4$ or $LaSrGa_3O_7$ can be formed when Sr in higher than 10 mol%. Oxygen vacancies can be also formed by doping an aliovalent cation into the Ga site in addition to the La site. Doping Mg into the Ga site increases the conductivity substantially, taking into account a maximum of 20 mol%. With this percentage of Mg, the solid solubility of Sr in the $LaGaO_3$ lattice increases up to 20 mol%. Feng and Goodenough [45] and Ishihara and co-workers [44] were the first researchers who proposed these materials of general stoichiometry $La_{1-x}Sr_xGa_{1-y}Mg_yO_{3-\delta}$, where, usually, x=0.1, 0.2 and y=0.2. The performance of doped $LaGaO_3$ at intermediate temperatures was found to be higher than some of the existing fluorite-type oxides and, indeed, would enable a lowering of the operating temperature of devices when compared with the traditional zirconia-based devices, usually operating at temperatures around 1273 K. The Arrhenius plots of the overall conductivity for several doped-$LaGaO_3$ materials i.e. $La_{0.9}A_{0.1}Ga_{0.8}Mg_{0.2}O_{2.85}$ (A= Ba, Ca and Sr), and $La_{0.9}Sr_{0.1}Ga_{1-x}Mg_xO_{3-(x+0.1)/2}$ (x=0.05, 0.10, 0.15, 0.20, 0.25 and 0.30) are illustrated in Figure 1.10. The highest conductivity in the temperature studied range corresponds to $La_{0.9}Sr_{0.1}Ga_{0.8}Mg_{0.2}O_{2.85}$ (LSGM) composition.

Several computational studies of cation defects in doped $LaGaO_3$ material reported how divalent and trivalent cations with ionic radii $\leq$ 0.8 Å (e.g. Fe, Mn, Sc, etc.) in six-coordination are predicted to substitute preferentially for Ga^{3+} position [46,47], hence the influence of different B-site substitutions on the transport and physicochemical properties of lanthanum gallate has been studied in order to develop novel materials for electrochemical applications [48,49]. Doping Cr or Fe on the Ga site induced hole conduction in the $LaGaO_3$, resulting in decreased stability against reduction [18]. Ishihara *et al.* [48] found that doping with small amounts of transition metals, particularly Co or Ni, increase the oxide ion conductivity of LSGM. The Arrhenius plot of the conductivity of LSGM doped with small amounts of cobalt is represented in Figure 1.11.

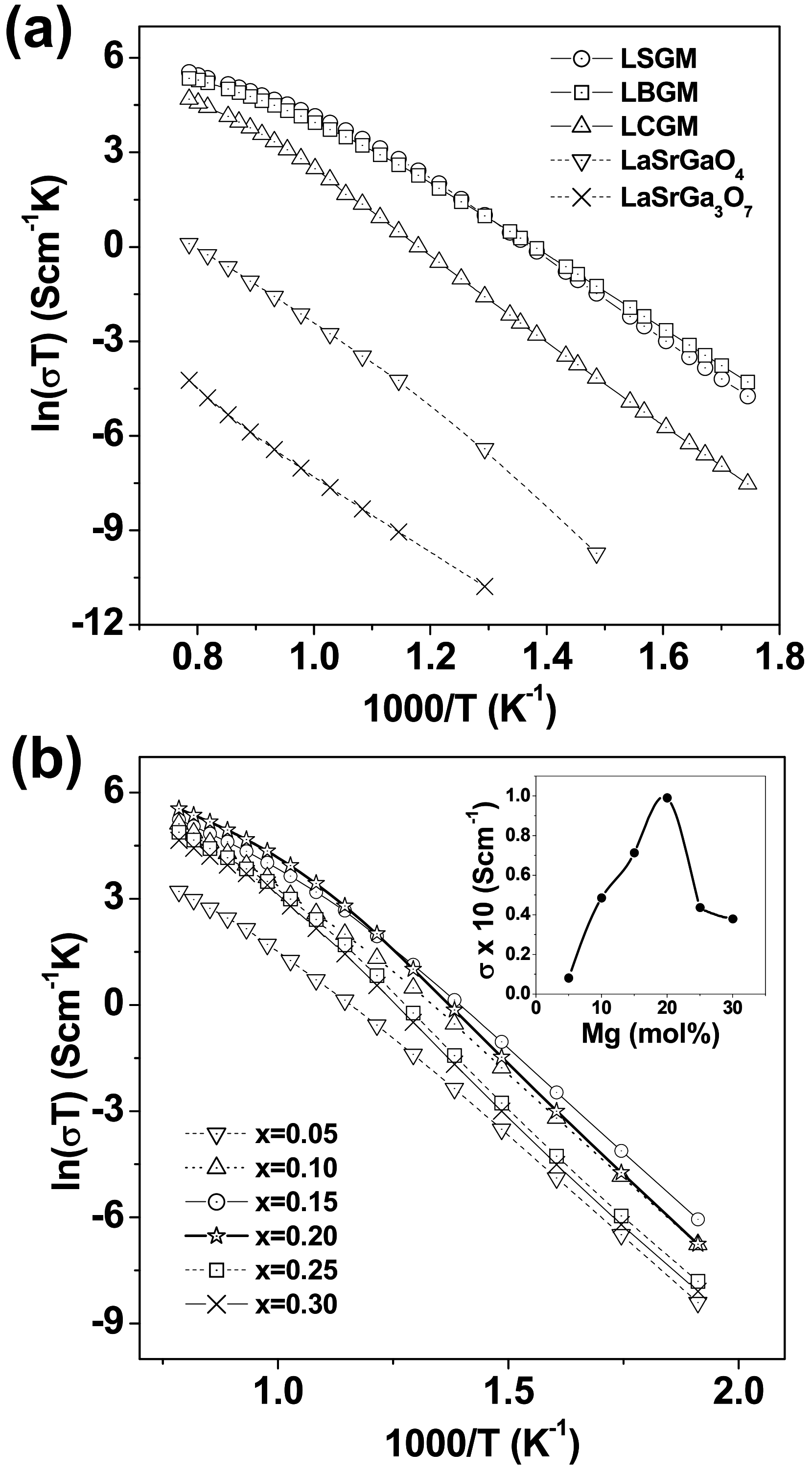

Figure 1.10. Arrhenius plot of the overall conductivity in air of $La_{0.9}A_{0.1}Ga_{0.8}Mg_{0.2}O_{2.85}$ (A= Ba, Ca and Sr), $LaSrGaO_4$ and $LaSrGa_3O_7$ (a); and $La_{0.9}Sr_{0.1}Ga_{1-x}Mg_xO_{3-(x+0.1)/2}$ (x=0.05, 0.10; 0.15, 0.20; 0.25 and 0.30) (b). The figure in the inset (b) illustrates the variation of the conductivity in function of the content of magnesium of the samples at 1073 K. The samples were prepared via ceramic route.

Many perovskite and perovskite-related mixed ionic-electronic conductors have been used mainly as cathodes in SOFCs [4,8,50]. Most of these works were for SOFCs based on zirconia electrolytes working at high temperatures. However it has been also used doped CeO_2 and doped $LaGaO_3$ as the electrolyte for applications at low and intermediate temperature. The criteria for using as a cathode or anode in a fuel cell includes the electrochemical performance, and also the compatibility with the other cell components, i.e. the electrolyte. Hence, it is necessary for the perovskite oxides initially identified as candidates for SOFC cathodes or anodes to be optimised through doping strategies. Early candidates for cathodic operation included the lanthanum cobaltite, $LaCoO_3$, and lanthanum manganite, $LaMnO_3$, based perovskites [8,18,20], whereas, candidates for anodic operation included the lanthanum chromites, $LaCrO_3$ [25-27]. It was found that the previous stoichiometric compositions were unsuitable in terms of electrochemical performance for a cathode/anode, however doping the A-site of the perovskite with an alkaline earth such as Sr, a dramatic improvement in the conductivity and, hence, in the performance of the cathode/anode could be achieved. The level of electronic and ionic conductivity depends on the material, e.g. $La_{1-x}Sr_xMnO_{3-\delta}$ (LSM) was found to have high electronic conductivity, but poor oxide ion conductivity [51,52].

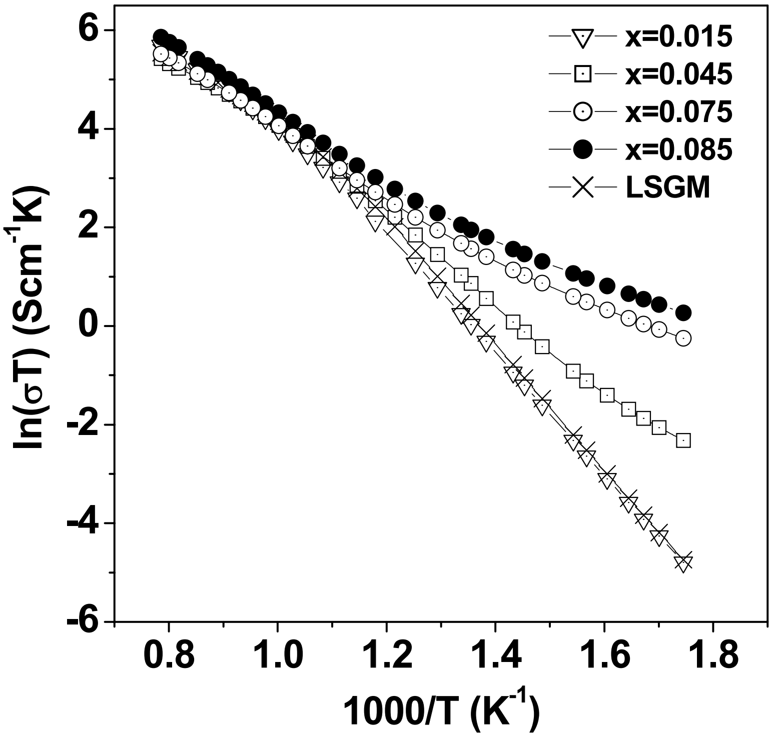

Figure 1.11. Arrhenius plot of the overall conductivity in air of $La_{0.9}Sr_{0.1}Ga_{0.8}Mg_{0.2-x}Co_xO_{3-\delta}$ (x=0.015, 0.045, 0.075 and 0.085) samples prepared via ceramic route.

LSM is the most popular cathode material for high temperature SOFCs because of its stability with zirconia electrolytes, high electronic conductivity and high catalytic behaviour towards oxygen reduction. Also, LSM is often mixed with YSZ to extend the triple phase boundary, reaction sites and significantly reduce electrode polarisation [8].

$La_{1-x}Sr_xFeO_{3-\delta}$ (LSF) is a candidate to replace LSM between 923 and 1073 K, and $La_{1-x}Sr_xCoO_{3-\delta}$ (LSC) is another candidate for lower temperature, although long term stability could be seriously affected by cobalt diffusion and phase segregations.

It has been also developed materials like $La_{1-x}Sr_XCo_{1-y}Fe_yO_{3-\delta}$ e.g. $La_{0.6}Sr_{0.4}Co_{0.2}Fe_{0.8}O_{3-\delta}$ which has an electronic conductivity around 280 Scm^{-1} at 1073 K while the ionic conductivity is $\sim 2\times 10^{-3}$ Scm^{-1}. However its thermal expansion coefficient (TEC) $\sim 15.1\times 10^{-6}$ K^{-1} (293-1073 K) is higher than the TECs of typical electrolyte materials such as YSZ ($\sim 10.8\times 10^{-6}$ K^{-1}) or LSGM ($\sim 11.6\times 10^{-6}$ K^{-1}). Therefore, a compromise between ion conductivity and thermal expansion has to be considered [22].

As example, the temperature dependence of the overall conductivity of several based lanthanum manganites, cobaltites, ferrites and chromites, synthesised in this work, is represented in Figure 1.12. The overall conductivity has been measured by a dc-four-probe method (Section 2.7.2). Further development of perovskite-type oxides, including conduct protons such as $BaCeO_3$, for fuel cells has been discussed in detail elsewhere [8,31,53-58].

1.4.4.3. LAMOX

The LAMOX family of oxide ion conductors is based on the $La_2Mo_2O_9$ compound [59]. They have been studied such as a possibly SOFC electrolytes at temperatures above 873 K at which point an α-β phase transition occurs. Associated with this transition there is a improvement in the ionic conductivity around two orders of magnitude, i.e. a value of 0.03 Scm^{-1} was achieved at ~993 K.

Unfortunately, the Mo content of this material is susceptible to reduction and, therefore, significant development of this material is needed, either as an electrolyte in fuel cells or indeed as an oxygen separator. In addition, there have been several studies using doping strategies to overcome both the reducibility of the material and the transition temperature at ~873 K [60-62].

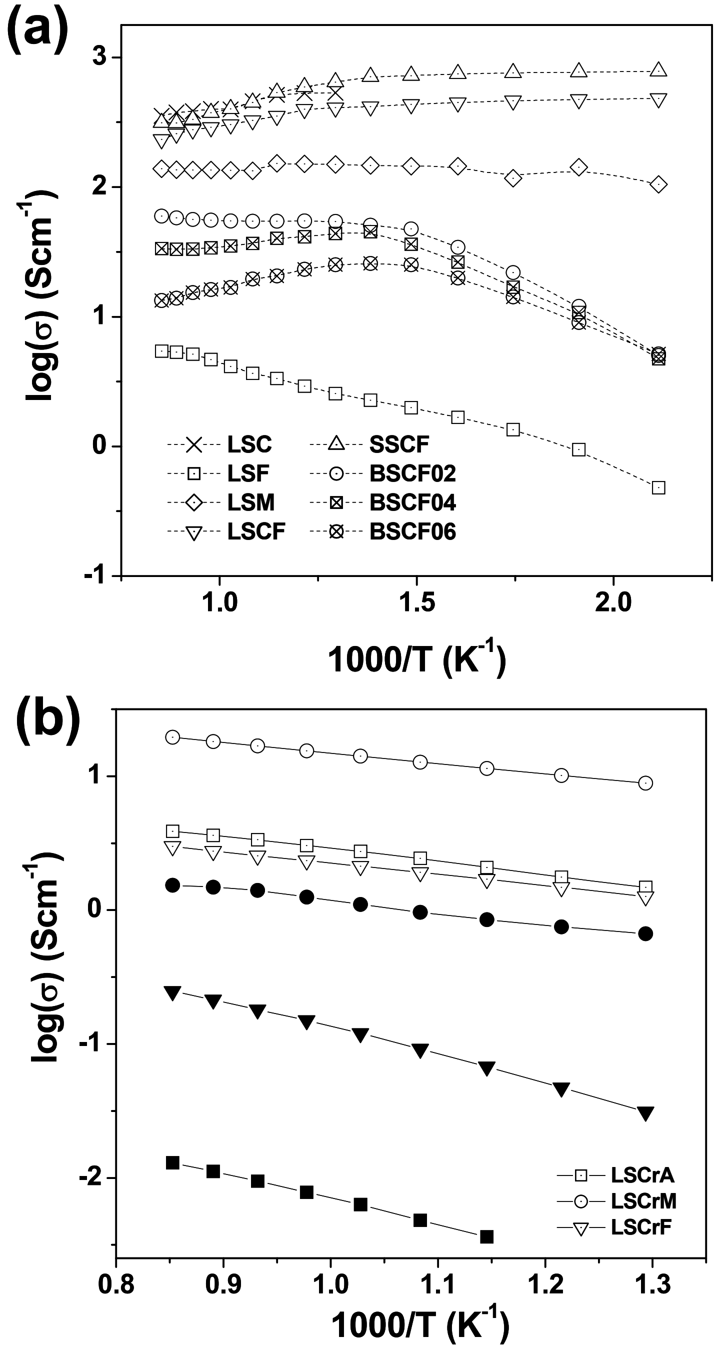

Figure 1.12. Temperature dependence of the overall conductivity of several MIECs, measured by a dc-four-probe method, in air (open symbols) and wet 5%H_2/Ar (close symbols). (a) Based lanthanum manganites, cobaltites and ferrites i.e. $La_{0.7}Sr_{0.3}FeO_{3-\delta}$ (LSF), $La_{0.7}Sr_{0.3}CoO_{3-\delta}$ (LSC), $La_{0.7}Sr_{0.3}MnO_{3-\delta}$ (LSM), $La_{0.5}Sr_{0.5}Co_{0.8}Fe_{0.2}O_{3-\delta}$ (LSCF), $Sm_{0.5}Sr_{0.5}Co_{0.8}Fe_{0.2}O_{3-\delta}$ (SSCF), $Ba_{0.5}Sr_{0.5}Co_{0.8}Fe_{0.2}O_{3-\delta}$ (BSCF02), $Ba_{0.5}Sr_{0.5}Co_{0.6}Fe_{0.4}O_{3-\delta}$ (BSCF04), and $Ba_{0.5}Sr_{0.5}Co_{0.4}Fe_{0.6}O_{3-\delta}$ (BSCF06). (b) Based lanthanum chromites i.e. $La_{0.75}Sr_{0.25}Cr_{0.5}Al_{0.5}O_{3-\delta}$ (LSCrA), $La_{0.75}Sr_{0.25}Cr_{0.5}Mn_{0.5}O_{3-\delta}$ (LSCrM), and $La_{0.75}Sr_{0.25}Cr_{0.5}Fe_{0.5}O_{3-\delta}$ (LSCrF).

1.4.4.4. Apatites

A relatively recent discovery in the field of ionic conductors has been the apatite-structured oxides. Several groups [63-65] have synthesized lanthanum-based compositions, i.e. germanates and silicates of composition $La_{10-x}Ge_6O_{26+y}$ and $La_{10-x}Si_6O_{26+y}$. These materials have been identified as having relatively high levels of oxide ion mobility with a Sr-doped material, $La_9SrGe_6O_{26.5}$ achieving 0.14 S cm^{-1} at 1223 K [66]. At lower temperatures, this composition has higher levels of ionic conductivity than YSZ by half an order of magnitude. Moreover, these materials require particularly high temperatures for synthesis and sintering. More research regarding their compatibility and performance with current electrode materials are also necessary.

1.4.4.5. Bi_2O_3 and BIVEMOX

Bi_2O_3 has a crystallographic polymorph, δ phase with a fluorite cubic structure above 1003 K, which exhibits high oxygen-ion conductivity, about 1 Scm^{-1} near the melting point of 1098 K. This phase can be stabilised at low temperatures by doping with certain metal oxides [20,67,69]. However the main drawback of this material is its small oxygen partial pressure range of stability. Stabilised Bi_2O_3 is easily reduced under low oxygen partial pressures and decomposes into bismuth metal at an oxygen partial pressure of about 10^{-13} atm at 873 K [69].

The BIMEVOX family of oxide ion conductors are based on the fluorite-related oxide Bi_2O_3 [20,70,71], where $Bi_4V_2O_{11}$ is the solid solution series end member and a typical composition would be $Bi_2Mg_xV_{1-x}O_{5.5-3x/2-\delta}$. These materials are doped with a transition metal and vanadium and have proven to be highly effective as oxygen separation membranes with ionic conductivity of the order of 0.1 Scm^{-1} at 873 K. In common with the LAMOX family, there is a phase transition in the BIMEVOX series and many of the doping studies have been concerned with the stabilization of the fast ion conducting, high temperature γ-phase.

1.4.4.6. Brownmillerites

Another interesting structure from the point of view of oxide ion conduction is brownmillerite with a general formula $A_2B_2O_5$. This structure can be viewed as a perovskite with oxygen vacancies ordered along the [101] direction in alternate layers. Several brownmillerite oxides have been studied [72] e.g. $Ba_2In_2O_5$ and the conductivities are rather high compared with those of fluorite-type structure oxides. Oxide ion conductivity in $Ba_2In_2O_5$ is comparable with that of YSZ at temperatures above 1173 K.

1.5. Aim of this study

Current SOFC technology has been based around the electrolyte yttria-stabilised zirconia (YSZ), cubic fluorite-type structure, which requires an operating temperature of 1273 K for reasonable oxide ion conduction. This high temperature requirement imposes severe constraints on material selection, in particular it excludes the use of stainless steel as interconnect and gas-tight sealing for the cell, which would have been the material of choice from engineering considerations. Additionally, the thermal compatibility of the electrolyte with the other components of the fuel cell; namely the anode, the cathode and the interconnector material is critical. A mismatch in expansion coefficients leads to large stresses, both during manufacture and operation, and will ultimately result in cracking on the ceramic structure, reducing the lifetime of the fuel cell and making it uneconomical. The difference in the relative thermal expansion of the materials increases with increasing temperature and therefore a lower operating temperature is desired, which in turn requires an electrolyte capable of equivalent or better conductivity at lower temperatures. It is necessary to research alternative electrode materials, either for use with YSZ or an advanced electrolyte, to improve the direct electrical conversion efficiency of the fuel cell.

The aim of this thesis is to study perovskite and perovskite related phases in order to develop an efficient all-perovskite intermediate temperature solid oxide fuel cell (IT-SOFC). Using only perovskite materials may maximize interface properties between the components of a SOFC, including thermal compatibility. Actually, it is not a new concept. An all-perovskite SOFC related project, named NEDO, was developed in 1999-2001 period by an international research program with researches from Imperial College of Science (UK), Oita University and Tokyo Institute of Technology (Japan), St. Andrews University (UK) and Dalian Institute of Chemical Physics (China). Nevertheless, new mixed conductors with perovskite-type structure e.g. $Ba_{0.5}Sr_{0.5}Co_{0.8}Fe_{0.2}O_{3-\delta}$ (BSCF) [55] and $La_{0.75}Sr_{0.25}Cr_{0.5}Mn_{0.5}O_{3-\delta}$ (LSCM) [26] have been developed in last few years and it is interesting to study the application of these new materials such as components of an all-perovskite SOFC.

Doped lanthanum gallates i.e. $La_{1-x}Sr_xGa_{1-y}Mg_yO_{3-\delta}$, were the electrolyte material used by the researches of the program NEDO, in fact they are the most promising perovskite-type materials as SOFC electrolyte due to its ionic conductivity which is higher than the ionic conductivity of YSZ in the range of intermediate temperatures. For this reason, doped $LaGaO_3$ materials have been also considered for electrolyte material in this work i.e. $La_{0.9}Sr_{0.1}Ga_{0.8}Mg_{0.2}O_{2.85}$ (LSGM) [44,45] and $La_{0.9}Sr_{0.1}Ga_{0.8}Mg_{0.115}Co_{0.085}O_{3-\delta}$ (LSGMC) [46] which show typical ionic conductivity of approximately 0.1 Scm^{-1} at 1073 K. LSGM is better ionic conductor than YSZ at intermediate temperatures (773 – 1073 K) and presents good chemical stability and negligible electronic conductivity over a wide range of oxygen partial pressures ($1\text{-}10^{-20}$ atm) [14].

However, the main drawbacks are the segregation of impurities during the synthesis e.g. $LaSrGa_3O_7$ and $LaSrGaO_4$ [73,75] and the reactivity with nickel [75], which is usually employed in the anode cermets. Feng *et al.* [76] reported that the success of LSGM as electrolyte relies on the identification of the adequate anode material and on the processing methods. Therefore, in this work it was decided to undertake an investigation on the compatibility and electrochemical performance of the two new electrode materials previously mentioned, LSCM and BSCF, with LSGM and LSGMC electrolyte materials at intermediate temperature (873-1073 K).

LSCM material was used, because it has been successfully tested as Ni-free anode material in YSZ based systems. Moreover, doped lanthanum chromites are promising materials to develop symmetric fuel cells [77,78] where the anode and cathode materials have the same composition. They can work as anode or cathode due to its phase stability under both reducing and oxidant atmospheres. However, fuel tests have to be performed. This kind of SOFC system could save costs and improve the design of the cells, e.g. the fuel cell could be assembled in a single thermal treatment, minimising problems related with the interdiffusion between cell components. Another important advantage is related to sulphur poisoning and carbon depositions, depending on the fuel used. In a symmetric design, the gas (fuel and oxidant) flows can be interchanged, hence the material which was under fuel conditions suffered sulphur poisoning or carbon deposition is now under oxidant gas flow, so the microstructure is cleaning, and the material which was under oxidant conditions offers a clean microstructure to the fuel oxidation. Thereby, electrochemical performance losses due to sulphur presence in the fuel and carbon depositions are avoided.

And BSCF material, because its high cathodic performance at low temperature (~773 K) with fluorite based electrolyte systems (samarium doped ceria) indicates this material as potential electrode material with perovskite-type electrolytes, e.g. doped $LaGaO_3$, at low and intermediate temperature. Additionally, other electrode materials i.e doped lanthanum manganites as well as doped lanthanum cobaltites, which have been widely used as cathode materials in high temperature (~1273 K) applications with YSZ based systems, can be compared with BSCF and investigated the reported drawbacks attending to the compatibility of them with LSGM, e.g. reactivity, overpotential, etc.

Taking into account the preparative methods, alternative precursor routes such as citrate and acetylacetonate sol-gel and freeze-drying method, as well as the conventional solid-state reaction, have been investigated in order to obtain better microstructures of the polycrystalline materials. Thin film electrolyte preparation via tape casting has been also carried out to reduce the ohmic losses of the electrolyte.

In short, the experimental procedure has mainly consisted in the following steps:

1. Synthesis and structural characterisation of the different materials by the conventional ceramic method and precursor routes.

2. Electrical characterisation by different techniques (electrochemical impedance spectroscopy and four probe method) including a polarisation resistance (area specific resistance, ASR) study of different electrode materials under oxidant and reducing conditions.

3. Preparation of the doped $LaGaO_3$ based SOFCs and analysis of the current-voltage characteristics, electrode overpotential, series and polarisation resistances and power density from fuel cell tests with fuel and oxidant gases in asymmetric and symmetric configurations.

1.5.1. Structure of this thesis

Chapter 1 and 2 provide a general overview of the fuel cells and SOFCs state-of-the-art, the aim of this work, the preparative methods, and the structural and electrical characterisation techniques used throughout this thesis.

The experimental procedure and data has been published in four articles, therefore every article is fully included in this thesis as a chapter, actually from chapter 3 to 6. Chapter 3 (paper one) is focused on the compatibility and performance of the anode material, $La_{0.75}Sr_{0.25}Cr_{0.5}Mn_{0.5}O_{3-\delta}$ (LSCM) [26], with doped lanthanum gallate electrolytes, i.e. LSGM and LSGMC, whereas Chapter 4 (paper two) is dedicated to the compatibility study of the cathode material, $Ba_{0.5}Sr_{0.5}Co_{0.8}Fe_{0.2}O_{3-\delta}$ (BSCF) [55] with LSGM electrolyte material. In Chapter 5 (paper three) the cathodic performances of $La_{0.8}Sr_{0.2}MnO_3$ (LSM), a LSM-LSGM composite and BSCF are compared. In addition, it has been investigated the use of a buffer material to avoid interfacial reactions between the electrode and electrolyte materials.

A new design of IT-SOFC based on symmetric fuel cells [77,78] using the same electrode material as cathode and anode with LSGM is advanced in Chapter 6 (paper four). This chapter also contains an area specific resistance (ASR) or polarisation resistance study on different electrodes in reducing and oxidant atmospheres.

A general discussion of the experimental data (Chapter 3 to 6) of this work is outlined in Chapter 7. The thesis finishes with the corresponding conclusions and several appendixes with additional information about structural and electrical characterisation of the phases and compounds prepared in this work.

1.6. References

[1] National Oceanic and Atmospheric Administration. Climate of 2001, Anual review.
[2] A. B. Stambouli, E. Traversa, *Renewable and Sustainable Energy Reviews* **6** (2002) 433-455.
[3] World Energy Outlook 2004. International Energy Agency (IEA).
[4] B.C.H. Steele, A. Heinzel, *Nature* **414** (2001) 345-352.
[5] S.C. Singhal, *Solid State Ion.* **135** (2000) 305-313.
[6] S.C. Singhal, *Solid State Ion.* **152-153** (2002) 405-410.
[7] Fuel Cell Handbook, 5th Edition. U.S. Department of Energy. October 2000.
[8] K.C. Wincewicz, J.S. Cooper, *J. Power Sources* **140** (2005) 280-296.
[9] W.R. Grove, *Philos Mag.* **14** (1839) 127-130.
[10] W. Nernst, *Z. Elecktrochem.* **6** (1899) 41-43.
[11] H. Baur, H. Preis, *Z. Elektrochem.***43** (1937) 727-732.
[12] J. Weissbart, R. Ruka, *J. Electrochem. Soc.* **109** (1962) 723-726.
[13] C.S. Tedmon, H.S. Spacil, S.P. Mitoff, *J. Electrochem. Soc.* **116** (1969) 1170-1175.
[14] O. Yamamoto, *Electrochim. Acta* **45** (2000) 2423-2435.
[15] F.J. Rohr, in: P. Hagenmuller, W. van Gool (Eds.), Solid Electrolytes, Academic Press, New York, 1978, p. 431.
[16] A. Mitsos, I. Palou-Rivera, P.I. Barton, *Ind. Eng. Chem. Res.* **43** (2004) 74-84.
[17] Z. Shao, S.M. Haile, J. Ahn, P.D. Ronney, Z. Zhan, S.A. Barnett, *Nature* **435** (2005) 795-798.
[18] Singhal, K. Kendall, High-temperature Solid Oxide Fuel Cells: Fundamentals, Design and Applications, Elsevier, 2004.
[19] G.M. Christie, P. Mammensma, J.P.P. Huijsmans, Proc. of the 4th Europ. Fuel Cell Forum, Lucerne, Switzerland, Ed.: A.J. McEvoy (2000) 29.
[20] N.Q. Minh, T. Takahashi, Science and Technology of Ceramic Fuel Cells, Elsevier, 1995.
[21] S. Primdahl, M. Mongensen, *J. Electrochem. Soc.* **146** (1999) 2827-2833.
[22] D. Stöver, H.P. Buchkremer, S. Uhlenbruck, *Ceram. Int.* **30** (2004) 1107-1113.
[23] R. Gorte, S Park, J. Vohs, C. Want, *Adv. Mater.* **12** (2000) 1465-1469.
[24] A. Atkinson, S. Barnett, R.J. Gorte, J.T.S. Irvine, A.J. McEvoy, M. Mogensen, S.C. Singhal, J. Vohs, *Nat. Mater.* **3** (2004) 17-27.
[25] J. Sfeirv, P.A. Buffat, P. Möckli, N. Xanthopoulos, R. Vasquez, H. J. Mathieu, J.Van herle, K. Ravindranathan Thampi, *J. Catal.* **202** (2001) 229-244.
[26] S. Tao, J.T.S. Irvine, *Nat. Mater.* **2** (2003) 320-323.
[27] S. Tao, J.T.S. Irvine, *Chem. Mater.* **16** (2004) 4116-4121.
[28] J.C. Ruiz-Morales, J. Canales-Vázquez, C.D. Savaniu, D. Marrero-López, W. Zhou, J.T.S. Irvine, *Nature* **439** (2006) 568-571.
[29] J Canales-Vázquez, S.W. Tao, J.T.S. Irvine, *Solid State Ion.* **159** (2003) 159-165.
[30] A. Ovalle, J.C. Ruiz-Morales, J. Canales-Vázquez, D. Marrero-López, J.T.S. Irvine, *Solid State Ion.* **117** (2006) 1997-2003.
[31] R.K.B. Gover , P. R. Slater, *Annu. Rep. Prog. Chem. Sect. A* **100** (2004) 525-552.
[32] P.J. Gellings, H.J.M. Bouwmester, *Catal. Today* **58** (2000) 1-53.
[33] S.J. Skinner, J.A. Kilner, *Materials Today* (March 2003) 30-37.
[34] I. Riess, *Solid State Ion.* **157** (2003) 1-17.
[35] A. Thursfield, I.S. Metcalfe, J. Mater. Chem. **14** (2004) 2475-2485.
[36] L. Smart, E. Moore, *Solid State Chemistry*, Chapman & Hall, 2nd Ed., 1995.
[37] F.A. Kröger, H.J. Vink, Solid State Phys. **3** (1956) 307.
[38] P. Kofstad, *Non-Stoichiometric Chemistry and Electrical Conductivity in Binary Metal Oxides*, Wiley 1972.
[39] S. Geller, *Solid Electrolytes*, Springer-Verlag 1977
[40] H. Rickert, Electrochemistry of Solids, Springer-Verlag 1982.
[41] P.R. Slater, J.T.S. Irvine, *Solid State Ion.* **124** (1999) 61-72.

[42] J.A. Kilner, *Solid State Ion.* **129** (2000) 13-23.

[43] M. Mogensen, N.M Sammes, G.A. Tompsett, *Solid State Ion.* **120** (2000) 63-94

[44] T. Ishihara, H. Matsuda, Y. Takita, *J. Am. Chem. Soc.* **116** (1994) 3801-3803.

[45] M. Feng, J.B. Goodenough, *Eur. J. Solid State Inorg. Chem.* **31** (1994) 663-672.

[46] M.S. Islam, *Solid State Ion.* **154-155** (2002) 75-85.

[47] M.S. Islam, R.A. Davies, *J. Mater. Chem*. **14** (2004) 86-93.

[48] T. Ishihara, H. Furutani, M. Honda, T. Yamada, T. Shibayama, T. Akbay, N. Sakai, H. Yokokawa, Y. Takita, *Chem. Matter.* **11** (1999) 2081-2088.

[49] V.V. Karton, A.P. Viskup, A.A. Yaremchenko, R.T. Baker, B. Gharbage, G.C. Mather, F.M. Figueiredo, E.N. Naumovick, F.M.B. Marques, *Solid State Ion.* **132** (2000) 119-130.

[50] M. Gödickemeier, K. Sasaki, L.J. Gauckler, I. Riess, *Solid State Ion.* **86-88** (1996) 691-701.

[51] R.A. De Souza, J.A. Kilner, *Solid State Ion.* **106** (1998) 175-187.

[52] V.V. Kharton, A.V. Kovalevsky, V.N. Tikhonovich, E.N. Naumovich, A.P. Viskup, *Solid State Ion.* **110** (1998) 53–60.

[53] S.J. Skinner, *J. Inorg. Mater.* **3** (2001) 113-121.

[54] J.R. Ralph, C. Rossignol, R. Kumar, *J. Electrochem .Soc.* **150** (2003) A1518-A1522.

[55] Z. Shao, S.M. Haile, *Nature* **431** (2004) 170-173.

[56] Y. H. Huang, R.I. Dass, Z.L. Xing, J.B. Goodenough, *Science* **312** (2006) 254-257.

[57] W.G. Coors, D.W. Ready, *J. Am. Ceram. Soc.* **85** (2002) 2637-2640.

[58] T. Norby, *Solid State Ion.* **125** (1999) 1-11.

[59] P. Lacorre, F. Goutenoire, O. Bohnke, R. Retoux, Y. Laligant, *Nature* **404** (2000) 856-858.

[60] J. A. Collado, M.A.G. Aranda, A. Cabeza, P. Olivera-Pastor, S. Bruque, *J. Solid State Chem.* **167** (2002) 80-85.

[61] D. Marrero-López, J. Peña-Martínez, D. Pérez-Coll, P. Núñez, *J. Alloys Compound* **422** (2006) 249-257.

[62] D. Marrero-López, J. Canales-Vázquez, J.C. Ruiz-Morales, J.T.S. Irvine, P. Núñez, *Electrochim. Acta* **50** (2005) 4385-4395.

[63] S. Nakayama, M. Sakamoto, *J. Eur. Ceram. Soc*. **18** (1998) 1413-1418.

[64] S.Tao, J.T.S. Irvine, *Mater. Res. Bull.* **36** (2001) 1245-1258.

[65] L. León-Reina, M.C. Martín-Sedeño, E.R. Losilla, A. Cabeza, M. Martínez-Lara, S. Bruque, F.M.B. Marques, D. V. Sheptyakov, M.A.G. Aranda, *Chem. Mater.* **15** (2003) 2099-2108.

[66] H. Arikawa, H. Nishiguchi, T. Ishihara, Y. Takita, *Solid State Ion*. **136-137** (2000) 31-37.

[67] J.A. Kilner, J. Drennan, P. Dennis, B.C.H. Steele, *Solid State Ion.* **5** (1981) 527-530.

[68] T. Takahashi, *Superionic Solids and Solid Electrolytes. Recend Trends*, A.L. Laskar and S. Chandra (eds.), Academic Press, 1989.

[69] T. Takahashi, T. Esaka, H. Iwahara, *J. Appl. Electrochem.* **7** (1977) 303-308.

[70] J.C. Boivin, G. Mairesse, *Chem. Mater.* **10** (1998) 2870-2888.

[71] I. Abrahams, F. Krok, *J. Mater. Chem.* **12** (2002) 3351-3362.

[72] J.B. Goodenough, J.E. Ruiz-Diaz and Y.S. Zhen, *Solid State Ion.* **44** (1990) 21-31.

[73] K. Huang, S.R. Tichy, J.B. Goodenough, *J. Am. Chem. Soc.* **81** (1998) 2565-2575.

[74] A. Matraszek, L. Singheiser, D. Kobertz, K. Hilpert, M. Miller, O. Schulz, M. Martin, *Solid State Ion.* **166** (2004) 343-350.

[75] K. Huang, J. Wan, J.B. Goodenough, *J. Electrochem. Soc.* **148** (2001) A788-A794.

[76] M. Feng, J.B. Goodenough, K. Huang, C. Milliken, *J. Power Sources* **63** (1996) 47-51.

[77] J.C. Ruiz-Morales, J. Canales-Vázquez, J. Peña-Martínez, D. Marrero-López, P. Núñez, *Electrochim. Acta* **52** (2006) 278-284.

[78] J.D.M. Bastidas, S. Tao, J.T.S. Irvine, *J. Mater. Chem.* **16** (2006) 1603-1605.

Chapter 2

Experimental

Abstract

This chapter contains general information concerning to the different synthesis methods used in the preparation of both electrode and electrolyte materials, and the structural and electrochemical techniques used throughout this thesis to characterise the aforementioned materials. Special attention was paid to the electrochemical characterisation and particularly to the electrochemical impedance spectroscopy (EIS).

2.1. Introduction

The experimental procedure has consisted basically in the synthesis and structural characterisation of the different polycrystalline materials (mainly perovskite-type structure materials) and its electrochemical characterisation. Materials have been prepared by conventional solid state method and alternative precursor routes such as sol-gel and freeze-drying methods. Tape casting technique was also used to obtain electrolyte thin films.

Structural characterisation has been performed by different techniques i.e. X-ray diffraction (XRD) to confirm the phase purity and the identity of the main impurities; thermal analysis (TG/DTA and TMA) to study the precursor temperature decomposition and thermal expansion coefficients; differential scanning calorimetry (DSC) to reveal possible phase transitions; scanning electronic microscopy (SEM) and energy dispersive scanning (EDS) to study the microstructure and the composition of the samples; and surface area and density analysis to evaluate the porosity rate of the studied materials and its apparent density, respectively.

Electrical characterisation allows obtaining relevant information about the electrochemical properties of materials under study and the performance of these materials assembled in a single fuel cell. In this sense, the overall conductivity has been measured by electrochemical impedance spectroscopy (EIS) or dc-four-probe Van der Pauw method. A modified *emf* method was used to estimate the ionic transport numbers of the electrolyte materials. In addition, the area-specific resistance (ASR) namely the polarisation resistance of several electrode materials under different atmospheres was studied. Fuel cell tests have been carried out to obtain the power density, electrode and electrolyte resistance and current-voltage characteristics of different single cells.

2.2 Preparative Methods

Several synthesis methods have been used in order to optimise the microstructure of the potential materials for IT-SOFC applications. The size of the grains and the grain boundary of the materials are strongly dependent on the employed synthesis method. The ceramic method based on the conventional solid state reaction is the simplest method, however it usually requires high temperature operation, thereby the product possesses a high grain size and heterogeneous distribution of the grains. Size and distribution of the grains, as well as, grain boundary affect the properties of the materials. For this reason, methods that allow the production of smaller particles, i.e. precursor routes as sol-gel and freeze-drying methods, have been preferentially used for electrode material preparation, because of the synthesis temperature is considerably lower and hence a reduction of the grain size of the synthesised polycrystalline materials and a homogenous distribution of the particles is expected.

2.2.1 Ceramic method

The ceramic method [1] consists of heating together an intimate mixture of the solid raw materials in an appropriate ratio which react to form the required product. This method is used widely both industrially and in the laboratory. Despite its widespread use, this method has several disadvantages such as high temperature requirement (> 1473 K), considerably time to complete the solid state reactions (~10-24 hours) and the product obtained is often not homogeneous in composition. The main limitation of this method is that the chemical reactions only take place at the interface of the reactants in contact, and once the surface layer has reacted, reaction can only continue as reactants diffuse across the interface. The diffusion is often the limiting step. Because of this, it is important that the starting materials are ground to give a small particle size, and a homogeneous mixture to maximize the surface contact area and minimize the distance that the reactants have to diffuse. Commonly the reaction mixture is removed during the heating process and reground to bring fresh surfaces in contact and so speed up the reaction. Nevertheless the reaction time scale is always measured in hours.

2.2.1.1 Powder preparation

The employed raw materials for solid state reaction were high purity stable metal oxides and carbonates, although sometimes nitrates are useful because the favourable kinetics of precursor nitrates lead to the formation of reactive oxide surfaces [2]. Some chemical reagents need a pre-treatment to remove water and/or adsorbed gases e.g. lanthanum oxide, which is extremely hygroscopic. In this work, metal oxides were pre-heated up to 1273 K for 5 hours in an alumina crucible before weighing to obtain an accurate stoichiometry.

The powders were ground in an agate mortar for improved mixing of the reactants with acetone. Pulverissete 7 and PM100 ball milling systems have been also used to achieve a more homogeneous mixture of the particles.

2.2.2 Precursor synthesis routes

The precursor method achieves mixing at the atomic level by forming an intermediate solid, the precursor, in which the metals of the desired compound are present in the correct stoichiometry. The precursor is then heated for decomposition to the final product. Homogeneous products are formed at relatively low temperatures. A disadvantage is the lack of a suitable precursor in some cases for certain compositions.

2.2.2.1 The sol-gel method

A sol is a colloidal suspension of particles in a liquid, typically 1-100 nm in diameter and a gel is a semi-rigid solid in which the solvent is contained in a framework of material which is either colloidal (essentially a concentrated sol) or polymeric. To prepare solids using the sol-gel method, a sol is firstly prepared of reactants in a suitable liquid. Sol preparation can either be simply the dispersal of an insoluble solid or addition of a precursor which reacts with the solvent to form a colloidal product. A typical example is the dispersal of oxides or hydroxides in water with the pH adjusted so that the solid particles remain in suspension rather than precipitate out. The sol is then either treated or simply left to form a gel. To obtain the final product, the gel is calcined. The solvent is removed and anions such as alkoxides or carbonates are decomposed to give oxides by calcination. It allows rearrangement of the structure of the solid and it allows crystallisation to occur. The main steps in the sol-gel process are outlined in Figure 2.1.

It should be considered that the sol-gel process is usually very sensitive to certain experimental parameters such as temperature, pH, chemical composition, concentration of the reactants, and nature of the solvent [3]. In this work, a modified sol-gel route based on the Pechini method [4] was carried out. This method consist in forming a chelate between mixed cations. The metallic salts, such as nitrates, carbonates, acetates, etc. are dissolved to form an aqueous solution, and a hydroxycarboxylic acic (i.e. citric acid) or acetylacetone is added as complexing agent. This solution is mild heated for allowing the polyesterification as well as to remove excess water.

Figure 2.1 Steps in the sol-gel synthesis route.

The original method includes the addition of a polyhydroxy alcohol such as ethyleneglycol to facilitate the polyesterification. Finally a solid polymer resin namely a gel is formed. Once the gel is dry the precursor is obtained by calcination.

The citrate sol-gel route [5] starts with a homogeneous dissolution of the raw materials, usually nitrates. Thus, the required amounts of nitrate solutions were mixed at room temperature. Afterwards, a citric acid solution - 1.5 % wt. in excess and in a ratio ligand/metal (L/M) of 1 and 2/3 for trivalent and divalent cations respectively - was also added. The pH was adjusted up to 9 with addition of ammonia solution (20% v/v). A gel was formed with continuous stirring and low heating (~ 338 K). It was dried at room temperature for more than 8 h. The dried gel was fired at 573 K for 30 min. The obtained powders were ground in an agate mortar and fired in air at the optimal temperature determined by thermogravimetric analysis.

In the case of acetylacetonate route [6], acetates were preferred to nitrates as raw materials. Figure 2.2 shows a diagram of this route.

Basically, acetic acid (HAc) in excess (10% v/v.) was added to an acetates solution to remain the corresponding acetates (Ac^-). A volume of acethylacetone (AcAc) solution was added in a molar ratio $AcAc/Ac^-$ of 3:1. The same volume of water and HAc was added and mixed. A gel was formed with stirring and low heating. The gel was dried and calcined as well as those obtained by citrate sol-gel method.

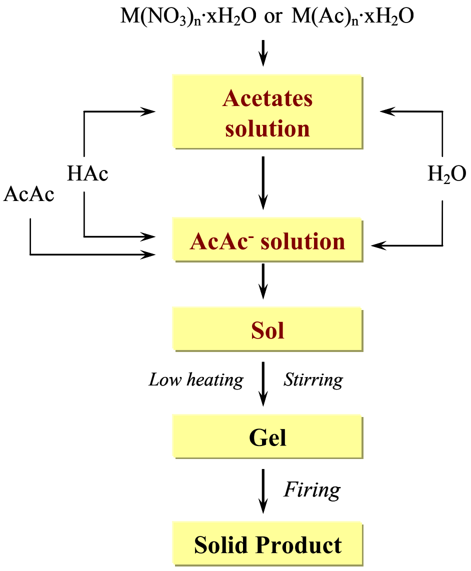

Figure 2.2 Acetylacetonate route diagram

2.2.2.2 Freeze-drying method

Freeze drying method [7] involves the removal of water or other solvent from a frozen product by sublimation. The freeze-drying process consists of three stages: pre-freezing, primary drying and secondary drying. Figure 2.3 illustrates this process. The primary and secondary drying has been carried out using a Heto Lyolab freeze-dryer (Figure 2.4) at 1-10 Pa and 218 K during 3 days. The resulted amorphous precursor powders were calcined at 573 K for an hour, grounded in agate mortar and finally fired at the optimal temperature determined by thermogravimetric analysis. In the following paragraphs it has been introduced a brief explanation of the different stages of the freeze-drying method in order to clarify this process.

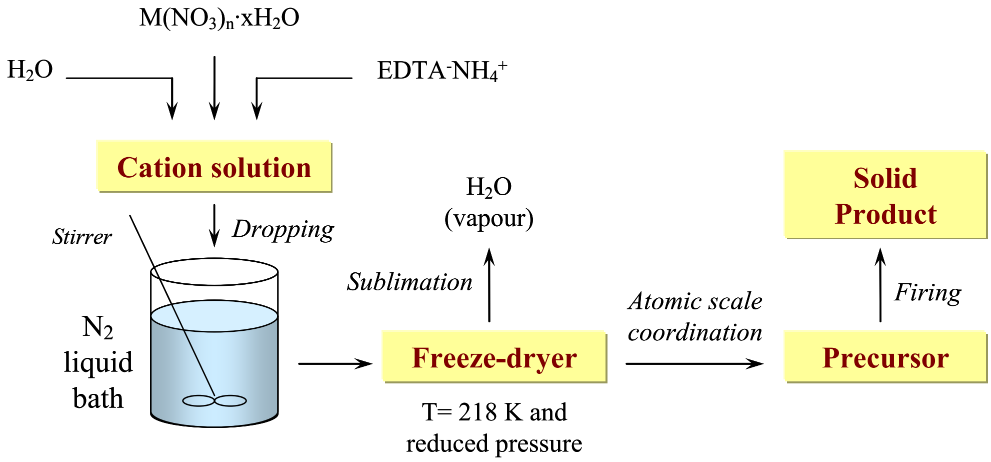

Figure 2.3 Freeze-drying process diagram.

Solution preparation

The freeze-drying method starts with the preparation of the corresponding aqueous cation solution according to the desired stoichiometry of the final product. Usually, nitrates are dissolved in distilled water and a solution of ammonium-EDTA in a molar ratio ligand/metal of 0.5 is added. The pH is adjusted up to 7 with addition of nitric acid [8]. However, it has been observed that certain material systems required basic conditions to obtain a proper freeze-dried product, see Figure 2.5.

Figure 2.4 Heto Lyolab freeze-dryer

Figure 2.5 Resulting products after freeze-dried the same raw cation solution (LSGM) at different pH: a) pH> 7, c) pH<6 and c) pH=7.

Pre-freezing

Pre-freezing is necessary since freeze-drying consist in a dehydration process at low temperature by sublimation (ice to vapour). The method of pre-freezing and the final temperature of the frozen product can affect the ability for freeze-drying the material. Rapid cooling results in small ice crystals, whereas slower cooling results in larger ice crystals. It has been preferred a rapid cooling in the present investigation, for instance the solutions of the corresponding cation were flash-frozen, drop by drop, into liquid nitrogen bath under vigorous stirring to avoid the agglomeration of the ice crystals.

Primary drying

After pre-freezing process, the formed ice has to be removed from the frozen product via sublimation. The rate of sublimation of ice from a frozen product depends upon the difference in vapour pressure at the surface of the sample compared to the vapour pressure of the ice collector. Water molecules migrate from the higher pressure sample to a lower pressure area. Conditions must be created to encourage the free flow of water molecules from the product. Therefore, heat must be applied to the sample to assist the water removal in form of vapour from the frozen sample. Heat can be applied by several means but the method used in this work, is to use ambient heat in a manifold dryer. A vacuum pump is also used to induce the low pressure on the sample surface and a cold trap is used to collect the moisture avoiding damage to the vacuum pump. The collector condenses out all condensable gases, i.e. the water molecules, and the vacuum pump removes all non-condensable gases.

Secondary drying.

After primary freeze drying is complete, and all ice has sublimed, bound moisture is still present in the product. The product appears dry, but the residual moisture content may be as high as 7-8%. Continued drying is necessary at the warmer temperature to reduce the residual moisture content to optimum values.

2.2.3. Thin film electrolyte preparation by tape casting

Tape casting technique has been used to prepare LSGM electrolyte thin film. Tape casting is a well known, simple and cost-effective method which has been successfully employed to prepare e.g. YSZ thin films [9].

In this work, the production of LSGM thin film by tape casting has been carried out under the supervision of Dr. C. Savaniu and Professor J.T.S. Irvine at the Centre of Advanced Materials in the University of St. Andrews (Scotland) [10].

Tape casting technique allows the production of *thin flat sheets*. Powders of the material to be deposited are mixed with different organic additives to produce an slurry. This slurry is deposited on a carrier film by the shearing action of a *doctor blade*. The obtained tape is then dried and removed from the carrier film. Afterwards, the tape is fired, burning out the organic materials and sintering the thin layer producing a dense tape. Figure 2.6 illustrates a schematic diagram and a picture of the tape caster used in this work. The slurry is drawn out beneath the doctor blade by the relative motion of the carrier film. The height of the adjustable blade above the film controls the thickness of the tape. The formulation of the ceramic slip is the most critical step, though drying and firing are also important in controlling process tolerances. Slips are multicomponent systems usually containing: the *powder*; a *surfactant* to stabilize the powder against colloidal forces; a *solvent* to reduce the mix viscosity to allow casting; a *binder* for green strength in the cast tape; and a *plasticizer* to modify the properties of the binder. These ingredients interact, especially in their competition for binding sites on the powder surface. For this reason the order of addition of components and their mixing time are also variables in slip design. The main advantage of this process is a high production rate. The technique is ideal for making flat components such as ceramic substrates. However, commercial systems usually contain environmentally unfriendly solvents.

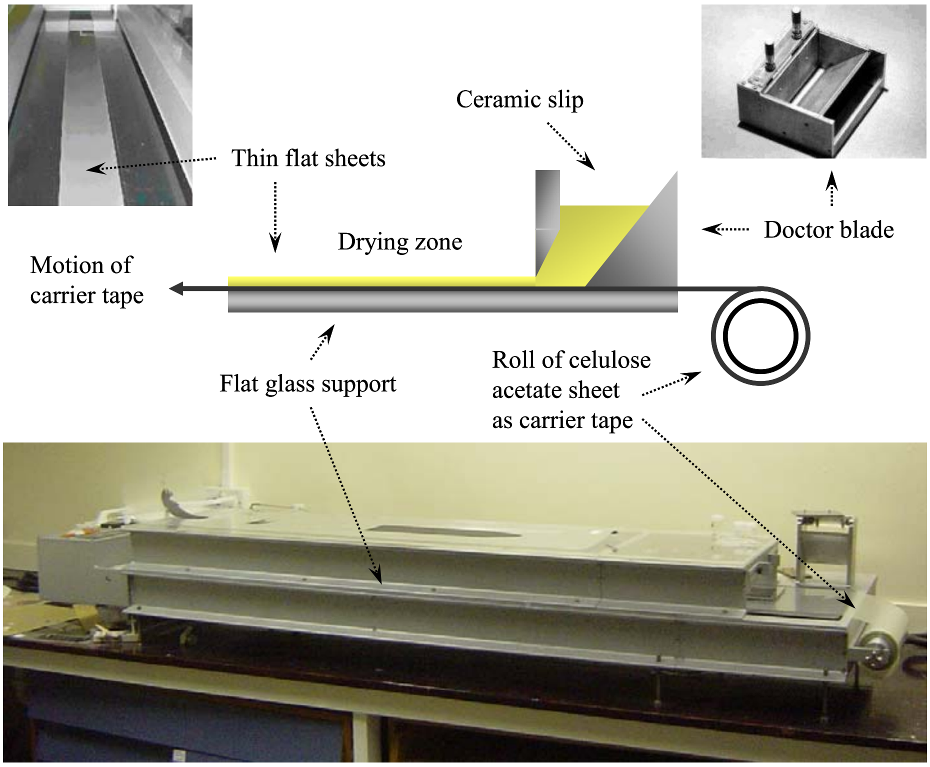

Figure 2.6 Schematic diagram of the principle and picture of St. Andrews's tape caster.

Specifically, the procedure for obtaining LSGM electrolyte thin layers by tape casting comprised:

1. Preparation of a slurry by mixing powders of dehydrated oxides in the appropriate stochiometry of La_2O_3, Ga_2O_3, $SrCO_3$ and MgO (these oxides have been previously ball milled and fired at 1173 K), methylethylketone (MEK) as solvent and Triton QS-44 (phosphate ester, acid form) as dispersant to reduce the interfacial tension between the surface of the particle and the liquid.
2. Ball milling for 18 hours and addition of Polyethylenglycol 300 as gelificant, di-n-butyl phthalate (DBP) as plasticizer to increase the flexibility of the tapes and BUTVAR B-98 as binder to enhance their strength after the evaporation of the solvent are added to the solution.
3. The solution was shacked 20 minutes to obtain a homogeneous mixture. After that, it was ball milled for another 4 hours.
4. The obtained ceramic slip was deposited in the tape caster using the doctor Blade. After drying, thin flat sheets are prepared. The tapes were cut into disks. The thin LSGM electrolyte for fuel cell testing were prepared by laminating two disks and firing both together at 1573 K with slow heating rate to get a dense and homogeneous layer of 120 µm thickness after firing.

The composition in weight of the different slurry components was: 50% of precursor powders, 35% of solvent, 0.5% of dispersant, 4.5% of gelificant, 4% of plasticizer and 6% of binder. This composition was initially founded as the optimal composition to produce tapes of YSZ by J.T.S. Irvine's research group. Therefore, this composition was chosen as starting point for the preparation of the LSGM tapes.

2.3 Structural characterisation

2.3.1 X-ray diffraction (XRD)

X-ray diffraction (XRD) is a versatile, non-destructive analytical technique for identification and quantitative determination of crystalline phases present in powder and solid samples. In this work, XRD patterns were recorded using different powder diffractometer, i.e. Siemens D5000 with Cu $K\alpha_1$ radiation (wavelength of 0.15406 nm) and Philips X′Pert with Cu $K\alpha_{1,2}$ both with automatic sample charger, and Philips X′Pert Pro with a primary monochromator and a X'Celerator detector with Cu $K\alpha_1$ radiation. The scans were performed in the 2θ range from 10 to 120° with 0.02° step and 10 s/step for routine identifications and 0.016° step and 500 s/step for high resolution studies. Identification was achieved by comparing the experimental X-ray diffraction pattern with PDF and ICSD data base using X'Pert HighScore plus [11] and FindIt [12] software.

The X-ray patterns were refined by the Rietveld method using FullProf and WinPlotr programs [13,14]. The Rietveld method refines a crystal structure by comparing the measured diffraction pattern with that calculated from a known crystal structure. A least-squares refinement is used to optimise the structure parameters. Examples of Rietveld method refinement of $LaGaO_3$ and doped $LaGaO_3$ samples are shown in Appendix I.

2.3.2. Scanning electron microscopy (SEM)

The solid surface structure can be examined by irradiation of the sample with a scanning beam of electrons and then collecting secondary electrons. In comparison with optical microscope, SEM gives much higher resolution and much larger depth of field. One example is illustrated in Figure 2.7.

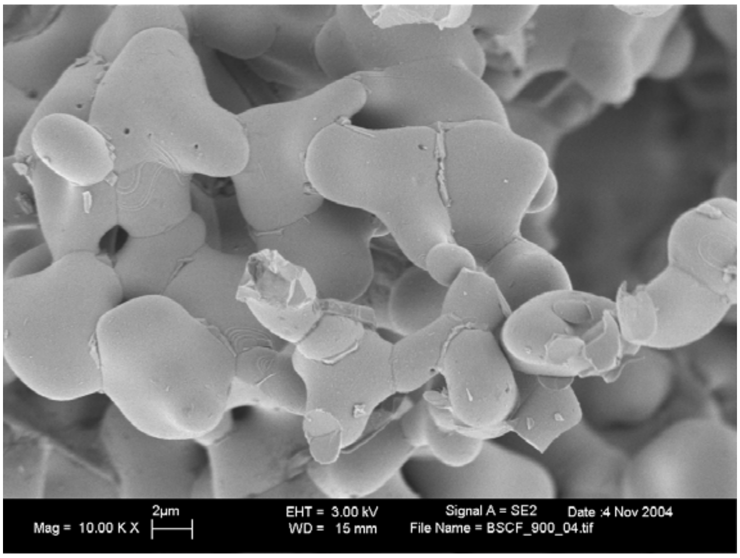

Figure 2.7. SEM image of $Ba_{0.5}Sr_{0.5}Co_{0.8}Fe_{0.2}O_{3-\delta}$ (BSCF) porous material.

In addition, Energy Dispersive X-Ray Spectroscopy (EDS) has been employed to study the stoichiometry of the sample and identify possible impurities. One example is given in Figure 2.8. where $LaSrGa_3O_7$ impurity presence is detected by EDS and XRD analysis in a $La_{0.9}Sr_{0.1}Ga_{0.8}Mg_{0.115}Co_{0.085}O_{3-\delta}$ sample.

Several SEM equipments have been used for the microstrutural characterisation. A Jeol JSM-5600 (University of St. Andrews), a JSM-6300 (University of La Laguna), and a LEO 1530 (ETH-Zurich) incorporating EDS NORAN Vantage, were used operating at voltages up to 30 kV, resolution until 3.5 nm and magnification up to 300,000x. This technique has been used for the characterisation of ceramic samples as powder, pellet, thin-film, dense or porous microstructure.

In the case of dense pellets, the surfaces were always polished using diamond pastes (10 - 1 µm) and afterwards a thermal etching was carried out to differentiate much better the grain boundaries. Gold sputtering was also used in several samples e.g. LSGM pellets to increase the resolution.

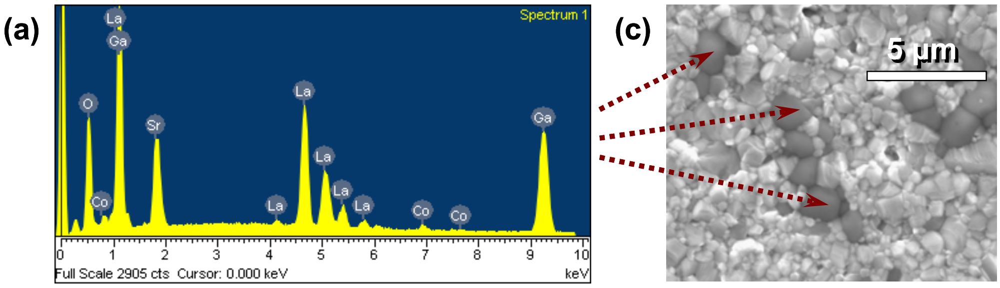

(b)

Spectrum	O	Co	Ga	Sr	La	Total
Spectrum 1	69.75	0.49	16.03	6.66	7.06	100.00
Spectrum 2	64.10	0.40	18.97	7.05	9.48	100.00
Spectrum 3	67.57	0.39	17.00	6.76	8.28	100.00
Spectrum 4	60.23	0.66	20.51	6.49	12.10	100.00
Spectrum 5	63.64	0.87	17.19	5.01	13.28	100.00
Spectrum 6	43.94	1.39	27.45	4.22	23.00	100.00
Spectrum 7	58.02	1.86	16.72	1.45	21.95	100.00

All results in Atomic Percent

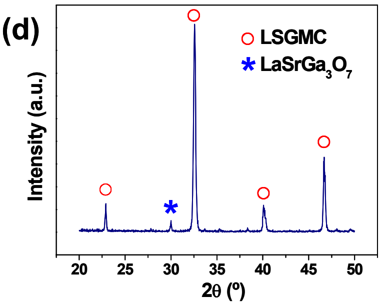

Figure 2.8. (a) EDS spectrum and (b) table with the percent distribution of each cation obtained by EDS spectra of $La_{0.9}Sr_{0.1}Ga_{0.8}Mg_{0.115}Co_{0.085}O_{3-\delta}$ sample, synthesised via ceramic route at 1573 K in air for 6 h. (c) SEM image showing $LaSrGa_3O_7$ impurities. (d) XRD pattern confirms the impurity presence.

2.4. Thermal analysis

2.4.1. Thermogravimetric/Differential Thermal Analysis (TG/DTA)

TG/DTA Perkin Elmer Pyris Diamond series and STA 449 C Jupiter NETZSCH thermal analysers have been used to study precursor materials decomposition, and crystallisation, and to determine the correct stoichiometry of the hygroscopic starting chemicals such as nitrates used in the precursor route synthesis. The operating temperature ranged between room temperature and 1273 K with heating/cooling ratio of 5-10 K/min. TG/DTA combines the flexibility of the differential temperature analysis (DTA or DSC) feature with the proven capabilities of the thermogravimetry (TG) measurement technology. The combination allows to determine whether an endothermic or exothermic transition is associated with a weight loss in contrast to a melting or crystallisation process. The TG determines the weight change of a sample whereas the DTA measures the change in temperature between a sample and the reference as a function of temperature and/or time. TG/DTA analysis is illustrated in Figure 2.9.

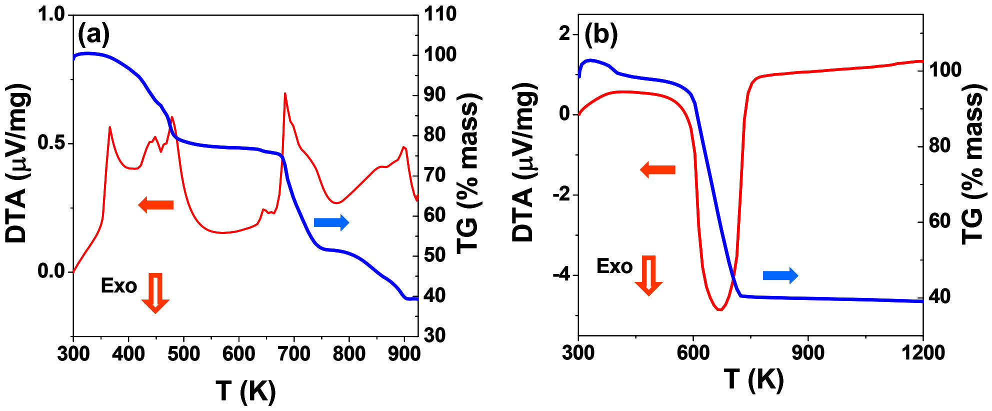

Figure 2.9. TG/DTA of (a) $La(NO_3)_3 \cdot H_2O$ decomposition in air and (b) crystallisation process of $Sm_{0.15}Ce_{0.85}O_{2-\delta}$ using a precursor obtained via sol-gel route.

2.4.2. Thermomechanical analysis (TMA)

A thermomechanical analyser TMA Perkin Elmer Pyris Diamond series has been used to study thermal expansion coefficients and the optimal sintering temperature of the ceramic materials.

Linear shrinkage of $La_2Mo_2O_9$ (LMO) and $LaGaO_3$ (LGO) synthesised by sol-gel route is illustrated in Figure 2.10. Linear shrinkage rate indicates optimal temperature of sintering, around 1050 K and 1400 K for LMO and LGO, respectively. Measurements were carried out using pellets of 6-8 mm thickness and 5 mm diameter. The temperature was varied from room temperature to 1773 K with a heating/cooling ratio of 1-10 $Kmin^{-1}$.

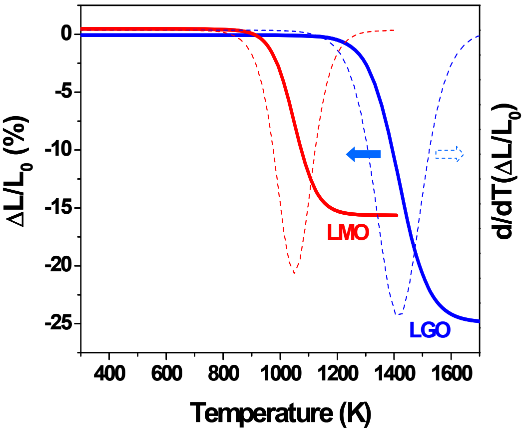

Figure 2.10. Linear shrinkage and linear shrinkage rate of $La_2Mo_2O_9$ (red) and $LaGaO_3$ (blue) samples.

2.4.3. Differential scanning calorimetry (DSC)

A Pyris Diamond DSC has been used to study possible phase transitions. The operating temperature ranged from 103 K to 973 K. The equipment was calibrated with different standard samples, i.e. indium and zinc which have known transition temperature and enthalpy energy: indium: 429.60 K and 28.450 Wg^{-1}, and zinc, 692.67 K and 108.370 Wg^{-1}.

DSC curves of $LaGaO_3$ sample synthesised at 1723 K, in air, is shown, as example, in Figure 2.11. The maximum peak temperature is ~ 421 K on heating and enthalpy change values are 0.36 kJ/mol. A hysteresis characteristic of a first order phase transition is also observed with an onset temperature of 418 K on heating and 414 K on cooling. This is in good agreement with the reported data in the literature [15,16], and it was confirmed by high temperature XRD (Appendix I).

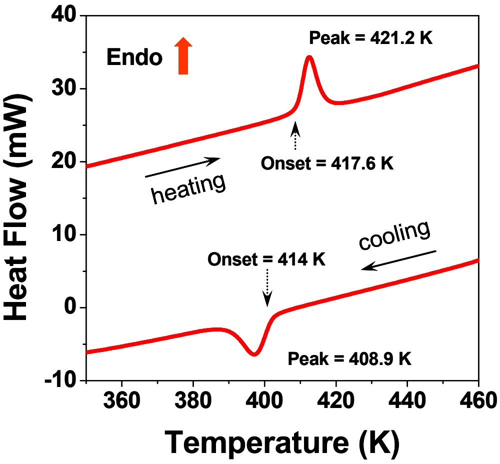

Figure 2.11. DSC measurement of polycrystalline powders of $LaGaO_3$.

2.5. Surface area determination by gas adsorption

Surface area helps to determine how solids react with other materials. BET surface area [17] of different materials has been determined in the present work by Micromeritic's physisorption analyser GEMINIS V using nytrogen gas as adsorptive. To determine the surface area, powdered solid samples have been pre-treated by applying a combination of heat, vacuum and/or flowing gas. Nytrogen was used to remove adsorbed contaminants acquired from atmospheric exposure. The solid was then cooled in a liquid nitrogen bath under vacuum. An adsorptive (nitrogen) was admitted to the solid in controlled increments. After each dose of adsorptive, the pressure was allowed and the quantity of gas absorbed was calculated. The gas volume absorbed at each pressure (at one constant temperature) defines an adsorption isotherm, from which the quantity of gas required to form a monolayer over the external surface of the solid and its pores is determined. With the area covered by each adsorbed gas molecule known, the surface can be calculated. Additional information regarding BET model theory and experimental data concerned to the studied materials can be seen in Appendix II.

2.6. Density determination by pycnometry

A Micromeritic's gas (helium) pycnometer, AccuPyc 1330, was used to obtain absolute material density. This is obtained when the volume measured excludes the pores as well as the void spaces between particles within the bulk sample [18]. The system was calibrated using as the sample precision steel spheres before starting the experiments. The powdered samples were also pre-treated as well as the samples studied in the surface analysis to remove adsorbed contaminants and water. Experimental data is given in Appendix III.

2.7. Electrical characterisation

Electrochemical characterisation of mixed and pure ionic conductors gives information of the different processes and contributions to the conductivity and their performance as a component of a fuel cell. All the components of a fuel cell have to fulfil specific requirements in order to contribute to the normal operation of a fuel cell. In this sense, several techniques have been employed for the electrochemical characterisation. These techniques are generally described in the following paragraphs and the use for them is outlined in table 2.1.

Table 2.1.
List of the electrochemical characterisation techniques used in this work.

Technique	Electrolyte	Electrode	Parameter obtained
Impedance spectroscopy	X	X	Area specific resistance
	X		Overall conductivity
Van der Pauw method		X	
Modified *emf* method	X		Transport numbers
Fuel cell tests	X	X	Open circuit voltage Power density Voltage-current curves

2.7.1. Electrochemical impedance spectroscopy (EIS)

The electrochemical impedance spectroscopy (EIS) technique [19] is based on the application of a sinusoidal ac-voltage with changing frequency to an electrochemical system. Therefore, the frequency-dependent resistance of the system, the impedance, is recorded over a wide range of frequencies. The electrical behaviour of the system could be modelled by equivalent circuits with defined electrical elements e.g. resistors, capacitors, inductances that yield to the same impedance response than the real system. Correlating the values of the electrical elements with the real physical processes allows a characterization of the different conductivity mechanisms contributing to the total electrical conductivity. This resolution is based on the fact that different physical phenomena often relax at very different frequencies. If a small sinusoidal voltage signal is applied to a linear physical system that contents ohmic resistances and energy storing elements, e.g. capacitances or inductances, the current response is shifted in phase and altered in amplitude, but remains in sinusoidal form. Hence, if the applied potential is given in complex Euler-form by

$$\widetilde{E}(t) = \Delta E e^{i\omega t} \qquad (2.1)$$

with a fixed angular frequency $\omega = 2\pi f$ (f frequency) and a voltage amplitude of ΔE, the current output is represented by

$$\widetilde{I}(t) = \Delta I e^{i(\omega t + \phi)} \qquad (2.2)$$

where ΔI is the current amplitude and ϕ is the phase difference. According to Ohm's law the impedance $\widetilde{Z}(\omega)$ of the system at any angular frequency ω is given by the ratio of the voltage signal divided by the current:

$$\widetilde{Z}(\omega) = \frac{\widetilde{E}(t)}{\widetilde{I}(t)} = |Z| e^{(-i\phi)} \tag{2.3}$$

Hereby $|Z|$ is the magnitude of the impedance. Written in polar and Cartesian coordinates with separated real and imaginary parts, the equation is given by

$$\widetilde{Z}(\omega) = |Z| \cos\phi - i|Z| \sin\phi = Z' - iZ'' \tag{2.4}$$

where Z' and Z'' are the real and the imaginary impedance parts. Using this nomenclature the impedances of the basic electrical elements ohmic resistor R, capacitor C and inductor L are given as follows:

- Ohmic resistor *R:* $\widetilde{Z}(\omega) = R + 0i$ (2.5)
- Capacitor *C:* $\widetilde{Z}(\omega) = 0 + \dfrac{1}{i\omega C}$ (2.6)
- Inductor *L:* $\widetilde{Z}(\omega) = 0 + i\omega L$ (2.7)

For the analytical description of so-called non ideal processes a constant-phase element (CPE) is introduced by:

- CPE: $\widetilde{Z}(\omega) = \dfrac{A}{(i\omega)^n}$ (2.8)

where A and n are constants. Depending on their values the CPE can turn to ideal elements: capacitor if $n = 1$ and $A = 1/C$, ohmic resistance when $n = 0$ and $A = 1$, and inductor in the case of $n = -1$ and $A = L$. The CPE is widely used in data fitting of recorded impedances and helps often to describe the real impedance response of solid electrolyte systems. The impedance of combined elements is determined following Kirchhoff's law, which means that the total impedance $\widetilde{Z}_{tot}(\omega)$ of a circuit is given by

$$\widetilde{Z}_{tot}(\omega) = \sum_{j=1}^{N} \widetilde{Z}_j(\omega) \tag{2.9}$$

$$\frac{1}{\widetilde{Z}_{tot}(\omega)} = \sum_{j=1}^{N} \frac{1}{\widetilde{Z}_j(\omega)} \tag{2.10}$$

in the case of a series combination, equation 2.9, or parallel arrangement, equation 2.10, of N impedance elements.

2.7.1.1. Impedance spectra

The Nyquist and the Bode diagrams are the typical diagrams commonly used to plot the impedance data acquired by EIS. In the Nyquist diagram the imaginary impedance part is plotted as a function of the real part, whereas, the Bode diagram shows the logarithmic scaled impedance magnitude |Z| and the phase difference as a function of the logarithmic scaled frequency *f*. Figure 2.12a shows the Nyquist plot of an ohmic resistance in parallel with a capacitance. The impedance response of this circuit plotted in the complex plane is a semicircle with its centre on the real axis (Z'). For angular frequencies with $\omega \to 0$, the capacitance is blocking and the impedance is governed by the ohmic resistance. For high angular frequencies $\omega \to \infty$, the capacitance is short-circuiting the resistor and the impedance approaches zero. The difference of low (right) and high (left) frequency intercepts on the semicircle on the real axis gives the value of the resistor. The value of the capacitance can be calculated from the characteristic angular frequency ω_0 at the top of the semicircle:

$$\varpi_0 = 2\pi f_0 = \frac{1}{\tau} = \frac{1}{RC} \tag{2.11}$$

τ is the time constant of the circuit, R and C are the values of the resistor and capacitor and f_0 is the characteristic relaxation frequency.

The corresponding Bode diagram is shown in Figure 2.12b, in the upper part, the impedance magnitude is plotted over the frequency *f*, both on a logarithmic scale. In the lower part the phase difference is shown as a function of the logarithmic scaled frequency. The phase difference approaches zero for angular frequencies $\omega \to 0$, where the impedance is controlled by the ohmic resistor, whereas it approaches -90° for $\omega \to \infty$ where capacitive behaviour is dominant.

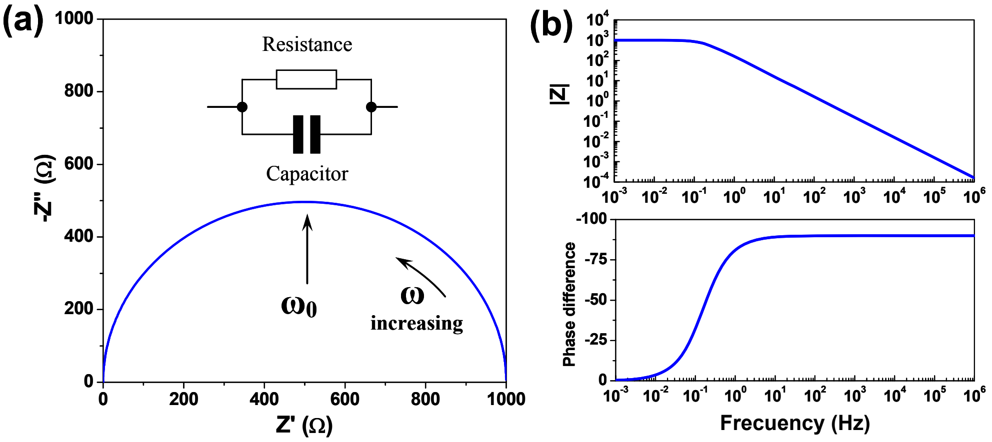

Fig. 2.12. Nyquist plot (a) and Bode plot (b) of 1 kΩ/1 mF parallel RC circuit

Figure 2.12b (top), shows a plateau at low frequencies, indicating that the magnitude of the impedance is dominated by the ohmic resistive part. On the other hand, at higher frequency, the magnitude shows a linear dependence with the frequency, slope minus one, indicating a capacitive dominated part. A plateau is observed now for theta, in this frequency range, Figure 2.12b (bottom).

Both diagrams have advantages and disadvantages: The Nyquist diagram allows an easy prediction of the circuit elements but does not include the frequency dependence of the impedance. For example the Nyquist plot illustrated in Figure 2.12a, show the same shape for any capacitance combined with the given resistor. The only difference between them would be the fact that the points on the semicircle would correspond to different frequencies. Meanwhile, the Bode diagram contents all the impedance information but is less suited for an intuitive prediction for the model of circuits.

2.7.1.2. Equivalent circuit modelling

Equivalent circuits represent the behaviour of the real electrochemical system. Thus, the electrical properties are correlated with the microstructure. The Brick Layer Model (BLM) [20], is the simplest model used for the characterisation of solid electrolyte materials. Within the BLM, the grains are modelled as cubes, see Figure 2.13, of equal size with an edge length D, surrounded by grain boundaries with a thickness δ_{gb} where $\delta_{gb} << D$. The current flow is assumed to be one dimensional, curvature of current paths is neglected. In general, the whole volume is passed by the current flow, but for conductivities σ_{gb} (grain boundary) and σ_{grain} (grain interior or bulk) that are very different, two different current flow paths can be formulated: blocking grain boundaries and highly conductive grain boundaries, see Figure 2.14.

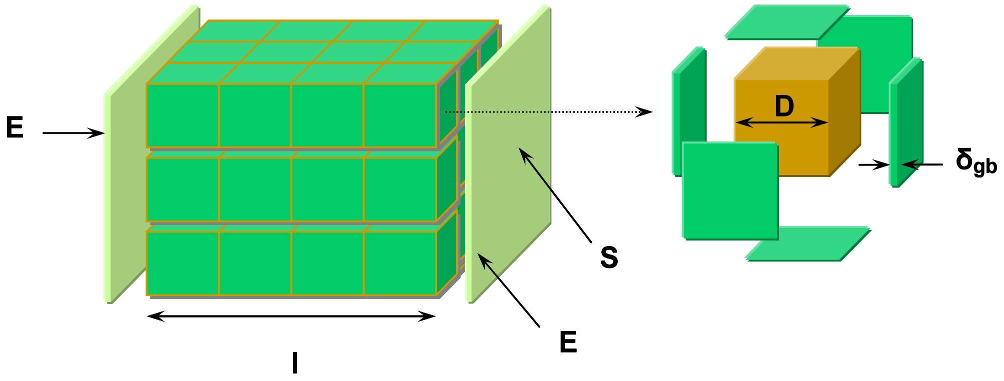

Figure 2.13. Schematic drawing of the Brick Layer Model, showing the grain diameter D, the grain boundary thickness δ_{gb}, the sample thickness l, the cross sectional area S and the electrodes E.

Current flow path 1: blocking grain boundaries

If the grain boundary conductivity σ_{gb} is much lower than the conductivity of the grain interior σ_{grain} ($\sigma_{gb} << \sigma_{grain}$) the current flow between the electrodes will cross the grain boundaries perpendicular to it and then flow through the grain interior volume. In this case current flowing along parallel grain boundaries, short-circuiting the grain interior can be neglected. This path can be seen in Figure 2.14, right side.

Current flow path 2: highly conductive grain boundaries

In the case of highly conductive grain boundaries ($\sigma_{gb} >> \sigma_{grain}$) the current flow along parallel grain boundaries short circuits the grain interior, current flowing through the grain interior volume can be neglected. This path is shown in Figure 2.14, left side.

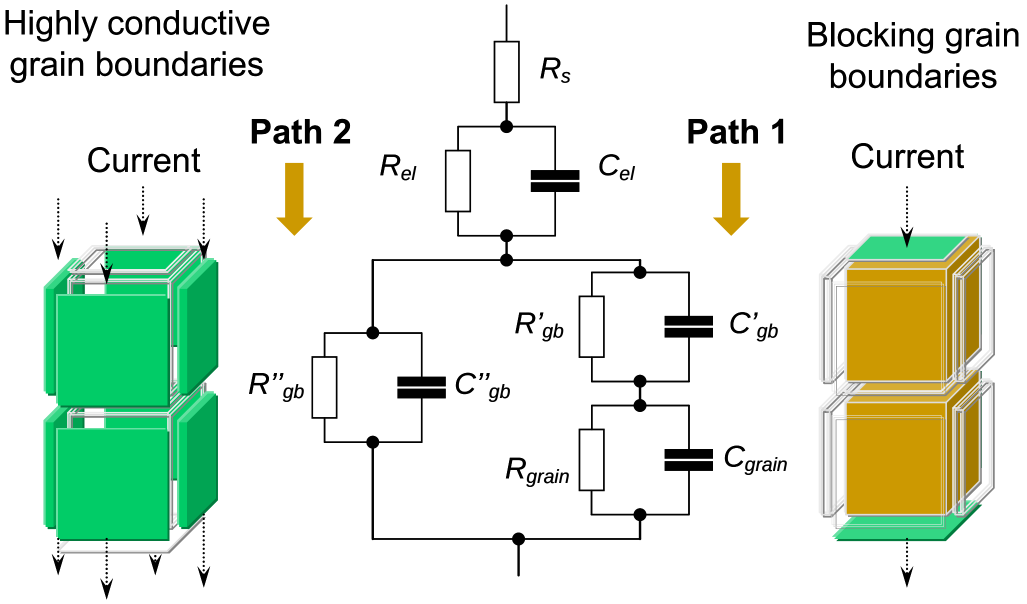

Figure 2. 14. Equivalent circuit model of the ceramic microstructure according to the Brick Layer Model, R_s represents the ohmic resistance of current leads and connectors, R_{el} and C_{el} are representing the electrode response, R''_{gb} and C''_{gb} model the behaviour of the grain boundaries passed by the current flow in line, R'_{gb} and C'_{gb} represent the grain boundaries passed perpendicular and R_{grain} and C_{grain} model the grain interior volume.

Figure 2.15 shows the impedance response of a polycrystalline electrolyte with blocking grain boundaries (BLM path 1) and the equivalent circuit used to model the material electrochemical behaviour.

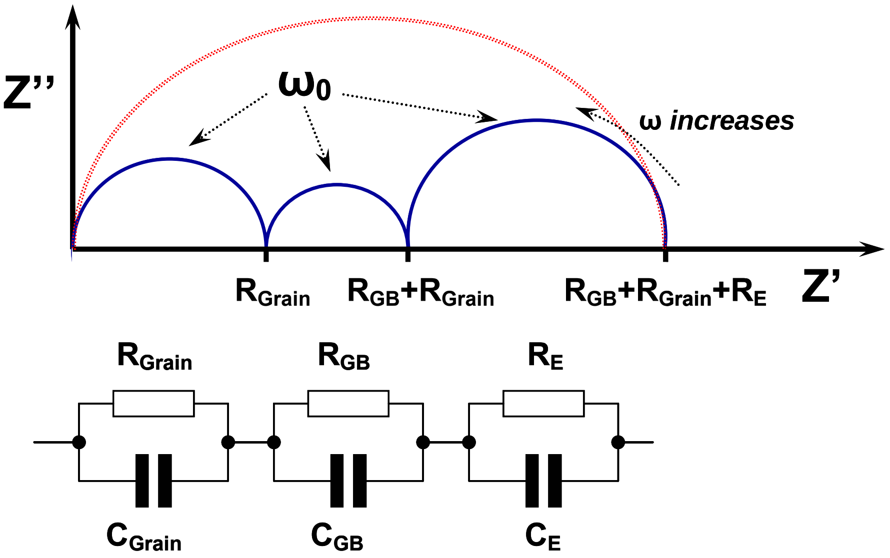

Figure 2.15. Idealised Nyquist plot showing a typical impedance response of a polycrystalline electrolyte with blocking grain boundaries (BLM path 1) and corresponding equivalent circuit model.

Each RC element yields to a semicircle in the complex plane plot with the characteristic relaxation frequencies ω_0 at the top. The ohmic resistances of the different elements can be derived from the intercepts of the semicircles on the real axis (Z'). The big red arc shows a behaviour of the impedance response occurring if the characteristic relaxation frequencies are overlapped, e.g. less than one order of magnitude as separation. The consequence is that the RC semicircles are no longer well separated.

A specific process can be assigned to the grain, grain boundary, etc., taking into account its capacity value. Usually, capacity values of 10^{-11}-10^{-12} Fcm^{-1} indicate process of grain interior or bulk, 10^{-8}-10^{-9} Fcm^{-1} is tipical of grain boundary processes, and electrode interfaces 10^{-5}-10^{-7} Fcm^{-1}.

Impedance spectra of real systems are typically more complex that the idealised plot shown in Figure 2.15. Slight distortions may occur due to the influence of measuring leads, or the impedance spectra may not be well resolved as also shown in Figure 2.16. There are several fitting software that help to fit the electrical elements of a given equivalent circuit model to the measured impedance spectra of the electrochemical cell. In this study the program ZView [21] was used. This program offers a tool to model equivalent circuits and to refine the introduced starting values for the different elements, by minimising the difference between real impedance data and the simulated one following a nonlinear least square procedure.

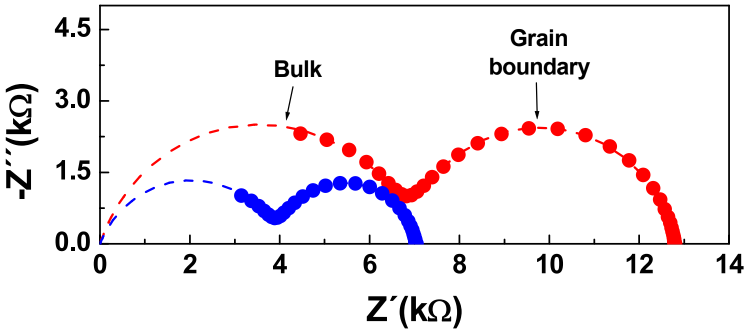

Figure 2.16. Impedance spectra for bulk and grain boundary of $La_{0.9}Sr_{0.1}Ga_{0.8}Mg_{0.115}Co_{0.085}O_{3-\delta}$ (LSGMC) at 348 K (red) and at 373 K (blue). Dash line is the fitted results obtained with equivalent circuits.

2.7.1.3. Calculation of electrical conductivities

Assuming that the grain boundary in a polycrystalline solid electrolyte is considerably more resistive than the grain interior and the Brick Layer Model for blocking grain boundaries is valid (path 1), the following equations can be formulated using the data acquired of the fitting procedure:

$$\sigma_{tot} = \frac{l}{SR_{tot}} \tag{2.12}$$

with

$$R_{tot} = R_{grain} + R_{gb} \tag{2.13}$$

where σ_{tot} is the total electrical conductivity, l is the distance between the electrodes, S is the total area that is passed perpendicular by the current flow. R_{tot} is the total resistance, R_{grain} is the resistance of the grain interior volume passed by the current flow, and R_{gb} is the resistance of all grain boundaries perpendicular to the current flow.

As $\delta_{gb} << D$, one can further calculate the grain conductivity as

$$\sigma_{grain} = \frac{l}{SR_{grain}} \tag{2.14}$$

The grain boundary conductivity σ_{gb} can be calculated as

$$\sigma_{gb} = \frac{l}{SR_{gb}}\frac{\delta_{gb}}{D} \tag{2.15}$$

with

$$\frac{\delta_{gb}}{D} = \frac{C_{grain}}{C_{gb}} \frac{\varepsilon_{gb}}{\varepsilon_{grain}} \qquad (2.16)$$

Here, ε_{gb} and ε_{grain} are the dielectric constants of the grain boundary and the grain interior, respectively. Equation 2.16 provides a direct correlation between the electrical and the microstructural properties of the material. Assuming that $\varepsilon_{gb} = \varepsilon_{grain}$, the grain boundary conductivity can be estimated as

$$\sigma_{gb} \approx \frac{l}{SR_{gb}} \frac{C_{grain}}{C_{gb}} \qquad (2.17)$$

If the activation energy of the grain boundary conductivity is of interest, it is also possible to calculate it using an apparent grain boundary conductivity $\sigma_{gb,app}$ given by

$$\sigma_{gb,app} = \frac{l}{SR_{gb}} \qquad (2.18)$$

Space charge model

Some authors [22,23] have proposed a space charge model to explain the blocking grain boundaries. In this model, the grain boundary is made up of two layers of charges separated by the grain boundary core. Oxygen vacancies depletion in this area could be the cause of the low grain boundary conductivity.

2.7.1.4. Experimental set-ups for electrical characterisation

2.7.1.4.1. Total conductivity

Impedance measurements were carried out on a 2-electrode arrangement, Figure 2.17, using ~7.5 mm diameter and ~1.5 mm thick dense pellets of the corresponding specimen. The density of these pellets was higher than 95% of the theoretical density estimated from the XRD data. Porous Pt electrodes were formed by coating platinum paste on both sides of the pellets and then fired at 1173 K for 1 hour in air. The impedance spectra were measured under air using a frequency response analyser (Solartron 1260) in the frequency range from 0.1 Hz to 1 MHz and with an excitation voltage of 100 mV.

The impedance spectra were collected once the sample was in thermal equilibrium. The design of the set-up includes a temperature control by computer using a controller Eurotherm 2604. The software used has been developed by Ruiz-Morales [24] to obtain the impedance measurement in an automatically procedure. A detail of the impedance cell is illustrated in Figure 2.18b.

2.7.1.4.2. Area specific resistance (ASR)

Area-specific resistance (ASR), namely polarisation resistance of electrode materials, was measured by EIS using a special impedance cell for working under different atmospheres (air, oxygen, argon, dry and wet 5%H_2/95%Ar), see Figure 2.18a.

Several electrode materials have been studied using LSGM electrolyte-dense-pellets. Thereby, a slurry of the studied electrode powders was prepared using Decoflux^{TM} as binder and a thin layer of the slurry was coated onto both surfaces of the electrolyte and then fired at 1373–1623 K for 2 hours in air. The thickness of the electrode layer after firing was around ~30-40 µm. The porosity and the microstructure of the deposited electrodes were studied by SEM revealing an average porosity of 30%. Current collector was formed by coating platinum paste on both sides of the pellets and then fired at 1173 K for 1 hour in air.

Finally, impedance spectra of the electrochemical cell was acquired under symmetric atmosphere in the frequency range from 0.1 Hz to 1 MHz and with an excitation voltage of 100 mV.

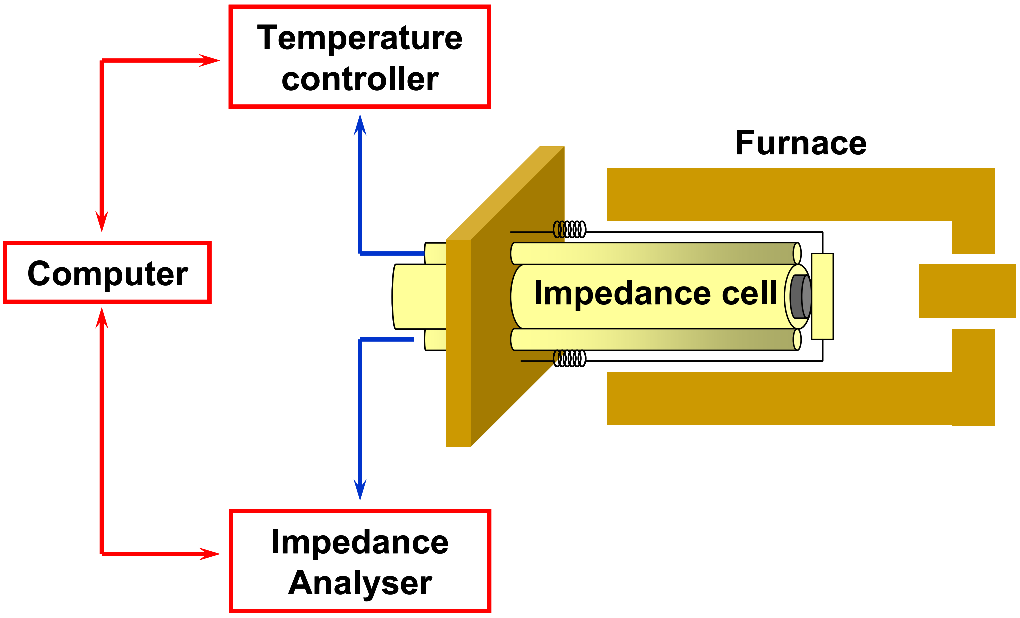

Figure 2.17. Scheme of the setup used for measuring impedance spectra.

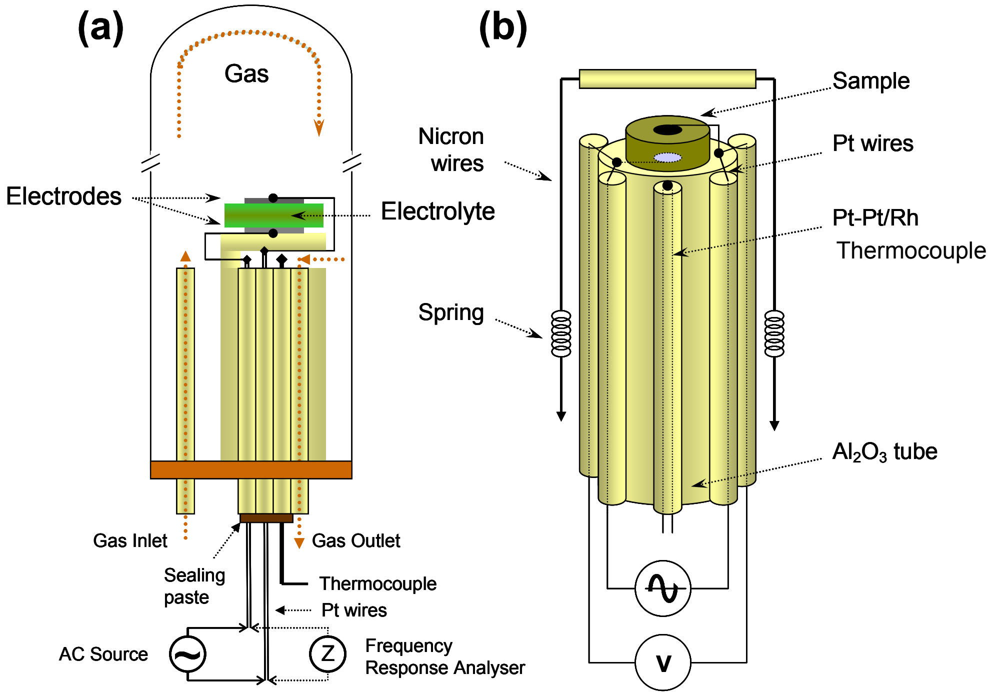

Figure 2.18. Schemes of the impedance cells used for electrical characterisation under controlled atmosphere (a), and air (b).

2.7.1.4.3. Conductivity *versus* oxygen partial pressure

A special set-up, Figure 2.19, has been used to measure the conductivity of the samples as a function of the oxygen partial pressure. The set-up consists on a tubular gas tight furnace of mullite. Oxygen partial pressure (Po_2) is monitored with an YSZ-tube gas sensor situated in the furnace and near of the studied sample. Electrical connections are similar to the electrical connections described in the normal set-up used to measure overall conductivity, see Figure 2.17. Before starting impedance spectra collection as a function of Po_2, the samples were reduced using 5%H_2/Ar gas flow, during hours or days depending on the reduction kinetics of the samples. When the samples are reduced, the gas flow is closed as well as the inlet and outlet of the cell. Impedance spectra now are automatically collected whereas re-oxidation of the sample is carried on due to a small gas leak.

A specific software [25] designed by Ruiz-Morales is used to control furnace temperature and to read the oxygen sensor potentials.

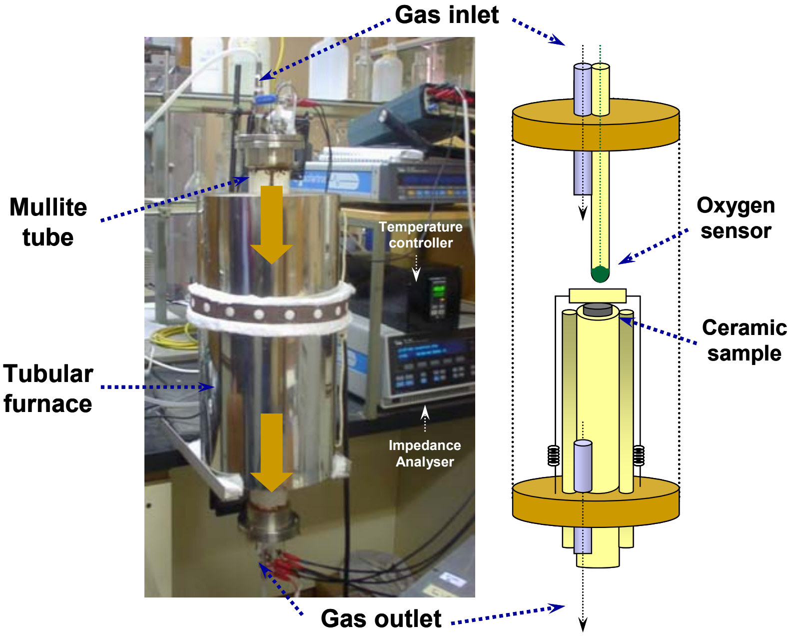

Figure 2.19. Scheme of the setup used for overall conductivity determination on function of different oxygen partial pressure.

In Figure 2.20 the overall conductivity of LSGM and LSGMC samples as a function of the oxygen partial pressure are shown as example of this technique. One should notice that the conductivity was stable in the range of oxygen partial pressure studied at 1073 K. It has to be considered that the speed of re-oxidation process from extreme reducing conditions to 10^{-12} atm is quite slow, so we can assume that the sample is in equilibrium with the surrounded atmosphere. However, from 10^{-12} to 10^{-5} atm the variation of the pressure is faster and the results have to be carefully analysed.

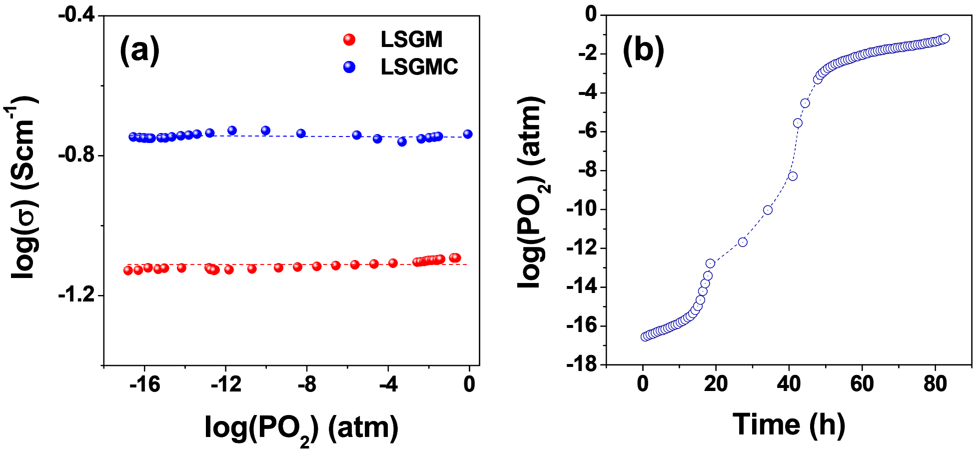

Figure 2.20. Po_2 dependence of overall conductivity of LSGM and LSGMC samples at 1073 K (a) and time dependence of the oxygen partial pressure (b).

2.7.2. Van der Pauw method

The overall conductivity of several mixed conducting oxides was measured using the dc-four-probe method of Van der Paw [26]. The resistivity of a material is the opposing force a material exerts to prevent flow of current when voltage is applied across it. Conductivity depends upon the number of free carriers (holes and/or electrons) and their mobility. In this method, four point contacts were painted onto dense pellets of 13.0 mm and 1.5 mm of diameter and thickness respectively, as indicated in Figure 2.21.

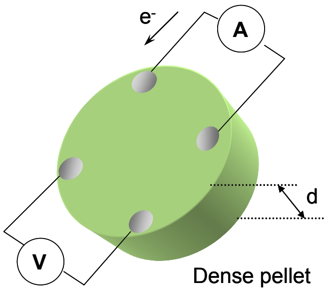

Figure 2.21. Scheme of the configuration used to apply the Van der Pauw's method.

The current is carried through the outer two contacts and the voltage drop is measured across the remaining contacts. Thus, the conductivity was calculated as

$$\sigma_{dc} = \frac{\ln(2)}{\pi d R} \tag{2.19}$$

where, *d* is the thickness of the pellet, and *R* is the resistance calculated as *V*/*I*. A Yokogawa 7651 was used as intensity source in the range 10-100 mA, and a Keitley 2700 multimeter was used to measure the voltages. An impedance cell was modified to introduce the samples with the four point contacts. Finally the whole setup was introduced into a tubular furnace to obtain the conductivity values *versus* the temperature.

2.7.3. Modified *emf* method of Gorelov

The *emf* technique is based on the measurement of the open-circuit voltage of a cell placed under a chemical potential gradient [27]. For an oxygen concentration cell with negligible electrode polarisation resistance, the oxygen ion transference number can be obtained from the ratio of the measured *emf* (E_{exp}) and theoretical Nernst voltage (E_{th}):

$$t_o = \frac{E_{\exp}}{E_{th}} \tag{2.27}$$

where

$$E_{th} = \frac{RT}{4F} \ln\left(\frac{p_2}{p_1}\right) \tag{2.28}$$

p_1 and p_2 are the values of the oxygen partial pressure at the electrodes. On the other hand, significant polarisation resistance leads to underestimated ion transference numbers. The electrode polarisation affects the measured *emf* of electrochemical cells with mixed ionic-electronic conductors [28]. Some authors [29,30] have proposed modified methods taking into account this effect. These methods are based on a modification of the equivalent circuit showed by Patterson [31], which included the overpotential term η and external variable resistance R_M. In this work, it has been followed the modification suggested by Gorelov [29]. An equivalent circuit for such a cell is illustrated in Figure. 2.22.

The electrical current (I) flowing through this cell may be expressed as:

$$I = \frac{E_{th} - \eta}{R_o + R_e} = \frac{E_{\exp}}{R_e} \tag{2.29}$$

where E_{exp} is the measured *emf* value, E_{th} is the theoretical *emf* defined by the Nerst equation, η is the sum of the electrode overpotentials, and R_o and R_e are the ionic and electronic resistances of the mixed conductor, respectively.

At low overpotentials, one can assume a linear dependence of overpotential on the current (I), and express the effects of electrode overpotentials in terms of a polarisation resistance (R_η):

$$\eta = IR_\eta \tag{2.30}$$

The oxygen-ion transference number may be expressed using the quantities R_o and R_e:

$$t_o = \frac{\sigma_o}{\sigma_o + \sigma_e} = \frac{R_e}{R_o + R_e} \tag{2.31}$$

where σ_o and σ_e are the partial oxygen ionic and electronic conductivities respectively. Substituting Eqs. (2.30) and (2.31) into Eq. (2.29), one obtains:

$$E_{\exp} = t_o E_{th} \left(1 + \frac{R_\eta}{R_o + R_e} \right)^{-1} \tag{2.32}$$

It can be see that obtained transference numbers of mixed ionic-electronic conductors as a ratio of measured and theoretical *emf* values may result in underestimation of the values due to the presence of the electrode polarisation resistance.

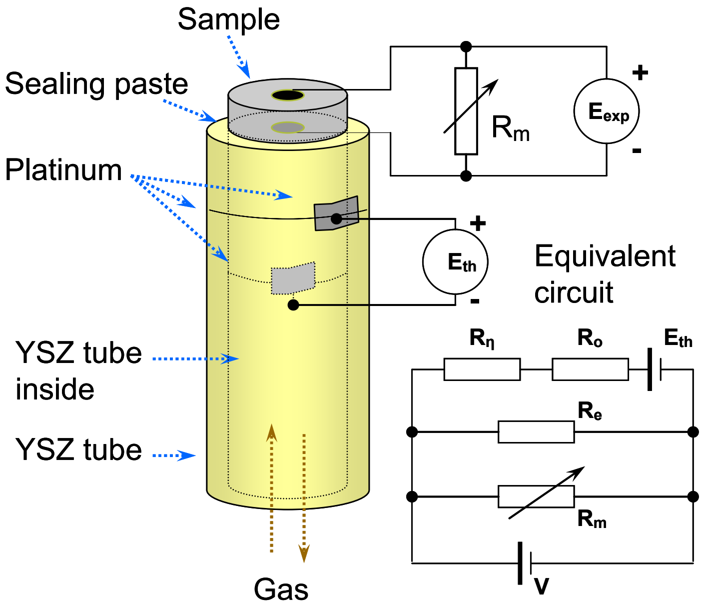

Figure 2.22. Scheme of the *emf* cell and its equivalent circuit where R_m is the external variable resistance, R_η is the polarisation resistance, R_o and R_e are the partial oxygen ionic and electronic resistances of the mixed conductor, E_{exp} is the experimental *emf* and E_{th} the theoretical *emf*.

Gorelov [36] proposed studying the *emf* as a function of an external variable resistance (R_M) closing the circuit, Figure 2.22. In this case:

$$\frac{E_{th}}{E_{\exp}} - 1 = (R_o + R_\eta)\left(\frac{1}{R_e} + \frac{1}{R_M}\right) \tag{2.33}$$

Thus, values of R_e could be calculated from a linear dependence fit:

$$\frac{E_{th}}{E_{\exp}} - 1 = A\left(\frac{1}{R_M}\right) + B \tag{2.34}$$

where $A= (R_o+R_\eta)$ and $B=(R_o+R_\eta)/R_e$ are regression parameters. One should notice that $R_e=A/B$ therefore, the oxygen ion transference numbers were calculated as:

$$t_o = 1 - t_e = 1 - \frac{R_{total}}{R_e} \tag{2.35}$$

where t_e is the electron transference number, and R_{total} is the overall resistance of the sample, measured independently by impedance spectroscopy.

Figure 2.23 gives an example of the dependence of Equation 2.33 obtained with a sample of $La_{0.9}Sr_{0.1}Ga_{0.8}Mg_{0.2}O_{2.85}$ at different temperatures under O_2/air (Figure 2.23a) and H_2/air (Figure 2.23b) gradients.

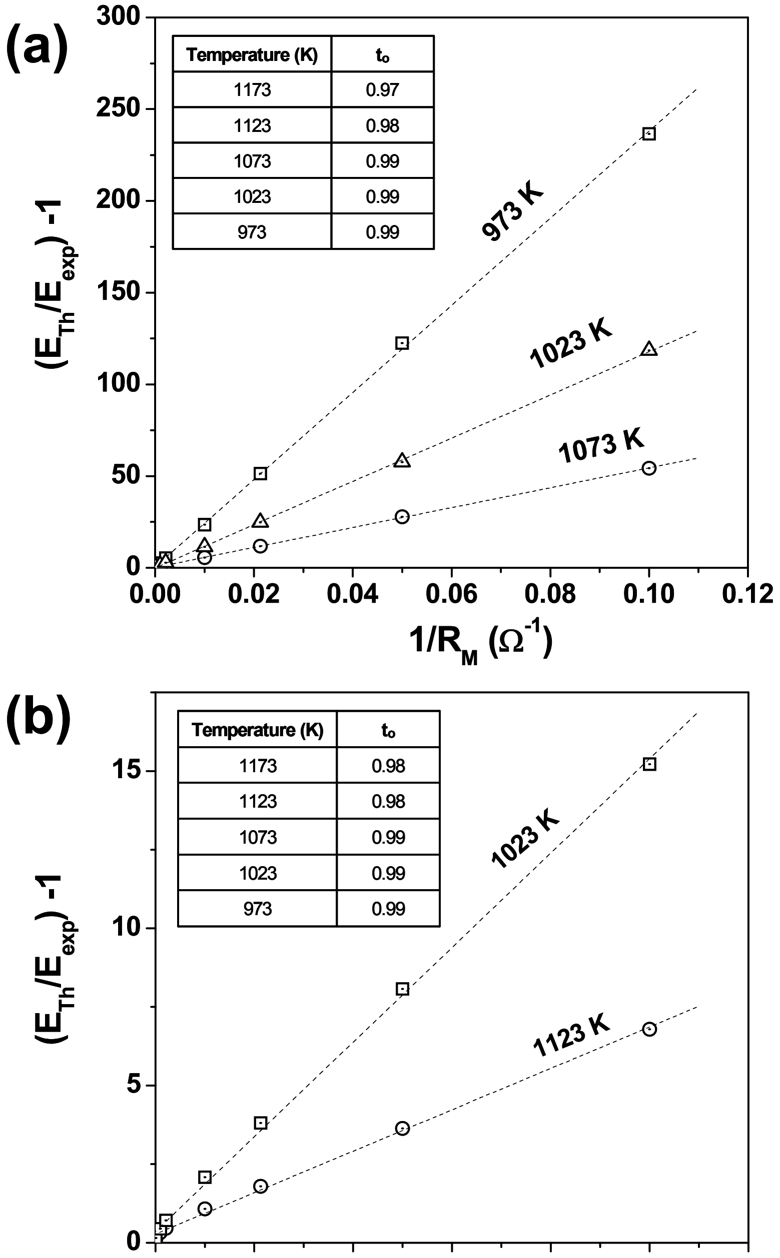

Figure 2.23. Experimental data from the modified *emf* method under O_2/air (a) and H_2/air (b) gradient for a $La_{0.9}Sr_{0.1}Ga_{0.8}Mg_{0.2}O_{2.85}$ sample. Dash line is the result of linear fitting. The insets show the tables with the ionic transport numbers calculated for different temperatures.

2.7.5. Fuel cell tests

2.7.5.1. Basic aspects

The ideal performance of a fuel cell depends on the electrochemical reactions that occur with different fuels and oxygen as summarised in Table 2.2. For example, low-temperature fuel cells (PEMFC, AFC, and PAFC) require noble metal electrocatalysts to achieve practical reaction rates at the anode and cathode, and H_2 is the only acceptable fuel. With high-temperature fuel cells (MCFC, IT-SOFC, and SOFC), the requirements for catalysis are relaxed, and the number of potential fuels expands.

Table 2.2.
Electrochemical reactions in fuel cells

Fuel cell	Anode reaction	Cathode reaction
PEMFC/PAFC	$H_2 \rightarrow 2H^+ + 2e^-$	$½\ O_2 + 2H^+ + 2e^- \rightarrow H_2O$
AFC	$H_2 + 2(OH)^- \rightarrow 2H_2O + 2e^-$	$½\ O_2 + H_2O + 2e^- \rightarrow 2(OH)^-$
MCFC	$H_2 + CO_3^{=} \rightarrow H_2O + CO_2 + 2e^-$ $CO + CO_3^{=} \rightarrow 2CO_2 + 2e^-$	$½\ O_2 + CO_2 + 2e^- \rightarrow CO_3^{=}$
SOFC	$H_2 + O^{=} \rightarrow H_2O + 2e^-$ $CO + O^{=} \rightarrow CO_2 + 2e^-$ $CH_4 + 4O^{=} \rightarrow 2H_2O + CO_2 + 8e^-$	$½\ O_2 + 2e^- \rightarrow O^{=}$

The ideal performance of a fuel cell is defined by its Nernst potential represented as cell voltage, see Section 1.3.1, Equation 1.1. The overall cell reactions corresponding to the individual electrode reactions listed in Table 2.2 are given in Table 2.3, along with the corresponding form of the Nernst equation:

Table 2.3.
Fuel cells reactions and the corresponding Nernst Equations

Cell reaction	Nernst Equation
$H_2 + ½O_2 \rightarrow H_2O$	$E = E^{o} + \frac{RT}{2F}\ln\left(\frac{P_{H_2}}{P_{H_2O}}\right) + \frac{RT}{2F}\ln\left(P_{O_2}^{1/2}\right)$
$H_2 + ½O_2 + CO_{2\,(c)} \rightarrow H_2O + CO_{2\,(a)}$	$E = E^{o} + \frac{RT}{2F}\ln\left(\frac{P_{H_2}}{P_{H_2O}P_{CO_2(a)}}\right) + \frac{RT}{2F}\ln\left(P_{O_2}^{1/2}P_{CO_2(c)}\right)$
$CO + ½\ O_2 \rightarrow CO_2$	$E = E^{o} + \frac{RT}{2F}\ln\left(\frac{P_{CO}}{P_{CO_2}}\right) + \frac{RT}{2F}\ln\left(P_{O_2}^{1/2}\right)$
$CH_4 + 2O_2 \rightarrow 2H_2O + CO_2$	$E = E^{o} + \frac{RT}{8F}\ln\left(\frac{P_{CH_4}}{P_{H_2O}^{2}P_{CO_2}}\right) + \frac{RT}{8F}\ln\left(P_{O_2}^{2}\right)$

a: anode P: gas pressure T: Temperature (absolute)
c: cathode R: gas constant E: equilibrium potential

It has to be considered that CO_2 is also produced when a carbon-containing fuel is involved in the anode reaction. For MCFCs, CO_2 is required in the cathode reaction to maintain an invariant carbonate concentration in the electrolyte. Because CO_2 is produced at the anode and consumed at the cathode in MCFCs, and because the concentrations in the anode and cathode feed streams are not necessarily equal, the Nernst equation in Table 2.3 includes the CO_2 partial pressure for both electrode reactions.

The Nernst equation provides a relationship between the ideal standard potential[1] (E^o) for the cell reaction and the ideal equilibrium potential (E) at other temperatures and partial pressures of reactants and products. Once the ideal potential at standard conditions is known, the ideal voltage can be determined at other temperatures and pressures through the use of these equations. According to the Nernst equation for hydrogen reaction, the ideal cell potential at a given temperature can be increased by operating at higher reactant pressures, and improvements in fuel cell performance have, in fact, been observed at higher pressures [32]. The ideal standard potential of an H_2/O_2 fuel cell (E^o) is 1.229 V with liquid water product and 1.18 V with gaseous product. This value is called the oxidation potential of H_2. The potential force also can be expressed as a change in Gibbs free energy for the reaction of H_2 and O_2. The change in Gibbs free energy increases as cell temperature decreases and that the ideal potential of a cell, is proportional to the change in the standard Gibbs free energy. Figure 2.24 shows the relation of E^o to cell temperature. Because the figure shows the potential of higher temperature cells, the ideal potential corresponds to a reaction where the water product is in a gaseous state. Hence, E^o is less than 1.229 V at standard conditions when considering gaseous water product.

Computer models are used to characterise the operation of fuel cells based on details of cell component design (dimensions, materials, etc.) along with transport phenomena, electrochemistry, etc. However, simpler approaches are normally used for system studies. One approach would be to conduct tests at every condition expected to be analysed in the system e.g. modifying various cell operating conditions such as temperature, pressure, and gas constituents.

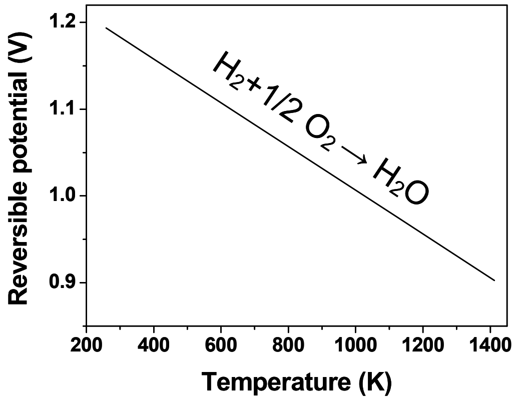

Figure 2.24. H_2/O_2 fuel cell ideal potential as a function of temperature.

---

[1] The standard Nernst potential (E^o) is the ideal cell voltage at standard conditions (one atmosphere and 298 K). It does not include losses that are found in an operating fuel cell.

Adjustments can be applied to a reference performance at known operating conditions to achieve the performance at the desired operating conditions. It has to be considered that useful work (electrical energy) is obtained from a fuel cell only when a reasonable current is drawn, but the actual cell potential is decreased from its equilibrium potential because of irreversible losses as shown in Figure 2.25. Several sources contribute to irreversible losses in a practical fuel cell. The losses, which are often called polarisation, overpotential or overvoltage (η), originate primarily from three sources: activation polarisation (η_{act}), ohmic polarisation (η_{ohm}), and concentration polarisation (η_{conc}). These losses result in a cell voltage (V) for a fuel cell that is less than its ideal potential. The activation polarisation loss is dominant at low current density. At this point, electronic barriers have to be overcome prior to current and ion flow. Activation losses show some increase as current increases. Ohmic polarisation (loss) varies directly with current, increasing over the whole range of current because ohmic cell resistance remains essentially constant. Gas transport losses occur over the entire range of current density, but these losses become prominent at high limiting currents where it becomes difficult to provide enough reactant flow to the cell reaction sites. Activation and concentration polarisation can exist at both the positive (cathode) and negative (anode) electrodes in fuel cells. The total polarisation at these electrodes is the sum of η_{act} and η_{conc}. In other words, the cell voltage in a fuel cell decreases because of losses by electrode and ohmic polarisations. The goal of fuel cell researchers is to minimise the polarisation. This is approached by modifications to fuel cell design (improvement in electrode structures, better electrocatalysts, more conductive electrolyte, thinner cell components, etc.).

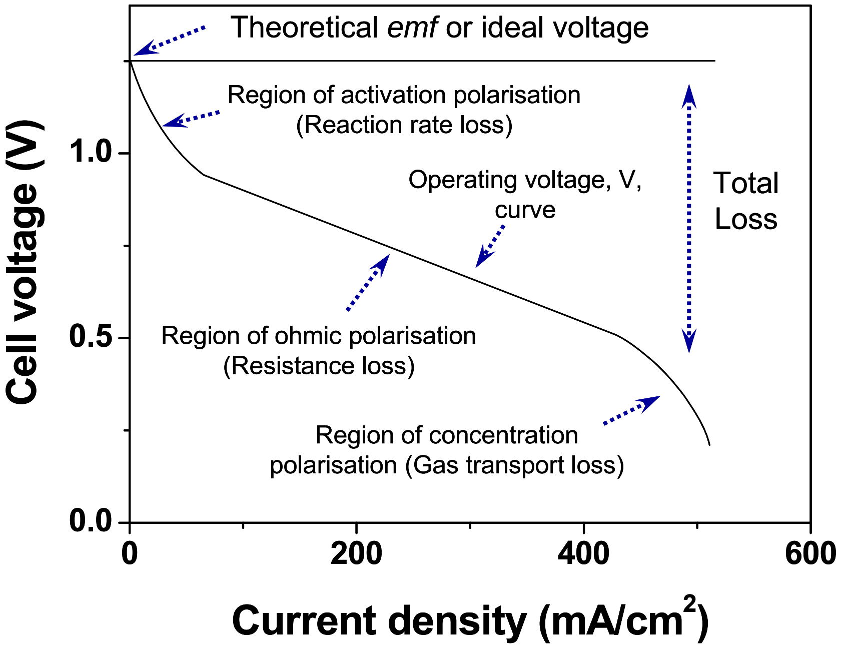

Figure 2.25. Ideal and actual fuel cell voltage-current characteristic

For a given cell design, it is also possible to improve the cell performance by modifying the operating conditions e.g. higher gas pressure, higher temperature, change in gas composition to lower the gas impurity concentration. However, for any fuel cell, compromises exist between achieving higher performance by operating at higher temperature or pressure and the problems associated with the stability/durability of cell components encountered at the more severe conditions. Operating conditions are based on defining specific system requirements, such as power level, voltage, etc. In this sense the power, voltage, and current requirements of the fuel cell stack and individual cells are determined experimentally, and one can find representations of the current-voltage characteristics as Figure 2.26a. Furthermore, Figure 2.26b presents more information in a way to highlight the maximum power density that peaks at a higher current density (right of the figure). However, operation at the higher power densities will mean operation at lower cell voltages or lower cell efficiency. Setting operation at the peak power density can cause instability in control because the system will have a tendency to oscillate between higher and lower current densities around the peak. It is usual practice to operate the cell to the left side of the power density peak and at a point that yields a compromise between low operating cost (high cell efficiency that occurs at high voltage/low current density) and low capital cost (less cell area that occurs at low voltage/high current density).

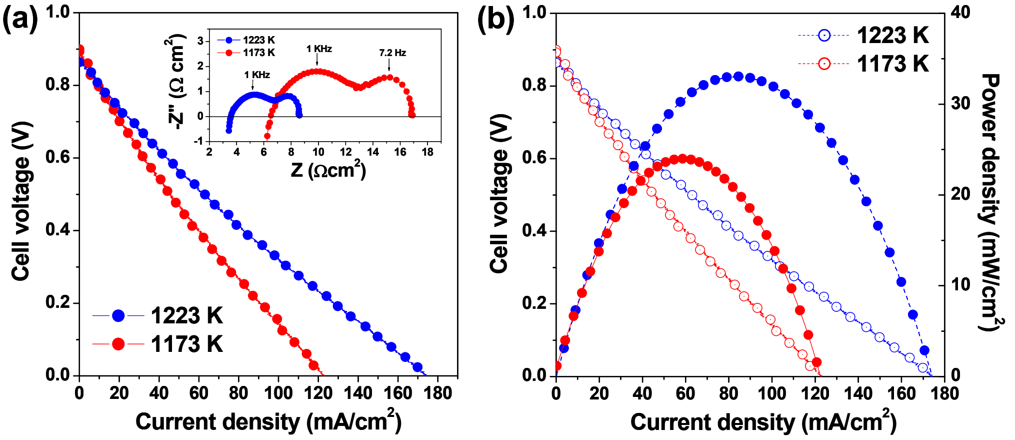

Figure 2.26. Voltage-current characteristics (a) and performance curves (b) of the LSCrA/YSZ/LSCrA system where LSCrA is $La_{0.75}Sr_{0.25}Cr_{0.5}Al_{0.5}O_{3-\delta}$, tested at 1223 and 1173 K using wet 5%H_2/Ar as fuel and air as oxidant. The thickness of the YSZ pellet was 1.6 mm and the electrode surface 0.36 cm^2. The inset (a) illustrates the impedance spectra acquired in the mentioned conditions.

2.7.5.2. Set-ups for fuel cell tests

Two-electrode configuration arrangements have been used to obtain the current-voltage characteristics, power and current density, electrode overpotential and polarisation and series resistance of the studied fuel cells. Wet pure H_2 and 5% H_2/Ar were used as fuel and, air and oxygen as oxidants.

Every set-up used is extensively described in chapters 3 and 4. One of them has been designed by Professor J.T.S. Irvine's research group [10] (University of St. Andrews) and the other by Professor L.J. Gauckler's research group [33] (ETH-Zurich). It has to be considered that both set-ups are prepared for working in double chamber configuration i.e. under asymmetric atmosphere, reducing conditions in the fuel side and oxidant conditions in the cathode side. However the main difference between them is due to the sealing. The fuel cell in the Scottish-design need to be sealed to avoid the contact between oxidant and reducing gases, whereas the Swiss-design set-up which is described in the following paragraphs, does not need to be sealed.

A scheme and some pictures of the set-up of ETH-Zurich are shown in Figure 2.27 and Figure 2.28, respectively. Using this set-up, the tests were performed with a moistened (3% water) gas mixture of H_2 (40 vol%) and N_2 as fuel and air as oxidant. The electrolyte-pellet dimensions were about 1.5 and 20 mm in thickness and diameter. The measurement setup consisted of two quartz tubes for the gas transport to the electrodes. The cell was mounted between two Al_2O_3 spacer rings and adjusted between the quartz tubes. High fuel and air flow gases were necessary, 300 ml/min on each side at a pressure of 1 atm, due to the unsealed arrangement to obtain high values of open circuit voltage (OCV). The entire setup was heated in a tubular furnace and the temperature was varied between 873 K and 1073 K.

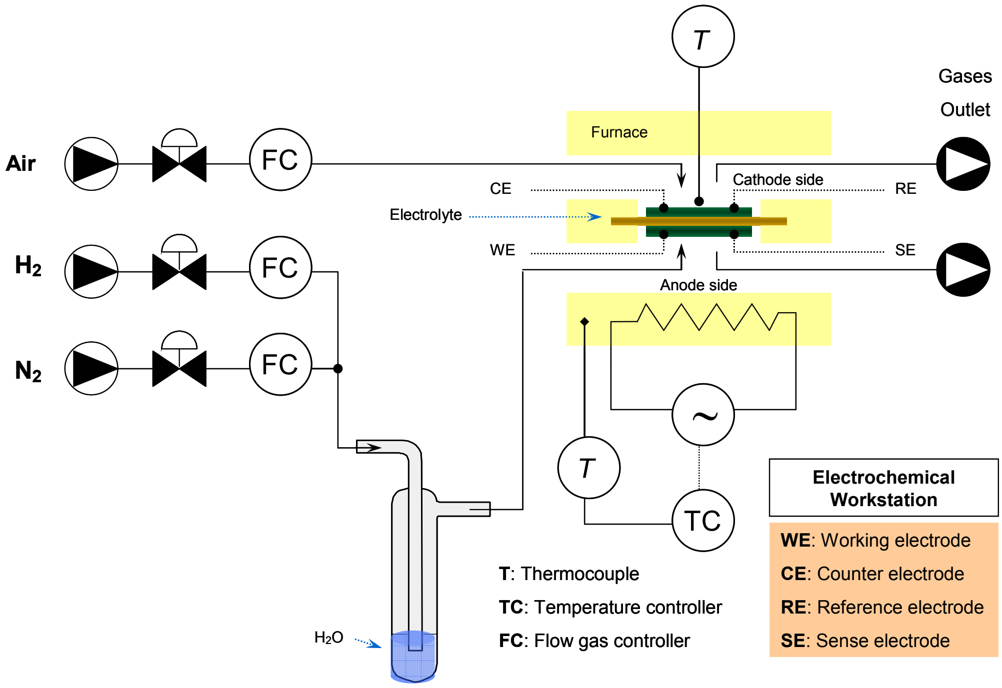

Figure 2.27. Scheme of the set-up used in ETH-Zurich for fuel cell tests.

In both designs of set-ups, the electrode materials were deposited via *screen printing* or *painting* on both sides of the electrolyte pellets with a surface of 0.25-1 cm^2 and fired at 1373–1623 K for 2 h in air to ensure adherence. The thickness of the electrode layer after firing was around ~30-40 µm, and the porosity and the microstructure of the deposited electrodes were studied by SEM. Platinum paste and mesh were used as current collector. Electrode/electrolyte interfaces after the tests were also observed by SEM. The current-voltage characteristics of the fuel cell were recorded by *cyclic-voltammetry*[2] at a 5 mVs^{-1} scan rate using a Zahner IM6 in pontentiostat mode and *Thales* [34] software. The electrochemical tests were performed after reducing for several hours the anode materials in 5% H_2/Ar at 1073 K. Impedance spectra of the electrochemical cell under asymmetric atmospheres were also acquired in the frequency range of 0.1 Hz to 1 MHz and with an AC perturbation of 20 mV.

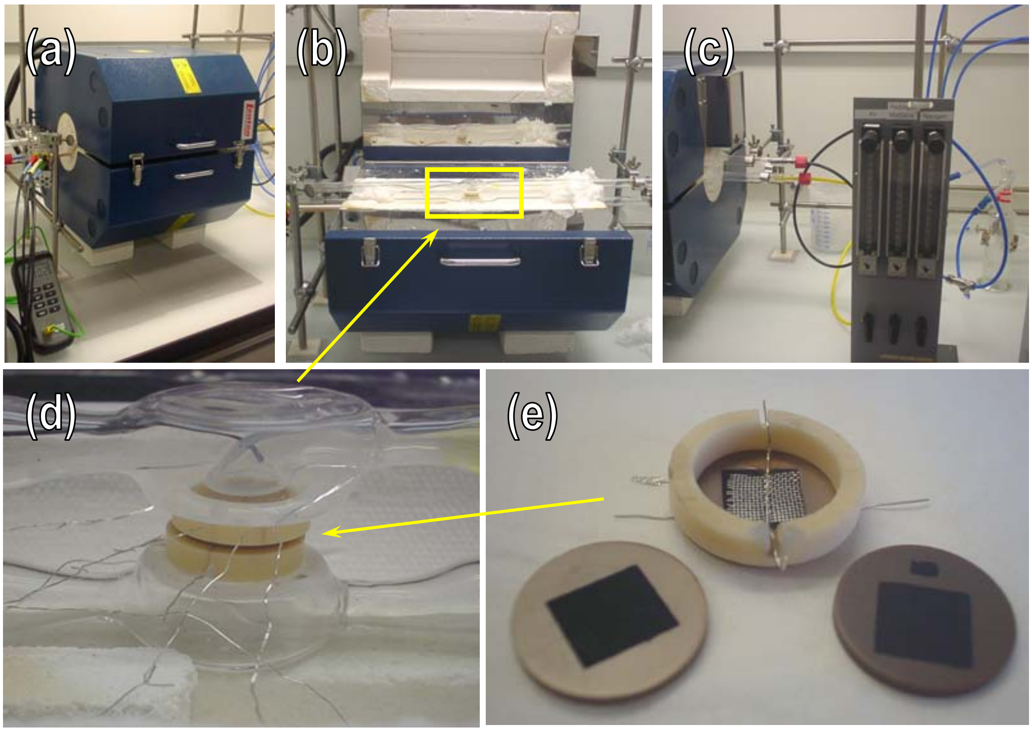

Figure 2.28. Set-up for fuel cell tests used in ETH-Zurich (a) indicating the disposition of the quartz tubes into the tubular furnace (b), the flow gas control system (c), a magnification of the cell adjusted between the quartz tubes (d), and some electrolyte pellets with deposited electrode materials (e).

---

[2] Cyclic-voltammetry is a type of potentiodynamic electrochemical measurement. The voltage is varied and the change in current is measured with respect to the change in voltage.

2.8. References

[1] L. Smart and E. Moore, *Solid State Chemistry*, Chapman & Hall, 2nd Ed., 1995.

[2] A. Chandrasekaran, A. Azad, *J. Mater. Sci.* **36** (2001) 4745-4757.

[3] Z. Wu, W. Zhou, W. Jin, N. Xu, *AICHE J.* **52** (2006) 769-776.

[4] M. Pechini, U.S. Patent 3 330 697, July 11, 1967.

[5] K. Huang, J. B. Goodenough, *J. Solid State Chem.* **136** (1998) 274-283.

[6] K. Huang, M. Feng, J.B. Goodenough, *J. Am. Ceram. Soc.* **79** (1996) 1100

[7] *A Guide To Freeze Drying for the Laboratory*, Labconco Corporation.

[8] D. Marrero-López, J.C. Ruiz-Morales, P. Nuñez, J.C.C. Abrantes, J.R. Frade, *J. Solid State Chemistry* **177** (7) 2378-2386.

[9] F.G.E. Jones, J.T.S. Irvine, *Ionics* **8** (2002) 339-343

[10] http://ch-www.st-andrews.ac.uk/staff/rem/stacam/stacam.html

[11] Philips X'Pert HighScore plus (ver. 2.0.1)

[12] FindIt (ver. 1.3.3), ICSD Database ver. 2004-02.

[13] J. Rodríguez-Carvajal, T. Roisnel, FullProf.98 and WinPLOTR: *New Windows 95/NT Applications for Diffraction Commission For Powder Diffraction*, International Union for Crystallography, Newletter N°20, 1998.

[14] T. Roisnel, J. Rodríguez-Carvajal, WinPLOTR: *A Windows tool for powder diffraction patterns analysis*. Materials Science Forum, Proceedings of the 7Th European Powder Diffraction Conference (EPDIC 7), 2000, 118-123, Ed. R. Delhez and E.J. Mittenmeijer.

[15] D.C. Dube, H. J. Scheel, I. Reaney, M. Daglish, N. Setter, *J. Appl. Phys.* **75** (1994) 4126- 4130.

[16] M. Lerch, H. Boysen, T. Hansen, *J. Phys. Chem. Solids* **62** (2001) 445-455.

[17] S. Brunauer, P.H. Emmett, E. Teller, *J. Am. Chem. Soc.* **60** (1938) 309-311.

[18] P.A. Webb and C. Orr, Analytical *Methods in Fine Particle Technology*, Micromeritics Instrument Corporation, Norcross, GA USA, 1997.

[19] A.R. West, Solid State Chemistry and its Applications, J. Wiley & Sons, Ed. 1995.

[20] N.M. Beekmans and L. Heyne, *Electrochimica Acta*, **21** (1976) 303-310.

[21] Zview version 2.80 from Scribner Associates Inc., USA

[22] X. Guo, J. Maier, *J. Electrochem. Soc.* **148** (2001) E121-E126.

[23] X. Guo, R. Waser, *Solid State Ion.* **173** (2004) 63-67.

[24] J.C. Ruiz-Morales, *CDT v3.0*, Reference: TF-176-02 (2002)

[25] J.C. Ruiz-Morales, *Cdsensor* (2002)

[26] L.J. van der Pauw, *Philips Res. Repts*. **13** (1958) 1-9

[27] C. Wagner, Z. *Phys. Chem. B*. **21** (1933) 25

[28] J.R. Frade, V.V. Kharton A.A. Yaremchenko, E.V. Tsipis, *J. Solid. State Electrochem*. **10** (2006) 96-103.

[29] V.P. Gorelov, *Elektrokhimiya* **24** (1988) 1380-1381.

[30] V.V. Kharton, A.P. Viskup, F.M. Figueiredo, E.N. Naumovich, A.A. Yaremchenko, F.M.B. Marques, *Electrochim. Acta* **46** (2001) 2879-2889.

[31] J.W. Patterson, In: Brubaker G. et al. (eds). ACS symposium series, no.89, Corrosion Chemistry, p. 96, American Chemical Society, Washington DC, pp. 96, 1979.

[32] Fuel Cell Handbook, 5th Edition. U.S. Department of Energy. October 2000.

[33] http://www.nonmet.mat.ethz.ch/

[34] Thales software, Zahner-Elektrik Gmbh & Co. KG

Chapter 3

Anodic performance of $La_{0.75}Sr_{0.25}Cr_{0.5}Mn_{0.5}O_{3-\delta}$ for IT-SOFC using doped Lanthanum Gallate electrolyte

Published in *Chemistry of Materials* 18 (2006) 1001-1006

J. Peña-Martínez[a,b], D. Marrero-López[a], J.C. Ruiz-Morales[a,b], C. Savaniu[b], P. Núñez[a], J.T.S. Irvine[b]
[a]Inorganic Chemistry Department, University of La Laguna, Tenerife, Canary Islands, Spain.
[b]School of Chemistry, University of St. Andrews, Scotland, U.K.

Abstract

This study is focused on the electrochemical performance of perovskite-type materials based on doped $LaGaO_3$ (LGO). $La_{0.9}Sr_{0.1}Ga_{0.8}Mg_{0.2}O_{3-\delta}$ (LSGM) and $La_{0.9}Sr_{0.1}Ga_{0.8}Mg_{0.115}Co_{0.085}O_{3-\delta}$ (LSGMCo) were used as electrolytes and $La_{0.8}Sr_{0.2}MnO_{3-\delta}$ (LSM) and $La_{0.75}Sr_{0.25}Cr_{0.5}Mn_{0.5}O_{3-\delta}$ (LSCM) as cathode and anode material, respectively. Much better performance was obtained at an LSGM electrolyte than at LSGMCo, probably due to interfacial reactions between LSGMCo and LSM. An LSGM electrolyte was prepared by tape casting with a thickness of about 120 μm and good values of power output in a conventional electrolyte-supported cell were achieved, 425 $mWcm^{-2}$ and 570 $mWcm^{-2}$ using wet 5% H_2/Ar and pure hydrogen as fuel respectively and pure O_2 as oxidant at 1073 K.

Keywords

SOFC, LSGM, LSCM, doped $LaGaO_3$, tape casting, electrochemical performance.

3.1. Introduction

Fuel cells are highly promising energy conversion systems for the new energy economy and especially in the future hydrogen scenery. The key advantage of fuel cells is high efficiency from a range of system sizes. Systems are being commercially developed from sub-kW to 10 MW. Solid oxide fuel cells (SOFCs) are of particular interest due to their fuel flexibility. For many applications such as combined cycle with gas turbines and heat cogeneration, the high SOFC temperature up to 1273 K offer significant advantages. These high temperatures present significant problems for materials selection and durability, especially for smaller scale applications, thus there is also considerable impetus to develop lower temperature SOFC systems. A decrease in the operation temperature means a loss of power density mainly due to a considerable reduction of both ionic conductivity of the electrolyte and catalytic activity of the electrodes. In order to avoid ohmic loss, the thickness of the electrolyte might be reduced or alternative electrolyte materials used, providing that they offer good performance for operation at intermediate temperatures (773 – 1073 K). For example, it is necessary to reduce the thickness of yttrium stabilized zirconia (YSZ) electrolyte to at least 15 μm to achieve comparable performances at 973 K [1]. Similarly, new electrode materials with enhanced electrode performance at lower temperatures should be achieved. Much attention has been given to the search for different electrolyte materials, e.g. with fluorite-type structure (AO_2), such as gadolinium doped ceria (CGO), which has a higher ionic conductivity than YSZ at intermediate temperatures [2]. However, this material has been reported short-circuit problems in low oxygen partial pressures due to partial reduction of Ce^{4+} to Ce^{3+} and so increasing *n*-type conductivity [3]. The ionic domain dominates at 773 K and below and, hence gadolinia ceria is well suited to operation at these temperatures, especially if a suitable cathode material is found for this temperature range [4]. The versatile perosvkite-type structure (ABO_3) based on the doped $LaGaO_3$ (LGO) is another interesting option as electrolyte. A good ionic conductor was found by doping with Sr^{2+} and Mg^{2+} in the A and B-site positions of the perovskite, creating oxygen vacancies as a consequence of the doping [5]. The best ionic conductivity was found in $La_{0.8}Sr_{0.2}Ga_{0.83}Mg_{0.17}O_{2.815}$ composition [6]. Although, $La_{0.9}Sr_{0.1}Ga_{0.8}Mg_{0.2}O_{2.85}$ (LSGM) is usually the preferred one [7-9]. In any case, LSGM is a better ionic conductor than YSZ at intermediate temperatures. Nevertheless, there are disadvantages such as undesired segregation of impurities during the synthesis procedure, e.g. $LaSrGa_3O_7$ and $LaSrGaO_4$ [10] and there is a reported chemical incompatibility with Ni-based anodes [11,12]. To date, it is necessary to use a buffer layer of CGO or samarium doped ceria (SDC) between LSGM and Ni-based anodes in order to avoid the formation of impurities such as $LaSrGa_3O_7$ and lanthanum-nickel oxide [13-15].

A new electrolyte material has been prepared and characterized in the literature [16], based on LSGM, but with the addition of Co^{2+} in the B site of the perovskite structure, i.e. $La_{0.9}Sr_{0.1}Ga_{0.8}Mg_{0.115}Co_{0.085}O_{3-\delta}$ (LSGMCo). Ishihara et al. [17] reported that the cobalt doping is effective for enhancing the oxide ion conductivity at low temperature compared to LSGM. Recent work [18] has demonstrated that $La_{0.75}Sr_{0.25}Cr_{0.5}Mn_{0.5}O_{3-\delta}$ (LSCM) [19-21] can be utilised as an appropriate anode with a LSGMCo electrolyte; however, the performance was limited by the performance of the gadolinium strontium cobaltite (GSC) cathode and the fairly thick electrolyte, 0.5 mm. The cobaltite cathode was chosen for the initial study due to its anticipated compability with LSCMCo and most importantly its high reported performance on gadolinia ceria [22]. Unfortunately, the GSC is expected to exhibit much higher thermal expansion (15-18 x 10^{-6} K^{-1}) than LSCM and LSGM or LSGMCo (~ (10 ± 1) x 10^{-6} K^{-1}) and the lattice volume which is about 6% smaller than LSCM and LSGM (or LSGMCo) which are within 1-2% of each other [18]. In this work LSGM and LSGMCo were tested as electrolytes using $La_{0.8}Sr_{0.2}MnO_{3-\delta}$ (LSM) and $La_{0.75}Sr_{0.25}Cr_{0.5}Mn_{0.5}O_{3-\delta}$ (LSCM) as cathode and anode respectively. LSM is well known as a stable SOFC cathode, although it does not exhibit the same degree of mixed conductivity as its cobalt analogue; however it is much better matched in terms of thermal expansion coefficient, ~12 x 10^{-6} K^{-1} [23]. Furthermore the primitive perovskite unit cell volume of LSM is 58.8 $Å^3$, only 1% different from either LSCM or LSGM [18].

3.2. Experimental procedures

3.2.1. Electrolyte and electrode preparation

LSGM and LSGMCo electrolytes and LSCM anode material have been prepared by conventional solid state reaction using powders of La_2O_3 (Alfa Aesar, 99.99%), Ga_2O_3 (Alfa Aesar, 99.999%), $(MgCO_3)_4 \cdot Mg(OH)_2 \cdot 5H_2O$ (Aldrich, 99%), $SrCO_3$ (Aldrich, 99.9%), $Co(Ac)_2 \cdot 4H_2O$ (Panreac, 98%), Mn_2O_3 (Aldrich 99%) and $Cr(NO_3) \cdot 9H_2O$ (ACROS, 99%); commercial powders of LSM (Praxair, 99.9%) were used as cathode. Before weighing, La_2O_3 was pre-dried at 1273 K for more than 3 hours in order to achieve decarbonation. The stoichiometric quantities of reactants were ball milled with acetone for the preparation of both electrolyte and anode materials. The resulting dried-mixture was fired at 1173 K for 10 hours and grounded again to obtain fine powders. LSCM powders were prepared via calcination at 1373 K (10 hours) and LSGM and LSGMCo electrolytes were prepared as dense pellets (99% of theoretical density) by sintering at 1623 - 1673 K for 6 hours in air after uniaxial pressing.

3.2.2. Tape casting preparation

The procedure for obtaining LSGM by tape casting samples comprised the preparation of a slurry containing powder, methylethylketone (MEK) as solvent; Triton QS-44 (phosphate ester, acid form) as dispersant to reduce the interfacial tension between the surface of the particle and the liquid; di-n-butyl phthalate (DBP) as plasticizer to increase the flexibility of the tapes and BUTVAR B-98 as binder to provide their strength after the evaporation of the solvent. Intermediate ball-milling steps are used for the preparation of the tapes that are finally cut into disks and sintered at 1573 K with slow heating rate. The thin electrolytes for fuel cell testing were prepared by laminating two layers of LSGM and firing both together at 1573 K to get a dense and homogeneous layer of 120 μm thickness after the firing.

3.2.3. Material characterisation

X-ray diffraction patterns (XRD) were collected with a Philips X'Pert Pro diffractometer, equipped with a primary monochromator and an X'Celerator detector.

The scans were performed in the high resolution mode in the 2θ range from 20 to 70º (step 0.016º and 500 s/step), using copper $K_{\alpha 1}$ radiation. Scanning electronic microscopy (SEM) and Energy Dispersive X-Ray Spectroscopy (EDS) were performed on JEOL JSM-5600 and Oxford INCA Energy 200 devices to characterize materials before and after tests. XRD studies were made to investigate the chemical compatibility of the electrolyte with the electrodes. Mixtures of LSGM with LSCM and LSM powders were prepared, in a 1:1 (w/w) ratio; ground in an agate mortar and fired at several temperatures for 10 hours. Additionally the redox stability of LSGM was studied by XRD after exposing the sample to a wet H_2 flow at 1073 K for 48 hours.

3.2.4. Electrochemistry measurements

Polarisation impedance and anodic overpotential fuel cell tests were carried out on a three-electrode arrangement (Figure 3.1) using 20 mm diameter LSGM pellets (2 mm thick) as electrolyte, LSM as cathode material and LSCM as anode. The anode was prepared by coating a layer of LSCM slurry, using Decoflux^{TM} as binder, onto the electrolyte and then firing at 1573 K for 2 hours in air. LSM was painted onto the other side of LSGM as counter-electrode and fired at 1473 K for 2 hours. A gold current collector layer was used to avoid any additional catalytic effect and it was applied onto the working electrode by brushing Au paste with Au mesh on top. Platinum paste was used as reference electrode and current collector on the cathode side. Finally, the specimen was fired at 1173 K for 2 hours.

The 3-electrode setup consists of 1 cm^2 aligned working and counter ring electrodes with a point reference placed at the centre of the counter electrode ring (Figure 3.1). Gold rings were used for sealing at 1198-1223 K. Ac impedance of the electrochemical cell was acquired using a Zahner IM600 unit at open circuit voltage (OCV) in the frequency range 0.1 Hz to 1 MHz. An ac perturbation of 20 mV was used, obtaining reproducible spectra. The impedance of the single cell was measured under asymmetric atmospheres at open circuit conditions.

Fuel-cell performance was investigated using a 120 µm-thick LSGM electrolyte prepared by tape-casting. A two-electrode setup was used to obtain the I-V plots using wet 5% H_2 and 100% H_2 gases as fuels and O_2 as oxidant. The anode and cathode were LSCM and LSM, respectively, and both were deposited in the same way as in the 3-electrode arrangement.

The fuel cell performance was recorded by cyclic-voltammetry at a scan rate of 4 mVs^{-1}. Electrochemical tests were performed after reducing the anode materials in 5% H_2 at 1073 K for several hours.

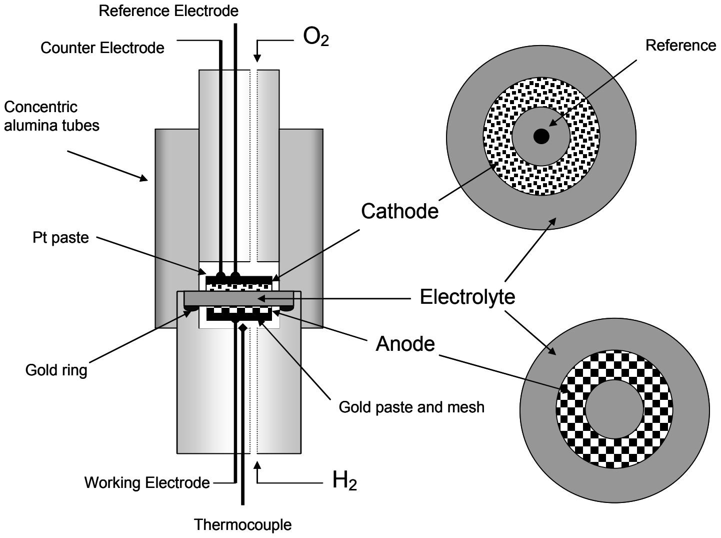

Figure 3.1. Three-electrode setup for polarisations measurements.

3.3. Results and discussions

3.3.1. Chemical compatibility

XRD patterns of the reacted intimate mixtures of LSGM/LSCM, LSGMCo/LSCM and LSGM/LSM pressed powders are shown in Figures 3.2, 3.3 and 3.4.

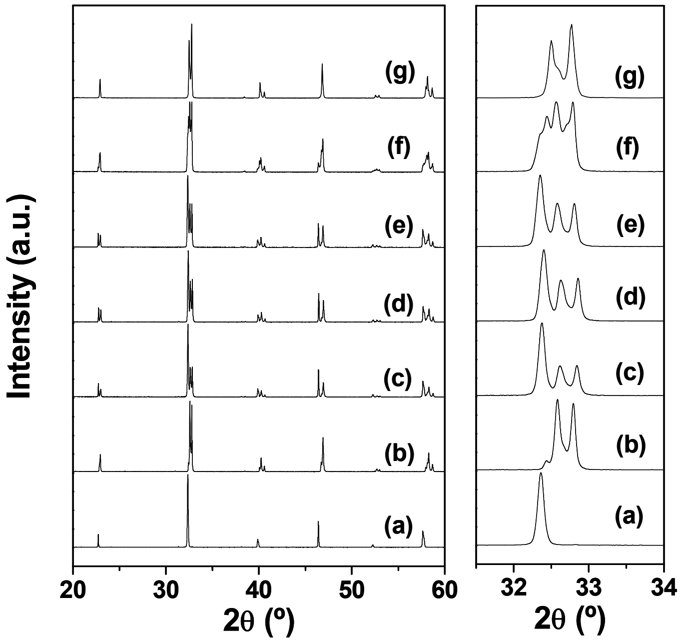

Figure 3.2. XRD Patterns of LSGM (a), LSCM (b) and LSGM+LSCM at the following temperatures: room temperature (c), 1173 K (d), 1373 K (e), 1623 K (f) and 1773 K (g).

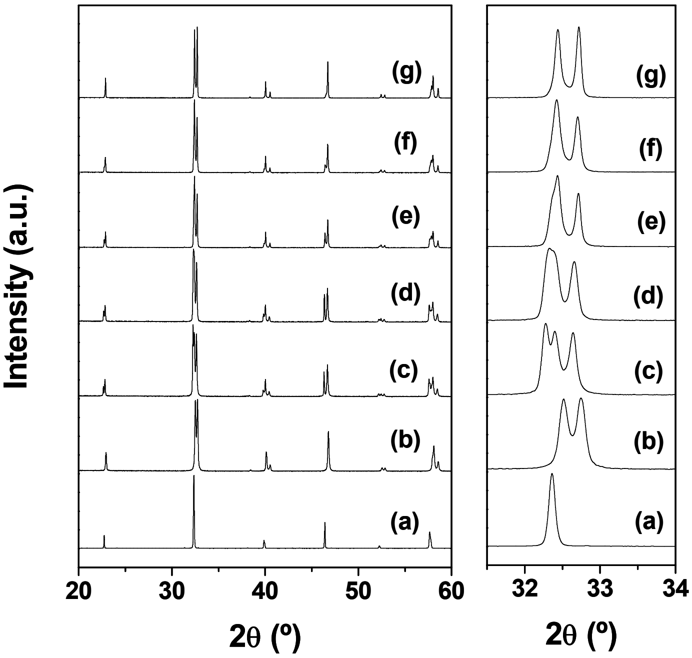

Figure 3.3. XRD Patterns of LSGM (a), LSM (b) and LSGM+LSM at the following temperatures: room temperature (c), 1173 K (d), 1373 K (e), 1473 K (f) and 1673 K (g).

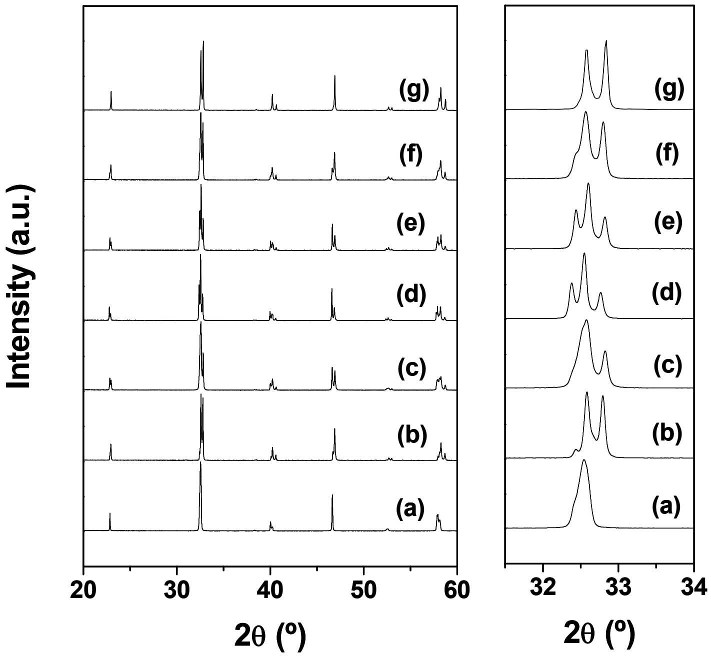

Figure 3.4. XRD Patterns of LSGMCo (a), LSCM (b) and LSGMCo+LSCM at the following temperatures: room temperature (c), 1173 K (d), 1373 K (e), 1623 K (f) and 1773 K (g).

Reactivity could be seen between LSM and LSGM above 1373 K, between LSGM and LSCM at 1623K, and between LSGMCo and LSCM above 1173 K. No reaction is showed for the LSGM/LSCM system at 1173 K. In this sense, Du and Sammes [24] reported that no interactions were detected from XRD data in their experiments of fabrication of bi-layer samples of LSGM and LSCM at 1773 K for 2 hours, however they found severe reactions in samples after 6 hours and over at 1773 K forming low conductive phases. They used energy-dispersive spectrometry (EDS) analysis to find reaction-diffusion zones between 50-150 μm. Nevertheless, they indicate from their overall results that LSCM is a thermomechanically and chemically compatible anode material with LSGM electrolyte at the fuel cell operating temperatures and fuel cell fabrication conditions (under 1773 K and dwell for 2 hours and shorter).

In this work LSCM material has been fixing at 1623 K for 2 hours, and LSGM and LSCM showed remarkable little signs of reaction in fired powder compacts, however XRD pattern of the mixture LSGM/LSCM at 1623 K for 10 hours, Figure 3.2f, shown a reaction which is stronger at 1773 K, Figure 3.2g.

The interaction between LSGM/LSCM has not further been studied and it is necessary more studies about it. In LSM/LSGM case, the previous studies on the interface between LSM and LSGM have shown that a reaction layer is formed between them and the thickness of the layer increased with the sintering temperature [25]. Huang et al. [13] reported that the high diffusion of La in LSGM electrolytes can modified the LSGM composition, leading to the formation of resistive phases such $LaSrGa_3O_7$ or $LaSrGaO_4$, at the electrolyte/electrode interfaces depending on whether La diffuses out of or into LSGM.

The LSM electrode fired at 1473 K onto LSGM did not show obvious signs of reaction, however based upon the powder mixture studies, it is anticipated that some interdiffusion will have occurred at the interface.

In addition, there are no noticeable changes or extra peaks (Figure 3.5) on exposure of LSGM to wet H_2 at 1073 K for 48 hours. This is in accord with the good stability in reducing conditions reported by Huang and Goodenough [14].

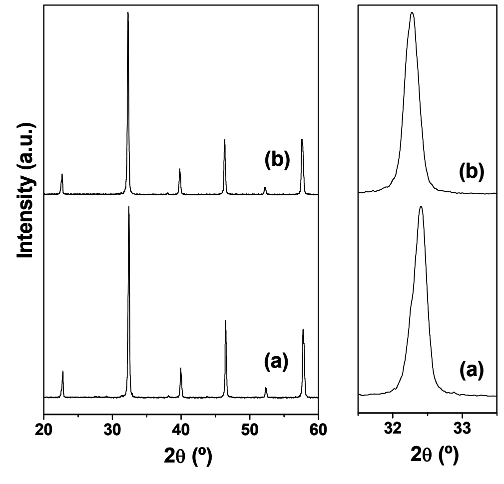

Figure 3.5. XRD patters of LSGM in air at room temperature (a) and after exposure in wet H_2 atmosphere (b) at 1073 K for 48 hours.

3.3.2. Fuel Cell Tests

3.3.2.1. Series and polarisation resistances

The polarisation resistances for LSCM at a LSGM electrolyte, were 0.15 and 0.16 Ωcm^2 at 1073 K in 3% H_2O/97% H_2 and 3% H_2O/4.8% H_2/92.2% Ar, respectively, see Figure 3.6a. These values are lower than those obtained by Tao *et al.* [19] at 1223 K on YSZ, indicating an enhancement at the perovskite/perovskite interface as previously reported by Tao *et al.* [18] at LSGMCo; however the polarisation resistances in the experiments reported here are considerably lower, perhaps indicating that improved processing was yielding better microstructures or that the presence of Co was downgrading performance. Even at 873 K the values of polarisation resistance were not that high being 1.0 and 1.4 Ωcm^2 in 3% H_2O/97% H_2 and 3% H_2O/4.8% H_2/92.2% Ar respectively, Figure 3.6b.

The results using LSGMCo were poor by comparison to LSGM and were slightly worse than those previously reported for LSGMCo using a thick pellet electrolyte [18]. Compared to the LSGM data and the previous LSGMCo report in this instance it was more difficult to obtain the intercept at low frequencies from the impedance plots, Figures 3.6c and 3.6d. This indicates a large diffusion reaction. It could be accord with the low conductive phases and a reaction/diffusion zone discovered by Du and Sammes in LSGM/LSCM interface [24].

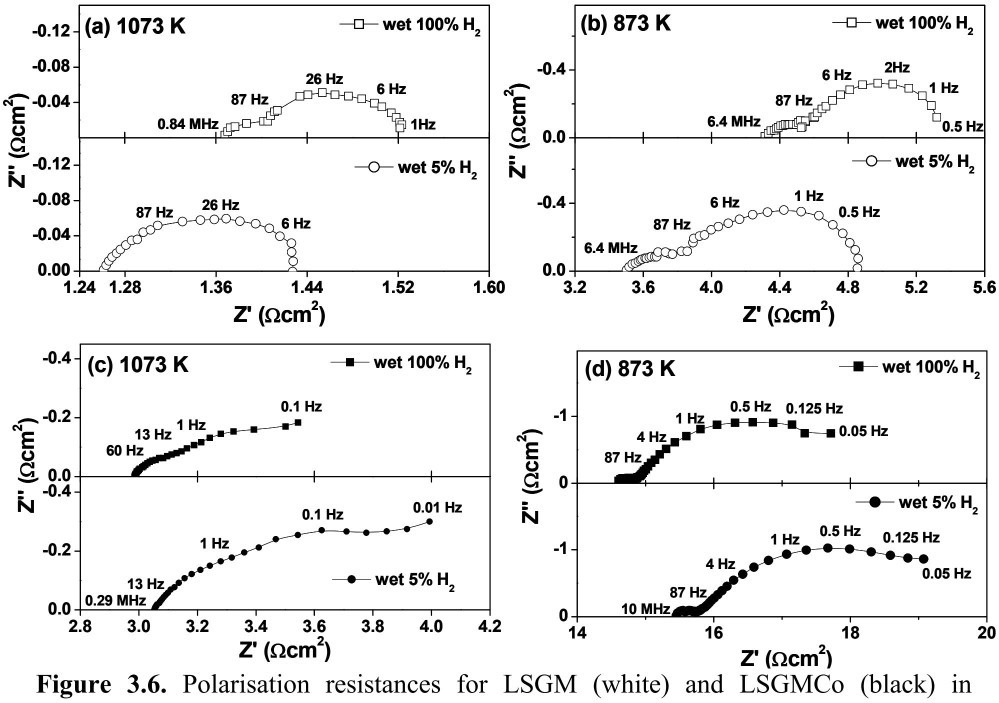

Figure 3.6. Polarisation resistances for LSGM (white) and LSGMCo (black) in different gas compositions, wet 100% H_2 (□) and wet 5%H_2/Ar (○), at 1073 K (a, c) and 873 K (b, d).

Tao *et al.* [18] reported that a slight cross-diffusion at the LSGMCo/LSCM interface may occur during long-term operation. The likely reaction /diffusion area at LSGMCo/LSCM interface seems to be the key to find an explanation of the impedance spectra behaviour. More measurements are now under investigations in order to clarify this reaction. Furthermore, the series resistance increases in the reducing conditions for LSGM-electrolyte samples, Figure 3.6a and b.

The increase in the series resistance in reducing conditions could be explained by the loss of conductivity for LSCM when decreasing the pO_2 (p-conductivity) [19], i.e. the total conductivity is lower and this may well be amplified by the interlayer described below from SEM investigation of this system. In contrast, the series resistance increases under reducting conditions for the LSGMCo-electrolyte samples, Figure 3.6c and d. Ishihara *et al.* [26,27] suggest that some p-conductivity can be assigned to the formation of Co^{3+} and the oxidation state of Co changes from +3 to +2 when decreasing oxygen partial pressure, leading to a loss of conductivity. In addition, the formation of an interdiffusion layer between the anode and the electrolyte, in reducing conditions, could affect the total conductivity of the samples.

3.3.2.2. Anodic overpotential

The anodic overpotentials for LSCM at the LSGM electrolyte, Figure 3.7a, were 28 mV and 67 mV, at 0.2 Acm^{-2}, at 1073 K, in wet H_2 and wet $5\%H_2/Ar$, respectively. At 873 K, these values are 125 mV and 200 mV, at the same current density in wet H_2 and wet $5\%H_2/Ar$, respectively. In contrast, the overpotentials for LSGMCo-electrolyte samples were too high, see Figure 3.7. Thus the performance was lower compared to LSGM-electrolyte samples. One possible explanation for this poor performance is likely to be due the poor contact between anode and electrolyte, Figure 3.8c.

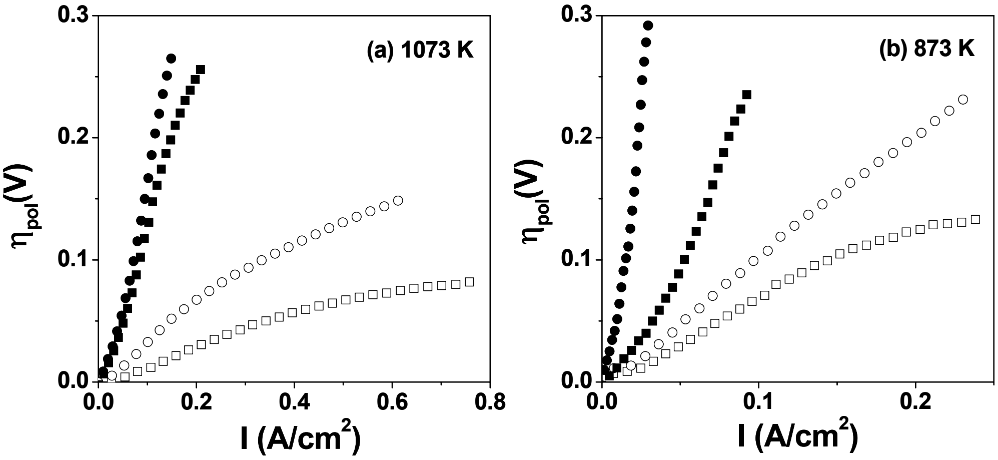

Figure 3.7. Anodic overpotential plots for LSGM (white) and LSGMCo (black) at 1073 K (a) and 873 K (b) in different gas compositions: wet 100% H_2 (□) and wet $5\%H_2/Ar$ (○).

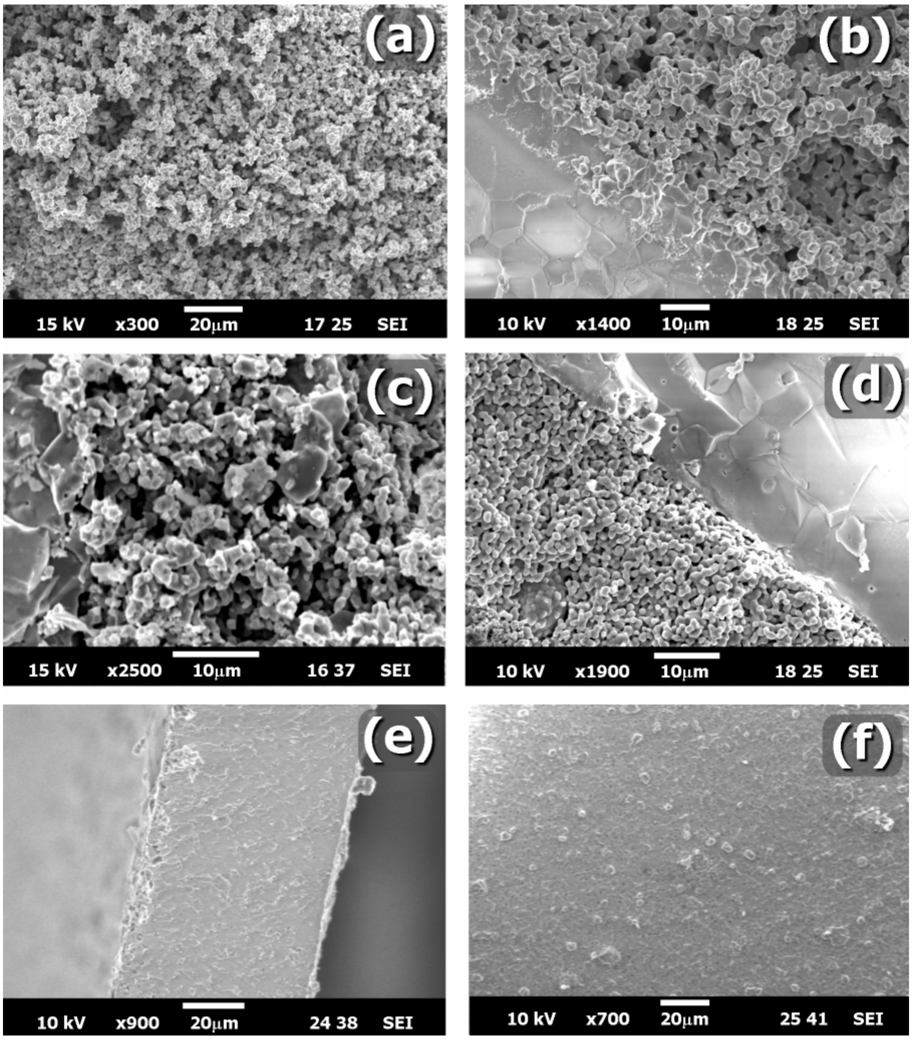

Figure 3.8. SEM images showing the LSCM anode of a fuel cell after testing, using LSGM as electrolyte, (a) top-section, (b) cross-section, and LSGMCo as electrolyte, (c) cross-section. LSM cathode of a fuel cell using LSGM as electrolyte, (d) cross-section. Cross-section (e) and surface (f) of a sintered layer of LSGM electrolyte prepared by tape-casting.

3.3.2.3. Power density

High fuel cell performances are expected from these obtained overpotentials using LSGM as electrolyte and LSCM as anode. In fact, fuel cell tests using thin electrolyte, Figure 3.9a and 3.9b, show high performances at 1073 K in either pure hydrogen, 570 mWcm^{-2}, and, 425 mWcm^{-2} in 5% H_2/Ar. At 873 K the electrical performance drops to around 120-160 mWcm^{-2}. Again the performance in 5%H_2/Ar is about 75% of the value obtained with pure hydrogen. Fukui *et al.* [8] reported a power density over 0.7 Wcm^{-2} at 1073 K and 0.4 Wcm^{-2} at 973 K in a cell with LSGM as electrolyte of ~130 μm of thickness prepared by tape-casting, $La_{0.6}Sr_{0.4}CoO_{3-\delta}$ (LSC) as cathode and NiO-$(CeO_2)_{0.8}(SmO_{0.15})_{0.2}$ (NiO-SDC) as anode material using 97%H_2 + 3% H_2O as fuel and air as oxidant. Our value of power-density at 1073 K is in the same range of Fukui values, although it is important to notice the differences about the used electrodes and the oxidant gas. Our data is also in accord with the preliminary tests of Goodenough and co-workers [28,29] which obtained a 430 $mWcm^{-2}$ power output at 1073 K with CH_4 as fuel using $SrCo_{0.8}Fe_{0.2}O_{3-\delta}$ as cathode, $La_{0.8}Sr_{0.2}Ga_{0.83}Mg_{0.17}O_{2.815}$ as electrolyte and LSCM as anode material.

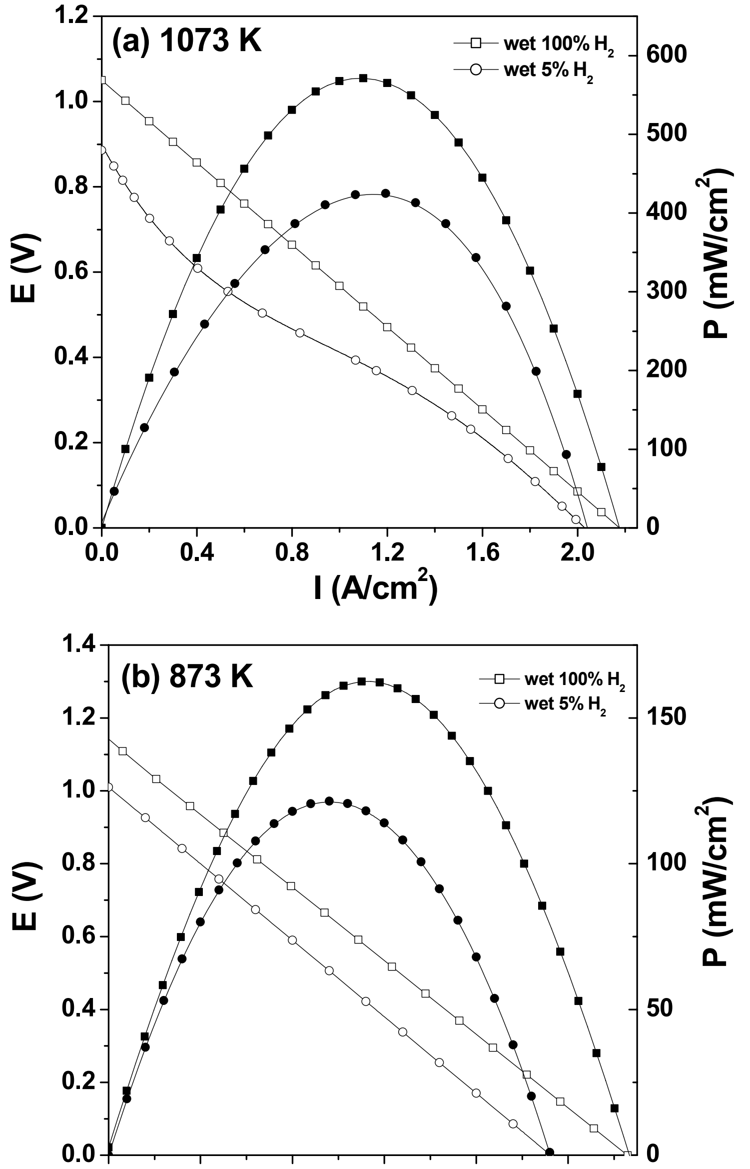

Figure 3.9. Performance (closed symbols) and I-V curves (open symbols), in different gas compositions with 3% of water, 100% H_2 (□) and 5% H_2 (○), at 1073 K (a) and 873 K (b).

SEM pictures were taken after performing the fuel cell tests to investigate the microstructure of the different components and possible degradation or diffusion of the anode/cathode and electrolyte. The anode shows a homogeneous distribution of particles and pores with grain size ranging from 1 to 2 µm, see Figure 8a and 8b. Thus, the ohmic overpotential due to the contact resistance can be neglected because the adherence seems to be good, as seen in Figure 8b. A loss of performance could be expected as it looks like there is a possible reaction between the anode and electrolyte, leading to the formation of a 10 µm-interdiffusion layer (Figure 3.8b). Microstructure and adherence of the LSM cathode also seem good, (Figure 3.8d), however the LSM/LSGM XRD study indicated possible interfacial reaction which could affect the electrical performance of the cell. Figure 3.8e illustrates the cross-section over 60 µm and relative density around 99% of a sintered layer of LSGM electrolyte prepared by tape-casting. Figure 3.8f shows the surface of this layer of LSGM with an average grain size of 2.5 µm. SEM pictures taken on LSGMCo cells, after tests, show that the contact between the anode and electrolyte was poor (Figure 3.8c) and seem to show more than one particle morphology. These factors could explain the high polarisation resistances obtained using this electrolyte and processing route. Tao *et al.* recently reported [18] that the diffusion of the transition elements such as Cr, Mn and Co into the LSGMCo electrolyte is insignificant at LSGMCo/LSCM interfaces. They studied these interfaces by inductively coupled plasma mass spectrometer (ICP-MS). On the other hand, it might be observed a strong reactivity between LSGMCo and LSCM mixture in his XRD pattern at 1173 K and above in Figure 3.4.

3.4. Conclusions

Current-potential, current power-density, anodic losses and overpotential of the LSM/LSGM/LSCM and LSM/LSGMCo/LSCM cells were investigated in this study at 1073 K and 873 K using wet pure hydrogen and 5% H_2/Ar as fuels and O_2 as oxidant. The performance of LSM/LSGMCo/LSCM at 1073 K was inferior to the performance obtained on LSM/LSGM/LSCM at 873 K in both H_2-containing atmospheres. The power-density value for LSM/LSGM/LSCM system with 5% H_2/Ar was 75% of the value obtained for pure H_2 case and the maximum power-density was 570 mW/cm^2 at 1073 K with an electrolyte thickness of about 120 µm.

3.5. Acknowledgements

The authors acknowledge financial support from EU Marie Curie (Contract no: HPMT-CT-2002-02001); European Science Foundation Program OSSEP; Spanish Research Program (MAT2001-3334 and MAT2004-3856 projects); Canary Islands Government (PI2004/093 and PhD grants); and the EPSRC for a Platform grant.

3.6. References

[1] B.C.H. Steele, A. Heinzel, *Nature* **414** (2001) 345-352.

[2] B.C.H. Steele, *High Conductivity Solid Ionic Conductors,* Ed.: T. Takahashi, World Scientific 1989, Singapore.

[3] H. Inaba, H. Tagawa, *Solid State Ion.* **83** (1996) 1-16.

[4] Z. Shao, S.M. Haile, *Nature* **431** (2004) 170-173.

[5] T. Ishihara, H. Matsuda, Y. Takita, *J. Am. Chem. Soc.* **116** (1994) 3801-3803.

[6] K. Huang, S.R. Tichy, J.B. Goodenough, *J. Am. Chem. Soc.* **81** (1998) 2565-2575.

[7] T. Ishihara, H. Matsuda, M. Azni, Y. Takita, *Solid State Ion.* **86-88** (1996) 197-201.

[8] T. Fukui, S. Ohara, K. Murata, H. Yoshida, K. Miura, T. Inagaki, *J. Power Sources* **106** (2002) 142-145.

[9] J.H. Kim, H.I. Yoo, *Solid State Ion.* **140** (2001) 105-113.

[10] A. Matraszek, L. Singheiser, D. Kobertz, K. Hilpert, M. Miller, O. Schulz, M. Martin, *Solid State Ion.* **166** (2004) 343-350.

[11] M. Guillodo, P. Vernoux, J. Fouletier, *Solid State Ion.* **127** (2000) 99-107.

[12] M. Feng, J.B. Goodenough, K. Huang, C. Milliken, *J. Power Sources* **63** (1996) 47-51.

[13] K. Huang, J. Wan, J.B. Goodenough, *J. Electrochem. Soc.* **148** (2001) A788-A794.

[14] K. Huang, J.B. Goodenough, *J. Alloy.Compd.* **303-304** (2000) 454-464.

[15] D. Stöver, H.P. Buchkremer, S. Uhlenbruck, *Ceramics International* **30** (2004) 1107-1113.

[16] T. Ishihara, T. Shibayama, S. Ishikawa, K. Hosoi, H. Nishiguchi, Y. Takita, *J. European Ceram. Soc.* **24** (2004) 1329-1335.

[17] T. Ishihara, H. Furutani, M. Honda, T. Yamada, T. Shibayama, T. Akbay, N. Sakai, H. Yokokawa, Y. Takita, *Chem. Mat.* **11** (1999) 2081-2088.

[18] S.W. Tao, J.T.S. Irvine, J.A. Kilner, *Adv. Mater.* **17** (2005) 1734-1737.

[19] S.W. Tao, J.T.S. Irvine, *Nat. Mater.* **2** (2003) 320-323.

[20] S.W. Tao, J.T.S. Irvine, *J. Electrochem. Soc.* **151** (2004) 151 A252-A259.

[21] S. Zha, P. Tsang, Z. Cheng, M. Liu, *J. Solid State Chem.* **178** (2005) 1847-1853.

[22] M. Ralph, C. Rossignol, R. Kumar, *J. Electrochem. Soc.* **150** (2003) A1518-A1522.

[23] S. Srilomsak, D.P. Schilling, H.U. Anderson, *Proceedings of the 1st International Symposium on Solid Oxide Fuel Cells*, The Electrochemical Society, Pennington, NJ (1989) 129-140.

[24] Y. Du, N.M. Sammes, *Proceedings of the 9th International Symposium on Solid Oxide Fuel Cells (SOFC-IX)*, The Electrochemical Society, PV 2005-07- ISBN 1-56677-465-9, Solid Oxide Fuel Cells (SOFC IX) (2005) 1127.

[25] J. Y. Yeon, G.M. Choi, *J. European Ceram. Soc.* **24** (2004) 1359-1363.

[26] T. Ishihara, T. Akbay, H. Furutani, Y. Takita, *Solid State Ion.* **113-115** (1998) 585-591.

[27] T. Ishihara, S. Ishikawa, M. Ando, H. Nishiguchi, Y. Takita, *Solid State Ion.* **173** (2004) 9-15.

[28] J.-H. Wan, J.-Q. Yan, J.B. Goodenough, *J. Electrochem. Soc.* **152** (2005) A1511-A1515.

[29] J.-H. Wan, J.H. Zhu, J.B. Goodenough, *Proceedings of the 9th International Symposium on Solid Oxide Fuel Cells (SOFC-IX)*, The Electrochemical Society, PV 2005-07- ISBN 1-56677-465-9, Solid Oxide Fuel Cells (SOFC IX) (2005) 429.

Chapter 4

SOFC test using $Ba_{0.5}Sr_{0.5}Co_{0.8}Fe_{0.2}O_{3-\delta}$ as cathode on $La_{0.9}Sr_{0.1}Ga_{0.8}Mg_{0.2}O_{2.85}$ electrolyte

Published in *Solid State Ionics* 177 (2006) 2143-2147

J. Peña-Martínez[a,b], D. Marrero-López[b], J.C. Ruiz-Morales[b], B.E. Buergler[a], P. Núñez[b], L.J.Gauckler[a]
[a]Department of Materials, ETH-Zurich, 8093 Zurich,Switzerland.
[b]Inorganic Chemistry Department, University of La Laguna, Tenerife, Spain.

Abstract

An intermediate temperature solid oxide fuel cell based on perovskite-type materials was tested. $La_{0.9}Sr_{0.1}Ga_{0.8}Mg_{0.2}O_{2.85}$ (LSGM) was used as electrolyte, $Ba_{0.5}Sr_{0.5}Co_{0.8}Fe_{0.2}O_{3-\delta}$ (BSCF) as cathode and $La_{0.75}Sr_{0.25}Cr_{0.5}Mn_{0.5}O_{3-\delta}$ (LSCM) as anode material. The maximum power-density value of the BSCF/LSGM/LSCM cell with 1.5 mm thick-electrolyte was 160 mWcm^{-2} at 1073 K, using moistened H_2 diluted with N_2 as fuel and air as oxidant.

Keywords

IT-SOFC, LSGM, BSCF, LSCM, electrochemical performance

4.1. Introduction

The versatile perosvkite-type structure is an interesting option to develop new electrolyte and electrode materials for intermediate temperature solid oxide fuel cells (IT-SOFCs). It is well known that the ionic conductivity of $La_{0.9}Sr_{0.1}Ga_{0.8}Mg_{0.2}O_{2.85}$ (LSGM) [1-4] is higher than the conductivity of yttria-stabilised zirconia (YSZ) at intermediate temperatures (773–1073 K). LSGM has an ionic conductivity of about 0.1 Scm^{-1} at 1073 K, good chemical stability and negligible electronic conduction over a broad range of oxygen partial pressures (10^{-20}-1 atm) [5]. However, it has some drawbacks as electrolyte such as undesired segregation of $LaSrGa_3O_7$ and $LaSrGaO_4$ during its synthesis [6] and chemical incompatibility with Ni-based anode materials [7-9]. Nevertheless, the synthesis can be optimized to reduce undesired phases and alternative anode material can be used.

Recently, it was found that $La_{0.75}Sr_{0.25}Cr_{0.5}Mn_{0.5}O_{3-\delta}$ (LSCM) material is a redox stable perovskite anode for SOFCs using YSZ or $La_{0.8}Sr_{0.2}Ga_{0.8}Mg_{0.15}Co_{0.05}O_{3-\delta}$ (LSGMC) [10-12] as electrolyte. The primitive perovskite unit cell volumes and the thermal expansion coefficients of LSCM and LSGM [11,13] are similar, indicating *a priori* a good match.

An LSGM-electrolyte supported cell with 120 μm thick electrolyte using LSM as cathode and LSCM as anode was tested in a previous work [14] and the power density reached the values of 570 mWcm^{-2} and 160 mWcm^{-2} at 1073 K and 873 K respectively, with moistened H_2 as fuel and O_2 as oxidant. The power density at 873 K was low because of the high ohmic losses of the electrolyte at low temperatures and the high polarisation resistance of LSM. For this reason, it seems advisable to use an alternative cathode material in order to increase the performance of LSGM-based cells at low temperatures. Recently, $Ba_{0.5}Sr_{0.5}Co_{0.8}Fe_{0.2}O_{3-\delta}$ (BSCF) has been proposed as alternative cathode material due to its high activity for the electrochemical reduction of oxygen in the temperature range from 773 to 973 K on samarium doped ceria (SDC) electrolytes [15]. In this work BSCF has been studied as cathode material on a LSGM electrolyte in an SOFC using LSCM as the anode material.

4.2. Experimental

4.2.1. Preparation and characterisation of the materials

LSGM electrolyte and LSCM anode materials have been prepared by conventional solid state reaction using high purity oxide powders. Before weighing in, La_2O_3 was calcined at 1273 K for more than 3 hours in order to decompose the carbonates. LSCM powders and LSGM dense pellets (98-99% of theoretical density) were prepared as described elsewhere [14]. The ceramic route was done by ball-milling stoichiometric quantities of the reagents with acetone. The resulting mixture was dried and fired in air at 1173 K for 10 h and ball-milled again. Dense pellets of LSGM were obtained by uniaxially pressing the synthesized powder at 140 MPa, in a dye of 3.0 cm diameter, and sintering the compacted powder at 1673 K for 6 h in air. LSCM powders were obtained after thermal treatment at 1673 K for 10 h. The BSCF cathode material was prepared by following the sol-gel route using highly pure nitrates of Ba, Sr, Co and Fe. The sol-gel route was carried out using citric acid and ethylendiaminetetraacetic acid (EDTA) as complex agents. An ammonium solution of EDTA, 1.5 % wt. in excess, with a ratio ligand/metal (L/M) of one was added to the solution of the corresponding nitrates prepared with distilled water to avoid the formation of $SrCoO_2$ [15]. Afterwards, the citric acid solution, 1.5 % wt. in excess and in a ratio L/M=1 and L/M=2/3 for trivalent and divalent cations respectively, was also added. The pH was adjusted up to 9 by adding ammonia solution (20% v/v). A gel was formed during continuous stirring and low heating (~ 338 K). It was dried at room temperature for more than 8 h and then fired at 573 K for 30 min. The obtained powders were ground in an agate mortar and fired in air at 923 K during 5 h, ground again and finally fired at 1173 K for 5 h in air. Electrode slurries of BSCF and LSCM were prepared with ethyl cellulose as binder and diethyleneglycol monobutyleter acetate as solvent. The composition (% wt.) of the slurries was 75% of electrode powders, 5% of binder and 20% of solvent.

X-ray Diffraction (XRD) patterns were collected using a Philips X´Pert Pro diffractometer, with a primary monochromator and a X'Celerator detector, for material characterisation. The scans were performed in the 2θ range from 20 to 90º (step 0.016º and 500 s/step), using Cu $K_{\alpha 1}$ radiation. Additional XRD studies were also carried out in order to investigate the chemical compatibility of LSGM with BSCF material. In this sense, powder mixtures of LSGM with BSCF, 1:1 (% wt.), were ground in an agate mortar and fired at 1173 K, 1373 K and 1473 K for 10 h. The interfaces between the electrodes and the electrolyte and the electrode microstructure were characterised by scanning electron microscopy (SEM, JEOL JSM-6300 and LEO 1530) before and after the tests. In addition, TG/DTA studies were carried out with a NETZSCH instrument (STA 449 C Jupiter) to determine the correct stoichiometry of the nitrates used in the synthesis and to estimate the optimal temperature of crystallisation of the powder precursors obtained by the sol-gel route.

4.2.2. Fuel cell tests

Fuel cell tests were performed with moistened mixtures of H_2 (40% vol.) and N_2 as fuel and air as oxidant. The electrodes were prepared by screen printing (~50 μm thickness and 1 cm^2 of surface) using the corresponding slurry and fired at 1273 – 1473 K in air for 1 h. Platinum paste and mesh were used as current collector for both the anode and the cathode. The electrolyte-pellet had a diameter of 20 mm and a thickness of 1.5 mm. The measurement setup shown in Figure 4.1 consisted of two quartz tubes for the gas transport to the electrodes. The cell was mounted between two Al_2O_3 spacer rings and positioned between the quartz tubes. The entire setup was heated in a tubular furnace and the temperature was varied between 873 K and 1073 K. The electrochemical tests were performed with a potentiostat (Zahner IM6) by sweeping the voltage from OCV to 0 V at a scan rate of 5 mVs^{-1}.

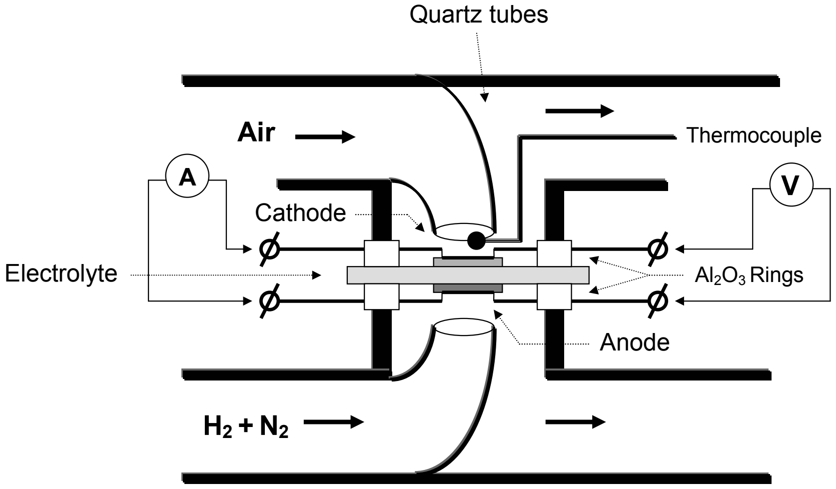

Figure 4.1. Measurement setup for fuel cell testing.

A two-electrode configuration was used to obtain I-V plots and electrode ohmic loss. Total overpotential was calculated by:

$$\eta_{pol}(\mathrm{V}) = OCV(\mathrm{V}) - E(\mathrm{V}) - I(\mathrm{Acm^{-2}})\cdot R_s(\Omega\mathrm{cm^2}) \qquad (4.1)$$

where η_{pol} is the value of the total overpotential due to the electrodes contribution, *OCV*, *E*, *I* and R_s are the measured open circuit voltage, voltage in the cell, current density and electrolyte resistance, respectively. The impedance of the electrochemical cell was acquired at open circuit voltage (OCV), with a frequency range from 0.1 Hz-1MHz and 20 mV of ac-amplitude, obtaining reproducible spectra.

4.3. Results and Discussion

4.3.1. Characterisation and compatibility of the materials

Structural characterisation by X-ray diffraction confirmed that LSGM, BSCF and LSCM materials are single phase after their synthesis at the temperatures of 1673 (6h), 1173 (5h) and 1673 K (10 h). The X-ray patterns were refined using FullProf and WinPlotr programs [16,17]. BSCF pattern was refined in a cubic cell, a= 3.9832(5) (space group Pm-3m); LSGM pattern was refined in an orthorhombic system, a=5.5216(6), b=7.8262 (9) and c=5.5413 (5) (space group IBMM). LSCM pattern was refined in a hexagonal cell, a=5.4924(7), c=13.315(1) (space group R-3c).

XRD patterns at room temperature, 1173 K, 1373 K and 1473 K of the binary-mixed-system LSGM/BSCF are shown in Figure 4.2. LSGM/LSCM compatibility was studied in a previous work and LSCM material reacts with the LSGM electrolyte above 1623 K [14]. On the other hand, no additional diffraction peaks were found in the LSGM/LSCM system as well as the new studied LSGM/BSCF system, between room temperature and 1173 K, indicating the chemical compatibility at intermediate temperature from 873-1073 K. Above 1273 K LSGM strongly reacted with BSCF as can be observed in Figure 4.2.

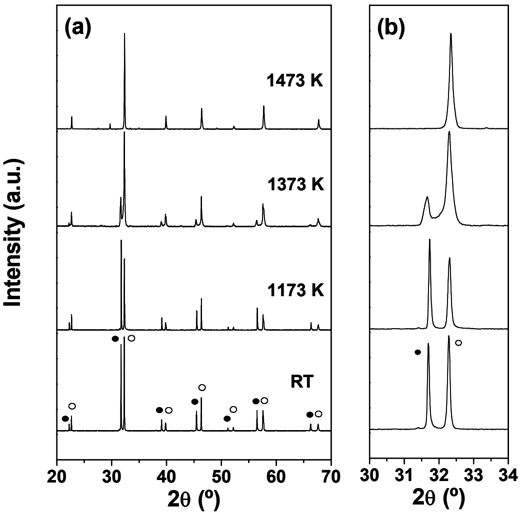

Figure 4.2. a) XRD patterns of the mixture LSGM/BSCF fired at different temperatures. LSGM (○) and BSCF peaks (●) are indicated. b) Magnification of the range 30°≤2θ≤34°. At 1373 K a reaction between LSGM and BSCF was evidenced.

In order to avoid the reaction between BSCF and LSGM the maximum temperature of sintering the BSCF electrode material on the LSGM electrolyte pellet was never higher than 1273 K.

4.3.2. Electrolyte and electrode resistances

The impedance spectra of the cell were measured under asymmetric atmospheres at open circuit conditions and they were fitted with equivalent circuits (Figure 4.3).

The values of the electrolyte resistance (R_s) have been normalised by the thickness of the electrolyte and the electrode surface area; and the values of polarisation resistance (Rp) has been normalised by the electrode surface. Thus, R_s and R_p were 7.6 Ωcm and 0.75 Ωcm^2 respectively at 1073 K. When the operational temperature was decreased to 873 K the R_s and R_p resistances increase to 31.2 Ωcm and 4.47 Ωcm^2 respectively.

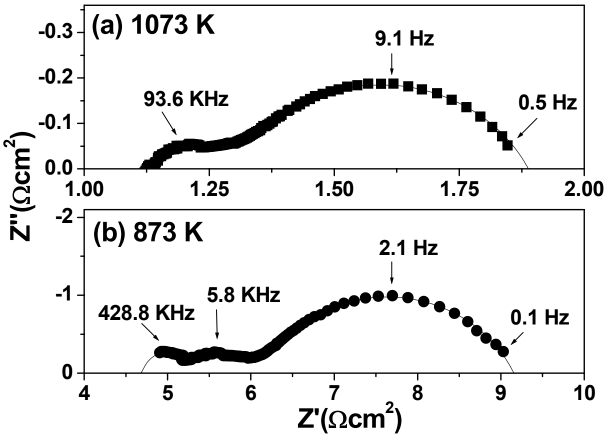

Figure 4.3. Impedance spectra of the BSCF/LSGM/LSCM system at 1073 K (■) and 873 K (●). The solid line is the fitted result obtained with equivalent circuits.

4.3.3. Power density

The power density reached a value of 160 mWcm^{-2} and 35 mWcm^{-2} at 1073 K and 873 K respectively (Figure 4.4). It is noticed the drastic drop of the power density at 873 K, due to the ohmic losses of the electrolyte and the high polarization of the electrodes. More efforts are necessary to increase the electrochemical performance below this temperature, e.g. optimising the microstructure of the electrodes [18] and reducing the thickness of the LSGM electrolyte.

4.3.4. Electrode overpotentials

The overall calculated electrode overpotentials at 873 and 1073 K are compared in the inset of Figure 4.4. The shapes of the overpotential-current density curve were practically linear in the current-density range studied, with a slope of 0.5 Ωcm^2 at 1073 K and 3.65 Ωcm^2 at 873 K. In a previous work [14], using a three-probe arrangement, the anodic overpotential of LSCM material was found quite low with a slope of 0.12 Ωcm^{-2}, e.g. 28 mV at 0.2 Acm^{-2}

(1073 K) using moistened H_2 as fuel and oxygen as oxidant for fuel cell tests. For instance, the low values of overpotential of the BSCF/LSGM/LSCM system indicate a low contribution of both cathode and anode material. The low cathodic overpotential contribution could be attributed to the low activation overpotential of cobaltite-based cathodes. In this sense, Huang et al. [8] found similar results comparing $SrCo_{0.8}Fe_{0.2}$ (SCF) with $La_{0.85}Sr_{0.15}MnO_3$ as cathode materials and both on doped $LaGaO_3$ (LGO) electrolytes, explaining this behavior in terms of a high oxygen flux of the cobalt-containing perovskite [19].

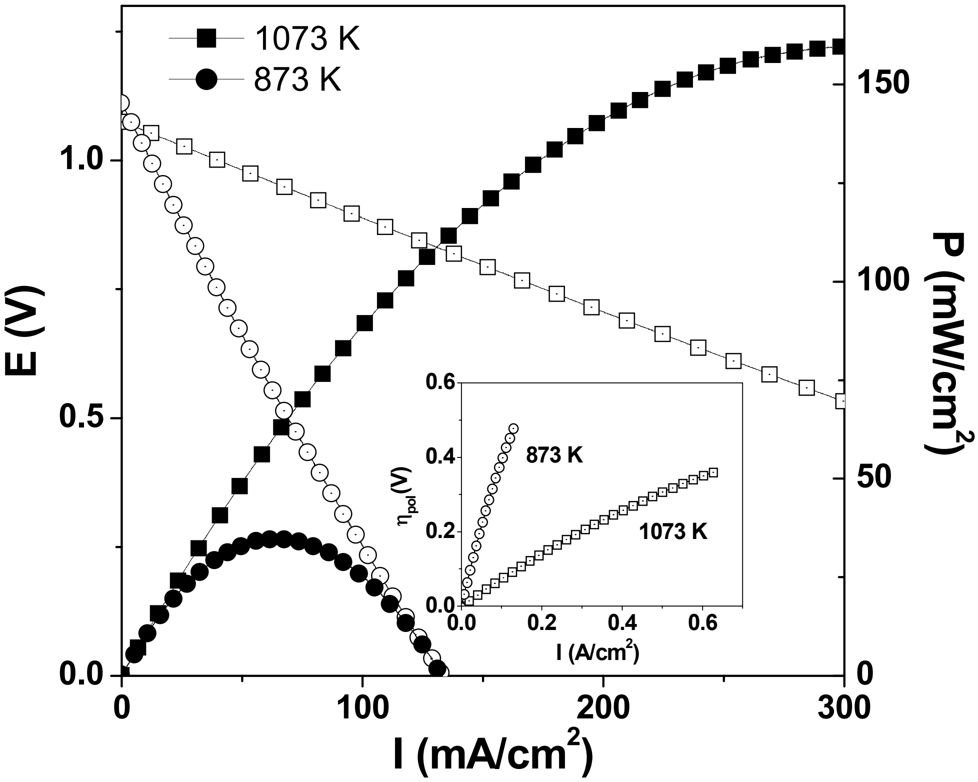

Figure 4.4. Current-voltage characteristics at 1073 K (■) and 873 K (●) and current-power density characteristics at 1073 K (□) and 873 K (○). Electrode overpotentials at 1073 K (□) and 873 K (○) are illustrated in the inset.

4.3.5. Electrode interfaces

SEM images of the BSCF/LSGM (Figure 4.5a) and LSCM/LSGM (Figure 4.5b) interfaces after the tests showed that there was a good contact between the electrode and the electrolyte, and this is in good agreement with the values of the polarisation and the electrolyte resistance. However the XRD study of chemical compatibility indicated a strong reaction above 1273 K and 1673 K in the BSCF/LSGM and LSGM/LSCM systems respectively. A long term operation could seriously affect the properties of the interfaces with a wide diffusion area.

Kostogloudis et al. [20] have investigated the chemical compatibility between Pr(Sr)Fe(Co)O_3 and Pr(Sr)Mn(Co)O_3 materials with LSGM by XRD analysis and diffusion experiments and they concluded that the transition metals diffuse in the order Mn<Fe<Co with a highest-diffusion of Co into the LSGM electrolyte. In another work, Sakai et al. [21] have recently reported an investigation about the reactivity and diffusion at the interface of $La_{0.8}Sr_{0.2}Ga_{0.8}Mg_{0.2}O_{2.9}$ and $La_{0.6}Sr_{0.4}Co_{0.2}Fe_{0.8}O_{3-\delta}$ by SIMS techniques and the results shown that the diffusion of metal components is not avoidable at the studied interface. Figure 4.5c and 4.5d show the microstructure of BSCF and LSCM electrodes both on LSGM surface after the tests with an average grain size of 5 μm and 1-2 μm respectively. The microstructure of BSCF material is apparently less suitable than the used LSM in our previous work with an average grain size of 1-2 μm and a more uniform porosity [14] although the obtained values of the power density and the total overpotential indicated that the microstructure is not the most critical factor, at least at 1073 K, on LSGM electrolyte. In this sense, Yi and Choi, working with LSM-LSGM composites instead of LSM material as cathode on LSGM electrolyte, reported that it is more important to reduce the cathodic overpotential than control the microstructure in LSGM systems at operation temperatures above 1073 K [22].

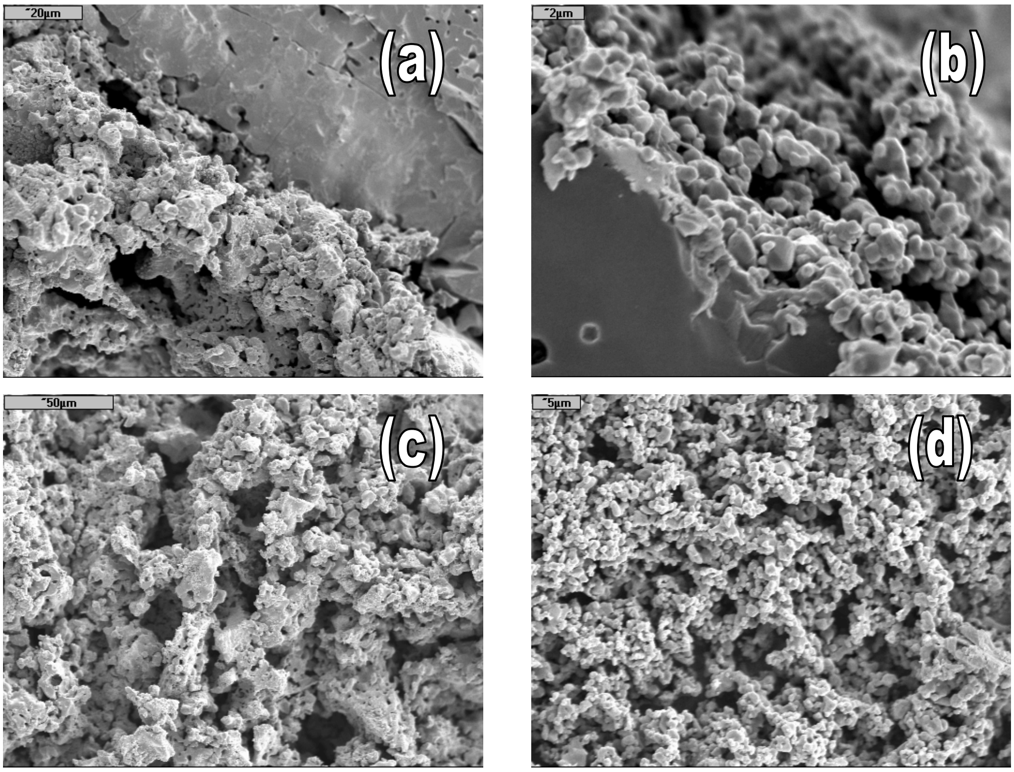

Figure 4.5. SEM images of a) the BSCF/LSGM and b) the LSCM/LSGM (b) interfaces. Topview of the microstructures of c) the BSCF cathode and d) the LSCM anode after the fuel cell tests.

4.4. Conclusions

Current-voltage, current-power density, electrode and electrolyte resistances and overpotential of a BSCF/LSGM/LSCM cell were investigated in this study at 1073 K and 873 K, using moistened hydrogen-nitrogen mixtures as fuels and air as oxidant. The values of power-density and polarisation resistance at 1073 K were 160 mWcm^{-2} and 0.75 Ωcm^2 respectively, with 1.5 mm thickness electrolyte (R_s= 7.6 Ωcm). The use of BSCF material on LSGM seems to be feasible but the sintering temperature must be kept below 1273 K in order to avoid the deleterious reaction between BSCF and LSGM. The long-term stability of the BSCF/LSGM interface at the intermediate operating temperatures from 773-973 K is an important factor that still needs to be studied.

4.5. Acknowledgements

The authors acknowledge financial support from Spanish Research Program (MAT-2001-3334 and MAT-2004-03856) and Canary Islands Government (COFI 2002-027, PhD and ETH sojourn grants).

4.6. References

[1] T. Ishihara, H. Matsuda, Y. Takita, *J. Am. Chem. Soc.* **116** (1994) 3801-3803.
[2] K. Huang, S.R. Tichy, J.B. Goodenough, *J. Am. Chem. Soc.* **81** (1998) 2565-2575.
[3] T. Ishihara, H. Matsuda, M. Azni, Y. Takita, *Solid State Ion.* **86-88** (1996) 197-201.
[4] J.H. Kim, H.I. Yoo, *Solid State Ion.* **140** (2001) 105-113.
[5] O. Yamamoto, *Electrochim. Acta* **45** (2000) 2423-2435.
[6] A. Matraszek, L. Singheiser, D. Kobertz, K. Hilpert, M. Miller, O. Schulz, M. Martin, *Solid State Ion.* **166** (2004) 343-350.
[7] M. Guillodo, P. Vernoux, J. Fouletier, *Solid State Ion.* **127** (2000) 99-107.
[8] K. Huang, J. Wan, J.B. Goodenough, *J. Electrochem. Soc.* **148** (2001) A788-A794.
[9] K. Huang, M. Feng, J.B. Goodenough, C. Milliken, *J. Electrochem. Soc.* **144** (1997) 3620-3624.
[10] S. Tao, J.T.S. Irvine, *Nat. Mater.* **2** (2003) 320-323.
[11] S. Tao, J.T.S. Irvine, *J. Electrochem. Soc.* **151** (2004) A252-A259.
[12] S. Tao, J.T.S. Irvine, J.A. Kilner, *Adv. Mater.* **17** (2005) 1734-1737.
[13] P.R. Slater, J.T.S. Irvine, T. Ishihara, Y. Takita, *J. Solid State Chem.* **139** (1998) 135-143.
[14] J. Peña-Martínez, D. Marrero-López, J.C. Ruiz-Morales, C. Savaniu, P. Núñez, J.T.S. Irvine, *Chem. Mater.* **18** (2006) 1001-1006.
[15] Z. Shao, S.M. Haile, *Nature* **431** (2004) 170-173.
[16] J. Rodríguez-Carvajal, FullProf Suite, LLB, CEA-Saclay, France 2004.
[17] T. Roisnel, J. Rodríguez-Carvajal, WinPLOTR, LLB-LCSI, France 2004.
[18] J.C. Ruiz-Morales, J. Canales-Vázquez, J. Peña-Martínez, D. Marrero-López, J.T.S. Irvine, P. Núñez, *J. Mater. Chem.* **16** (2006) 540-542.
[19] K. Huang, J.B. Goodenough, *J. Electrochem. Soc.* **148** (2001) E203-E214.
[20] G. Ch. Kostogloudis, Ch. Ftikos, A. Ahmad-Khanlou, A. Naoumidis, D. Stöver, *Solid State Ion.* **134** (2000) 127-138.
[21] N. Sakai, T. Horita, K. Yamaji, M.E. Brito, H. Yokokawa, A. Kawakami, S. Matsuoka, N. Watanabe, A. Ueno, *J. Electrochem. Soc.* **153** (2006) A621-A625.
[22] J.Y. Yi, G.M. Choi, *Solid State Ion.* **175** (2004) 145-149.

Chapter 5

Fuel cell studies of perovskite-type materials for IT-SOFC

Published in *Journal of Power Sources* 159 (2006) 914-921

J. Peña-Martínez[a,b], D. Marrero-López[b], J.C. Ruiz-Morales[b], B.E. Buergler[a], P. Núñez[b], L.J.Gauckler[a]
[a]Department of Materials, ETH-Zurich, 8093 Zurich,Switzerland.
[b]Inorganic Chemistry Department, University of La Laguna, Tenerife, Spain.

Abstract

The electrochemical performance of solid oxide fuel cells (SOFCs) based on perovskite-type materials (ABO_3) was investigated. $La_{0.9}Sr_{0.1}Ga_{0.8}Mg_{0.2}O_{2.85}$ (LSGM) ceramics were used as electrolyte and a composite containing $La_{0.8}Sr_{0.2}MnO_{3-\delta}$ (LSM) as cathode. $Ba_{0.5}Sr_{0.5}Co_{0.8}Fe_{0.2}O_{3-\delta}$ (BSCF) was also used as cathode and $La_{0.75}Sr_{0.25}Cr_{0.5}Mn_{0.5}O_{3-\delta}$ (LSCM) as anode materials. Furthermore, fluorite-type $Sm_{0.15}Ce_{0.85}O_{2-\delta}$ (SDC) material was used as buffer layer between the electrolyte and the anode to avoid possible interfacial reactions. The maximum power-density value of BSCF/LSGM/LSCM with 1.5 mm thick-electrolyte supported cell was 160 mWcm^{-2} at 1073 K, using moist H_2 diluted with N_2 as fuel and air as oxidant.

Keywords

Perovskite-type oxides, electrochemical performance, solid oxide fuel cell, $Ba_{0.5}Sr_{0.5}Co_{0.8}Fe_{0.2}O_{3-\delta}$, $La_{0.75}Sr_{0.25}Cr_{0.5}Mn_{0.5}O_{3-\delta}$, $La_{0.9}Sr_{0.1}Ga_{0.8}Mg_{0.2}O_{2.85}$

5.1. Introduction

The versatile perosvkite-type structure (ABO_3) is an interesting option to develop new materials for intermediate temperature solid oxide fuel cells (IT-SOFCs). It is well known that the ionic conductivity of $La_{0.9}Sr_{0.1}Ga_{0.8}Mg_{0.2}O_{2.85}$ (LSGM) [1-5] is higher compared to the yttria doped zirconia (YSZ) at intermediate temperatures (773 – 1073 K). This material has an ionic conductivity about 0.1 Scm^{-1} at 1073 K, good chemical stability and negligible electronic conduction over a broad range of oxygen partial pressures (1-10^{-20} atm) [6]. On the other hand, LSGM has some disadvantages as electrolyte, such as undesired segregation of impurities during its synthesis, e.g. $LaSrGa_3O_7$ and $LaSrGaO_4$ [7], and chemical incompatibility with Ni-based anode materials [8,9]. Ni reacts with LSGM to form $LaNiO_3$ [10]. However, the synthesis can be optimised to reduce undesired phases and alternative anode material without Nickel or a buffer layer, between electrolyte and Ni-based anode, can be used to avoid interfacial reactions [11].

Results from LSGM-electrolyte supported cells with $La_{0.8}Sr_{0.2}MnO_{3-\delta}$ (LSM) as cathode and $La_{0.75}Sr_{0.25}Cr_{0.5}Mn_{0.5}O_{3-\delta}$ (LSCM) [12,13] as anode were reported in a previous work [14]. Dense LSGM samples were prepared by tape casting. The power density reached a value of 570 $mWcm^{-2}$ at 1073 K with moistened H_2 and O_2 as oxidant. However, the output power density drastically decreased at 873 K, mainly due to the high polarisation resistance of LSM and higher ohmic losses of the electrolyte. Therefore, different strategies were envisaged in order to increase the performance of LSGM-based cells using LSCM as anode material at low temperature: reducing the electrode overpotential and avoiding the possible interfacial reactions between the electrodes and the electrolyte. For the first option, a composite of LSM and LSGM in a 30-70% molar ratio (LSM-LSGM) was used. A lower cathodic overpotential had been reported using LSGM- LSM as composite than with LSM only, both on LSGM electrolyte [15]. In addition, the recently proposed $Ba_{0.5}Sr_{0.5}Co_{0.8}Fe_{0.2}O_{3-\delta}$ (BSCF) material was used in this study as alternative cathode, due to the good properties for electrochemical reduction of oxygen in the range of 773 – 973 K [16]. For the second option, $Sm_{0.15}Ce_{0.85}O_{2-\delta}$ (SDC) was used as buffer layer between the electrolyte and the anode material. LSM/LSGM/LSCM, LSM/LSGM/SDC/LSCM, LSM-LSGM/LSGM/LSCM and BSCF/LSGM/LSCM cells were prepared and tested in this work and their performances are compared.

5.2. Experimental

5.2.1. Electrodes and electrolyte preparation

LSGM electrolyte, LSM-LSGM cathode and LSCM anode materials have been prepared by conventional solid state reaction, using powders of La_2O_3 (Fluka, 99.98%), Ga_2O_3 (Fluka, 99.99%), MgO (Fluka, 99%), $SrCO_3$ (Aldrich, 99.9%), Mn_2O_3 (Aldrich 99.999%) and Cr_2O_3 (ABCR, 99.999%). La_2O_3 and MgO were fired at 1273 K for more than 3 h before weighing to remove water and impurities, in order to ensure the correct stoichiometry. Commercial powders of LSM obtained via combustion spray pyrolysis (SSC. Inc. Worthingtong, USA, 99.9%) were used to prepare the LSM-cathode specimens. BSCF cathode and SDC interlayer materials have been prepared via sol-gel, using powders of $Ba(NO_3)_2$ (Fluka, 99.95%), $Sr(NO_3)_2$ (Fluka, 99%), $Co(NO_3)_2{\cdot}6H_2O$ (Fluka, 98%), $Fe(NO_3)_3{\cdot}9H_2O$ (Merck, 99%), $Sm(NO_3)_3{\cdot}6H_2O$ (Alfa Aesar, 99.9%) and $Ce(NO_3)_3{\cdot}6H_2O$ (Alfa Aesar, 99.9%). The ceramic route was done by ball-milling stoichiometric quantities of the reagents with acetone. The resulted mixture was dried and fired in air up to 1173 K for 10 h and ground again. Dense samples of LSGM were obtained by uniaxial pressing into a disk at 140 MPa, for five minutes (ø = 3.0 cm) of the synthesised powders and sintered at 1673 K for 6 h. LSCM and LSM-LSGM powders were obtained after treatment at 1373 K for 10 h and 1473 K for 6 h, respectively.

The sol-gel route was carried out, using citric acid and ethylendiaminetetraacetic acid (EDTA) as complex agents to prepare BSCF and SDC materials. Stoichometric cation solution of the corresponding nitrates was prepared with distilled water. An ammonium solution of EDTA, 1.5 % wt. in excess, with a ratio ligand/metal (L/M) of one was added. Afterwards, the citric acid solution, 1.5 % wt. in excess and in a ratio L/M=1 and L/M=2/3 for trivalent and divalent cations respectively, was also added. The pH was adjusted up to 9 with addition of ammonia solution (20% v/v). A gel was formed with continuous stirring and low heating (~ 338 K). It was dried at room temperature for more than 8 h. The dried gels were fired at 573 K for 30 min. The obtained powders were ground in an agate mortar and fired in air at 923 K and 723 K for BSCF and SDC respectively during 5 h, ground again and finally fired at 1173 K for 5 h in air.

Electrode slurries were prepared with ethyl cellulose as binder and diethyleneglycol monobutyleter acetate as solvent. The composition (% wt.) of the slurries was 75% of electrode powders, 5% of binder and 20% of solvent.

5.2.2. Material characterisation

X-ray Diffraction (XRD) patterns were recorded using a Siemens D5000 with $K\alpha_1$ copper radiation wavelength of 0.15406 nm. The scans were performed in the 2θ range (5-120º) with 0.02º step and 10 s/step. XRD studies were also carried out to investigate the chemical compatibility of the electrolyte with the electrodes. Powder mixtures of LSGM with BSCF, LSGM with SDC and LSCM with SDC, 1:1 (% wt.) were ground in agate mortar and fired at 1173 K and 1473 K for 10 h. The morphology and composition of ceramic materials were observed by scanning electron microscopy (SEM) (JEOL JSM-6300 and LEO 1530) and Energy Dispersive X-Ray Spectroscopy (EDS) (NORAN Vantage) before and after the tests. TG/DTA studies were carried out with a STA 449 C Jupiter NETZSCH (TG/DTA) to determine the correct stoichiometry of the nitrates used in the synthesis and to estimate the optimal temperature of crystallization on powder precursors obtained by sol-gel route.

5.2.3. Fuel cell tests

Fuel cell tests were performed with a moistened (3% water) gas mixture of H_2 (40 vol%) and N_2 as fuel and air as oxidant. Different electrolyte supported cells were investigated: LSM/LSGM/LSCM, LSM/LSGM/SDC/LSCM, BSCF/LSGM/LSCM and LSM-LSGM/LSGM/LSCM. The electrodes and the buffer layer were deposited via screen printing (~50 μm thickness and 1 cm^2 of surface) using the corresponding slurry and fired at 1273 – 1573 K in air for 1 h. Platinum paste and mesh were used as current collector. The electrolyte-pellet dimensions were about 1.5 and 20 mm in thickness and diameter for all the cells.

The measurement setup consisted of two quartz tubes for the gas transport to the electrodes (Figure 5.1). The cell was mounted between two Al_2O_3 spacer rings and adjusted between the quartz tubes. High fuel and air flow gases were necessary, 300 ml/min on each side at a pressure of 1 atm, due to the unsealed arrangement to obtain high values of OCV. The entire setup was heated in a tubular furnace and the temperature was varied between 873 K and 1073 K. The electrochemical analyses were performed with a Zahner IM6 potentiostat.

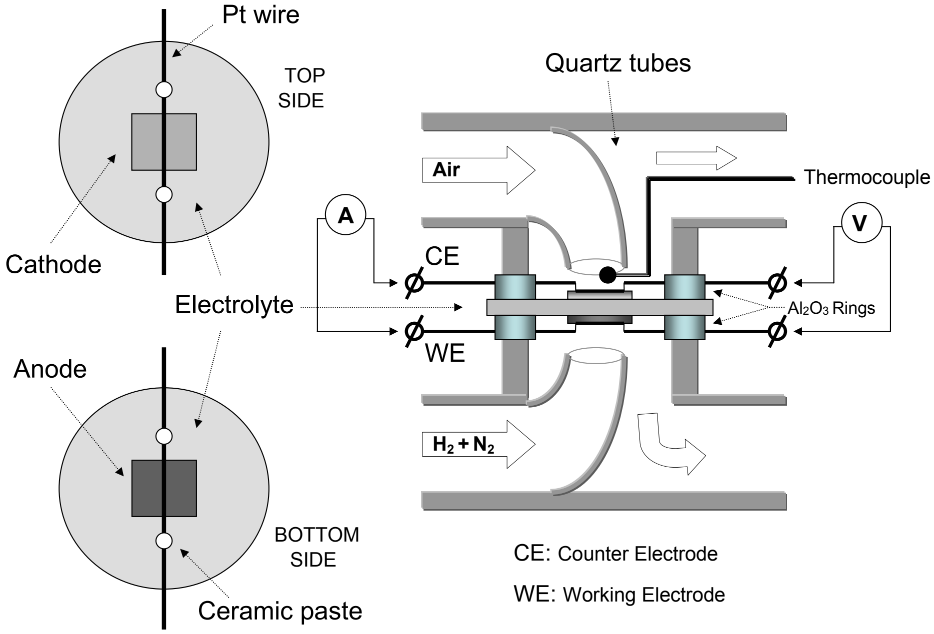

Figure 5.1. Scheme of the Setup for fuel cell tests.

Two-electrode configuration was used to obtain I-V plots, total overpotential and electrode ohmic loss. The fuel cell performance was recorded by cyclic-voltammetry at a scan rate of 5 mVs^{-1} and the impedance of the electrochemical cell was acquired at open circuit voltage (OCV), with a frequency ranging between 0.1 Hz-1 MHz and 20 mV of ac amplitude, obtaining reproducible spectra.

5.3 Results and Discussion

5.3.1. BSCF and SDC characterisation

TG/DTA in air for BSCF and SDC precursors are shown in Figure 5.2. It can be observed that no mass loss occurs above 1073 K and 723 K for BSCF and SDC, respectively. According with these results, BSCF and SDC precursor gels were calcined. Final synthesis temperature was 1173 K in both cases. The thermal evolution of XRD patterns is shown in Figure 5.3, showing single phases at 1173 K and 723 K for BSCF and SDC respectively.

BSCF and SDC patterns were refined, using FullProff and WinPlotr programs [17, 18], in a symmetric cubic system with space groups Pm3m and Fm3m, and cell parameters a=3.9810(8) Å and 5.4289(5) Å, for BSCF and SDC respectively.

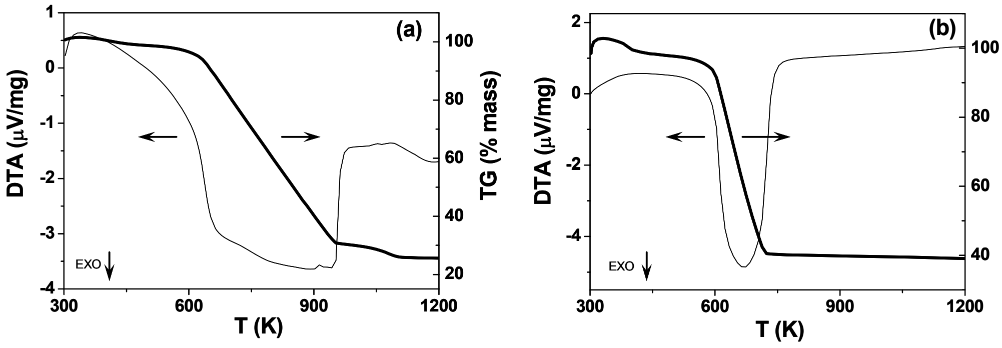

Figure 5.2. TG/DTA curves of the dried precursor obtained by sol-gel route for (a) BSCF and (b) SDC.

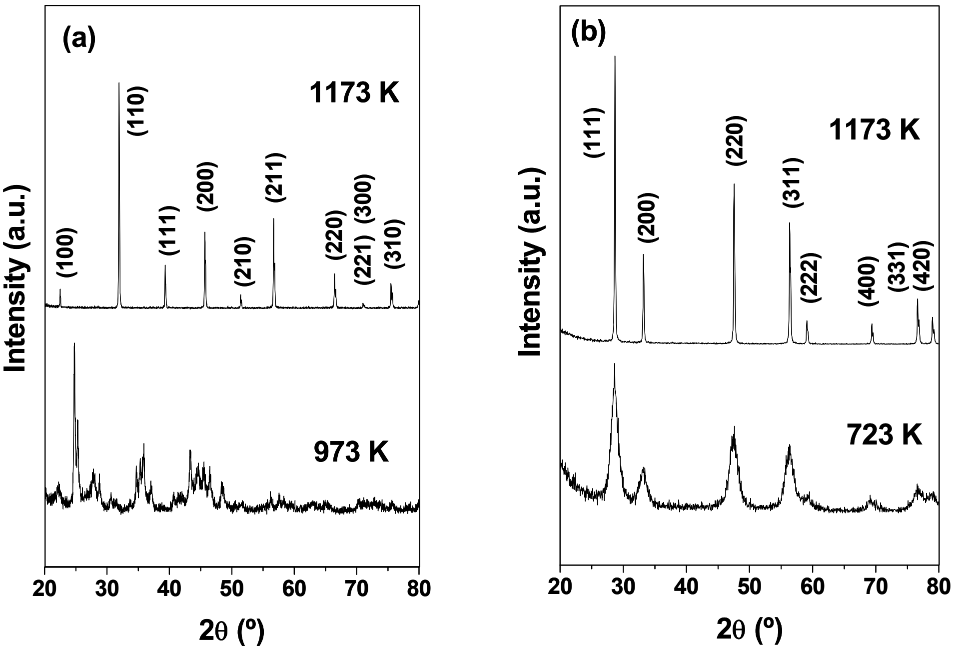

Figure 5.3. Thermal evolution of XRD patterns of (a) BSCF and (b) SDC obtained both by sol-gel route.

5.3.2. Chemical compatibility

XRD patterns at room temperature, 1173 K and 1473 K of the binary-mixed-systems LSGM/BSCF, LSGM/SDC and LSCM/SDC are shown in Figures 5.4, 5.5 and 5.6 respectively. LSGM/LSM and LSCM/LSGM compatibility were studied in a previous work [14] and certain reactivity was found between LSGM and LSM at temperature above 1173 K and between LSGM and LSCM at 1623 K, however only LSGM/LSCM interface showed by SEM a possible cross-diffusion of Cr, Mn or La [9,19]. For this reason, the use of the SDC material as buffer layer was studied. No additional diffraction peaks were found in the LSGM/SDC (Figure 5.5) and LSCM/SDC (Figure 5.6) systems between room temperature and 1173 K, neither in the BSCF/LSGM mixed system. Two small additional peaks, identified as La_2O_3, were observed in the LSGM/SDC system (Figure 5.5e) and one (unknown) in the LSCM/SDC system (Figure 5.6e) for the samples fired at 1473 K. The XRD pattern of the LSGM/BSCF system at 1473 K showed only peaks of a perovskite phase, indicating the total reaction between the LSGM and BSCF phases to a new one (Figure 5.4e). Therefore, it seems there are not any chemical incompatibility between the pairs LSGM/BSCF, LSCM/SDC and LSGM/SDC at intermediate temperature (873-1073 K). It indicates that SDC material can avoid the likely interfacial reaction between LSCM anode and LSGM electrolyte at this temperature. In fact, SEM images of the electrode-electrolyte interfaces after fuel cell testing (Figure 5.7) did not show any diffusion zone or any reaction. Furthermore, the three layers of the LSCM/SDC/LSGM system can be distinguished (Figure 5.7e). However, the BSCF electrode material could be affected and seriously react with the LSGM electrolyte above 1373 K. Thus, this value was the maximum temperature used for sintering the BSCF electrode on the LSGM electrolyte.

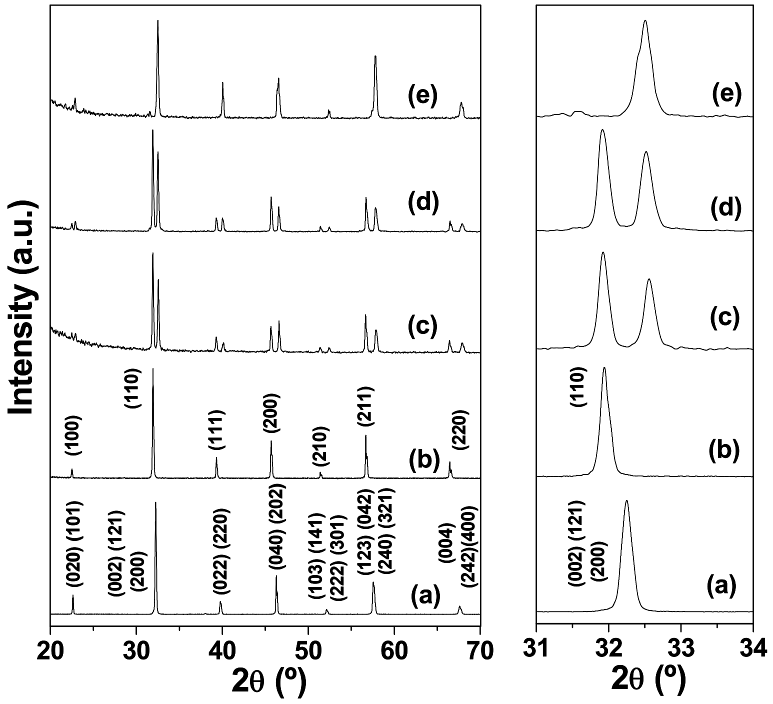

Figure 5.4. XRD patterns of (a) LSGM, (b) BSCF, (c) mixture of LSGM and BSCF at room temperature, (d) LSGM + BSCF at 1173 K and (e) LSGM + BSCF at 1473 K.

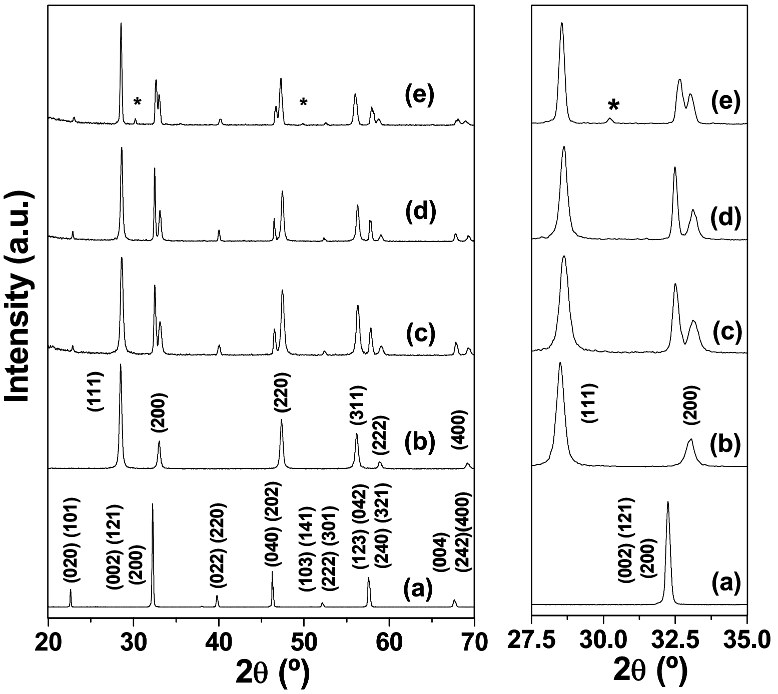

Figure 5.5. XRD patterns of (a) LSGM, (b) SDC, (c) mixture of LSGM and SDC at room temperature, (d) LSGM + SDC at 1173 K and (e) LSGM + SDC at 1473 K. Additional peaks identified as La_2O_3 (*).

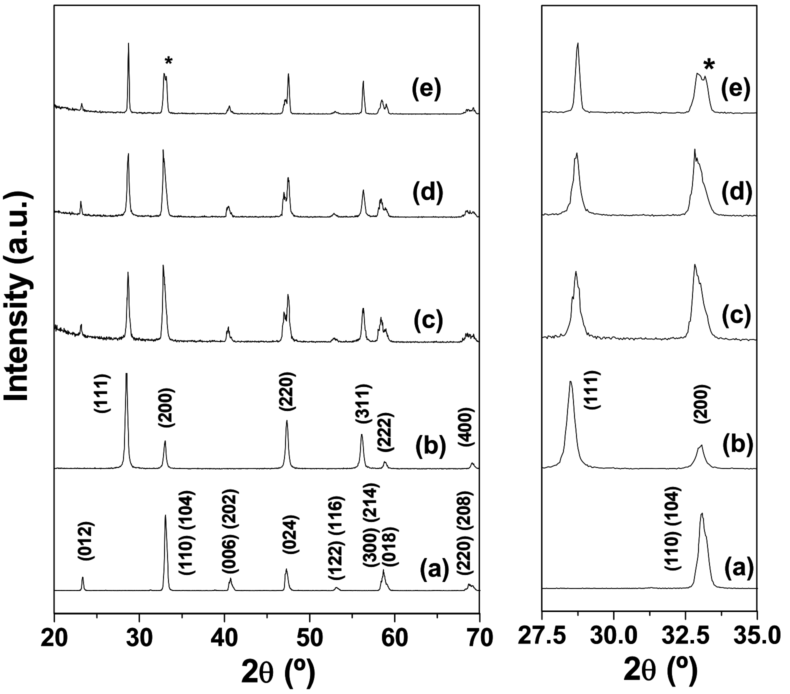

Figure 5.6. XRD patterns of (a) LSCM, (b) SDC, (c) mixture of LSCM and SDC at room temperature, (d) LSCM + SDC at 1173 K and (e) LSCM + SDC at 1473 K. Additional peak, no identified (*).

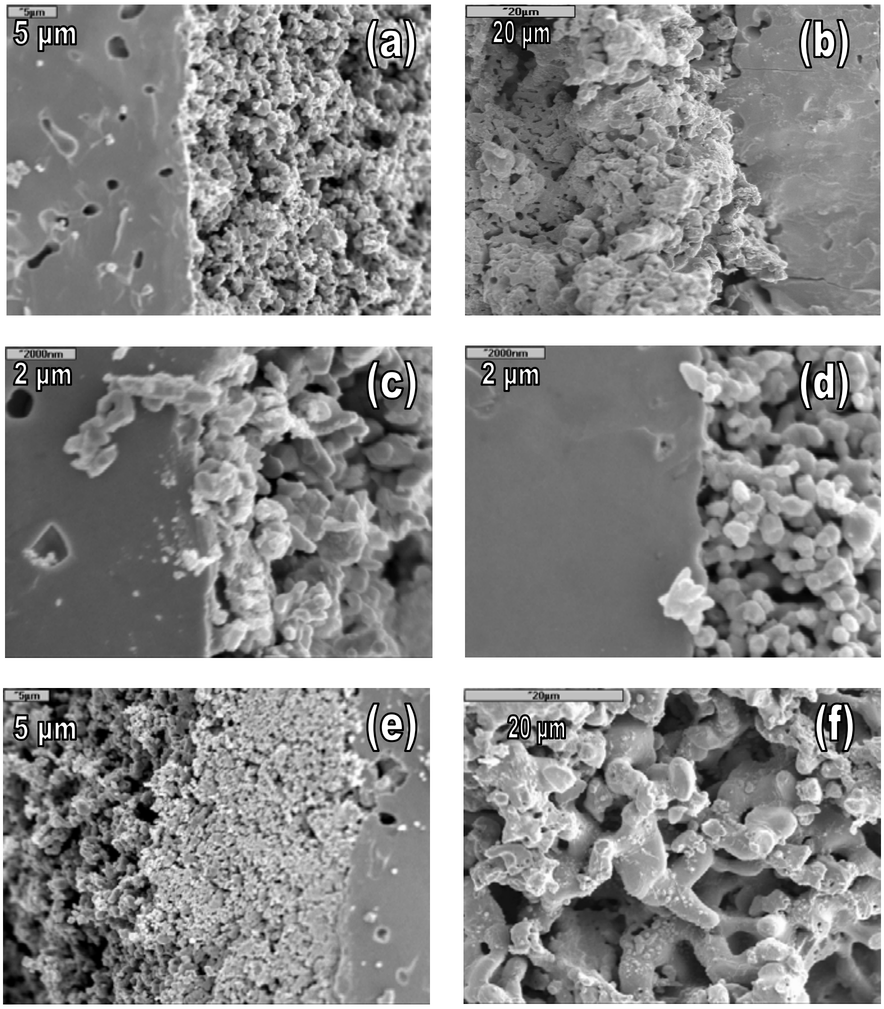

Figure 5.7. SEM images of the cells after testing. Cross sections of (a) LSGM/LSCM, (b) BSCF/LSGM, (c) LSGM/LSM-LSGM, (d) LSGM/LSM and (e) LSCM/SDC/LSGM interfaces. (f) SEM image of BSCF surface. (Temperature of sintering the electrode materials on LSGM electrolyte before fuel cell testing for 1 hour: BSCF/LSGM 1273 K; SDC/LSGM, LSM/LSGM and LSM-LSGM/LSGM 1473K; LSCM/LSGM and LSCM/SDC/LSGM 1573 K).

5.3.3. Electrochemical characterisation

5.3.3.1. Electrolyte and electrode resistances

The impedances of the cells were measured under asymmetric atmospheres at open circuit conditions. These impedance spectra (Figure 5.8) were fitted with equivalent circuits [20]. Three serial (RC) elements and a series resistance were used as equivalent circuit to fit the impedance data, except for LSM/LSGM/LSCM and BSCF/LSGM/LSCM system at 1073 K where only two serial (RC) elements and a series resistance were used, i.e. the electrolyte contribution (the series resistance) and the cathode and anode contribution (two serial (RC) circuits). Electrolyte resistances were approximately the same for LSM/LSGM/SDC/LSCM, LSM/LSGM/LSCM and BSCF/LSGM/LSCM systems, see Table 5.1.

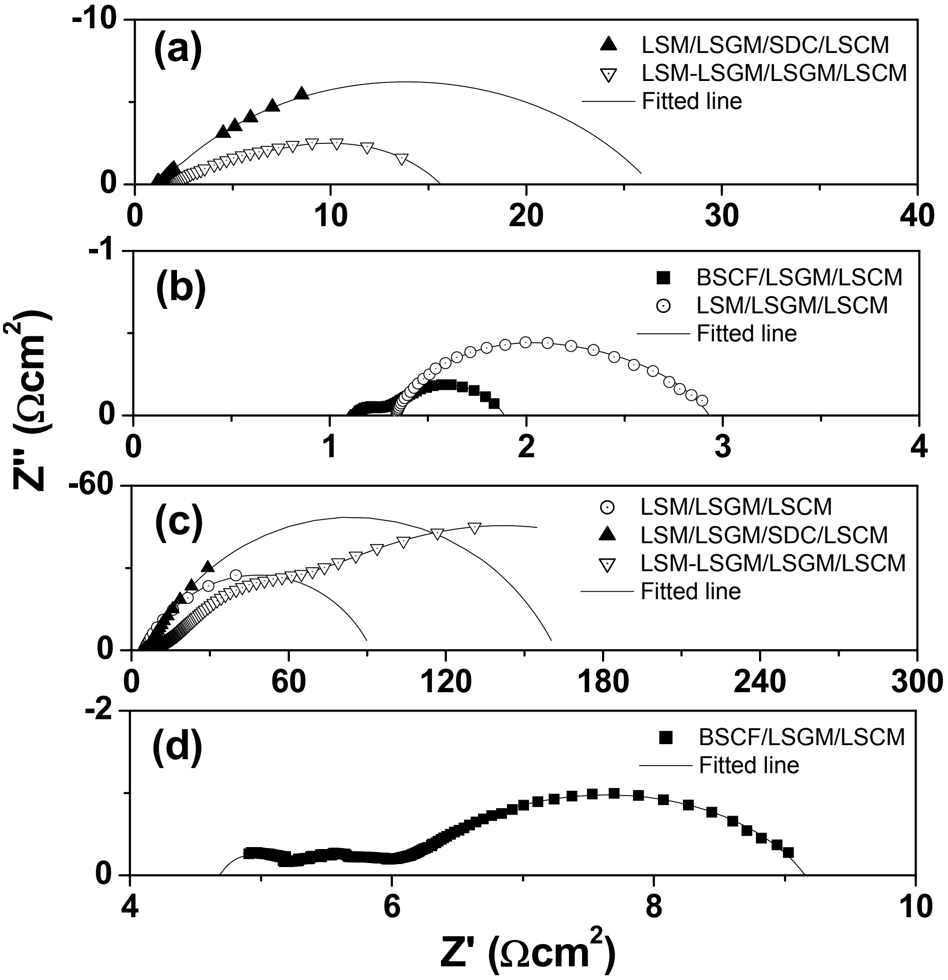

Figure 5.8. Impedance spectra of the different cells at 1073 K (a,b) and 873 K (c,d). The solid line is the fitted result obtained with equivalent circuits.

Table 5.1
Series (R_s) and polarization (R_p) resistances of the different cells at 873 and 1073 K.

Fuel cell system	1073 K		873 K	
	R_S (Ωcm)	R_P (Ωcm^2)	R_S (Ωcm)	R_P (Ωcm^2)
BSCF/LSGM/LSCM	7.53	0.75	31.33	4.47
LSM/LSGM/LSCM	8.93	1.64	32.66	86.85
LSM-LSGM/LSGM/LSCM	14.13	13.73	53.20	248.29
LSM/LSGM/SDC/LSCM	8.40	25.15	39.13	156.27

The value of the electrolyte resistance (R_s) of LSM-LSGM/LSGM/LSCM is higher than those of the three systems studied at 873 and 1073 K, and it was probably due to the reaction between LSGM and LSM in the preparation of the composite via co-calcination. On the other hand, the highest polarisation resistance (R_p) at 1073 K corresponded to the LSM/LSGM/SDC/LSCM system and this could be consequence of the effect of the SDC buffer layer. The polarisation resistances were obtained with extrapolated data of the fitted impedance spectra. Nevertheless, the polarization resistances of the LSM/LSGM/LSCM, LSM-LSGM/LSGM/LSCM and LSM/LSGM/SDC/LSCM systems at 873 K are not enough reliable. Anyway, it is obvious than the lowest values were obtained for the BSCF/LSGM/LSCM cell, 7.53 Ωcm and 0.75 Ωcm^2 for R_s and R_p respectively at 1073 K. When the operational temperature was decreased to 873 K the R_s and R_p resistances increase to 31.33 Ωcm and 4.47 Ωcm^2 respectively.

5.3.3.2. Power density

The same configuration, two probe-method, was used to obtain I-V plots, using humidified mixture of pure H_2 in N_2 as fuel and air as oxidant. The highest maximum power density of 160 mWcm^{-2} at 1073 K was reached with the system BSCF/LSGM/LSCM and this represents about 20% more of the maximum power density of the system LSM/LSGM/LSCM at the same temperature. Furthermore, this difference is increased up to 43% at 873 K. The others systems, LSM/LSGM/SDC/LSCM and LSM-LSGM/LSGM/LSCM, did not to reach 50% of the value obtained with the corresponding BSCF/LSGM/LSCM configuration (Figure 5.9). I-V curves of LSM/LSGM/SDC/LSCM and LSM-LSGM/LSGM/LSCM cells showed a drastical drop of the cell voltage at low current density which became less pronounced at larger current. This strong drop of the potential could be related to a high activation polarization loss. The use of a SDC buffer layer do not help to improve the electrochemical performance of the LSGM based cell with LSCM as anode material. In fact, the maximum power density of the LSM/LSGM/LSCM system is about 50 and 60% at 1073 and 873 K, respectively, higher than the buffered system LSM/LSGM/SDC/LSCM. This result does not follow the trend proposed by Tao and Irvine [13] using $Ce_{0.8}Gd_{0.2}O_{2-\delta}$ (GDC) buffer layer between YSZ/LSCM systems. They found that the anode polarization resistance could be further decreased if a thin layer of GDC was deposited between YSZ electrolyte and LSCM anode and they suggest the combination of LSCM and GDC as anode material. On the other hand, Huang and Goodenough [11] used a thin buffer layer of SDC (~10 μm) placed between an anode NiO-composite and a LSGM electrolyte to avoid the reaction between Ni and LSGM electrolyte to form a lanthanum-nickel oxide. Furthermore, the reducing atmosphere at the anode creates a mixed Ce^{4+}/Ce^{3+} increasing the electronic conductivity. It helps the oxidation of the fuel and the ionic transport across this layer. Goodenough and coworkers [21] also reported the use of a thin film of $La_{0.4}Ce_{0.6}O_{2-\delta}$ (LDC) as a buffer between LSGM electrolyte and NiO-LDC anode composite and they concluded that the LDC buffer layer successfully prevented formation of undesired phases. In our case, more studies of the effect of SDC layer between LSGM and LSCM materials are now under investigation in order to clarify its influence in the electrochemical performance of the LSGM based cells.

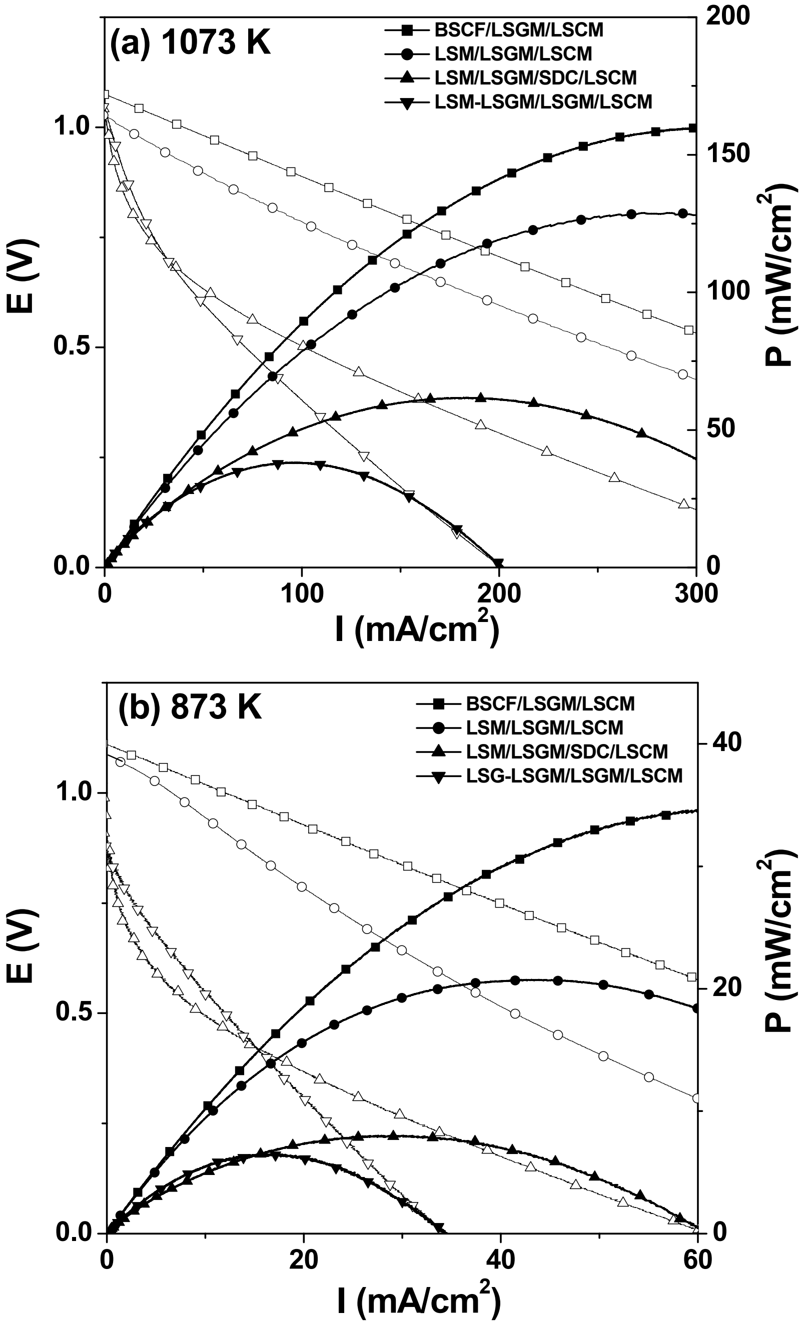

Figure 5.9. Current-voltage characteristics at (a) 1073 K and (b) 873 K.

5.3.3.3. Electrode overpotentials

Figure 5.10 compares the overall electrode overpotentials in a single-cell configuration at 873 and 1073 K. The lowest value of overpotential corresponded to the BSCF/LSGM/LSCM system. For example, the overpotential of this system at 300 $mAcm^{-2}$ and 1073 K is 2.6 times lower than the value of LSM/LSGM/SDC/LSCM system and 1.45 times lower than the value of LSM/LSGM/LSCM. The shape of the overpotential-current density curve in BSCF-cell was practically linear in the current-density range studied, with a slope of 0.6 Vcm^2A^{-1}.

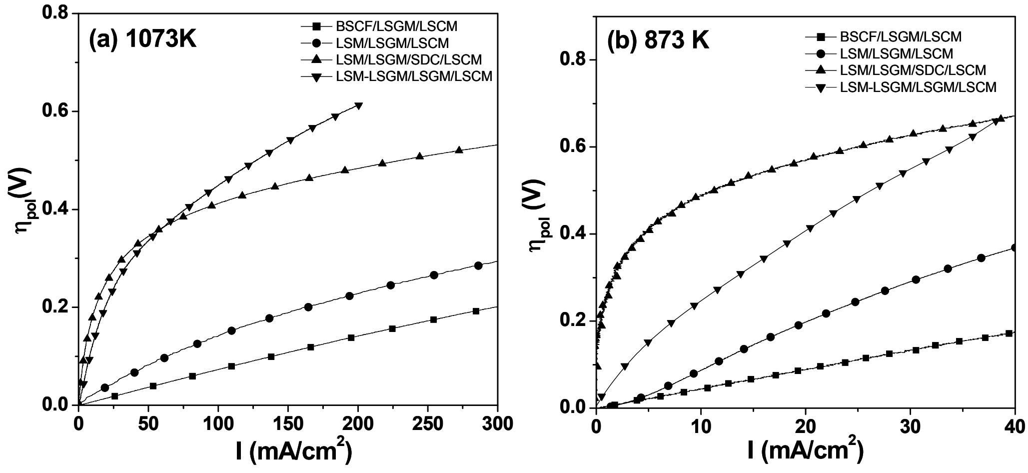

Figure 5.10. Electrode overpotentials of the different cells at (a) 1073 K and (b) 873 K.

However, the others systems showed a non linear trace. LSM-LSGM/LSGM/LSCM and LSM/LSGM/SDC/LSCM also had high overpotential even at lower values of current density. The lowest value of overpotential obtained for the BSCF/LSGM/LSCM system compared with LSM/LSGM/LSCM system could be attributed to the low activation overpotential of cobaltite-based cathodes. In this sense, Huang et al. [9] found similar results comparing $SrCo_{0.8}Fe_{0.2}$ (SCF) with $La_{0.85}Sr_{0.15}MnO_3$ as cathode materials and both on doped $LaGaO_3$ (LGO) electrolytes, explaining this behavior in terms of a high oxygen flux of the cobalt-containing perovskite [22]. The LSM-LSGM composite was used as cathode material instead of LSM in order to reduce the cathodic overpotential. Yi and Choi found a lower cathodic overpotential using this kind of composite than using only LSM, both on LGO-based electrolyte [23]. It was reported that it is more important to reduce the cathodic overpotential and the reaction between electrode and electrolyte than the control of the microstructure. In our case, it should be noted that the electrode overpotential of LSGM-LSM/LSGM/LSCM is higher than for LSM/LSGM/LSCM at 873 and 1073 K (Figure 5.10a and 5.10b). In this study a large difference between the LSM/LSGM (Figure 5.7d) and LSM-LSGM/LSGM interface (Figure 5.7c) was observed.

The microstructure of LSM appears to be more porous than the LSM-LSGM. This corresponds to the better performance of the LSM/LSGM/LSCM than LSM-LSGM/LSGM/LSCM in the current-voltage characteristics at 873 K and 1073 K, see Figure 5.9a and 5.9b. In addition, the shape of the voltage-current curve at low values of current density of LSM-LSGM/LSGM/LSCM system compared with LSM/LSGM/LSCM indicates a high activation polarisation loss possibly due to the higher activation energy for the oxygen reduction. Definitively, the obtained power density of the LSM-LSGM/LSGM/LSCM cell at 873 and 1073 K (Figure 5.9a and 5.9b), suggested that the use of LSM-LSGM composite prepared by co-calcination instead of LSM as cathode with LSGM as electrolyte and LSCM as anode is not a possibly solution to increase the obtained electrochemical performance of the LSM/LSGM/LSCM system at low temperature (873 K) [14].

Comparing the use of different alternative cathodes, BSCF system showed the best overpotential, resistance and power density. For this reason, it seems advisable to study in depth in a future work the system BSCF/LSGM/LSCM with thin electrolyte layer. In addition, it can be seen in Figure 5.7b and 5.7d a large difference in the microstructure and morphology of BSCF and LSM. LSM material possesses a better structure than BSCF, but worse overpotential. Thus, according to Yi and Choi, it is probably more important in LSGM-electrolyte-based cells to reduce electrode overpotential than to control the electrode microstructure to increase the electrochemical performance at intermediate temperatures.

5.4. Conclusions

Current-potential, current power-density, electrode and electrolyte resistances and overpotential of the LSM-LSGM/LSGM/LSCM, LSM/LSGM/SDC/LSCM, LSM/LSGM/LSCM and BSCF/LSGM/LSCM cells were investigated in this study at 1073 K and 873 K, using moistened hydrogen-nitrogen mixtures as fuels and air as oxidant. The lowest electrode overpotential, highest power-density and lowest polarisation resistance values were obtained for BSCF/LSGM/LSCM system, i.e. 160 mWcm^{-2} at 1073 K with 1.5 mm thickness electrolyte, R_s= 7.53 Ωcm and R_p= 0.75 Ωcm^2. The use of a SDC buffer layer between LSGM electrolyte and LSCM anode material do not help to improve the electrochemical performance of the LSM/LSGM/LSCM cell, neither using a LSM-LSGM composite prepared via co-calcination instead of LSM cathode material.

5.5 Acknowledgements

The authors acknowledge financial support from Spanish Research Program (MAT-2001-3334 and MAT-2004-03856) and Canary Islands Government (COFI 2002-027, PhD and ETH sojourn grants).

5.6. References

[1] T. Ishihara, H. Matsuda, Y. Takita, *J. Am. Chem. Soc.* **116** (1994) 3801-3803.
[2] K. Huang, S.R. Tichy, J.B. Goodenough, *J. Am. Chem. Soc.* **81** (1998) 2565-2575.
[3] T. Ishihara, H. Matsuda, M. Azni, Y. Takita, *Solid State Ion.* **86-88** (1996) 197-201.
[4] P.R. Slater, J.T.S. Irvine, T. Ishihara, Y. Takita, *J. Solid State Chem.* **139** (1998) 135-143.
[5] J.H. Kim, H.I. Yoo, *Solid State Ion.* **140** (2001) 105-113.
[6] O. Yamamoto, *Electrochim. Acta* **45** (2000) 2423-2435.
[7] A. Matraszek, L. Singheiser, D. Kobertz, K. Hilpert, M. Miller, O. Schulz, M. Martin, *Solid State Ion.* **166** (2004) 343-350.
[8] M. Guillodo, P. Vernoux, J. Fouletier, *Solid State Ion.* **127** (2000) 99-107.
[9] K. Huang, J. Wan, J.B. Goodenough, *J. Electrochem. Soc.* **148** (2001) A788-A794.
[10] K. Huang, M. Feng, J.B. Goodenough, C. Milliken, *J. Electrochem. Soc.* **144** (1997) 3620-3624.
[11] K. Huang, J.B. Goodenough, *J. Alloy. Compd..* **303-304** (2000) 454-464.
[12] S.Tao, J.T.S. Irvine, *Nat. Mater.* **2** (2003) 320-323.
[13] S. Tao, J.T.S. Irvine, *J. Electrochem. Soc.* **151** (2004) A252-A259.
[14] J. Peña-Martínez, D. Marrero-López, J.C. Ruiz-Morales, C. Savaniu, P. Núñez, J.T.S. Irvine, *Chem. Mater.* **18** (2006) 1001-1006.
[15] J.Y. Yi, G.M. Choi, *J. European Ceram. Soc.* **24** (2004) 1359-1363.
[16] Z. Shao, S. M. Haile, *Nature* **431** (2004) 170-173.
[17] J. Rodríguez-Carvajal, FullProf Suite, Laboratoire Léon Brillouin, CEA-Saclay, France (2004).
[18] T. Roisnel, J. Rodríguez-Carvajal. WinPLOTR, Laboratoire Léon Brillouin-LCSI, France (2004).
[19] S. Tao, J.T.S. Irvine, J.A. Kilner, *Adv. Mater.* **17** (2005) 1734-1737.
[20] D. Johnson, Zview Program, version 2.8, Scribner Associates, Inc., Southern Pines, North Carolina, 1990 -2002.
[21] J.-H. Wan, J.-Q. Yan, J.B. Goodenough, *J. Electrochem. Soc.* **152** (2005) A1511-A1515.
[22] K. Huang, J.B. Goodenough, *J. Electrochem. Soc.* **148** (2001) E203-E214.
[23] J.Y. Yi, G.M. Choi, *Solid State Ion.* **175** (2004) 145-149.

Chapter 6

Performance of XSCoF (X=Ba, La and Sm) and LSCrX’ (X’=Mn, Fe and Al) perovskite-structure materials on LSGM electrolyte for IT-SOFC

Published in *Electrochimica Acta* 52 (2007) 2950-2958

J. Peña-Martínez, D. Marrero-López, D. Pérez-Coll, J.C. Ruiz-Morales, P. Núñez
Inorganic Chemistry Department, University of La Laguna, Tenerife, Spain.

Abstract

$X_{0.5}Sr_{0.5}Co_{0.8}Fe_{0.2}O_{3-\delta}$ (X=Ba, La and Sm) and $La_{0.75}Sr_{0.25}Cr_{0.5}X'_{0.5}O_{3-\delta}$ (X’=Mn, Fe and Al) mixed ionic-electronic conducting perovskite-based oxides have been tested as SOFC electrode materials on $La_{0.9}Sr_{0.1}Ga_{0.8}Mg_{0.2}O_{2.85}$ (LSGM) electrolytes under different atmospheres (air, oxygen, argon and dry and wet 5% H_2/Ar) and the area-specific resistance (ASR) were compared. $Ba_{0.5}Sr_{0.5}Co_{0.8}Fe_{0.2}O_{3-\delta}$ (BSCoF) possesses the lowest ASR values in air (0.04 Ωcm^2 at 1073 K) whilst $La_{0.75}Sr_{0.25}Cr_{0.5}Mn_{0.5}O_{3-\delta}$ (LSCrM) possesses the lowest ASR values in wet 5%H_2/Ar (0.28 Ωcm^2 at 1073 K). In addition, fuel cell tests were carried out using wet 5%H_2/Ar as fuel and air as oxidant. The maximum power density (~123 $mWcm^{-2}$) at 1073 K was reached with the electrolyte-supported system BSCoF/LSGM/LSCrM (~1.5 mm thickness). Furthermore, LSCrX’ materials were used simultaneously as cathode and anode in fuel cell tests and the symmetric system LSCrM/LSGM/LSCrM (~1.5 mm thickness) reached a maximum power density of ~54 $mWcm^{-2}$ at 1073 K.

Keywords

SOFC, symmetric fuel cells, MIEC, polarisation resistance, fuel cell tests, LSGM

6.1. Introduction

In the last few years, much attention has been directed to a more efficient use of our energy resources. Solid oxide fuel cell (SOFC) technology offers the possibility of converting energy with high efficiency in an environmentally friendly way. SOFC power based systems are ideal distributed power generation units: reliable, clean, quiet, pollution-free and fuel conserving [1]. However, some technological problems like the high temperature requirements (~1273 K) of the materials used for the different cell components must be solved to develop applications at low (773-873 K) and intermediate temperatures (873-1073 K) [2]. Ralph *et al.* [3] have studied potential cathode materials using yttria-stabilised zirconia (YSZ) and gadolinia doped ceria (CGO) electrolytes for intermediate and low temperature applications respectively. These authors found that ferrites and cobaltites showed the best performances in YSZ and CGO-based cells in terms of the chemical compatibility and the lower area-specific resistance (ASR).

Doped lanthanum gallate perovskites have been also considered as alternative electrolyte materials for intermediate temperature solid oxide fuel cells (IT-SOFC) [4]. Several high solid ionic conductors based on $LaGaO_3$, e.g. $La_{0.9}Sr_{0.1}Ga_{0.8}Mg_{0.2}O_{2.85}$ (LSGM) [5,6] and $La_{0.8}Sr_{0.2}Ga_{0.8}Mg_{0.115}Co_{0.085}O_{3-\delta}$ (LSGMCo) [7] have been found showing typical ionic conductivity of approximately 0.10 Scm^{-1} at 1073 K. LSGM is better ionic conductor than YSZ at intermediate temperatures (773 – 1073 K) and presents good chemical stability and negligible electronic conductivity over a wide range of oxygen partial pressures ($1\text{-}10^{-20}$ atm) [8]. The main drawbacks are the segregation of impurities during the synthesis e.g. $LaSrGa_3O_7$ and $LaSrGaO_4$ [9,10] and the reactivity with nickel [11], which is usually employed in the anode cermets. Consequently, Feng *et al.* [12] reported that the success of LSGM as electrolyte relies on the identification of the adequate anode material and on the processing methods. Yan *et al.* [13] reported that the addition of Fe_2O_3 to Ni cermets may increase the chemical compatibility between LSGM and NiO. However, Ni-free anodes such as $La_{0.75}Sr_{0.25}Cr_{0.5}Mn_{0.5}O_{3-\delta}$ (LSCrM) [14,15] have been successfully tested using doped lanthanum gallates as electrolytes [16-18]. The work recently reported by Huang *et al.* [19] confirms the viability of LSCrM under fuels with low sulphur contents, although they have suggested a new composition based on a double perovskite, i.e. $Sr_2MgMoO_{6-\delta}$ with stable performances and better tolerance to sulphur.

In our previous investigations, several cathode materials reported in the literature [11,20,21] have been evaluated in LSGM based systems using LSCrM as anode [18,22], i.e. LSM, LSM-LSGM composites and $Ba_{0.5}Sr_{0.5}Co_{0.8}Fe_{0.2}O_{3-\delta}$ (BSCoF). The best results were achieved using BSCoF cathodes, e.g. performances 20% higher than with LSM cathodes at 1073 K. The use of LSM-LSGM composites did not help to improve the results, rendering on the hand, large values of both series and polarisation resistances. Yan *et al.* [13] and Huang *et al.* [19] have recently reported high performance in LSGM based fuel cells using cobaltites, i.e. $Sm_{0.6}Sr_{0.4}CoO_{3-\delta}$ and $SrCo_{0.8}Fe_{0.2}O_{3-\delta}$ as cathode materials. Therefore, in the work presented herein we have investigated different cobalt-based perovskites as potential cathode materials, $X_{0.5}Sr_{0.5}Co_{0.8}Fe_{0.2}O_{3-\delta}$ (XSCoF) with X= Ba, La and Sm, and $Sm_{0.5}Sr_{0.5}CoO_{3-\delta}$ (SSCo). Additionally, different lanthanum chromites, $La_{0.75}Sr_{0.25}Cr_{0.5}X'_{0.5}O_{3-\delta}$ (LSCrX') with X'= Mn, Fe and Al, were also investigated as potential anode materials, following our previous results [18] and compared with standard Ni-cermets and SDC-LSCrM and SDC-LSGM composites. Moreover, Ruiz-Morales *et al.* [23] and Irvine and co-workers [24] have recently introduced an interesting new symmetric SOFC concept, where the anode and the cathode are constituted by the same electrode material. These authors have reported good performance results using LSCrM material as anode and cathode, and YSZ as electrolyte. Thus, the area-specific resistance (ASR) for BSCoF, $La_{0.5}Sr_{0.5}Co_{0.8}Fe_{0.2}O_{3-\delta}$ (LSCoF), $Sm_{0.5}Sr_{0.5}Co_{0.8}Fe_{0.2}O_{3-\delta}$ (SSCoF), $Sm_{0.5}Sr_{0.5}CoO_{3-\delta}$ (SSCo), LSCrM, $La_{0.75}Sr_{0.25}Cr_{0.5}Fe_{0.5}O_{3-\delta}$ (LSCrF) and $La_{0.75}Sr_{0.25}Cr_{0.5}Al_{0.5}O_{3-\delta}$ (LSCrA), NiO-$Sm_{0.15}Ce_{0.85}O_{2-\delta}$ (Ni-SDC), SDC-LSCrM and SDC-LSGM on LSGM electrolyte under symmetric atmospheres has been measured and analysed.

Finally, fuel cell tests of the systems BSCoF/LSGM/LSCrX' and the symmetric SOFCs using LSCrX' materials as cathode and anode i.e. LSCrX'/LSGM/LSCrX' were performed.

6.2. Experimental

6.2.1. Synthesis of electrodes and electrolytes

LSGM and LSCrM materials have been prepared by conventional solid state reaction, using powders of La_2O_3 (Aldrich, 99.99%), Ga_2O_3 (Aldrich, 99.99%), MgO (Aldrich, 99.999%), $SrCO_3$ (Aldrich, 99.9%), Mn_2O_3 (Aldrich 99%) and $Cr(NO_3)_3{\cdot}9H_2O$ (Aldrich, 99%). La_2O_3 was pre-dried for over 3 hours at 1273 K in order to achieve decarbonation and dehydration. LSCrM powders and LSGM dense pellets were prepared as described elsewhere [18]. The ceramic route was carried out by ball-milling stoichiometric quantities of the reagents with acetone. The resulting mixture was dried and fired in air up to 1173 K for 10 h and further ground. Dense LSGM samples (98-99% of theoretical density) were obtained by uniaxially pressing powders into a disk at 120 MPa, for 5 minutes (ø = 1.0 cm) and sintering at 1673 K for 6 h. LSCM powders were obtained after thermal treatment at 1673 K for 10 h.

Electrode materials, except LSCrM, were prepared via precursor routes i.e. sol-gel or freeze-drying method, using powders of $Ba(NO_3)_2$ (Aldrich, 99%), $Sr(NO_3)_2$ (Aldrich, 99+%), $La(NO_3)_3{\cdot}6H_2O$ (Aldrich, 99.999%), $Al(NO_3)_3{\cdot}6H_2O$ (Aldrich, 98%), $Co(NO_3)_2{\cdot}6H_2O$ (Aldrich, 98%), $Fe(NO_3)_3{\cdot}9H_2O$ (Aldrich, 98+%), $Sm(NO_3)_3{\cdot}6H_2O$ (Aldrich, 99.9%), $Cr(NO_3)_3{\cdot}9H_2O$ (Aldrich, 99%), and $Ce(NO_3)_3{\cdot}6H_2O$ (Aldrich, 99.99%). The sol-gel route was carried out using citric acid as complexing agent. Stoichiometric cation solutions of the corresponding nitrates were prepared with distilled water. Afterwards, the citric acid solution, 1.5 % wt. in excess and in a ratio ligand/metal L/M=1 and L/M=2/3 for trivalent and divalent cations respectively, was also added. The pH was adjusted up to 9 with addition of ammonia solution (20% v/v). A gel was formed with continuous stirring and mild heating (~338 K). The gel was dried at room temperature for over 8 h and then fired at 573 K for 30 min. The resulting powders were ground in an agate mortar and fired in air at 973 K during 5 h, ground again and finally fired at 1173-1673 K for 5 h in air (Table 6.1).

BSCoF, SSCoF and LSCoF materials were prepared using etilendiaminthetraacetic acid (EDTA) as complexing agent in addition to the citric acid to avoid the formation of $SrCoO_2$ [20]. An ammonium solution of EDTA, 1.5 % wt. excess, with L/M=1 ratio was added before the citric acid solution.

SSCo was synthesised by freeze-drying method [25]. In this method, a stoichiometric solution of metal cations was prepared from metal nitrates in distilled water. An ammonium-EDTA solution was added in a molar ratio L/M=0.5 to the cation solution and the pH was adjusted up to 7 with nitric acid addition. The resulting mixed solution was dropped and flash-frozen into liquid nitrogen under vigorous stirring to avoid the agglomeration of the ice crystal. The ice crystals were freeze-dried at a pressure of 1-10 Pa in a Heto Lyolab freeze-dryer during two days. The obtained amorphous precursor powders were calcined at 573 K for 1 hour, grounded and finally fired at 1273 K for 5 hours.

SDC-LSCrM, SDC-LSGM and Ni-SDC composites, 25% wt. of SDC, were prepared by ceramic method, via ball milling, using SDC, LSCrM, LSGM and NiO (Aldrich, 99%) powders. NiO weighing was adjusted to finally obtain 75% wt. of Ni.

6.2.2. Materials characterisation

X-ray diffraction (XRD) patterns were collected with a Philips X´Pert Pro diffractometer with a primary monochromator (Cu $K_{\alpha 1}$ radiation) and an X'Celerator detector to characterise the structure of the specimens. The scans were performed in the 2θ range 20-90º (step 0.016º and 500 s/step).

Further XRD studies were also carried out to investigate the chemical compatibility of LSGM with LSCrF, LSCrA and Ni-SDC materials. Powder mixtures of LSGM with LSCrF, LSGM with LSCrA and LSGM with Ni-SDC, in a relation 1:1 (% wt.), were ground in an agate mortar and fired at 1173 K, 1473 K and 1773 K for 10 h.

Thermogravimetric analysis (TG/DTA) studies were carried out with a Perkin Elmer Instrument (Pyris Diamond series), in static air at heating/cooling rate of 10 $Kmin^{-1}$, to determine the stoichiometry of the nitrates used in the synthesis and to estimate the optimal crystallisation temperature of the precursor powders obtained by sol-gel route and freeze-drying method.

BET surface areas of the polycrystalline powders were determined using a surface area analyser (Gemini^{TM} 2365, Micromeritics Instrument) with nitrogen as adsorptive and the BET surface area was rather low, between 1.0 and 4.5 m^2g^{-1} (Table 6.1), for all the studied samples.

Table 6.1.
Synthesised compositions indicating final temperature, BET surface and lattice parameters calculated by Rietveld method refinement from their XRD-patterns.

Composition	Label	Synthesis method	Synthesis Temp. (K)	BET ($m^2 g^{-1}$)	Space group	Lattice parameter (Å)
$La_{0.9}Sr_{0.1}Ga_{0.8}Mg_{0.2}O_{2.85}$	LSGM	Ceramic	1723	0.92	Ibmm	a=5.5216(6) b=7.8262(9) c=5.5413(5)
$Ba_{0.5}Sr_{0.5}Co_{0.8}Fe_{0.2}O_{3-\delta}$	BSCoF	Sol-gel	1173	3.50	Pm-3m	a=3.9832(5)
$La_{0.5}Sr_{0.5}Co_{0.8}Fe_{0.2}O_{3-\delta}$	LSCoF	Sol-gel	1273	2.92	Pm-3m	a=3.8384(5)
$Sm_{0.5}Sr_{0.5}Co_{0.8}Fe_{0.2}O_{3-\delta}$	SSCoF	Sol-gel	1273	1.48	Pm-3m	a=3.8126(1)
$Sm_{0.5}Sr_{0.5}CoO_{3-\delta}$	SSCo	Freeze-dried	1273	2.00	Pnma	a=5.4009(1) b=7.5861(2) c=5.3645(1)
$La_{0.75}Sr_{0.25}Cr_{0.5}Mn_{0.5}O_{3-\delta}$	LSCrM	Ceramic	1673	1.32	R -3c	a=5.4924(7) c=13.315(1)
$La_{0.75}Sr_{0.25}Cr_{0..5}Fe_{0.5}O_{3-\delta}$	LSCrF	Sol-gel	1473	4.11	Pnma	a=5.4995(9) b=7.7764(1) c=5.5347(8)
$La_{0.75}Sr_{0.25}Cr_{0..5}Al_{0.5}O_{3-\delta}$	LSCrA	Sol-gel	1673	1.86	Pbnm	a=5.3972(2) b=5.4167(1) c=7.6406(2)
$Sm_{0.15}Ce_{0.85}O_{2-\delta}$	SDC	Sol-gel	1173	11.12	Fm3m	a=5.4289(5)

6.2.3. Electrochemical characterisation

6.2.3.1. Area-specific resistance (ASR) measurements

Polarisation impedance measurements were carried out on a 2-electrode arrangement using ~7.5 mm diameter and ~1.5 mm thick LSGM dense pellets as electrolyte. A slurry of the electrode powders was prepared using Decoflux^{TM} as binder and a thin layer of the slurry was coated onto both surfaces of the electrolyte and then fired at 1373–1623 K for 2 hours in air: BSCoF 1373 K, LSCrM 1623 K, LSCrF 1623 K, LSCrA 1473 K and Ni-SDC 1473 K. The thickness of the electrode layer after firing was in every case ~30-40 μm. The porosity and the microstructure of the deposited electrodes were studied by scanning electron microscopy (SEM) (JEOL JSM-6300) revealing an average porosity of ~30%. Current collector was formed by coating platinum paste on both sides of the pellets and then fired at 1173 K for 1 hour in air. The impedance spectra of the electrochemical cell was measured under symmetric atmosphere (air, oxygen, argon, dry and wet 5%H_2/95%Ar) using a frequency response analyser (Solartron 1260) in the frequency range from 0.1 Hz to 1 MHz and with an excitation voltage of 100 mV.

6.2.3.2. Fuel cell tests

Fuel cell tests of the LSGM-electrolyte supported systems using BSCoF as cathode and LSCrM, LSCrF, LSCrA and Ni-SDC as anode materials were carried out in addition to some other symmetric configurations such as LSCrM/LSGM/LSCrM, LSCrF/LSGM/LSCrF and LSCrA/LSGM/LSCrA using 1.5 mm thick LSGM pellets. A two-electrode setup, as described elsewhere [18], was used to obtain the I-V plots using wet 5% H_2/Ar as fuel and air as oxidant. The electrode materials were deposited on both sides (surface of 0.81 cm^2) of the LSGM pellets and fired at 1373–1623 K for 2 h in air to ensure adherence. Electrode-electrolyte interfaces after the tests were observed by SEM. The current-voltage characteristics of the fuel cell were recorded by cyclic-voltammetry at a 5 mVs^{-1} scan rate using a Zahner IM6 unit. The electrochemical tests were performed after reducing for several hours the anode materials in 5% H_2 at 1073 K. Impedance spectra of the electrochemical cell under asymmetric atmospheres were also acquired at open circuit voltage (OCV) in the frequency range of 0.1 Hz to 1 MHz and with an AC perturbation of 20 mV.

6.3. Results and Discussion

6.3.1. Structural characterisation

Structural characterisation by XRD confirmed that all the prepared materials are single phase after their synthesis at the temperatures given in Table 6.1. The XRD patterns were refined using FullProf and WinPlotr programs [26,27] and the cell parameters obtained by Rietveld method and the corresponding space groups (s.g.) are presented in Table 6.1.

6.3.2. Chemical compatibility study

XRD patterns at room temperature, 1173 K, 1473 K and 1773 K of the binary-mixed-systems LSGM/LSCrF, LSGM/LSCrA and LSGM/Ni-SDC are shown in Figures 6.1-6.3. No additional diffraction peaks were found after firing mixtures of LSGM with LSCrM, BSCoF, LSCrF, LSCrA and Ni-SDC (Figures 6.1-6.3), between room temperature and 1173 K indicating a priori a good chemical compatibility at intermediate temperature (873-1073 K). Nevertheless, LSGM strongly reacts with LSCrF above 1173 K, forming a new perovskite as can be observed in Figure 6.4 where the cell volume of both phases is shown as a function of the firing temperature. In the case of the LSGM/LSCrA and LSGM/Ni-SDC systems, a strong reaction above 1473 K is also observed, Figure 6.2 and 6.3. The new phases after firing at 1473 K were identified as $LaSrGa_3O_7$, $LaGaO_3$, Sm_2O_3, La_2NiO_4, $MgNiO_2$ and $MgGa_2O_4$ for LSGM/Ni-SDC system and $LaCrO_3$, $LaGaO_3$ and $SrCrO_4$ for LSGM/LSCrA system.

LSGM/LSCrM and LSGM/BSCoF compatibility was studied in a previous work [18,22] and BSCoF and LSCrM materials react with LSGM above 1373 K and 1623 K, respectively. The high reactivity of these materials with LSGM could influence negatively in the performances of the LSGM based cells due to the need of high temperatures of fixing necessary to obtain an adequate adherence between the electrodes and the electrolyte.

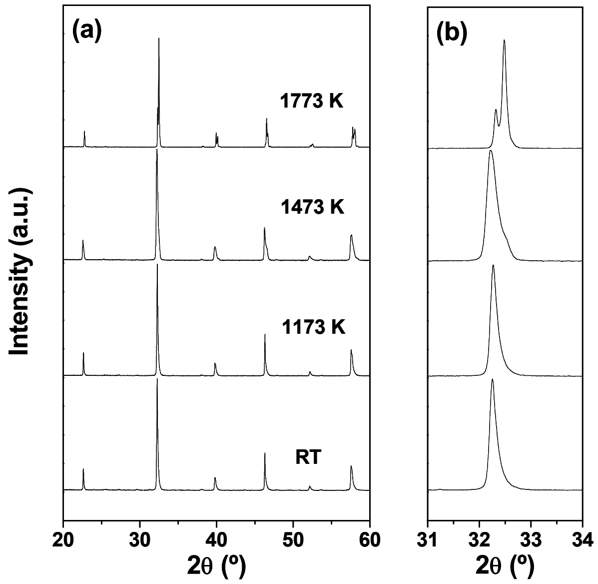

Figure 6.1. XRD patterns of the system LSGM/LSCrF at room temperature (RT), 1173 K, 1473 K and 1773 K (a) and magnification in the 2θ range 31-34° (b).

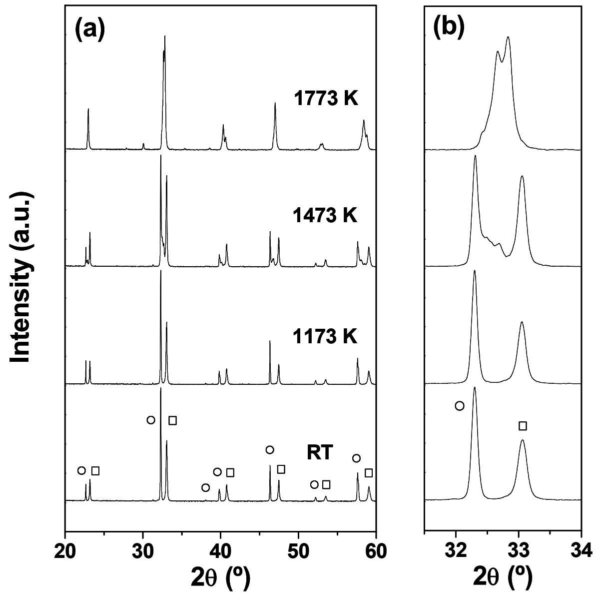

Figure 6.2. XRD patterns of the system LSGM/LSCrA at room temperature (RT), 1173 K, 1473 K and 1773 K (a) and magnification in the 2θ range 31-34° (b). Open circles and squares symbols in the pattern at RT correspond to LSGM and LSCrA phases respectively.

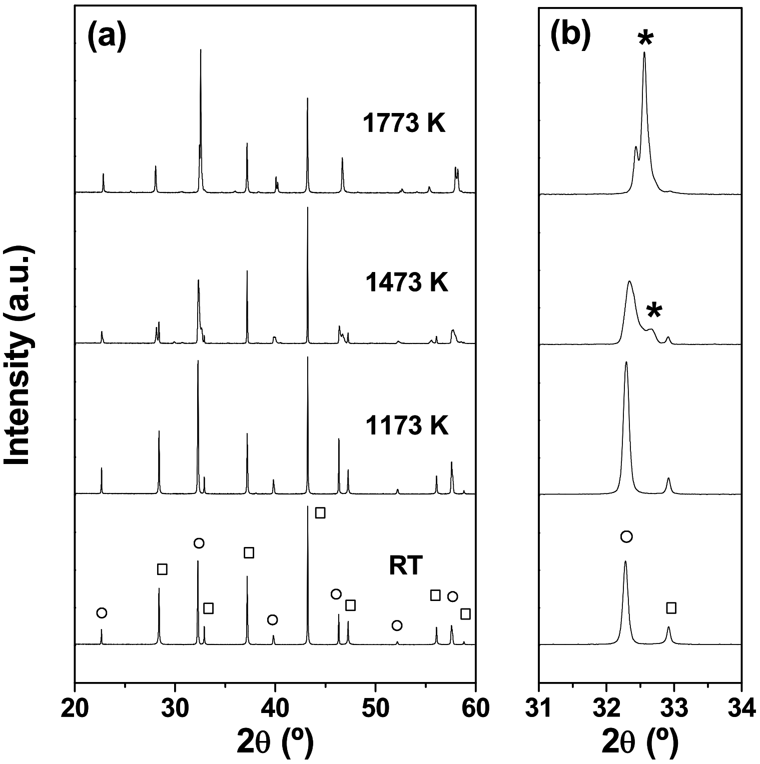

Figure 6.3. XRD patterns of the system LSGM/Ni-SDC at room temperature (RT), 1173 K, 1473 K and 1773 K (a) and magnification in the 2θ range 31-34° (b). Open circles and squares symbols in the pattern at RT correspond to LSGM and Ni-SDC phases respectively.

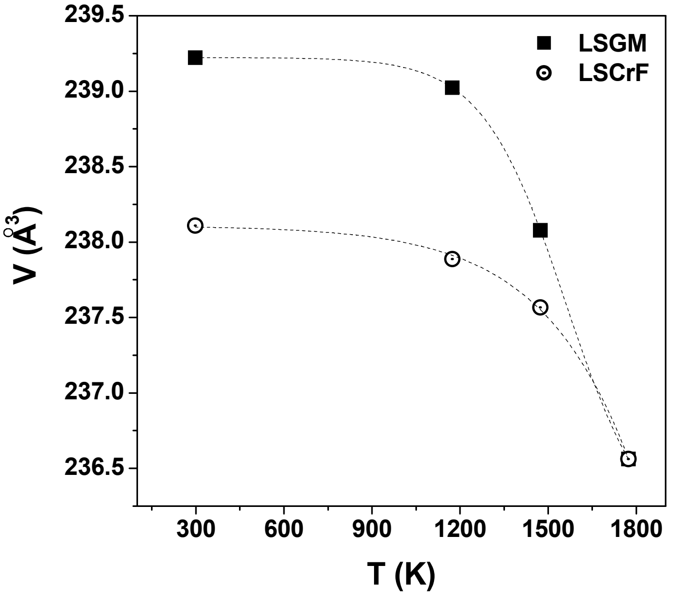

Figure 6.4. Variation of the cell volume of LSGM and LSCrF phases *vs.* temperature.

6.3.3. Electrochemical characterisation

6.3.3.1 Area-specific resistance (ASR)

The polarisation resistances, measured in symmetric cell configuration, provided further information regarding the viability of the electrode-electrolyte system. McIntosh *et al.* [28] have also reported that symmetric cell measurements are only quantitative when electrodes have a linear voltage-current (V-I) dependence and non hysteretic behaviour, and therefore the relation between the cell performance and the polarisation resistance value is not straightforward. These authors found that the data obtained in symmetrical configurations were not reproducible with a large difference of values. However it is very likely that the source of such difference in the ASRs is due to the symmetrical setup rather than to the materials themselves. For instance, the use of the same setup to test whether one material performs better than another under the same experimental conditions could be considered as a valid procedure to carry out preliminary studies on electrode materials. A three-electrode arrangement is desirable to achieve full characterisation, although several groups have found that the measurement of electrode overpotentials using a reference electrode is difficult, and it should be used with a precise defined geometry [29]. In our case, the values of the polarisation resistance, matched nicely with the V-I data from the fuel cell tests (two-electrode configuration) despite of the indicated limitations of symmetric cell measurements and they were useful parameters for the electrochemical characterisation of these materials.

6.3.3.1.1 ASR of XSCoF (X=Ba, La and Sm) and SSCo

ASR values of XSCoF (X=Ba, La and Sm) and SSCo on LSGM electrolyte in air, oxygen and argon are presented in Figures 6.5a and 6.5b. The lowest ASR values in air and oxygen (Figure 6.5a) correspond to BSCoF, typically less than 0.1 Ωcm^2 at temperatures above 1025 K. If we assume an acceptable polarisation resistance of 0.3 Ωcm^2, we can reduce the operation temperature to 950 K, using air or oxygen as oxidant gas. For the other electrode materials studied, it is necessary a temperature operation above 1125 K to get a value nearly of 0.1 Ωcm^2.

A study of the variation of ASR (in air) and the series resistance (R_s) as a function of the operation time for BSCoF on LSGM was carried out. The ASR and the series resistance variation was about 0.013 Ωcm^2 and 0.1 Ωcm (~1.5 mm thick LSGM pellet) respectively, after 30 h of operation at 1073 K. This series resistance variation could influence negatively on the performance of thin film LSGM electrolyte based cells during long-term operation.

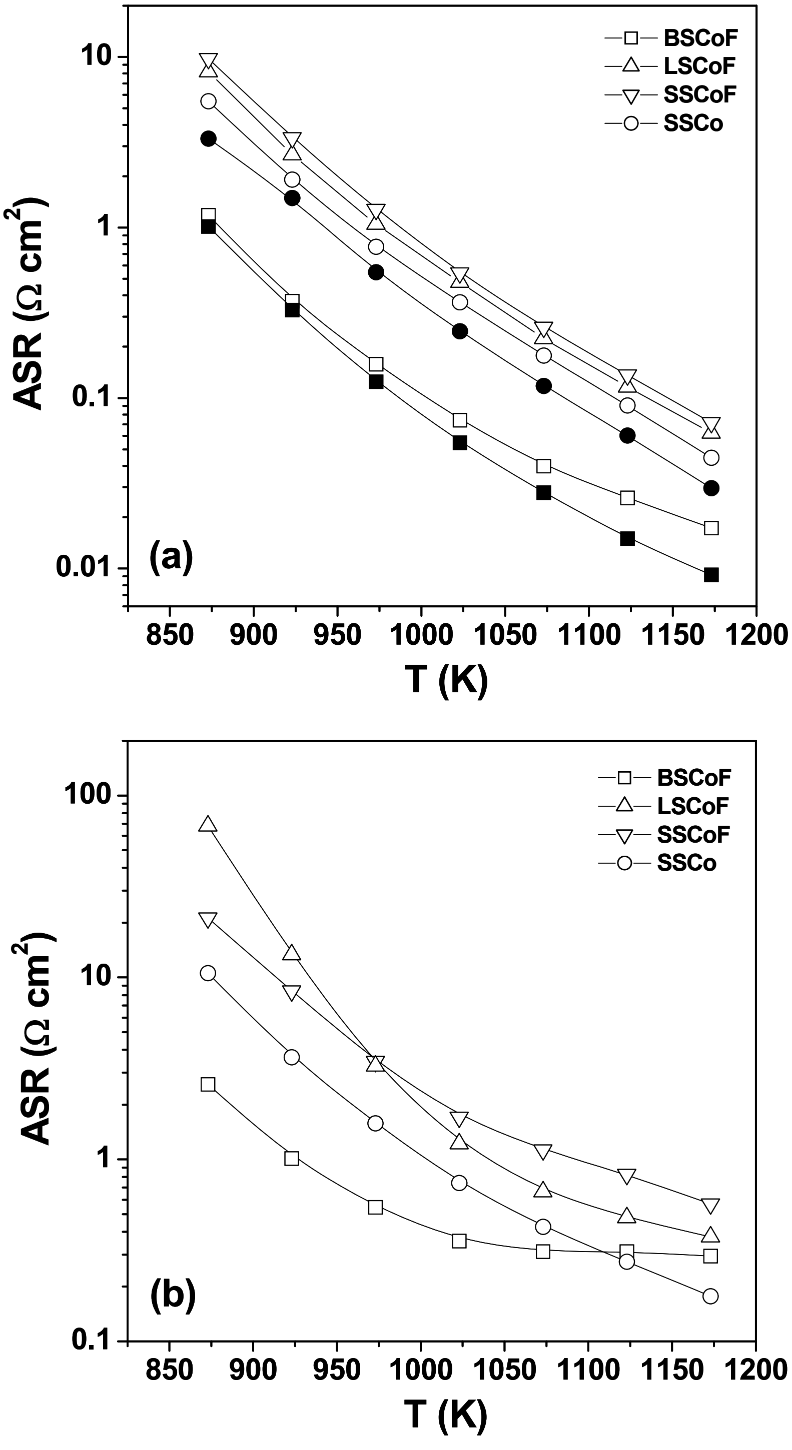

Figure 6.5. ASRs of BSCoF, LSCoF, SSCoF and SSCo on LSGM under different atmospheres: air (open symbols) and oxygen (closed symbols) (a); and argon (b).

6.3.3.1.2. ASR of LSCrX' (X'=Mn, Fe and Al)

The ASRs in air and wet and dry 5%H_2/Ar for LSCrX' (X'=Mn, Fe and Al) on LSGM, are represented in Figures 6.6a and 6.6b, respectively. The lowest values in reducing conditions are found for LSCrM, ~0.3 Ωcm^2 under wet 5%H_2/Ar at 1073 K. LSCrA presents similar ASR values in both wet and dry 5%H_2/Ar. Moreover, LSCrM and LSCrF have been reported as potential anode materials with LSGM, LSGMCo and YSZ electrolytes [14-18,30]. On the other hand, the ASR values of LSCrX' materials are higher under air atmosphere than under reducing conditions even in the case of LSCrM-LSGM composites as can be observed in Figure 6.6a. Only LSCrA presents an ASR value below 1 Ωcm^2 under air above 1098 K. The variation of the polarisation resistance (ASR) and the series resistance (R_s) for LSCrM on LSGM in wet 5%H_2/Ar are not significant, about 0.01 Ωcm^2 and 0.03 Ωcm respectively, after 10 h of operation at 1073 K. However, more studies are necessary to evaluate the variation of the ASR and R_s during long-term operation.

6.3.3.1.3. ASR of SDC composites

ASR values as a function of the temperature for Ni-SDC, SDC-LSCrM and SDC-LSGM composites on LSGM are represented in Figure 6.7. The ASR values of Ni-SDC and SDC-LSCrM under reducing conditions are quite similar, ~0.4 Ωcm^2 at 1073 K. One should notice that the values of ASR in wet 5%H_2/Ar of LSCrM (Figure 6.6b) are slightly lower than the values of SDC-LSCrM composite in the same temperature range ~0.3 Ωcm^2 at 1073 K.

6.3.3.2. Fuel cell tests

6.3.3.2.1. Power density

Voltage-current (V-I) and performance curves of LSGM based cells with BSCoF as cathode and LSCrX' (X'=Mn, Fe and Al) and Ni-SDC as anode materials, using air as oxidant and wet 5%H_2/Ar as fuel, are shown in Figure 6.8a. A power density of ~122 $mWcm^{-2}$ at 1073 K was reached with the BSCoF/LSGM/LSCrM system (1.5 mm thick pellet). An approximation of the theoretical power can be calculated [31] as

$$P = \frac{(OCV)^2}{4R} \qquad (6.1)$$

where OCV is the theoretical open circuit voltage (0.96 V at 1073 K, wet 5%H_2/Ar), and R is the total resistance of the cell. If the resistance contribution for the electrode materials is negligible, namely considering very good cathode and anode materials, the total resistance can be given by the electrolyte resistance. Thus, R can be calculated by Ohm's law, considering the geometric dimensions of the used pellet (0.15 cm and 0.81 cm^2 of thickness and surface, respectively) and a typical value of the LSGM electrolyte conductivity in air of 0.1 Scm^{-1} at 1073 K. Thus, the calculated power, 152 mWcm^{-2}, is comparable to the experimental power density.

The maximum power density reached in the systems BSCoF/LSGM/Ni-SDC, BSCoF/LSGM/LSCrA and BSCoF/LSGM/LSCrF under the same operating conditions are 105, 79 and 50 mWcm^{-2} respectively, being lower than in the case of the BSCoF/LSGM/LSCrM system.

Attending the symmetric SOFCs, the system LSCrM/LSGM/LSCrM reached the best performance ~ 54 mWcm^{-2} at 1073 K, Figure 6.8b. It should be noted that the obtained performance is in agreement with the data obtained by ASR measurements. The ASR values of LSCrM in air are higher than those of BSCoF in the temperature range 873-1173 K, and this seems to explain the relatively poor performance of the symmetric LSCrX'/LSGM/LSCrX' (X'=Mn, Fe and Al) cells in comparison with the BSCoF/LSGM/LSCrX' cells. If we extrapolate the performance considering a 120 µm thick LSGM electrolyte layer, the maximum power density could reach a value of ~0.7 Wcm^{-2} at 1073 K. The same calculation performed with the same electrolyte thickness, for the system BSCoF/LSGM/LSCrM, indicates that a power density of ~1.6 Wcm^{-2} could be achieved and this is again comparable to the theoretical power, ~1.7 Wcm^{-2}, calculated from the Equation 6.1.

6.3.3.2.2. Series and polarisation resistance

The values of series (R_s) and polarisation (R_p) resistances of the fuel cells are listed in Table 6.2. The impedance spectra of the electrode contribution are illustrated in Figure 6.9 where the series resistance R_s has been subtracted for better comparison. The lowest R_s values correspond to BSCoF/LSGM/LSCrM and LSCrM/LSGM/LSCrM, in agreement with the highest maximum power density in the BSCoF based cells and the symmetric cells, respectively. Furthermore, the polarisation resistance (R_p) of the system BSCoF/LSGM/LSCrM is the lowest, ~0.12 Ωcm^2 at 1073 K and this value agrees with the lowest ASR values measured of BSCoF (in air) and LSCrM (in wet 5%H_2/Ar) on LSGM in the 850-1175 K range, see Figure 6.5a and Figure 6.6b. On the other hand, one should notice that the R_p of the system BSCoF/LSGM/LSCrA, is lower than the R_p of the system BSCoF/LSGM/Ni-SDC, whereas the maximum of performance shows the opposite trend, which means that the ohmic losses (R_s), is more important in the present case. The influence of R_s is clear in the case of the LSCrX' (X'=Mn, Fe and Al) symmetric systems. LSCrM/LSGM/LSCrM system which has the highest R_p, should have rendered the lowest performance and contrary to what was expected, this system gave higher power density than the LSCrA and LSCrF systems.

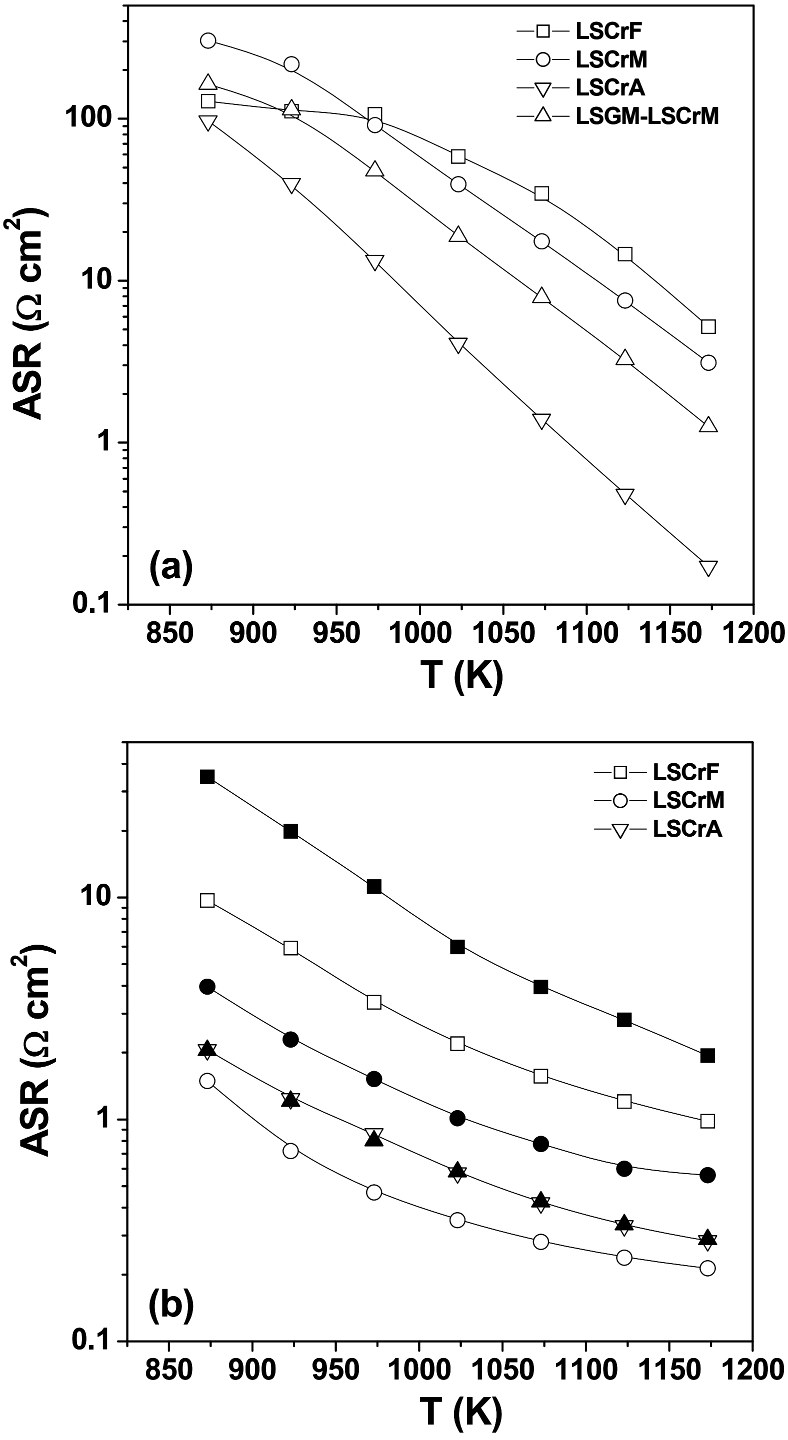

Figure 6.6. ASRs of LSCrX (X= Mn, Fe, Al) on LSGM in air (a) and 5% H_2/Ar (b), dry (closed symbols) and wet (open symbols). For comparison it is also presented the ASR for LSCrM-LSGM composite.

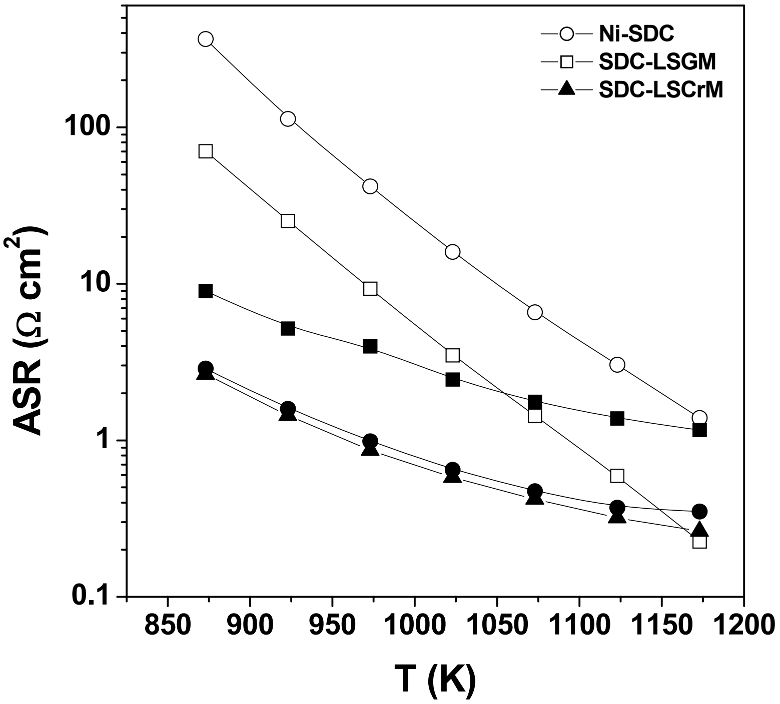

Figure 7. ASRs of SDC-LSGM and SDC-LSCrM composites and Ni-SDC cermet on LSGM, in air (open symbols) and wet 5%H_2/Ar (closed symbols).

The LSCrM system shows a value of R_s ~55% lower than the LSCrA and LSCrF systems. This is possibly due to the lower level of reaction between LSCrM and LSGM [18] compared to LSCrF or LSCrA and LSGM as indicated in the chemical compatibility study at the electrode fixing temperature (~ 1573-1648 K). The lowest R_s is the reason of the highest performance of the LSCrM system respect to the LSCrA and LSCrF systems.

Attending to the microstructure, the SEM images of the LSCrM/LSGM, LSCrF/LSGM, LSCrA/LSGM and BSCoF/LSGM interfaces are illustrated in Figure 6.10. In general, the distribution of the grains in the electrode materials is fairly homogeneous with an average grain size of 1 μm.

6.3.3.2.3. Electrode overpotential

Figure 6.11 compares the overall electrode overpotentials calculated from the different fuel cell tests at 1073 K. The lowest overpotential values corresponded to the BSCoF/LSGM/LSCM system, e.g. at 0.3 Acm^{-2} the overpotential of BSCoF/LSGM/LSCrM system is ~95 and 75% lower than the overpotential values of the LSCrM/LSGM/LSCrM and BSCoF/LSGM/LSCrA systems, respectively.

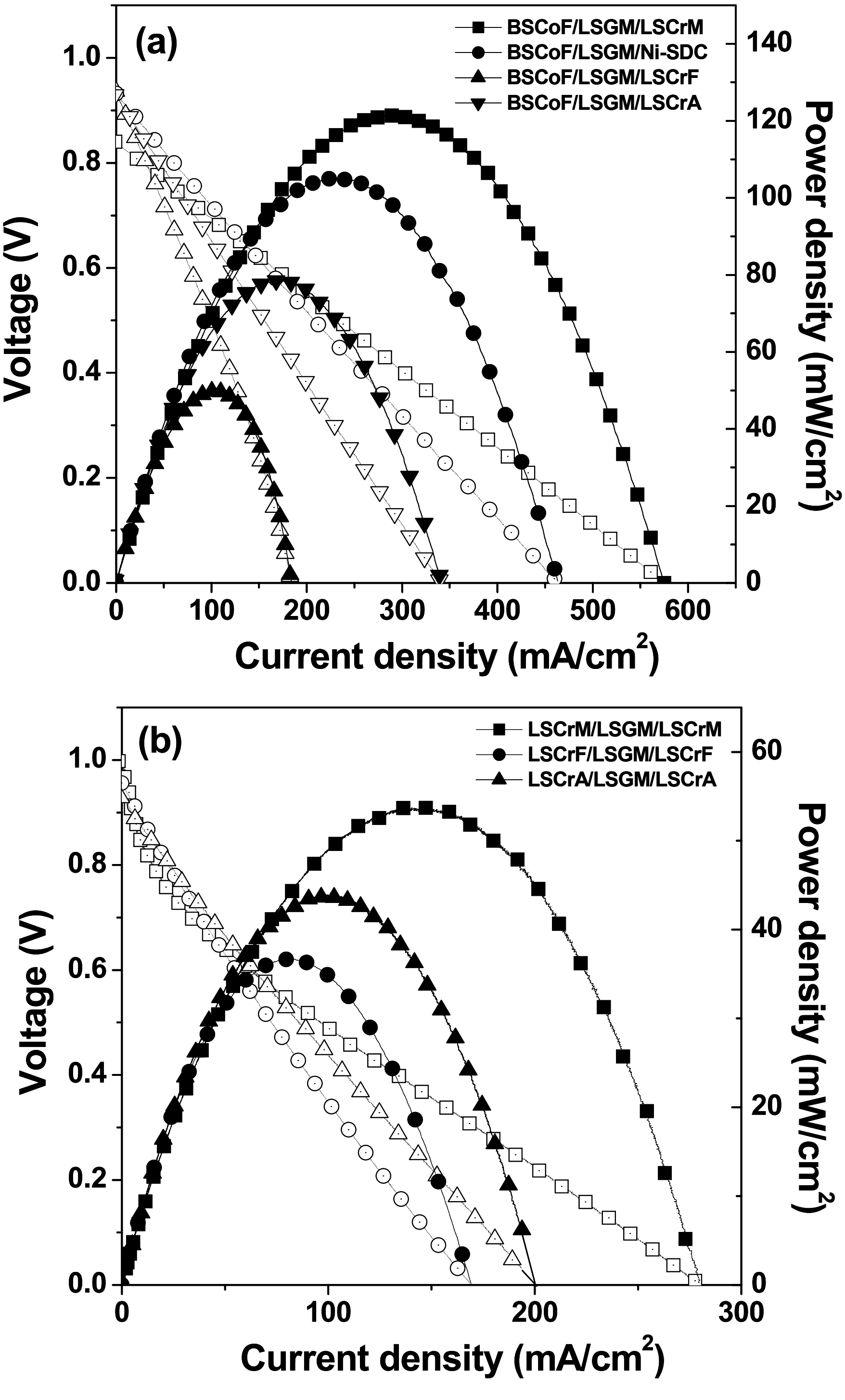

Figure 6.8. Voltage-current density and performance curves of BSCoF based cells (a) and the symmetric systems of LSCrM, LSCrF and LSCrA (b) at 1073 K using wet 5% H_2/Ar as fuel and air as oxidant. Open and closed symbols correspond to the current-voltage and current-power characteristics, respectively.

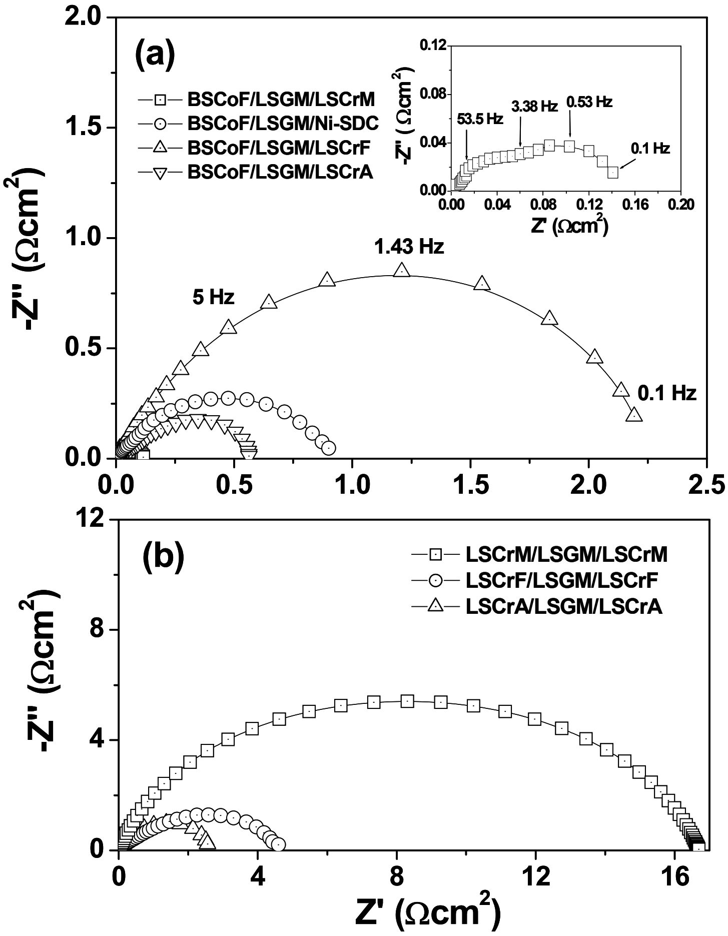

Figure 6.9. Impedance spectra of the BSCoF based cells (a) and the symmetric LSCrX' (X'=Mn, Fe and Al) cells (b) at 1073 K, in asymmetric atmosphere: wet 5%H_2/Ar and air in the anode and cathode side respectively. A magnification of the spectrum of BSCoF/LSGM/LSCrM system is presented in the inset of Figure 6.9a.

Table 6.2.
Series (R_s) and polarization (R_p) resistances of the different cells at 1073 K.

Fuel cell system	R_S (Ωcm)	R_P (Ωcm^2)
BSCoF/LSGM/LSCrM	8.90	0.12
BSCoF/LSGM/LSCrA	14.92	0.56
BSCoF/LSGM/LSCrF	16.03	2.25
BSCoF/LSGM/Ni-SDC	9.85	0.92
LSCrM/LSGM/LSCrM	8.55	16.65
LSCrF/LSGM/LSCrF	19.81	4.60
LSCrA/LSGM/LSCrA	15.45	2.53

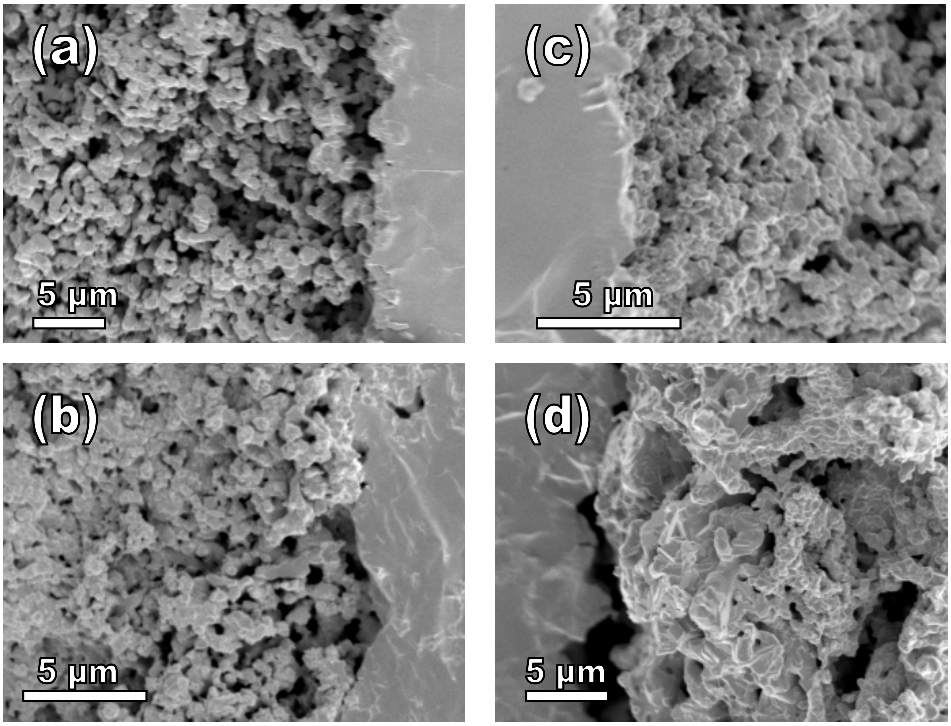

Figure 6.10. SEM images of the interfaces LSCrM/LSGM (a), BSCoF/LSGM (b), LSCrF/LSGM (c) and LSCrA/LSGM (d) after fuel cell tests.

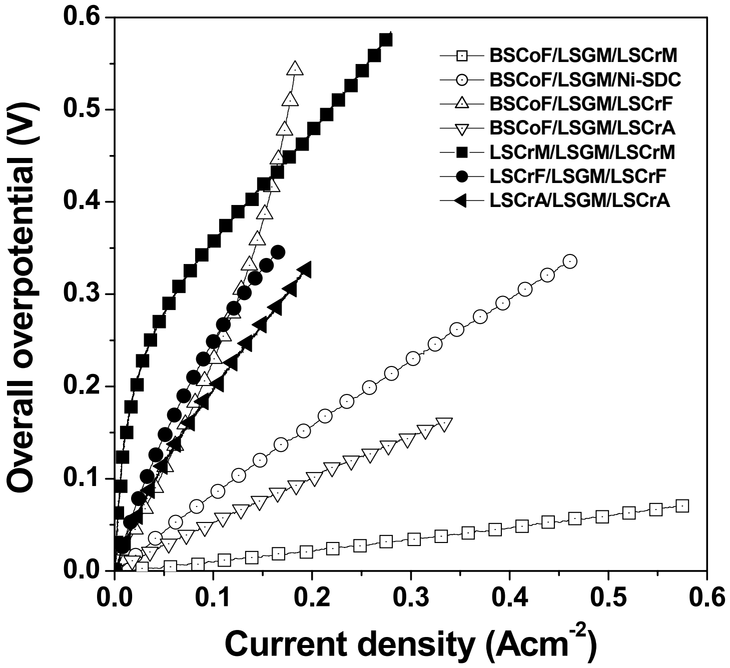

Figure 6.11. Electrode overpotentials from the different fuel cell tests at 1073 K.

The shapes of the overpotential-current density curves are practically linear in the current-density range studied, with a slope of 125 mΩcm^2 in the case of BSCoF/LSGM/LSCrM. However, BSCoF/LSGM/LSCrF system and LSCrX’ symmetric systems show a non linear trace and they also have high overpotential even at lower values of current density. Attending the symmetric cell systems, the overpotential values of the LSCrM/LSGM/LSCrM system are higher than the corresponding values of LSCrF and LSCrA systems at the same current-density. Nevertheless, the performance of the first system are quite higher than the performance of the LSCrF and LSCrA symmetric systems, see Figure 6.8b. This agrees with the high R_p and low R_s values of the LSCrM/LSGM/LSCrM system.

6.4. Conclusions

Area-specific resistance (ASR) measurements of XSCoF (X=Ba, La and Sm), SSCo and LSCrX’ (X’=Mn, Fe and Al) electrode materials, and SDC-LSGM, SDC-LSCrM and Ni-SDC composites on LSGM electrolyte were carried out using a two-probe arrangement in oxidant and reducing conditions. ASR values of BSCoF were the lowest under air whilst ASR values of LSCrM were the lowest under wet 5%H_2/Ar, in the temperature range of 875-1175 K. In addition, current-potential, current-power density, series and polarisation resistances and overpotential of the BSCoF/LSGM/LSCrX’ (X’=Mn, Fe and Al), BSCoF/LSGM/Ni-SDC and the symmetric LSCrX’/LSGM/LSCrX’ cells were investigated at 1073 K, using wet 5%H_2/Ar as fuel and air as oxidant. The lowest electrode overpotential, highest power-density and lowest polarisation resistance values were obtained for BSCoF/LSGM/LSCrM system, i.e. 122 mWcm^{-2}, R_s= 9 Ωcm and R_p= 0.12 Ωcm^2 at 1073 K with ~1.5 mm thickness electrolyte. A theoretical extrapolation indicates a possible maximum power density around 1.6 Wcm^{-2} (120 µm thick LSGM electrolyte layer) at 3.6 Acm^{-2}. The symmetric system LSCrM/LSGM/LSCrM reached a maximum power density of 54 mWcm^{-2} at 1073 K, nearly 50% of the maximum power density of the system BSCoF/LSGM/LSCrM.

6.5. Acknowledgements

The authors are grateful to Professor J.T.S. Irvine for helpful discussions regarding symmetric SOFC development and for the design of the fuel cell tests setup. Special thanks to Dr. J. Canales-Vázquez (Renewable Energy Research Institute, Albacete) for interesting discussions and wise suggestions and to Mr. Luis Hernández-González (Inorganic Chemistry Department, ULL) for his technical assistance. The authors also acknowledge financial support from Spanish Government (MAT2004-3856 project) and Canary Islands Government, (PhD grants).

6.6 References

[1] S.C. Singhal, *Solid State Ion.* **135** (2000) 305-313.

[2] B.C.H. Steele, A. Heinzel, *Nature* **414** (2001) 345-352.

[3] M. Ralph, C. Rossignol, R. Kumar, *J. Electrochem. Soc.* **150** (2003) A1518-A1522.

[4] K. Huang, R. Tichy, J.B. Goodenough, C. Milliken*, J. Am. Ceram. Soc.* **81** (1998) 2581-2585.

[5] T. Ishihara, H. Matsuda, Y. Takita, *J. Am. Chem. Soc.* **116** (1994) 3801-3803.

[6] M. Feng, J.B. Goodenough, *Eur. J. Solid State Inorg. Chem.* **31** (1994) 663-672.

[7] T. Ishihara, H. Furutani, M. Honda, T. Yamada, T. Shibayama, T. Akbay, N. Sakai, H. Yokokawa, Y. Takita, *Chem. Matter.* **11** (1999) 2081-2088.

[8] O. Yamamoto, *Electrochim. Acta* **45** (2000) 2423-2435.

[9] K. Huang, S.R. Tichy, J.B. Goodenough, *J. Am. Chem. Soc.* **81** (1998) 2565-2575.

[10] A. Matraszek, L. Singheiser, D. Kobertz, K. Hilpert, M. Miller, O. Schulz, M. Martin, *Solid State Ion.* **166** (2004) 343-350.

[11] K. Huang, J. Wan, J.B. Goodenough, *J. Electrochem. Soc.* **148** (2001) A788-A794.

[12] M. Feng, J.B. Goodenough, K. Huang, C. Milliken, *J. Power Sources* **63** (1996) 47-51.

[13] J. Yan, H. Matsumoto, M. Enoki, T. Ishihara, *Electrochem. Solid-State Lett.* **8** (2005) A389-A391.

[14] S.W. Tao, J.T.S. Irvine, *Nat. Mater.* **2** (2003) 320-323.

[15] S.W. Tao, J.T.S. Irvine, *J. Electrochem. Soc.* **151** (2004) A252-A259.

[16] S.W. Tao, J.T.S. Irvine, J.A. Kilner, *Adv. Mater.* **17** (2005) 1734-1737.

[17] J.-H. Wan, J.-Q. Yan, J.B. Goodenough, *J. Electrochem. Soc.* **152** (8) (2005) A1511-A1515.

[18] J. Peña-Martínez, D. Marrero-López, J.C. Ruiz-Morales, C. Savaniu, P. Núñez, J.T.S. Irvine, *Chem. Mater.* 18 (2006) 1001-1006.

[19] Y. H. Huang, R.I. Dass, Z.L. Xing, J.B. Goodenough, *Science* **312** (2006) 254-257.

[20] J.Y.Yeon, G.M. Choi, *J. European Ceram. Soc.* **24** (2004) 1359-1363.

[21] Z. Shao, S.M. Haile, *Nature* **431** (2004) 170-173.

[22] J. Peña-Martínez, D. Marrero-López, J.C. Ruiz-Morales, B.E. Buergler, P. Núñez, L.J. Gauckler, *J. Power Sources* **159** (2006) 914-921.

[23] J.C. Ruiz-Morales, J. Canales-Vázquez, J. Peña-Martínez, D. Marrero-López, P. Núñez, *Electrochim. Acta* **52** (2006) 278-284.

[24] J. D.M. Bastidas, S. Tao, J.T.S. Irvine, *J. Mater. Chem.* **16** (2006) 1603-1605.

[25] D. Marrero-López, J. Canales-Vázquez, J.C. Ruiz-Morales, A. Rodríguez, J.T.S. Irvine, P. Nuñez, *Solid State Ion.* **176** (2005) 1807-1816.

[26] J. Rodríguez-Carvajal, T. Roisnel, FullProf.98 and WinPLOTR: New Windows 95/NT Applications for Diffraction Commission For Powder Diffraction, International Union for Crystallography, Newletter N°20, 1998.

[27] T. Roisnel, J. Rodríguez-Carvajal, WinPLOTR : a Windows tool for powder diffraction patterns analysis. Materials Science Forum, Proceedings of the 7Th European Powder Diffraction Conference (EPDIC 7), 2000, 118-123, Ed. R. Delhez and E.J. Mittenmeijer.

[28] S. McIntosh, S.B. Adler, J.M. Vohs, R.J. Gorte, *Electrochem. Solid-State Lett.* **7** (2004) A111-A114.

[29] S. McIntosh, J.M. Vohs, R.J. Gorte, *J. Electrochem. Soc.* **150** (2003) A1305-A1312.

[30] S.Tao, J.T.S. Irvine, *Chem. Mater.* **16** (2004) 4116-4121.

[31] N. Q. Minh, T. Takahashi, Science and Technology of Ceramic Fuel Cells, Elsevier. Amsterdam, 1995.

Chapter 7

Outlook

Abstract

A general discussion of the experimental results described in Chapters 3 to 6 is outlined in this chapter. Considering the experimental results further work is highly recommended to optimise an efficient all-perovskite IT-SOFC.

7.1. Perovskite-type structure materials

The aim of this thesis has been to study perovskite-type structure materials in order to develop an efficient all-perovskite intermediate temperature solid oxide fuel cell (IT-SOFC). Using only perovskite materials may maximise interface properties between the components of a SOFC, including thermal compatibility [1]. In this sense, doped $LaGaO_3$ materials have been investigated as electrolytes and several mixed ionic-electronic conductors as cathode and anode materials.

7.1.1. Doped $LaGaO_3$ compounds as electrolyte materials

Only few oxides with perovskite structure (ABO_3) are pure ionic conductors. Considering the literature [2-5] the most promising perovskite materials for IT-SOFC applications as dense ceramic electrolytes are those based on doped lanthanum gallates. Cation substitution in the A and/or B position of the $LaGaO_3$ perovskite enhances the ion oxide conductivity. In case of Sr^{2+} and Mg^{2+} cation substitution, i.e. $La_{1-x}Sr_xGa_{1-y}Mg_yO_{3-(x+y)/2}$, the ionic conductivity is higher than the oxygen ion conductivity of yttria-stabilised zirconia (YSZ) at intermediate temperature (773-1073 K) [6,7]. Furthermore, a low level of cobalt substitution in Ga position has been also reported [8] as a method to improve the oxide ion conductivity, although an increase of the electronic conductivity was involved.

On the other hand, doped lanthanun gallates are not free of disadvantages, the main drawbacks are the segregation of impurities during the synthesis e.g. $LaSrGa_3O_7$ and $LaSrGaO_4$ [9] and the reactivity with nickel [10-12], which is commonlly employed in the anode cermets, see Figure 2.8 and 6.3. Thereby, Feng et al. [13] reported that the success of LSGM as electrolyte relies on the identification of the suitable anode material and on the optimization of the processing methods.

The overall conductivity of several doped lanthanum gallate materials, i.e. $La_{0.9}Sr_{0.1}Ga_{1-x}Mg_xO_{3-(x+0.1)/2}$ (x=0.05, 0.10, 0.15, 0.20, 0.25 and 0.30), $La_{0.9}A_{0.1}Ga_{0.8}Mg_{0.2}O_{2.85}$ (A= Ba, Ca) and $La_{0.9}Sr_{0.1}Ga_{0.8}Mg_{0.2-x}Co_xO_{3-\delta}$ (x=0.015, 0.045, 0.075 and 0.085) has been studied by electrochemical impedance spectroscopy (EIS). The composition $La_{0.9}Sr_{0.1}Ga_{0.8}Mg_{0.2}O_{2.85}$ (LSGM) in a good agreement with the literature [6,7] was the composition without partial cobalt substitution with higher conductivity, 0.1 Scm^{-1} at 1073 K. (Figure 1.10). Considering to the partial cobalt substitution, $La_{0.9}Sr_{0.1}Ga_{0.8}Mg_{0.115}Co_{0.085}O_{3-\delta}$ (LSGMC) showed the highest overall conductivity, ~0.12 Scm^{-1} at 1073 K (Figure 1.11).

Studying the oxygen partial pressure dependence for the overall conductivity of LSGM and LSGMC compositions (Figure 2.21), it has to be noticed that the ionic conductivity is predominant in a wide range of oxygen partial pressures ($1\text{-}10^{-16}$ atm). Otherwise, the ionic transport numbers of these compositions were determined by a modified *emf* method (Section 2.7.3) in oxidant and reduced atmospheres. $La_{0.9}Sr_{0.1}Ga_{0.8}Mg_{0.2}O_{2.85}$ sample showed an ionic transport number, around 0.99, in both O_2/air and 5%H_2-Ar/air gradient, in the temperature range 900 - 1173 K, whereas cobalt-doped samples showed lower values of ionic transport number (See Appendix IV).

Additionally, the redox stability of LSGM and LSGMC was studied by XRD after exposing the LSGM and LSGMC samples to a wet H_2 flow at 1073 K and 973 K for 48 hours, and no changes or extra peaks in the XRD pattern were found (Figure 3.5 and AI.6).

7.1.2. MIECs as cathode and anode materials

Several MIECs with perovskite-type structure have been synthesised and structural and electrical characterised, using the methods described in Chapter 2. Table AII.1 (Appendix II) contains a list of them including method of synthesis, temperature and BET surface area. The temperature dependence for the overall conductivity of some of them is illustrated in Figure 1.12, and one should noticed that their electronic conductivity is usually high, at least ten times higher than the ionic conductivity of LSGM. The chemical compatibility of these materials with LSGM has been also studied by XRD and it is commented in the following paragraphs. Perovskite-type structure is a versatile structure and this is an advantage for developing new materials by cation substitution or doping, however it is also a disadvantage for interfacial reactions with the possibility of cation diffusions. Nevertheless, these kind of reactions can be avoided optimising buffers layers and controlling the sintering temperature of the electrodes onto the electrolyte.

7.1.2.1 $La_{0.75}Sr_{0.25}Cr_{0.5}Mn_{0.5}O_{3-\delta}$ as anode

The first electrode materials studied for LSGM and LSGMC based SOFC were $La_{0.75}Sr_{0.25}Cr_{0.5}Mn_{0.5}O_{3-\delta}$ (LSCM) material, which was successfully tested as Ni-free anode material with YSZ-based SOFCs by Tao and Irvine [14], and $La_{0.8}Sr_{0.2}MnO_{3-\delta}$ (LSM) which was the typical cathode material used also with YSZ-based SOFCs. Their thermal expansion coefficients (TEC) are analogous of the LSGM one ($\sim 10 \pm 1 \times 10^{-6}$ K^{-1}). Furthermore, the primitive perovskite unit cell volume of LSM is 58.8 Å3, only 1% different from that of either LSCM or LSGM. It implicates *a priori* a good match between them. Current-potential, current power-density, anodic losses, and overpotential of the LSM/LSGM/LSCM and LSM/ LSGMC/LSCM cells were investigated at 1073 and 873 K using wet pure hydrogen and 5%H_2/Ar as fuels and O_2 as oxidant.

The performance of LSM/LSGMC/LSCM at 1073 K was inferior to the performance obtained on LSM/LSGM/LSCM at 873 K in both H_2-containing atmospheres. The maximum power-density value for the LSM/LSGM/LSCM system with 5%H_2/Ar was 75% of the value obtained for the pure H_2 case i.e. 570 mWcm^{-2} and 160 mWcm^{-2} at 1073 K and 873 K respectivley, with an electrolyte thickness of about 120 μm, prepared by tape casting (section 2.2.3).

As a consequence of these results, it was envisaged to continue working with LSGM as electrolyte and LSCM as anode. LSGMC was not still considered as electrolyte material due to the rather low performance of the LSM/LSGMC/LSCM cell and the strong reactivity between a LSGMC and LSCM powdered mixture observed in their XRD pattern at 1173 K and above (Figure 3.4). In the case of LSM and LSCM, only certain reactivity could be observed between LSM and LSGM above 1373 K, and between LSGM and LSCM at 1623 K (Figures 3.3 and 3.2).

7.1.2.2 $Ba_{0.5}Sr_{0.5}Co_{0.8}Fe_{0.2}O_{3-\delta}$ as cathode

The power density at 873 K of the previous LSGM-electrolyte supported cell with 120 μm thick electrolyte using LSM as cathode and LSCM as anode was quite low because of the high ohmic losses of the electrolyte at low temperatures and the high polarisation resistance of LSM at temperatures below 1073 K. For this reason, it seemed advisable to use an alternative cathode material in order to increase the performance of LSGM-based cells at low temperatures. $Ba_{0.5}Sr_{0.5}Co_{0.8}Fe_{0.2}O_{3-\delta}$ (BSCF) had been proposed as alternative cathode material due to its high activity for the electrochemical reduction of oxygen in the temperature range from 773 to 973 K on samarium doped ceria (SDC) electrolytes [15], and it was decided to investigate it as cathode material on LSGM electrolyte.

The chemical compatibility of BSCF and LSGM was studied by XRD, and it was found a strong reaction between them above 1273 K. Therefore, in order to avoid the reaction between BSCF and LSGM the maximum temperature of sintering the BSCF electrode material on the LSGM electrolyte pellet was never higher than 1273 K.

Fuel cell tests of the system BSCF/LSGM/LSCM were carried out at 1073 K and 873 K, using moistened hydrogen–nitrogen mixtures as fuels and air as oxidant. The values of power density and polarisation resistance (R_p) at 1073 K were 160 mWcm^{-2} and 0.75 Ωcm^2, respectively, with 1.5 mm thick electrolyte, series resistance (R_s) of 7.6 Ωcm^2, meanwhile the power density dramatically drop at 35 mWcm^{-2} at 873 K.

7.1.2.3. Fuel cell studies of perovskite-type materials for IT-SOFC

Despite of the previous test of $Ba_{0.5}Sr_{0.5}Co_{0.8}Fe_{0.2}O_{3-\delta}$ (BSCF) material as cathode, it was also decided to investigate a composite of LSM and LSGM in a 30–70% molar ratio (LSM–LSGM) because a lower cathodic overpotential was reported using this material than with LSM only, both on LSGM electrolyte [16]. In addition, the use of a samarium doped ceria, $Sm_{0.15}Ce_{0.85}O_{2-\delta}$ (SDC), as a buffer layer between the LSGM electrolyte and the LSCM anode material was also investigated to avoid possible cation diffusion and interfacial reactions. Hence, the systems LSM–LSGM/LSGM/LSCM, LSM/LSGM/SDC/LSCM, and LSM/LSGM/LSCM were tested and compared with the BSCF/LSGM/LSCM system. It was used moistened hydrogen–nitrogen mixtures as fuel and air as oxidant. The lowest electrode overpotential, highest power density and lowest polarisation resistance values were obtained for BSCF/LSGM/LSCM system.

The power density reached with the system BSCF/LSGM/LSCM represents about 20% more of the maximum power density of the system LSM/LSGM/LSCM at the same temperature. Furthermore, this difference is increased up to 43% at 873 K. The other systems, LSM/LSGM/SDC/LSCM and LSM–LSGM/LSGM/LSCM, did not to reach 50% of the value obtained with the corresponding BSCF/LSGM/LSCM configuration (see Figure 5.9). The current–voltage curves of LSM/LSGM/SDC/LSCM and LSM–LSGM/LSGM/LSCM cells showed a drastical drop of the cell voltage at low current density which became less pronounced at larger current. This strong drop of the potential could be related to a high activation polarisation loss. The use of a SDC buffer layer between LSGM electrolyte and LSCM anode material did not help to improve the electrochemical performance of the LSM/LSGM/LSCM cell, neither using a LSM–LSGM composite instead of LSM cathode material. Taking into account the chemical compatibility studied by XRD, the corresponding XRD patterns did not show any evidence of chemical incompatibility between the pairs LSCM/SDC and LSGM/SDC at intermediate temperature (873–1073 K) (Figures 5.4, 5.5 and 5.6).

7.1.2.4 XSCoF (X=Ba, La, Sm) and LSCrX' (X'=Mn, Fe, Al)

The next step in the present investigation consisted in to study different cobalt-based perovskites as potential cathode materials, following the composition $X_{0.5}Sr_{0.5}Co_{0.8}Fe_{0.2}O_{3-\delta}$ (XSCoF) with X= Ba, La and Sm, and $Sm_{0.5}Sr_{0.5}CoO_{3-\delta}$ (SSCo), following our previous results and the works of Yan *et al.* [17] and Huang *et al.* [18] who reported high performance in LSGM-based fuel cells using cobaltites, i.e. $Sm_{0.6}Sr_{0.4}CoO_{3-\delta}$ and $SrCo_{0.8}Fe_{0.2}O_{3-\delta}$ as cathode materials. Additionally, different lanthanum chromites, $La_{0.75}Sr_{0.25}Cr_{0.5}X'_{0.5}O_{3-\delta}$ (LSCrX') with X' = Mn, Fe and Al, were also investigated as potential anode materials, attending to our previous results [19-21] and compared with standard Ni-cermets, NiO-$Sm_{0.15}Ce_{0.85}O_{2-\delta}$ (Ni-SDC) and SDC–LSCrM and SDC–LSGM composites. Furthermore, Ruiz-Morales *et al.* [22] and Irvine and co-workers [23] had introduced an interesting new symmetric SOFC concept, where the anode and the cathode are constituted by the same electrode materials. These authors had reported good performance results using LSCrM material as anode and cathode, and YSZ as electrolyte, and it was envisaged to test LSCrX' materials as cathode and anode materials using LSGM as electrolyte.

Firstly, the area-specific resistance (ASR) for BSCoFe, $La_{0.5}Sr_{0.5}Co_{0.8}Fe_{0.2}O_{3-\delta}$ (LSCoF), $Sm_{0.5}Sr_{0.5}Co_{0.8}Fe_{0.2}O_{3-\delta}$ (SSCoF), SSCo, LSCrM, $La_{0.75}Sr_{0.25}Cr_{0.5}Fe_{0.5}O_{3-\delta}$ (LSCrF) and $La_{0.75}Sr_{0.25}Cr_{0.5}Al_{0.5}O_{3-\delta}$ (LSCrA), SDC-LSCrM and SDC-LSGM on LSGM electrolyte under symmetric atmospheres was measured and analysed. And secondly, fuel cell tests of the systems BSCoF/LSGM/LSCrX', BSCoF/LSGM/Ni-SDC and the symmetric SOFCs using LSCrX' materials as cathode and anode i.e. LSCrX/LSGM/LSCrX' were performed. The ASR values of BSCoF were the lowest under air whilst ASR values of LSCrM were the lowest under wet 5% H_2/Ar, in the temperature range of 875–1175 K. On the ASR values of the studied composites i.e. Ni-SDC and SDC-LSCrM, see Figure 6.7, are quite similar under reducing conditions, ~0.4 Ωcm^2 at 1073 K, and it has to be noticed that the values of ASR in wet 5%H_2/Ar of LSCrM (Figure 6.6b) are slightly lower than the values of SDC-LSCrM composite in the same temperature range ~0.3 Ωcm^2 at 1073 K. In addition, the lowest electrode overpotential, highest power–density and lowest polarisation resistance values were obtained again for BSCoF/LSGM/LSCrM system, i.e. 122 $mWcm^{-2}$, R_s=9 Ωcm and R_p=0.12 Ωcm^2 at 1073 K with ~1.5 mm thickness electrolyte. A theoretical extrapolation indicates a possible maximum power density around 1.6 Wcm^{-2} (120 µm thick LSGM electrolyte layer) at 3.6 Acm^{-2}. Whereas, the symmetric system LSCrM/LSGM/LSCrM reached a maximum power density of 54 $mWcm^{-2}$ at 1073 K, nearly 50% of the maximum power density of the system BSCoF/LSGM/LSCrM. If we extrapolate the performance considering a 120 µm thick LSGM electrolyte layer, the maximum power density could reach a value of ~0.7 Wcm^{-2} at 1073 K.

7.2. Preparative methods

Regarding the preparative methods, doped $LaGaO_3$ materials have been prepared as dense ceramic electrolytes using conventional solid state reaction and alternative precursor routes. XRD patterns of LSGM synthesised by different methods can be observed in Appendix I, Figure AI.4. However, the highest density (> 95% compared with the crystallographic density) has been achieved by the conventional ceramic route. A SEM image of a LSGMC sample prepared by solid state reaction is illustrated in the Figure 7.1a, whereas a SEM image of another LSGMC sample prepared by sol-gel route is illustrated in Figure 7.1b. One should notice that the image in Figure 7.1a represents the typical microstructure of an electrolyte material. Otherwise, the reduction of the grain size using precursor routes has been considerable (Figure 7.1b)

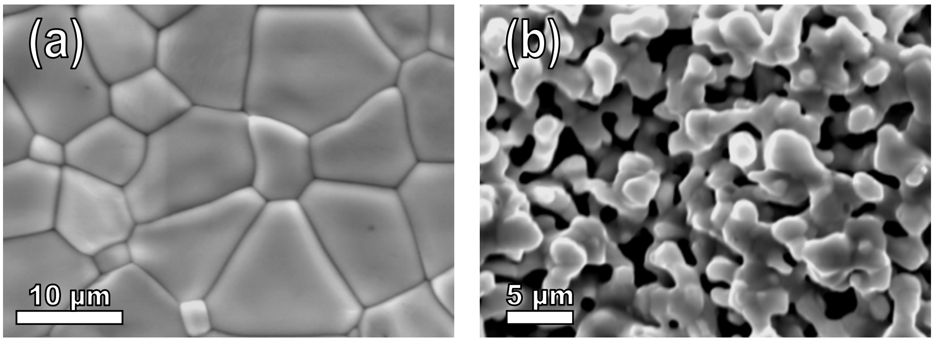

Figure 7.1. SEM images of $La_{0.9}Sr_{0.1}Ga_{0.8}Mg_{0.115}Co_{0.085}O_{3-\delta}$ prepared at 1648 K in air by solid state reaction (a) and sol-gel route (b).

Precursor synthesis routes have been successfully used and the microstructure of the electrode materials has been improved, as one can see, for example, in the SEM images illustrated of LSCF material prepared by solid state reaction and freeze-drying method, in Figure 7.2a and 7.2b, respectively. The main drawback of precursor routes is that not always it could be used, e.g. LSCM anode material has been prepared with a good microstructure using conventional ceramic route, meanwhile with precursor routes it was not suitable to get single phase, and impurities as $SrCrO_4$ were stabilised.

7.3. Future works

It is general accepted, that the microstructure has an important influence on the electrochemical performance of electrodes. A good electrode microstructure was achieved within this work using precursor route methods as sol-gel and freeze-drying, however a continuing research is necessary to optimise the microstructure and improve the electrochemical performance. Recently a new method using poly(methyl methacrylate) (PMMA) microspheres has been proposed [21] and the performance of YSZ-based SOFC tested was considerably improved, thereby it should be applied to LSGM-based SOFCs.

Taking into account the LSGM material as electrolyte, more efforts to obtain thin films are required. In this sense, the ceramic slip formulation for LSGM tape casting process (section 2.2.3) should be optimised. In addition, the recently work of Ishihara and co-workers [17] using LSGM thin films prepared by pulsed laser deposition (PLD) indicate this technique as a promising preparative method for LSGM thin films. In any case, a detailed study on the improvement of the electrochemical performance of BSCF/LSGM/LSCM system using LSGM thin film prepared by tape casting and/or PLD could follow up.

Another issue to be considered is the operation with hydrocarbons as fuel. Anodes directly fueled with hydrocarbons are of high interest, and the optimisation of the symmetric SOFCs, could allow the use of hydrocarbons fuel even with sulphur traces. Carbon deposition effect in the anode side could be also minimised using these types of SOFC. Otherwise, it is neccesary the development of a good material which could work as anode and cathode in a double chamber configuration, paying special attention to its electro-catalysis activity due to it has to work at low and intermediate temperature. Therefore, it could be interesting to investigate the anodic performance of LSCM material with LSGM-based SOFC using hydrocarbons as fuel.

The experimental and operating conditions influence highly the electrochemical performance, e.g. sealing, fuel composition, fuel utilization, conditioning of the electrode. These factors are the origin for the widely values that can be found in literature on electrode performances. However, industrial preparation and optimisation interests, like long term stability, upscaling, are necessary to assess the limits of the material combination in a all-perovskite SOFC, overall in the new symmetric SOFC design.

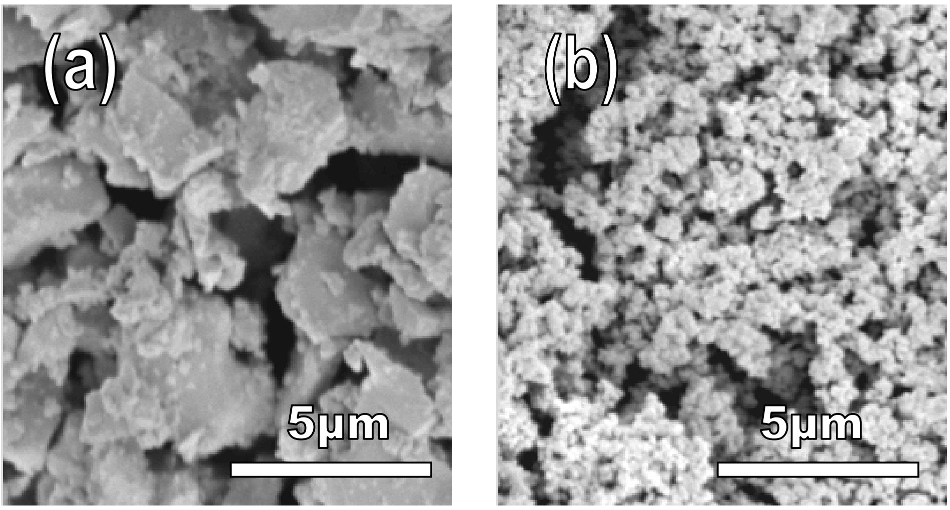

Figure 7.2. SEM images of $La_{0.75}Sr_{0.25}Cr_{0.5}Fe_{0.5}O_{3-\delta}$ prepared at 1473 K in air by solid state reaction (a) and freeze-drying method (b).

7.4 References

[1] S.W. Tao, J.T.S. Irvine, J.A. Kilner, *Adv. Mater.* **17** (2005) 1734-1737.

[2] B.C.H. Steele, A. Heinzel, *Nature* **414** (2001) 345-352.

[3] O. Yamamoto, *Electrochim. Acta* **45** (2000) 2423-2435.

[4] K.C. Wincewicz, J.S. Cooper, *J. Power Sources* **140** (2005) 280-296.

[5] Singhal, K. Kendall, High-temperature Solid Oxide Fuel Cells: Fundamentals, Design and Applications, Elsevier, 2004

[6] M. Feng, J.B. Goodenough, *Eur. J. Solid State Inorg. Chem.* **31** (1994) 663-672.

[7] T. Ishihara, H. Matsuda, Y. Takita, *J. Am. Chem. Soc.* **116** (1994) 3801-3803.

[8] T. Ishihara, H. Furutani, M. Honda, T. Yamada, T. Shibayama, T. Akbay, N. Sakai, H. Yokokawa, Y. Takita, *Chem. Matter.* **11** (1999) 2081-2088.

[9] A. Matraszek, L. Singheiser, D. Kobertz, K. Hilpert, M. Miller, O. Schulz, M. Martin, *Solid State Ion.* **166** (2004) 343-350.

[10] M. Guillodo, P. Vernoux, J. Fouletier, *Solid State Ion.* **127** (2000) 99-107.

[11] K. Huang, J. Wan, J.B. Goodenough, *J. Electrochem. Soc.* **148** (2001) A788-A794.

[12] K. Huang, M. Feng, J.B. Goodenough, C. Milliken, J. Electrochem. Soc. **144** (1997) 3620-3624.

[13] M. Feng, J.B. Goodenough, K. Huang, C. Milliken, *J. Power Sources* **63** (1996) 47-51.

[14] S. Tao, J.T.S. Irvine, *Nat. Mater*. **2** (2003) 320-323.

[15] Z. Shao, S.M. Haile, *Nature* **431** (2004) 170-173.

[16] J.Y. Yi, G.M. Choi, *J. European Ceram. Soc.* **24** (2004) 1359-1363.

[17] J. Yan. H. Matsumoto, M. Enoki, T. Ishihara, Electrochem. *Solid-State Lett.* **8** (2005) A389-A391.

[18] Y.H. Huang, R.I. Dass, Z.L. Xing, J.B. Goodenough, *Science* **312** (2006) 254-257.

[19] J. Peña-Martínez, D. Marrero-López, J.C. Ruiz-Morales, C. Savaniu, P. Núñez, J.T.S. Irvine, *Chem. Mater*. **18** (2006) 1001-1006.

[20] J. Peña-Martínez, D. Marrero-López, J.C. Ruiz-Morales, B. E. Büergler, P. Núñez, L.J. Gauckler, *Solid State Ion*. **177** (2006) 2143-2147.

[21] J. Peña-Martínez, D. Marrero-López, J.C. Ruiz-Morales, B. E. Büergler, P. Núñez, L.J. Gauckler, *J. Power Sources* **159** (2006) 914-921.

[22] J.C. Ruiz-Morales, J. Canales-Vázquez, J. Peña-Martínez, D. Marrero-López, P. Núñez, *Electrochim. Acta* **52** (2006) 278-284.

[23] J.D.M. Bastidas, S. Tao, J.T.S. Irvine, *J. Mater. Chem.* **16** (2006) 1603-1605.

Conclusions

1. The overall conductivity of several doped lanthanum gallate materials, i.e. $La_{0.9}Sr_{0.1}Ga_{1-x}Mg_xO_{3-(x+0.1)/2}$ (x=0.05, 0.10, 0.15, 0.20, 0.25 and 0.30), $La_{0.9}A_{0.1}Ga_{0.8}Mg_{0.2}O_{2.85}$ (A= Ba, Ca) and $La_{0.9}Sr_{0.1}Ga_{0.8}Mg_{0.2-x}Co_xO_{3-\delta}$ (x=0.015, 0.045, 0.075 and 0.085) has been measured by impedance spectroscopy. The composition $La_{0.9}Sr_{0.1}Ga_{0.8}Mg_{0.2}O_{2.85}$ (LSGM) was the composition, without partial cobalt substitution, with higher conductivity in the range 873-1073 K, i.e. 0.1 Scm^{-1} at 1073 K. Whereas, $La_{0.9}Sr_{0.1}Ga_{0.8}Mg_{0.115}Co_{0.085}O_{3-\delta}$ (LSGMC) showed the highest overall conductivity in the range 873-1073 K, i.e. 0.12 Scm^{-1} at 1073 K.
2. The ionic conductivity of LSGM and LSGMC was predominant in a wide range of oxygen partial pressures ($1\text{-}10^{-16}$ atm).
3. The ionic transport numbers of LSGM and LSGMC compositions were determined by a modified *emf* method in oxidant and reduced atmospheres. LSGM sample showed an ionic transport number, around 0.99, in both O_2/air and 5%H_2-Ar/air gradient, in the temperature range 900 - 1173 K, whereas LSGMC sample showed lower values, around 0.5 in O_2/air gradient.
4. The redox stability of LSGM was studied by XRD after exposing a LSGM sample to a wet H_2 flow at 1073 K for 48 hours, and no changes or extra peaks in the XRD pattern were found.
5. $La_{0.75}Sr_{0.25}Cr_{0.5}Mn_{0.5}O_{3-\delta}$ (LSCM) and $La_{0.8}Sr_{0.2}MnO_{3-\delta}$ (LSM) materials were tested as anode and cathode, respectively with LSGM as electrolyte, in a double chamber configuration and electrolyte-supported design, and the maximum power-density values for the LSM/LSGM/LSCM system using wet pure H_2 as fuel and oxygen as gas oxidant were 570 $mWcm^{-2}$ and 160 $mWcm^{-2}$ at 1073 K and 873 K, respectively, with an electrolyte thickness of 120 μm, prepared by tape casting. The maximum power density decreases 25% using wet 5%H_2/Ar as fuel and O_2 as gas oxidant.
6. A chemical compatibility study by XRD indicated a strong reactivity between a LSGMC and LSCM powdered mixture at 1173 K and above. In the case of LSM and LSCM, only certain reactivity could be observed between LSM and LSGM above 1373 K, and between LSGM and LSCM at 1623 K.
7. $Ba_{0.5}Sr_{0.5}Co_{0.8}Fe_{0.2}O_{3-\delta}$ (BSCF) material was tested as cathode material on LSGM electrolyte, in a double chamber configuration and electrolyte-supported design. Fuel tests of the system BSCF/LSGM/LSCM were carried out at 1073 K and 873 K, using wet H_2–N_2 mixtures as fuels and air as oxidant. The values of power density and polarisation resistance (R_p) at 1073 K were 160 mW cm^{-2} and 0.75 Ωcm^2, respectively, with 1.5 mm thick electrolyte, series resistance (R_s)=7.6 Ωcm, meanwhile the power density dramatically drop at 35 $mWcm^{-2}$ at 873K.
8. The chemical compatibility of BSCF and LSGM was studied by XRD, and a strong reaction between them above 1273 K was found. For this reason, in

order to avoid the reaction between BSCF and LSGM the maximum sintering temperature of the BSCF electrode material onto LSGM electrolyte pellet should not be higher than 1273 K.

9. The systems LSM/LSGM/LSCM and BSCF/LSGM/LSCM were tested and compared. The maximum power density reached with the system BSCF/LSGM/LSCM represents about 20% more of the maximum power density of the system LSM/LSGM/LSCM at the same temperature, using wet H_2–N_2 mixtures as fuel and air as oxidant. This difference was increased up to 43% at 873 K.
10. A composite of LSM and LSGM (LSM–LSGM) in a 30–70% molar ratio was tested on on LSGM electrolyte, and a samarium doped ceria, $Sm_{0.15}Ce_{0.85}O_{2-\delta}$ (SDC), as a buffer layer between the LSGM electrolyte and the LSCM anode material was also investigated. The systems LSM–LSGM/LSGM/LSCM, LSM/LSGM/SDC/LSCM, were tested and compared with the BSCF/LSGM/LSCM and LSM/LSGM/LSCM systems. Wet H_2–N_2 mixtures were used as fuel and air as oxidant. The maximum power density values of LSM/LSGM/SDC/LSCM and LSM–LSGM/LSGM/LSCM systems did not to reach 50% of the value obtained with the BSCF/LSGM/LSCM system.
11. The area-specific resistance (ASR) for $X_{0.5}Sr_{0.5}Co_{0.8}Fe_{0.2}O_{3-\delta}$ (XSCF) (X=Ba, La and Sm), $Sm_{0.5}Sr_{0.5}CoO_{3-\delta}$ (SSCo), $La_{0.75}Sr_{0.25}Cr_{0.5}X'_{0.5}O_{3-\delta}$ (LSCX') (X'=Mn, Fe and Al), SDC-LSCM and SDC-LSGM on LSGM electrolyte under air, oxygen, argon, dry and wet 5%H_2/95%Ar was measured and analysed. The ASR values in the 875–1175 K range, of BSCF (or BSCoF) were the lowest under air, less than 0.1 Ωcm^2 at temperatures above 1025 K, whilst ASR values of LSCM (or LSCrM) were the lowest under wet 5% H_2/Ar, ~0.3 Ωcm^2 at 1073 K.
12. The ASR of BSCF on LSGM and the series resistance variation was about 0.013 Ωcm^2 and 0.1 Ωcm (~1.5 mm thick LSGM pellet) respectively, after 30 h of operation at 1073 K under air atmosphere. Meanwhile, the variation of ASR and R_s for LSCM on LSGM in wet 5%H_2/Ar were not significant, about 0.01 Ωcm^2 and 0.03 Ωcm respectively, after 10 h of operation at 1073 K.
13. Fuel cell tests of the systems BSCF/LSGM/LSCX', BSCF/LSGM/Ni-SDC and LSCX'/LSGM/LSCX' were performed. The lowest electrode overpotential, highest power–density and lowest polarisation resistance values at 1073 K were obtained for BSCF/LSGM/LSCM system, i.e. 122 $mWcm^{-2}$, R_s =9 Ωcm and R_p = 0.12 Ωcm^2 (~1.5 mm thick electrolyte). A theoretical extrapolation indicates a maximum power density of 1.6 Wcm^{-2} (120 μm thick LSGM electrolyte) at 3.6 Acm^{-2}. Whereas, the symmetric system LSCM/LSGM/LSCM reached 54 $mWcm^{-2}$ at 1073 K, nearly 50% of the maximum power density of the system BSCF/LSGM/LSCM. Theoretical extrapolation indicates a possibly value of 0.7 Wcm^{-2} at 1073 K.

Conclusiones

1. La conductividad total de varios compuestos basados en el galato de lantano: $La_{0,9}Sr_{0,1}Ga_{1-x}Mg_xO_{3-(x+0,1)/2}$ (x=0,05; 0,10; 0,15; 0,20; 0,25 y 0,30), $La_{0,9}A_{0,1}Ga_{0,8}Mg_{0,2}O_{2,85}$ (A= Ba, Ca) y $La_{0,9}Sr_{0,1}Ga_{0,8}Mg_{0,2-x}Co_xO_{3-\delta}$ (x=0,015; 0,045; 0,075 and 0,085), ha sido determinada mediante espectroscopía de impendancia compleja. La composición $La_{0,9}Sr_{0,1}Ga_{0,8}Mg_{0,2}O_{2,85}$ (LSGM) fue la composición sin sustitución parcial del catión galio por cobalto, con la mayor conductividad en el rango de 873-1073 K, obteniéndose 0.1 Scm^{-1} a 1073 K. Mientras que la composición con cobalto $La_{0,9}Sr_{0,1}Ga_{0,8}Mg_{0,115}Co_{0,085}O_{3-\delta}$ (LSGMC) mostró la conductividad más alta para el mismo rango de temperaturas, 873-1073 K, obteniéndose 0.12 Scm^{-1} a 1073 K.
2. La conductividad iónica es predominante en los compuestos LSGM y LSGMC en un amplio intervalo de presiones parciales de oxígeno ($1\text{-}10^{-16}$ atm).
3. Los números de transporte iónicos de las composiciones LSGM y LSGMC fueron determinados mediante un método modificado de fuerza electromotriz (*emf*) en condiciones oxidantes y reductoras. A la composición LSGM le corresponde un número de transporte iónico de 0,99 en los gradientes O_2/aire y 5%H_2-Ar/aire, y rango de temperaturas 900-1173 K; mientras que el número de transporte iónico de LSGMC en un gradiente O_2/aire es bastante inferior, alrededor de un valor de 0,5.
4. La estabilidad redox de LSGM fue estudiada mediante XRD después de exponer una muestra de LSGM a una corriente de H_2 humedecido durante 48 horas, permaneciendo la muestra a una temperatura constante de 1073 K y no se encontraron picos extras o adicionales en el correspondiente difractograma.
5. Los materiales $La_{0,75}Sr_{0,25}Cr_{0,5}Mn_{0,5}O_{3-\delta}$ (LSCM) y $La_{0,8}Sr_{0,2}MnO_{3-\delta}$ (LSM) fueron investigados como material de ánodo y cátodo, respectivamente, utilizando LSGM como electrolito, en configuración de *double chamber* y diseño de electrolito soportado. Los valores de máxima densidad de potencia del sistema LSM/LSGM/LSCM usando H_2 humedecido como combustible y oxígeno como gas oxidante fueron de 570 $mWcm^{-2}$ y 160 $mWcm^{-2}$ a 1073 K y 873 K, respectivamente, con un espesor de electrolito de 120 μm, preparado por *tape casting*. Los mencionados valores de densidad de potencia disminuyeron en un 25% usando 5%H_2/Ar humedecido en vez de H_2 puro como combustible.
6. Un estudio de compatibilidad química, utilizando la técnica de XRD, ha indicado que existe una fuerte reactividad en una muestra en polvo con mezcla de LSGMC y LSCM a temperaturas igual o superiores a 1173 K. Cierta reactividad también se observó entre LSM y LSGM, y entre LSGM y LSCM, por encima de 1373 K y 1623 K, respectivamente.
7. El material $Ba_{0,5}Sr_{0,5}Co_{0,8}Fe_{0,2}O_{3-\delta}$ (BSCF) fue investigado como material de cátodo junto LSGM como electrolito, en configuración de *double*

chamber y diseño de electrolito soportado. Se efectuaron tests con combustible del sistema BSCF/LSGM/LSCM a 1073 K y 873 K, usando una mezcla de hidrógeno-nitrógeno humedecido como combustible y aire como gas oxidante. Los valores de densidad de potencia y resistencia de polarización (R_p) a 1073 K fueron 160 mWcm^{-2} y 0,75 Ωcm^2, respectivamente, con un electrolito de 1,5 mm de espesor, siendo la resistencia del electrolito (R_s) de 7,6 Ωcm. Sin embargo, el valor de densidad de potencia disminuyó drásticamente hasta 35 mWcm^{-2} cuando la temperatura de operación era 873 K.

8. El estudio de compatibilidad química entre BSCF y LSGM mediante XRD, indicó una fuerte reacción entre dichos compuestos a temperaturas superiores a 1273 K. Debido a ello, la temperatura para fijar el material BSCF sobre LSGM nunca debe ser superior a esta temperatura, precisamente para evitar la reacción entre BSCF y LSGM.
9. El rendimiento de los sistemas LSM/LSGM/LSCM y BSCF/LSGM/LSCM fueron comparados. El valor máximo de densidad de potencia del sistema BSCF/LSGM/LSCM era 20% más elevado que el máximo valor de densidad de potencia del sistema LSM/LSGM/LSCM a la misma temperatura y usando el mismo combustible, mezcla de hidrógeno-nitrógeno humedecido, y el mismo gas oxidante, aire. La diferencia llega a un 43% trabajando a 873 K.
10. Un *composite* de LSM y LSGM (LSM–LSGM) en una proporción de 30–70% en moles fue investigado como material de cátodo con LSGM como electrolito. Además, el efecto en el rendimiento electroquímico de la celda de una capa de *buffer* constituida por ceria dopada con samario, $Sm_{0,15}Ce_{0,85}O_{2-\delta}$ (SDC), entre el electrolito LSGM y el material de ánodo (LSCM) también fue investigada. Así, los sistemas LSM–LSGM/LSGM/LSCM y LSM/LSGM/SDC/LSCM, fueron comparados con los sistemas BSCF/LSGM/LSCM y LSM/LSGM/LSCM. Se utilizó una mezcla de hidrógeno-nitrógeno humedecido como combustible y aire como gas oxidante. Los valores de densidad de potencia de los sistemas LSM/LSGM/SDC/LSCM y LSM–LSGM/LSGM/LSCM ni siquiera alcanzarón un 50% de los valores obtenidos con el sistema BSCF/LSGM/LSCM.
11. La resistencia de polarización o *area-specific resistance* (ASR) de los compuestos $X_{0,5}Sr_{0,5}Co_{0,8}Fe_{0,2}O_{3-\delta}$ (XSCF o XSCoF) (X=Ba, La y Sm), $Sm_{0,5}Sr_{0,5}CoO_{3-\delta}$ (SSC), $La_{0,75}Sr_{0,25}Cr_{0,5}X'_{0,5}O_{3-\delta}$ (LSCX' o LSCrX') (X'=Mn, Fe y Al), así como de los composites SDC-LSCM y SDC-LSGM, fijados a un electrolito de LSGM fueron medidas y analizadas en diferentes gases: aire, oxígeno, argon, 5%H_2/95%Ar seco y humedecido. Los valores de resistencia de polarización en el rango de temperaturas 875–1175 K, del material BSCF (o BSCoF) fueron los más bajos en condiciones oxidantes, menos de 0,1 Ωcm^2 a temperaturas superiores a 1025 K, mientras que los más bajos en condiciones reductoras (5% H_2/Ar humedecido) pertenecen al material LSCM (o LSCrM), ~0,3 Ωcm^2 a 1073 K.

12. La variación de la resistencia de polarización (ASR) y de electrolito (R_s) del sistema BSCF/LSGM fue de 0,013 Ωcm^2 y 0,1 Ωcm (con un electrolito, LSGM, de ~1,5 mm de espesor) respectivamente, después de 30 horas de operación a 1073 K en aire. Mientras que la variación de la resistencia de polarización y R_s de LSCM fijado a LSGM no fue significativa, alrededor de 0,01 Ωcm^2 y 0,03 Ωcm respectivamente, después de 10 horas de operación a 1073 K en una atmósfera reductora (5%H_2/Ar humedecido).
13. Se efectuaron pruebas con combustible de los sistemas BSCF/LSGM/LSCX', BSCF/LSGM/Ni-SDC y LSCX'/LSGM/LSCX', y los valores más bajos de sobrepotencial de electrodo, resistencia de polarización (0,12 Ωcm^2) y resistencia de electrolito (9 Ωcm), a 1073 K, fueron los del sistema BSCF/LSGM/LSCM, que además alcanzó el máximo valor de densidad de potencia 122 mWcm^{-2}, a dicha temperatura, con un electrolito de 1,5 mm de espesor. Una extrapolación teórica indica un valor máximo posible de densidad de potencia de 1,6 Wcm^{-2} (con un electrolito de 120 µm de espesor) a una densidad de corriente de 3,6 Acm^{-2}. En cambio, con el sistema simétrico LSCM/LSGM/LSCM se alcanzó una valor máximo de densidad de potencia de 54 mWcm^{-2} a 1073 K, cerca de un 50% del valor máximo obtenido con el sistema BSCF/LSGM/LSCM. Sin embargo, una extrapolación teórica indica un valor máximo de 0,7 Wcm^{-2} a 1073 K.

Appendix I

Structural studies by X-ray diffraction

AI.1. $LaGaO_3$ and doped $LaGaO_3$ structures at room temperature

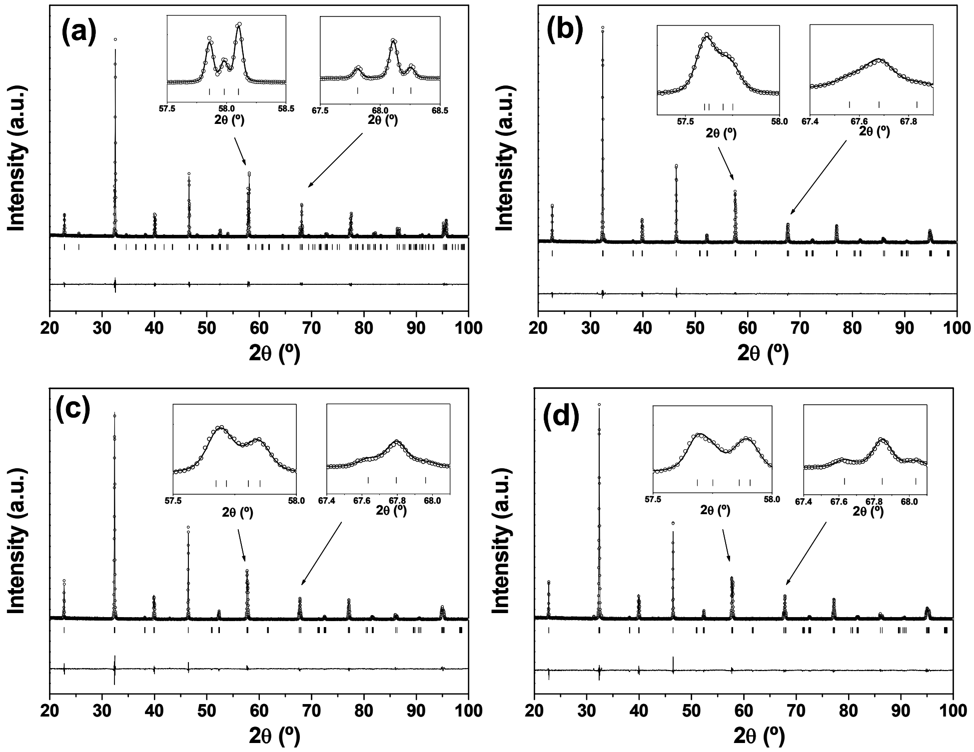

Figure AI.1. XRD patterns of LaGaO3 (a) $La_{0.9}Sr_{0.1}Ga_{0.8}Mg_{0.2}O_{2.85}$ (b), and $La_{0.9}Sr_{0.1}Ga_{0.8}Mg_{0.2-x}Co_xO_{3-\delta}$ where x=0.015 (c) and x=0.045 (d) at room temperature refined by Rietveld method.

Table AI.1.
Lattice parameters at room temperature of $LaGaO_3$ and doped $LaGaO_3$ samples

Composition	Space group	Lattice parameters (Å)			χ^2
		a	b	c	
$LaGaO_3$	Pnma	5.4917(2)	7.7735(3)	5.5234(2)	1.60
$La_{0.9}Sr_{0.1}Ga_{0.8}Mg_{0.2}O_{2.85}$	Ibmm	5.5218(6)	7.8263(9)	5.5415(5)	1.85
$La_{0.9}Sr_{0.1}Ga_{0.8}Mg_{0.185}Co_{0.015}O_{3-\delta}$	Ibmm	5.5127(5)	7.8132(6)	5.5360(4)	2.01
$La_{0.9}Sr_{0.1}Ga_{0.8}Mg_{0.155}Co_{0.045}O_{3-\delta}$	Ibmm	5.5073(5)	7.8066(7)	5.5363(4)	2.51
$La_{0.9}Sr_{0.1}Ga_{0.8}Mg_{0.125}Co_{0.075}O_{3-\delta}$	Ibmm	5.4920(9)	7.783(1)	5.5224(9)	2.78
$La_{0.9}Sr_{0.1}Ga_{0.8}Mg_{0.115}Co_{0.085}O_{3-\delta}$	Ibmm	5.4902(2)	7.7787(3)	5.5196(3)	2.80

AI.2. LaGaO3 and doped LaGaO3 structures by high temperature-XRD

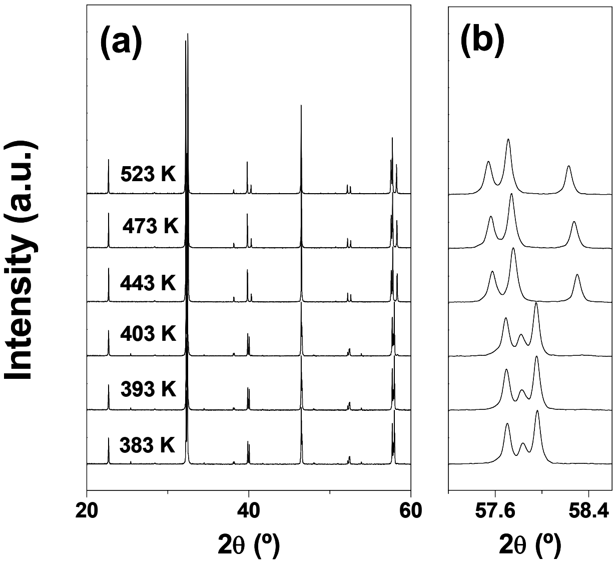

Figure AI.2. XRD patterns at different temperatures of $LaGaO_3$ (a) indicating a phase transition, in the range 403-443 K, from orthorhombic crystal system (Pnma) to rhombohedral (R-3c). Magnification in the range 2θ: 57.5-58.5° is illustrated (b) to clarify the phase transition.

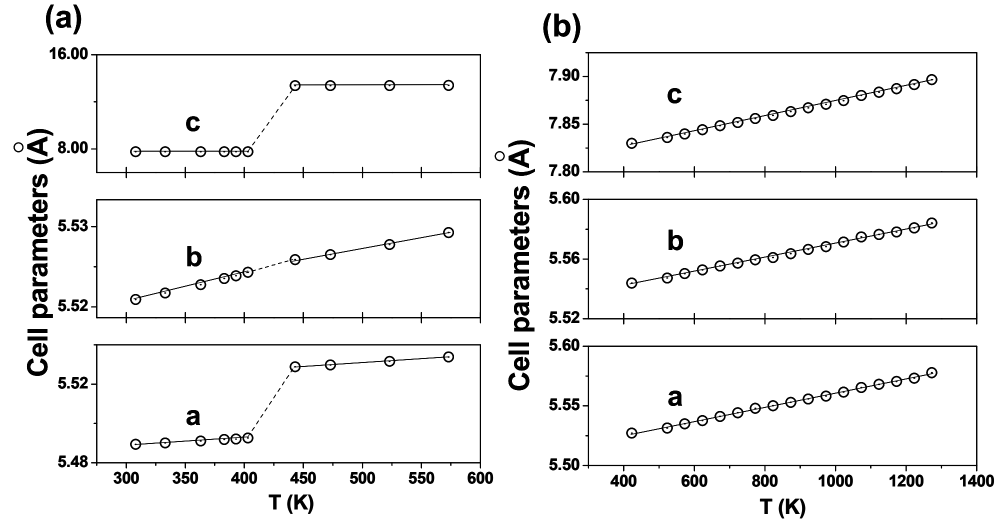

Figure AI.3. Variation of the cell parameter of LGO (a) and LSGM (b) *versus* temperature. The cell parameter variation is in a good agreement with the studies by neutron diffraction reported in the literature[1,2] whereas XRD patterns at high temperature of LSGM did not show any phase transition in the studied range and this is also in accord with the results of Shibasaki et al.[3]

---

[1] M. Kajitani, M. Matsuda, A. Hoshikawa, K. Oikawa, S. Torii, T. Kamiyama, F. Izumi, M. Miyake, *Chem. Mater.* **15** (2003) 3468-3473.

[2] M. Lerch, H. Boysen, T Hansen, *J.Phys. Chem. Solids* **62** (2001) 445-455.

[3] T. Shibasaki, T. Furuya, S. Wang, T. Hashimoto, *Solid State Ion.* **174** (2004) 193-203.

AI.3. XRD patterns of LSGM

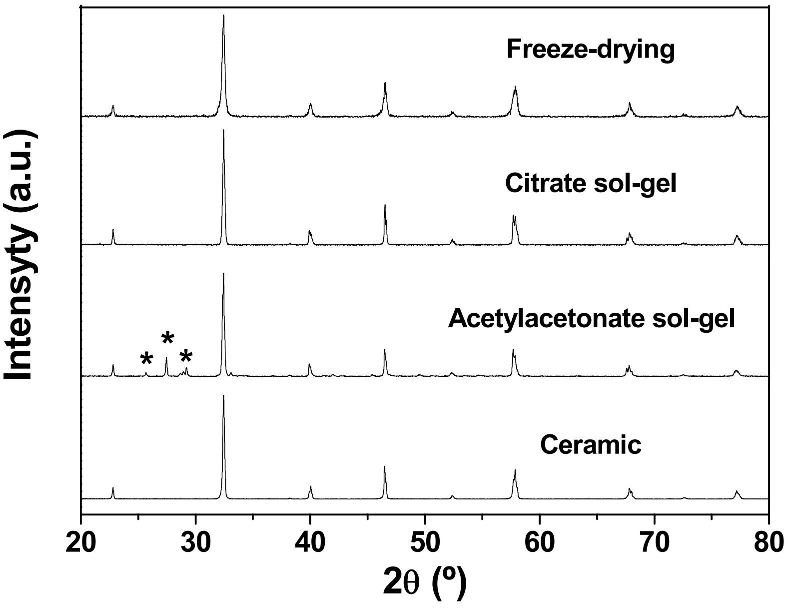

Figure AI.4. XRD patterns of LSGM samples synthesised by different methods fired at 1673 K for 6h. The extra peaks marked with * correspond to impurities phases.

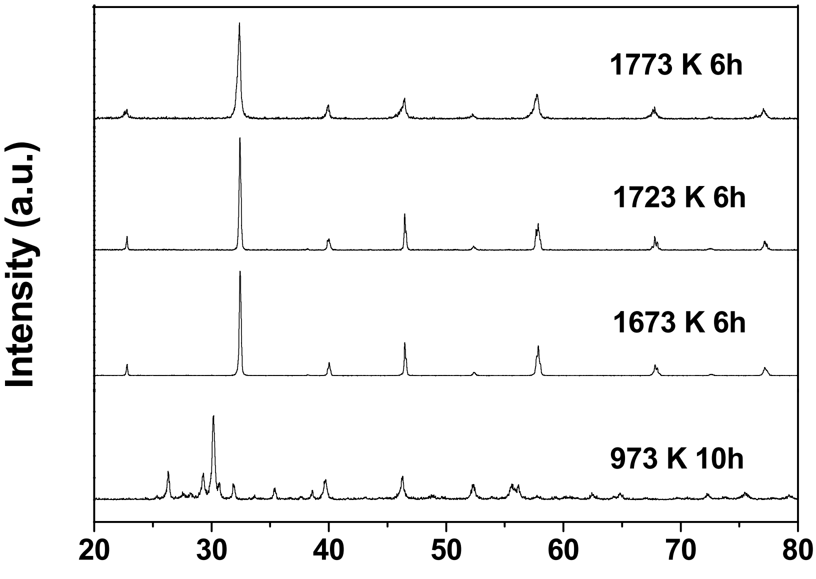

Figure AI.5. Temperature and time dependendence of XRD pattern of LSGM synthensised via solid state reaction.

AI.4. XRD patterns after exposure of wet 5%H_2/Ar gas flow

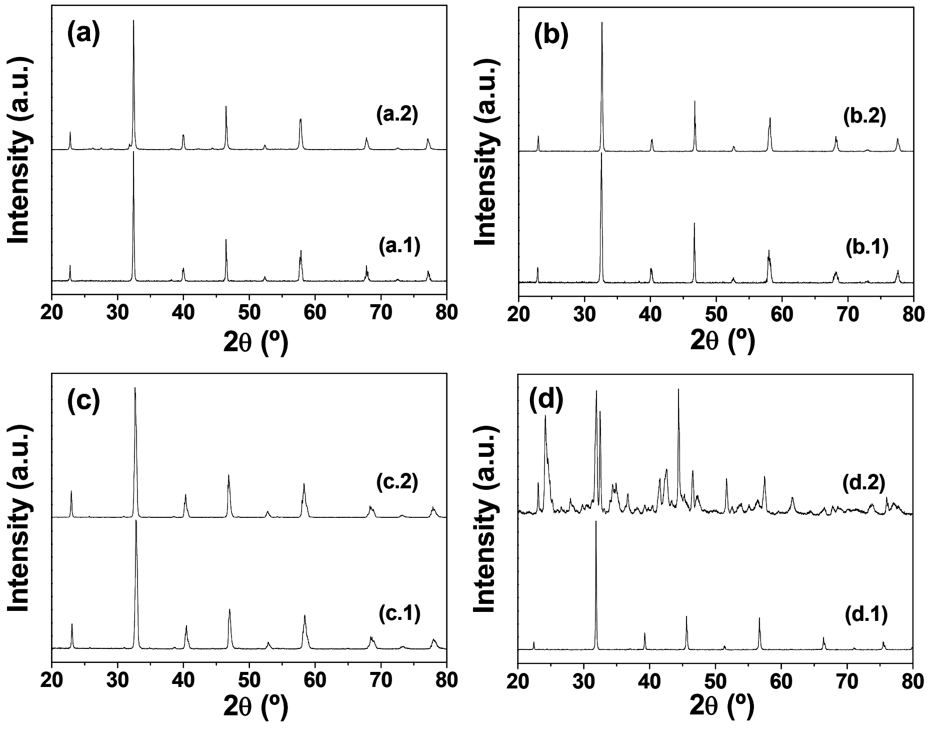

Figure AI.6. XRD pattern of a LSGM (a), LSGMC (b), LSCM (c) and BSCF (d) samples in air at room temperature (a.1, b.1, c.1, and d.1) and after exposure of wet 5%H_2/Ar gas flow at 973 K for 48 h (a.2, b.2, c.2 and d.2).

AI.5. XRD patterns of XSCF (X=Ba, La and Sm)

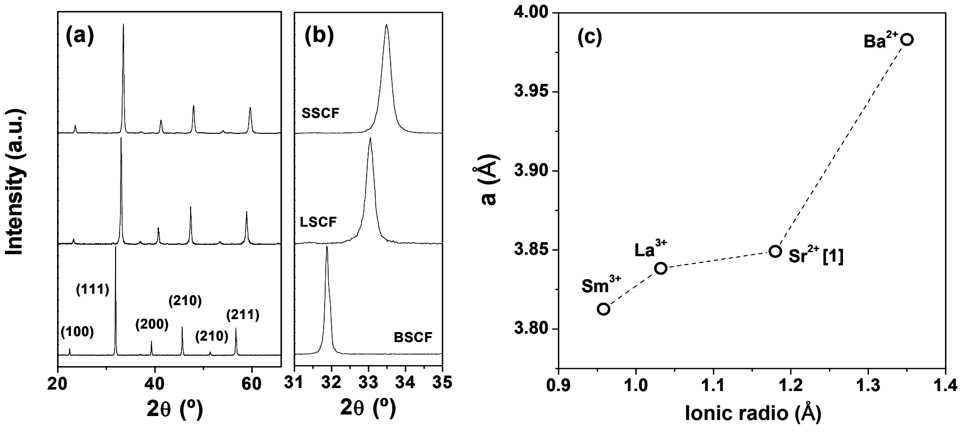

Figure AI.7. XRD patterns of BSCF, LSCF and SSCF (a) which are focused around the main peak (b).Variation of the cell parameter "a" of BSCF, LSCF, SSCF samples and $SrCo_{0.8}Fe_{0.2}O_{3-\delta}$ [1] *versus* the ionic radio of their corresponding cation, considered coordination number of six: Ba^{2+}, La^{3+}, Sm^{3+} and Sr^{2+}. [1] W.T.A. Harrison, T.H. Lee, Y.L. Yang, D. P. Scarfe, L.M. Liu, A.J. Jacobson, *Materials Reseach Bulletin* **30** (1995) 621-630.

Appendix II

BET surface area

The fundamental assumption in BET model is that the forces active in the condesation of gases are also responsible for the binding energy in multimolecular adsortion. By equating the rate of condensation of gas molecules onto an already adsorbed layer to the rate of evaporation from that layer and summing for an infinite number of layers, the expression

$$V_a = \frac{V_m CP}{\left(P_0 - P\right)\left[1 + \left(C-1\right)\frac{P}{P_0}\right]} \tag{II.1}$$

is obtained where C is a constant, P the actual gas pressure, P_0 the saturation pressure of the gas, V_a the gas adsorbed at standard conditions of temperature and pressure (0°C and 760 torr, signified by STP), V_m the quantity of gas adsorbed when the entire surface is covered with a monomolecular layer. Notice that $Q_a=V_a/g$ and $Q_m=V_m/g$. The value of C in simplest terms is

$$C \propto \exp\frac{q_1 - q_L}{RT} \tag{II.2}$$

where q_1 is the heat of adsortion of the firs layer, q_L the heat of liquefaction of the adsorptive, R the gas constant, and T the absolute temperature. Eq. II.1 also can be written in the linear form

$$\frac{P}{V_a\left(P_0 - P\right)} = \frac{1}{V_m C} + \frac{C-1}{V_m C}\left(\frac{P}{P_0}\right) \tag{II.3}$$

from which, if applicable, a plot of $P/[Q_a\ (P_0\text{-}P)]$ *versus* P/P_0 should yield a straight line with intercept $1/V_mC$ and slope $(C\text{-}1)/V_mC$. The values of V_m and C may then be obtained from a plot of a straight line, or regression line, through the points.

When nitrogen is the adsorptive,

$$s(m^2/g) = \frac{4.35V_m(cm^3 at\, STP)}{mass\,(g)} = 4.35Q_m(cm^3/g\ STP) \tag{II.4}$$

Isotherm data using nitrogen as the adsorptive and plotting them in accordance with Eq. II.3 yield a straight line, see Figure AII.1, between P/P_0 values from about 0.05 to 0.3, however the upper limit is sometimes as low as 0.2 and occasionally even lower. The value of C is most frequently between 50 and 300 when using nitrogen at 77 K. When the BET specific surface area is above 500 m^2/g and, particularly if the C value is above 300, the results should be questioned.

The BET surface areas of the different ceramic powdered materials studied in this work, using nitrogen gas as adsortive are listed in Table II.1. The temperature and method of synthesis are also indicated for better comparison. Freeze-drying method is named as 'FD'.

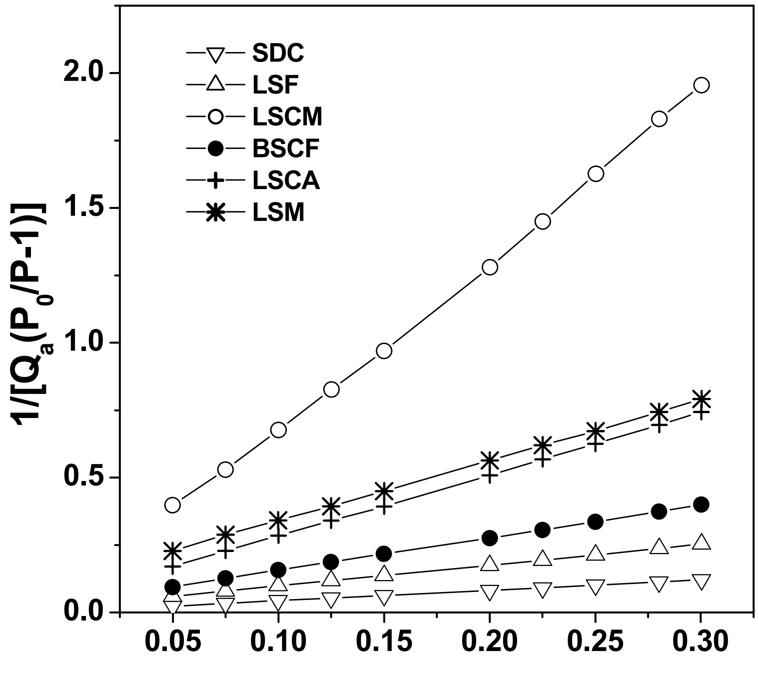

Figure AII.1. BET surface plots of several mixed-ionic conductors: $Sm_{0.5}Sr_{0.5}CoO_{3-\delta}$ (SDC), $La_{0.7}Sr_{0.3}FeO_{3-\delta}$ (LSF), $La_{0.75}Sr_{0.25}Cr_{0.5}Mn_{0.5}O_{3-\delta}$ (LSCM), $Ba_{0.5}Sr_{0.5}Co_{0.8}Fe_{0.2}O_{3-\delta}$ (BSCF), $La_{0.75}Sr_{0.25}Cr_{0.5}Al_{0.5}O_{3-\delta}$ (LSCA), and $La_{0.7}Sr_{0.3}MnO_{3-\delta}$ (LSM).

Table AII.1.
BET surface area of different perovskite-type structure materials and SDC fluorite material

Composition	T (K)	Synthesis method	BET surface area (m^2/g)	C	Q_m (cm^3/g STP)
$Ba_{0.5}Sr_{0.5}Co_{0.8}Fe_{0.2}O_{3-\delta}$	1323	Sol-gel	3.49 ± 0.01	35.63	0.8034
$La_{0.5}Sr_{0.5}Co_{0.8}Fe_{0.2}O_{3-\delta}$	1273	Sol-gel	2.99 ± 0.02	30.45	0.6705
$Sm_{0.5}Sr_{0.5}Co_{0.8}Fe_{0.2}O_{3-\delta}$	1323	Sol-gel	1.48 ± 0.02	13.39	0.3412
$Sm_{0.5}Sr_{0.5}Co_{0.8}Fe_{0.2}O_{3-\delta}$	1173	FD	3.71 ± 0.02	158.25	0.8525
$Sm_{0.5}Sr_{0.5}CoO_{3-\delta}$	1323	FD	1.99 ± 0.01	15.83	0.4586
$La_{0.75}Sr_{0.25}Cr_{0.5}Mn_{0.5}O_{3-\delta}$	1423	Ceramic	1.32 ± 0.01	88.27	0.3037
$La_{0.75}Sr_{0.25}Cr_{0.5}Mn_{0.5}O_{3-\delta}$	1723	Ceramic	0.68 ± 0.01	121.14	0.1581
$La_{0.75}Sr_{0.25}Cr_{0.5}Fe_{0.5}O_{3-\delta}$	1473	Sol-gel	4.11 ± 0.02	44.72	0.9448
$La_{0.75}Sr_{0.25}Cr_{0.5}Fe_{0.5}O_{3-\delta}$	1373	FD	6.83 ± 0.02	113.76	1.5691
$La_{0.75}Sr_{0.25}Cr_{0.5}Fe_{0.5}O_{3-\delta}$	1673	Ceramic	1.82 ± 0.04	105.58	0.4186
$La_{0.75}Sr_{0.25}Cr_{0.5}Al_{0.5}O_{3-\delta}$	1673	Sol-gel	1.86 ± 0.01	41.90	0.4283
$La_{0.7}Sr_{0.3}MnO_{3-\delta}$	1273	Sol-gel	1.85 ± 0.01	20.23	0.4249
$La_{0.7}Sr_{0.3}MnO_{3-\delta}$	1173	FD	8.29 ± 0.05	211.64	1.9064
$La_{0.7}Sr_{0.3}CrO_{3-\delta}$	1673	Sol-gel	1.93 ± 0.02	17.38	0.4424
$La_{0.7}Sr_{0.3}FeO_{3-\delta}$	1273	Sol-gel	5.51 ± 0.03	36.28	1.2670
$La_{0.7}Sr_{0.3}CoO_{3-\delta}$	1173	FD	3.30 ± 0.02	152.63	0.7587
$La_{0.9}Sr_{0.1}Ga_{0.8}Mg_{0.2}O_{2.85}$	1723	Ceramic	0.92 ± 0.01	34.38	0.2114
$La_{0.9}Sr_{0.1}Ga_{0.8}Mg_{0.115}Co_{0.085}O_{3-\delta}$	1648	Ceramic	0.31 ± 0.01	33.99	0.0728
$Sm_{0.15}Ce_{0.85}O_{2-\delta}$	773	Sol-gel	64.4 ± 0.2	82.81	14.8003
$Sm_{0.15}Ce_{0.85}O_{2-\delta}$	1173	Sol-gel	11.12 ± 0.03	87.83	2.5552

Appendix III

Density by helium pycnometry

Table AIII.1
Apparent density by helium pycnometry

Composition	T (K)	Synthesis method	Density (g/cm^3)	Standard deviation (g/cm^3)
$Ba_{0.5}Sr_{0.5}Co_{0.8}Fe_{0.2}O_{3-\delta}$	1323	Sol-gel	5.57	0.05
$La_{0.5}Sr_{0.5}Co_{0.8}Fe_{0.2}O_{3-\delta}$	1273	Sol-gel	7.32	0.30
$Sm_{0.5}Sr_{0.5}Co_{0.8}Fe_{0.2}O_{3-\delta}$	1323	Sol-gel	6.94	0.11
$Sm_{0.5}Sr_{0.5}Co_{0.8}Fe_{0.2}O_{3-\delta}$	1173	FD	6.75	0.09
$Sm_{0.5}Sr_{0.5}CoO_{3-\delta}$	1323	FD	6.40	0.07
$La_{0.75}Sr_{0.25}Cr_{0.5}Mn_{0.5}O_{3-\delta}$	1423	Ceramic	6.32	0.02
$La_{0.75}Sr_{0.25}Cr_{0.5}Mn_{0.5}O_{3-\delta}$	1723	Ceramic	6.77	0.05
$La_{0.75}Sr_{0.25}Cr_{0.5}Fe_{0.5}O_{3-\delta}$	1473	Sol-gel	6.12	0.04
$La_{0.75}Sr_{0.25}Cr_{0.5}Fe_{0.5}O_{3-\delta}$	1373	FD	6.66	0.08
$La_{0.75}Sr_{0.25}Cr_{0.5}Fe_{0.5}O_{3-\delta}$	1673	Ceramic	8.28	0.33
$La_{0.7}Sr_{0.3}MnO_{3-\delta}$	1273	Sol-gel	6.15	0.07
$La_{0.7}Sr_{0.3}MnO_{3-\delta}$	1173	FD	7.59	0.23
$La_{0.7}Sr_{0.3}CrO_{3-\delta}$	1673	Sol-gel	5.89	0.05
$La_{0.7}Sr_{0.3}FeO_{3-\delta}$	1273	Sol-gel	6.16	0.14
$La_{0.7}Sr_{0.3}CoO_{3-\delta}$	1173	FD	6.69	0.09
$Sm_{0.15}Ce_{0.85}O_{2-\delta}$	773	Sol-gel	6.76	0.03

Appendix IV

Ionic transport numbers

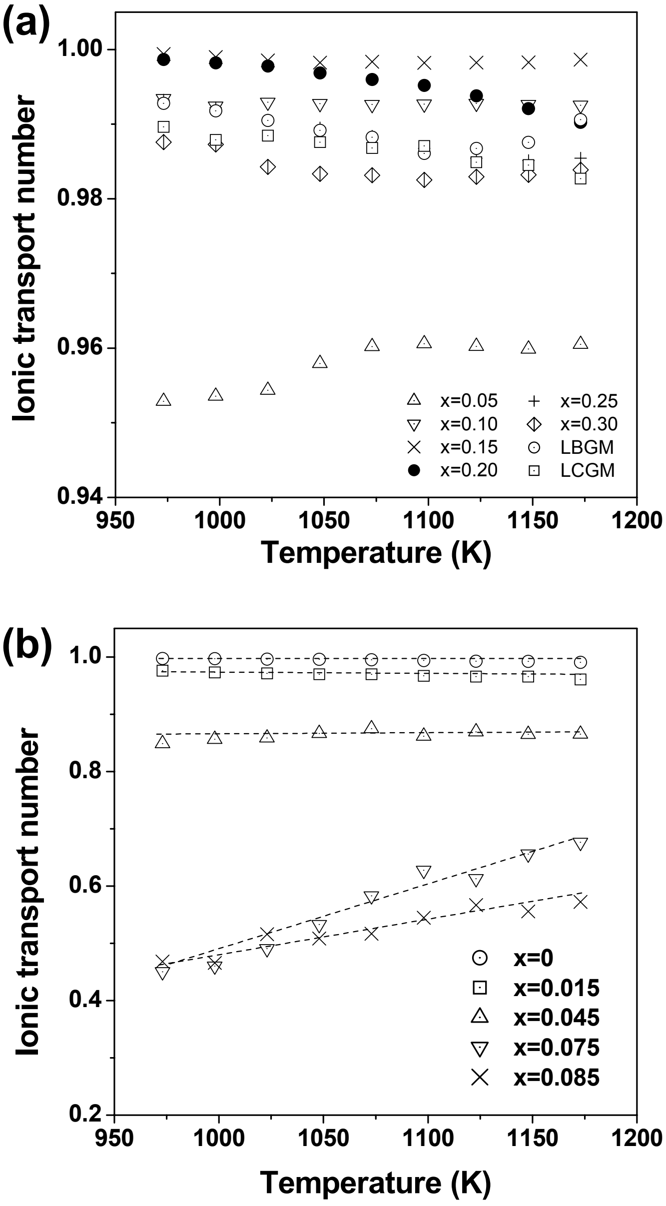

Figure AIV.1. Temperature dependence of the ionic transport numbers, estimated by a modified *emf* method under O_2/air gradient of (a) $La_{0.9}Sr_{0.1}Ga_{1-x}Mg_xO_{3-(0.1+x)/2}$ (x=0.05, 0.10, 0.15, 0.20, 0.25, 0.30) and $La_{0.9}A_{0.1}Ga_{0.8}Mg_{0.2}O_{2.85}$ (A=Ba, Sr), and (b) $La_{0.9}Sr_{0.1}Ga_{0.8}Mg_{0.2-x}Co_xO_{3-\delta}$ (x=0, 0.015, 0.045, 0.075 and 0.085).

Abbreviations

AC	Alternate Current
AFC	Alkaline Fuel Cell
BET	Brunauer-Emmet-Teller adsorption model
BSCF/BSCoF	$Ba_{0.5}Sr_{0.5}Co_{0.8}Fe_{0.2}O_{3-\delta}$
Cermet	Ceramic-Metal composite
CGO	Cerium-Gadolinium-Oxide
CPE	Constant Phase Element
DC	Direct Current
DSC	Differential Scanning Calorimetry
EDS	Energy Dispersive X-Ray Spectroscopy
EIS	Electrochemical Impedance Spectroscopy
FD	Freeze-drying method
ICP	Inductively Coupled Plasma
IT-SOFC	Intermediate Temperature Solid Oxide Fuel Cell
LSC/LSCo	$La_{1-x}Sr_xCoO_{3-\delta}$
LSCF/LSCrF	$La_{0.75}Sr_{0.25}Cr_{0.5}Fe_{0.5}O_{3-\delta}$
LSCoF	$La_{0.5}Sr_{0.5}Co_{0.8}Fe_{0.2}O_{3-\delta}$
LSCM/LSCrM	$La_{0.75}Sr_{0.25}Cr_{0.5}Mn_{0.5}O_{3-\delta}$
LSCA/LSCrA	$La_{0.75}Sr_{0.25}Cr_{0.5}Al_{0.5}O_{3-\delta}$
LSGM	$La_{0.9}Sr_{0.1}Ga_{0.8}Mg_{0.2}O_{2.85}$
LSGMC/LSGMCo	$La_{0.9}Sr_{0.1}Ga_{0.8}Mg_{0.115}Co_{0.085}O_{3-\delta}$
LSM	$La_{1-x}Sr_xMnO_{3-\delta}$
MCFC	Molten Carbonate Fuel Cell
MIEC	Mixed Ionic Electronic Conduction / Conductor
Ni -YSZ	Cermet of Nickel and YSZ
OCV	Open Circuit Voltage
PAFC	Phosphoric Acid Fuel Cell
PEMFC	Proton Exchange Membrane Fuel Cell
PLD	Pulsed Laser Deposition
SDC	Samaria Doped Ceria
SEM	Scanning Electron Microscopy
SOFC	Solid Oxide Fuel Cell
SSCo	$Sm_{0.5}Sr_{0.5}CoO_{3-\delta}$
SSCoF	$Sm_{0.5}Sr_{0.5}Co_{0.8}Fe_{0.2}O_{3-\delta}$
TEC	Thermal Expansion Coefficient
TEM	Transmission Electron Microscopy
TG/DTA	Thermogravimetry/ Differential Thermal Analysis
TMA	Thermo Mechanical Analysis
TPB	Triple Phase Boundary
YSZ	Yttria Stabilized Zirconia
XRD	X-Ray Diffraction

Symbols

E_A	[eV]	Activation energy
emf	[V]	Electromotive force
E_{th}	[V]	Theoretical *emf*
E_{exp}	[V]	Experimental *emf*
f	[s-1, Hz]	Frequency
F	[C/mol]	Faraday constant
I	[A]	Electrical current
k_B	[J/K]	Boltzmann constant
N_A	[1/mol]	Avogadro number
O^{2-}	[-]	Oxygen ion
P_{O2}	[atm]	Partial pressure of oxygen
R_s	[Ωcm]	Electrolyte resistance
R_p	[Ωcm^2]	Polarisation resistance
T	[K]	Temperature
V	[V]	Voltage/ potential difference
Z	[Ω]	Total electrochemical impedance
$\|Z\|$	[Ω]	Absolute impedance
Z'	[Ω]	Real part of the impedance
Z''	[Ω]	Imaginary part of the impedance

Greek symbols

ε	[C V^{-1} m^{-1}]	Dielectric constant
η	[V]	Overpotential
η_a	[V]	Anodic overpotential
η_c	[V]	Cathodic overpotential
σ	[Scm^{-1}]	Conductivity
σ_o	[Scm^{-1}]	Ionic conductivity
σ_e	[Scm^{-1}]	Electronic conductivity
ω	[s^{-1}]	Angular frequency

List of Publications

- J. Peña-Martínez, D. Marrero-López, J.C. Ruiz-Morales, C. Savaniu, P. Núñez, J.T.S. Irvine, *Anodic Performance and Intermediate Temperature Fuel Cell Testing of* $La_{0.75}Sr_{0.25}Cr_{0.5}Mn_{0.5}O_{3-\delta}$ *at Lanthanum Gallate Electrolytes,* Chemistry of Materials 18 (2006) 1001-1006.
- J. Peña-Martínez, D. Marrero-López, J.C. Ruiz-Morales, B. E. Buergler, P. Núñez, L.J. Gauckler, *SOFC test using* $Ba_{0.5}Sr_{0.5}Co_{0.8}Fe_{0.2}O_{3-\delta}$ *as cathode on* $La_{0.9}Sr_{0.1}Ga_{0.8}Mg_{0.2}O_{2.85}$ *electrolyte*, Solid State Ionics 177 (2006) 2143-2147.
- J. Peña-Martínez, D. Marrero-López, J.C. Ruiz-Morales, B. E. Buergler, P. Núñez, L.J. Gauckler, *Fuel cell studies of perovskite-type materials for IT-SOFC*, Journal of Power Sources 159 (2006) 914-921.
- J. Peña-Martínez, D. Marrero-López, D. Pérez-Coll, J.C. Ruiz-Morales, P. Nuñez, *Performance of XSCoF (X = Ba, La and Sm) and LSCrX' (X' = Mn, Fe and Al) perovskite-structure materials on LSGM electrolyte for IT-SOFC*, Electrochimica Acta 52 (2007) 2950-2958.
- D. Marrero-López, J. Peña-Martínez, D. Pérez-Coll, P. Núñez, *Effects of preparation method on the microstructure and transport properties of* $La_2Mo_2O_9$ *based materials*, Journal of Alloys and Compounds 422 (2006) 249-257.
- J.C. Ruiz-Morales, J. Canales-Vázquez, J. Peña-Martínez, D. Marrero-López, P. Núñez, *On the simultaneous use of as both anode and cathode material with improved microstructure in solid oxide fuel cells*, Electrochimica Acta 52 (2006) 278-274.
- J.C. Ruiz-Morales, J. Canales-Vázquez, J. Peña-Martínez, D. Marrero-López, J.T.S. Irvine, P. Núñez, *Microstructural optimisation of materials for SOFC applications using PMMA microspheres*, Journal of Materials Chemistry 16 (2006) 540-542.
- D. Pérez-Coll, P.Núñez, J.C. Ruiz-Morales, J. Peña-Martínez, J.R. Frade, *Re-examination of bulk and grain boundary conductivities of* $Ce_{1-x}Gd_xO_{2-\delta}$ *ceramics*, Electrochimica Acta 52 (2007) 2001-2008.